# Proceedings of the High Energy Density Matter (HEDM) Contractors' Conference Held 5-7 June 1996 in Boulder CO

Patrick G. Carrick, Editor
Lt. Neal T. Williams, Editor

March 1997

Special Report

19970522 035

DTIC QUALITY INSPECTED 3

**PHILLIPS LABORATORY**
**Propulsion Directorate**
**AIR FORCE MATERIEL COMMAND**
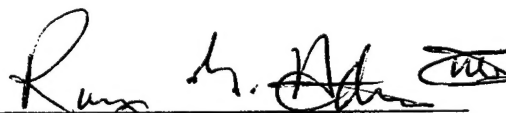**EDWARDS AIR FORCE BASE CA 93524−7048**

## NOTICE

When U.S. Government drawings, specifications, or other data are used for any purpose other than a definitely related Government procurement operation, the fact that the Government may have formulated, furnished, or in any way supplied the said drawings, specifications, or other data, is not to be regarded by implication or otherwise, or in any way licensing the holder or any other person or corporation, or conveying any rights or permission to manufacture, use or sell any patented invention that may be related thereto.
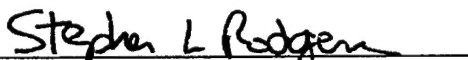
## FOREWORD

This Conference Proceedings was compiled and edited by Dr. Patrick G. Carrick and Lt. Neal Williams, OL-AC Phillips Laboratory, Edwards AFB CA.

This report has been reviewed and is approved for release and distribution in accordance with the distribution statement on the cover and on the SF Form 298.


PATRICK G. CARRICK
Project Manager

RANNEY G. ADAMS III     OLAC PL-PAS
Public Affairs Director     97-046


STEPHEN L. RODGERS
Director
Propulsion Sciences Division

DTIC QUALITY INSPECTED 3

| REPORT DOCUMENTATION PAGE | | Form Approved OMB No 0704-0188 |
|---|---|---|

Public reporting burden for this collection of information is estimated to average 1 hour per response, including the time for reviewing instructions searching existing data sources gathering and maintaining the data needed, and completing and reviewing the collection of information. Send comments regarding this burden estimate or any other aspect of this collection of information, including suggestions for reducing this burden to Washington Headquarters Services, Directorate for Information Operations and Reports, 1215 Jefferson Davis Highway, Suite 1204, Arlington, VA 22202-4302, and to the Office of Management and Budget, Paperwork Reduction Project (0740-0188), Washington DC 20503,

| 1. AGENCY USE ONLY (LEAVE BLANK | 2. REPORT DATE March 1997 | 3. REPORT TYPE AND DATES COVERED Special Report 8 Jun 95 – 7 Jun 96 |
|---|---|---|

| 4. TITLE AND SUBTITLE | 5. FUNDING NUMBERS |
|---|---|
| **Proceedings of the High Energy Density Matter (HEDM) Contractors' Conference Held 5-7 June 1996 in Boulder CO** | C: <br> PE: 62302F <br> PR: 2303 <br> TA: M2C8 |

**6. AUTHOR(S)**

**Patrick G. Carrick, Editor**
**Lt. Neal T. Williams, Editor**

| 7. PERFORMING ORGANIZATION NAME(S) AND ADDRESS(ES) | 8. PERFORMING ORGANIZATION REPORT NUMBER |
|---|---|
| Phillips Laboratory <br> OL-AC PL/RKS <br> 10 E. Saturn Blvd. <br> Edwards AFB CA 93524-7680 | PL-TR-96-3037 |

| 9. SPONSORING/MONITORING AGENCY NAME(S) AND ADDRESS(ES) | 10. SPONSORING/MONITORING AGENCY REPORT NUMBER |
|---|---|
| | |

11. SUPPLEMENTARY NOTES: Extended abstracts from the Tenth High Energy Density Matter Contractors' Conference

COSATI CODE(S): 2005; 2109

| 12a. DISTRIBUTION/AVAILABILITY STATEMENT | 12b. DISTRIBUTION CODE |
|---|---|
| **APPROVED FOR PUBLIC RELEASE** <br> **DISTRIBUTION IS UNLIMITED** | A |

13. ABSTRACT (MAXIMUM 200 WORDS)

This report documents the information presented at the tenth annual High Energy Density Matter (HEDM) Contractors' Conference held 5-7 June 1996 in Boulder CO. This report contains the extended abstracts of the oral, workshop, and poster presentations given by the Air Force funded contractors and by the in-house researchers from the Phillips Laboratory.

| 14. SUBJECT TERMS | 15. NUMBER OF PAGES |
|---|---|
| HEDM; high energy density matter; propellant; solid hydrogen; cryogenic materials; potential energy surfaces | 257 |
| | 16. PRICE CODE |

| 17. SECURITY CLASSIFICATION OF REPORT | 18. SECURITY CLASSIFICATION OF THIS PAGE | 19. SECURITY CLASSIFICATION OF ABSTRACT | 20. LIMITATION OF ABSTRACT |
|---|---|---|---|
| Unclassified | Unclassified | Unclassified | SAR |

NSN 7540-010280-5500

i/ii

Standard Form 298 (Rev 2-89)
Prescribed by ANSI Std 239-18
298-102

# TABLE OF CONTENTS

## TABLE OF CONTENTS (Continued)

# TABLE OF CONTENTS (Continued)

## Introduction

The main purpose of the High Energy Density Matter (HEDM) program is to research and develop advanced high energy propellants containing increased energy densities (energy to mass ratio) to produce greater specific impulse (thrust per weight flow rate of propellant), which will enable significantly increased payloads for rockets and missiles. With these advanced propellants, future space-bound payloads could be potentially four times greater than current systems for the same overall size and weight. Theoretical and experimental research is carried out by in-house researchers at the Phillips Laboratory, Propulsion Directorate, at Edwards Air Force Base and through Air Force funded contracts with numerous researchers in academic and industrial laboratories.

The HEDM program is administered by a steering group made up of representatives from the Phillips Laboratory Propulsion Directorate and the Air Force Office of Scientific Research (AFOSR). A technical panel administered by the Universal Energies Systems assisted the steering group in ensuring the high technical content of the program.

Annual conferences, hosted by the AFOSR and the Phillips Laboratory, are arranged to allow in-house and contract researchers to report on their progress and new developments. The Tenth High Energy Density Matter Contractors' Conference was held 5-7 June 1996 in the auditorium of the JILA Tower on the campus of the University of Colorado, Boulder, CO. The conference consisted of a kick-off BBQ at Flagstaff, MT on Wednesday afternoon with registration and a HEDM poster session that night. Thursday began with introductory remarks and continued with technical sessions on cryogenic solids, theory, synthesis, and advanced concepts. Thursday night concluded with a Theory/Synthesis Workshop. Friday was a continuation of technical talks.

This report documents the information presented at this conference and contains extended abstracts of the oral presentations, special sessions, and poster session given at the conference. The next HEDM conference is scheduled for 1-4 June 1997 in Washington, DC.

## Wednesday, 5 June 1996

Afternoon            BBQ at Flagstaff Mt. (Joint with Molecular Dynamics)

6:00 - 7:00          Registration

7:00 - 9:30          HEDM Poster Session

## Thursday, 6 June 1996

8:30 - 8:45          Introductory Remarks, *Dr. Michael Berman, AFOSR*

8:45 - 9:00          Phillips Laboratory Remarks
                     *Dr. Pat Carrick, Phillips Laboratory*

9:00 - 9:15          Phillips Laboratory Remarks
                     *Dr. Stephen L. Rodgers, Phillips Laboratory*

9:15 - 9:30          *Break*

9:30 - 10:00         Solid Hydrogens Doped with Atomic and Molecular Oxygen
                     *Dr. V. Ara Apkarian, University of California*

10:00 - 10:30        Mass Spectrometry Studies of Pick Up by Helium Clusters
                     *Dr. Ken Janda, University of California*

10:30 - 11:00        Calorimetric Measurements of O Atom Concentration in a Solid Ar
                     Matrix
                     *Dr. Peter Taborek, University of California, Irvine*

11:00 - 11:30        Status Report of Cryogenic Solid Hybrid Rocket Engine
                     Development for HEDM Demonstrations
                     *Dr. Eric Rice, Orbitec, Inc.*

11:30 - 12:45        *Lunch*

12:45 - 1:15         Progress Toward Depositions of Velocity Selected Aluminum
                     Atoms into Cryogenic para-Hydrogen Matrices
                     *Dr. Mario E. Fajardo, Phillips Laboratory*

**Thursday, 6 June 1996 (cont'd)**

| | |
|---|---|
| 1:15 - 1:45 | Spectral Theory of Physical and Chemical Binding in HEDM Systems<br>*Dr. Jeffrey A. Sheehy, Phillips Laboratory* |
| 1:45 - 2:15 | Quantum Molecular Dynamics Simulations of Low Temperature Hydrogen Systems<br>*Dr. Gregory A. Voth, University of Pennsylvania* |
| 2:15 - 2:45 | The Interaction of Alkali Atoms with Large Clusters of $n$-$H_2$, $p$-$H_2$, and $p$-$D_2$ Probed by Laser Spectroscopy<br>*Dr. Giacinto Scoles, Princeton University* |
| 2:45 - 3:00 | *Break* |
| 3:00 - 3:30 | Resonant Photoionization Spectroscopy of $Al(Ar)_n$ Clusters<br>*Dr. Mitchio Okumura, California Institute of Technology* |
| 3:30 - 4:00 | Spectroscopic Characterization of Non-Bonding Interactions of the Boron Atom<br>*Dr. Paul J. Dagdigian, The Johns Hopkins University* |
| 4:00 - 4:30 | Structure and energetics of $B(Ar)_n$ and $B(N_2)$ Clusters<br>*Dr. Millard H. Alexander, University of Maryland* |
| 7:30 | Theory/Synthesis Workshop |

**Friday, 7 June 1996**

| | |
|---|---|
| 8:15 - 8:45 | Cryogenic Solid Combustion<br>*Dr. William Larson, Phillips Laboratory* |
| 8:45 - 9:15 | Generation of Energetic Species in Solid Oxygen with Tunable Ultraviolet Light<br>*Dr. Richard A. Copeland, SRI International* |
| 9:15 - 9:45 | The Overtone $Q_v(0)$ Transitions in Hydrogen<br>*Dr. Takeshi Oka, The University of Chicago* |
| 9:45 - 10:15 | Search for Metallic Hydrogen in the Extended Infrared<br>*Dr. Isaac F. Silvera, Harvard University* |
| 10:15 - 10:45 | *Break* |

| | |
|---|---|
| 10:45 - 11:15 | Reactions of Laser-Ablated Boron Atoms with $NH_3$, $CH_3NH_2$ and NO to Form Novel Boron Insertion Products<br>*Dr. Lester Andrews, University of Virginia* |
| 11:15 - 11:45 | Excited States for Molecules and Clusters<br>*Dr. Rodney J. Bartlett, University of Florida* |
| 11:45 - 12:15 | Nonadiabatic Processes Affecting Detection and Preparation of Energetic Materials<br>*Dr. David R. Yarkony, Johns Hopkins University* |
| 12:15 - 12:45 | Potential Energy Surfaces and dynamics for High Energy Species<br>*Dr. Mark S. Gordon, Iowa State University* |
| 12:45 - 2:00 | *Lunch* |
| 2:00 - 2:30 | Discussion |
| 2:30 - 3:00 | Quantum Mechanical Study of the Energetics of $C_8H_8$ Hydrocarbons<br>*Dr. E. J. Wucherer, Phillips Laboratory* |
| 3:00 - 3:30 | Synthesis of High-Energy Density Materials Based on Strain-Ring compounds<br>*Dr. William P. Dailey, University of Pennsylvania* |
| 3:30 - 3:45 | *Break* |
| 3:45 - 4:15 | Recent Progress in the Theory and synthesis of Novel High Energy Density Materials<br>*Dr. Karl O. Christe, Hughes STX and Propulsion Sciences Division* |
| 4:15 - 4:45 | Extra-High energy Oxidizers and Fuels<br>*Dr. Robert J. Schmitt, SRI International* |
| 4:45 - 5:00 | Closing Remarks, adjournment |

Millard H. Alexander
Dept of Chemistry & Biochemistry
University of Maryland
College Park, MD  20742-2021
301-405-1823
Fax - 301-314-9121
mha@mha-ibm2.umd.edu

Scott L. Anderson
Dept. of Chemistry
University of Utah
1216 HEB -
Salt Lake City City, UT  84112
801-585-7289
Fax - 801-581-8433
anderson@chemistry.utah.edu

Lester Andrews
Dept. of Chemistry
University of Virginia
McCormick Road
Charlottesville, VA  22901
804-924-3513
Fax -804-924-3710
LSA@virginia.edu

Eric B. Anthony
Leone Group
JILA, University of Colorado
Campus Box 440
Boulder, CO  80309
303-492-7771
Fax - 303-492-5235
anthonye@jila.colorado.edu

V. Ara Apkarian
Dept. of Chemistry
University of California
Irvine, CA   92717-1875
714-824-6851
Fax - 714-824-8571
aapkaria@uci.edu

Peter S. Armstrong
Stewart Radiance Laboratory
139 Great Road
Bedford, MA  01730-2796
617-377-7380
Fax - 617-377-8900
armstrong@plh.af.mil

Jon Baker
Dept. of Chemistry
University of Arkansas
Fayetteville, AR  72701
501-575-5080
Fax - 501-575-4049
baker@uafchem1.uark.edu

Rodney J. Bartlett
Dept. of Chemistry
University of Florida
Quantum Theory Project
362 Williamson Hall
Gainesville, FL  32611
352-392-1597
Fax -352-392-8722
bartlett@qtp.ufl.edu

Michael J. Bastian
Phillips Laboratory
PL/GPID
29 Randolph Road
Hanscom AFB, MA  01731
617-377-2331
Fax - 617-377-8202
bastian@zircon.plh.af.mil

Michal Ben-Nun
Dept. of Chemistry
University of California, San Diego
9500 Gilman Drive, MS 0339
San Diego, CA  92093
619-534-0290
Fax - 619-534-7645
mbennun@sdchemw1.ucsd.edu

David J. Benard
Rockwell Science Center
Dept D/252, MS A-27
P.O. Box 1085
Thousand Oaks, CA 91358
805-373-4278
Fax - 805-373-4158

Michael R. Berman
AFOSR/NL
110 Duncan Ave., Ste B115
Bolling AFB, DC 20332-8080
202-767-4963
Fax - 202-404-7475
berman@afosr.af.mil

Veronica M. Bierbaum
Dept. of Chemistry & Biochemistry
University of Colorado
MS CB 215
Boulder, CO 80309-0215
303-492-7081
Fax - 303-492-5894
veronica.bierbaum@colorado.edu

William A.M. Blumberg
Phillips Laboratory
PL/GPOS
29 Randolph Road
Hanscom AFB, MA 01731-3010
617-377-3688
Fax - 617-377-8900
blumberg@plh.af.mil

Jerry A. Boatz
Phillips Laboratory
Propulsion Sciences Division
10 East Saturn Boulevard
Edwards AFB, CA 93524-7680
805-275-5364
Fax - 805-275-5471
jerry@helium.ple.af.mil

Michael T. Bowers
Dept. of Chemistry
University of California
Santa Barbara, CA 93106-9510
805-893-2893
bowers@sbmml.ucsb.edu

Christopher R. Brazier
PL/RKS
Hughes STX
10 East Saturn Boulevard
Edwards AFB, CA 93524-7680
805-275-5951
Fax - 805-275-5471
brazier@lablink.ple.af.mil

Berton E. Callicoatt
Dept. of Chemistry
Univsity of California, Irvine
Irvine, CA 92717
714-824-2613
Fax - 714-824-3168
bert@salt.ps.uci.edu

Patrick G. Carrick
PL/RKS
10 E. Saturn Blvd
Edwards AFB, CA 93524-7680
805-275-5883
Fax - 805-275-5471
patrick_carrick@ple.af.mil

Michael P. Casassa
National Institute of Standards and
  Technology
MS B208/221
Gaithersburg, MD 20899-0001
301-975-2371
Fax - 301-869-5700
mpc@micf.nist.gov

A. Welford Castleman, Jr.
Dept. of Chemistry
The Pennsylvania State University
152 Davey Laboratory
University Park, PA 16802-6300
814-865-7242
Fax - 814-865-5235
awc@psuvm.psu.edu

Galina Chaban
Dept. of Chemistry
Iowa State University
201 Spedding Hall
Ames, IA 50011
515-294-4604
Fax - 505-294-0105
galina@si.fi.ameslab.gov

Karl O. Christe
Phillips Laboratory
Hughes STX
Edwards AFB, CA 93524-7680
805-275-5194
Fax - 805-275-5471
karl_christe@ple.af.mil

Ara Chutjian
Jet Propulsion Laboratory
4800 Oak Grove Drive, MS 121-114
Pasadena, CA 91109
818-393-1899
Fax - 818-393-1899
ara.chutjian@jpl.nasa.gov

Robert E. Continetti
Dept. of Chemistry & Biochemistry
University of California, San Diego
9500 Gilman Drive, MS 0314
La Jolla, CA 92093-0314
619-534-5559
Fax - 619-534-7042
rcontinetti@ucsd.edu

Robert D. Coombe
Dept. of Chemistry
University of Denver
Denver, CO 80208
303-871-2993
Fax - 303-871-2254
rcoombe@du.edu

Richard A. Copeland
SRI International
Molecular Physics Laboratory
333 Ravenswood Avenue
Menlo Park, CA 94025
415-859-6534
Fax - 415-859-6196
rich@mplvax.sri.com

F. Fleming Crim
Dept. of Chemistry
University of Wisconsin
1101 University Avenue
Madison, WI 53706
608-263-7364
Fax - 608-262-9918
fcrim@chem.wisc.edu

Paul J. Dagdigian
Dept. of Chemistry
Johns Hopkins University
34th and Charles Streets
Remsen Hall
Baltimore, MD 21218
410-516-7438
Fax - 410-516-8420
pjdagdigian@jhu.edu

William P. Dailey
Dept. of Chemistry
University of Pennsylvania
Philadelphia, PA 19104-6323
215-898-2704
Fax - 215-573-2112
dailey@dailey6.chem.upenn.edu

Christopher E. Dateo
ELORET
Thermosciences Institute
NASA Ames Research Center
MS 230-3
Moffett Field, CA 94035-1000
415-604-6209
Fax - 415-604-0350
dateo@pegasus.arc.nasa.gov

Steven J. Davis
Physical Sciences, Inc.
20 New England Business Center
Andover, MA 01810
508-689-0003
Fax - 508-689-3232
sdavis@psicorp.com

Joost A. de Gouw
JILA, University of Colorado
Campus Box 440
Boulder, CO 80309-0440
303-492-0918
Fax - 303-492-5235
degouw@jila.colorado.edu

James A. Dodd
Stewart Radiance Laboratory
139 Great Road
Bedford, MA 01730
617-377-3626
Fax - 617-377-8900
dodd@pldac.plh.af.mil

Rainer A. Dressler
PL/WSAI
29 Randolph Road
Hanscom AFB, MA 01731-3010
617-377-2332
Fax - 617-377-5571
dressler@plh.af.mil

Michael A. Duncan
Dept. of Chemistry
University of Georgia
Athens GA 30602
706-542-1998
Fax - 706-542-9454
maduncan@uga.cc.uga.edu

Michael A. Everest
Dept. of Chemistry
Stanford University
Box 147
Stanford, CA 94305
415-723-4332
Fax - 415-725-0259
mikus@leland.stanford.edu

Mario E. Fajardo
USAF Propulsion Directorate
OL-AC PL/RKS
Edwards AFB, CA 93524-7680
805-275-5946
Fax - 805-275-5471
fajardom@lablink.ple.af.mil

Michael D. Fayer
Dept. of Chemistry
Stanford University
Stanford, CA 94305
415-723-4446
Fax - 415-723-4817
fayer@d31mf0.stanford.edu

Robert W. Field
Dept. of Chemistry
Massachusetts Institute of Technology (MIT)
77 Massachusetts Avenue
Room 6-219
Cambridge, MA 02139-4307
617-253-1489
Fax - 617-253-7030
rwfield@mit.edu

Thomas M. Flynn
CRYOCO, Inc.
511 N. Adams Avenue
Louisville, CO 80027
303-665-8302
Fax - 303-665-0222
tflynn3313@aol.com

Bruce C. Garrett
Pacific Northwest National Laboratory
Environmental Moledular Sciences Lab
Battelle Boulevard, MS K 1-96
Richland, WA 99352
509-375-2587
Fax - 509-375-6631
bc_garrett@pnl.gov

Julanna V. Gilbert
Dept. of Chemistry
University of Denver
Denver, CO 80208
303-871-2993
Fax - 303-871-2254
jgilbert@du.edu

Mark S. Gordon
Dept. of Chemistry
Iowa State University
201 Spedding Hall
Ames, IA 50011
515-294-0452
Fax - 515-294-0105
mark@si.fi.ameslab.gov

8

Richard J. Green
Dept. of Chemistry
Stanford University
Roth Way
Stanford, CA  94305-5080
415-725-4332
Fax - 415-725-0259
rjg@lyman.stanford.edu

Craig F. Hansen
Hansen Engineering
8011 S. Ireland Way
Aurora, CO  80016
303-699-1974
Fax - 303-699-1974
th55@msn.com

Clark W. Hawk
Dept. of Mechanical & Aerospace Engrg
University of Alabama in Huntsville
MS R1 Bldg E-26
Huntsville, AL  35899
205-890-7200
Fax - 205-890-7205
hawkc@email.uah.edu

Thomas L. Henshaw
Phillips Laboratory
PL/LIDD MS Bldg 243
3550 Aberdeen Avenue SE
Kirtland AFB, NM  87117-5776
505-846-4776
Fax - 505-846-5041
henshawt@ug1.plk.af.mil

Wadih Homsi
Dept. of Physics
Brown University
Box 1843
Providence, RI  02912
401-863-2854
Fax - 401-863-2024
wadih_homsi@brown.edu

Dennis C. Jacobs
Dept. of Chemistry
University of Notre Dame
Notre Dame, IN  46556
219-631-8023
Fax - 219-631-6652
jacobs.z@nd.edu

Kenneth C. Janda
Dept. of Chemistry
University of California, Irvine
44 Ulrey Court
Irvine, CA  92717-1875
714-824-5266
Fax - 714-824-3168
kcjanda@uci.edu

Rajiv K. Kalia
Conc Comp Lab for Matl's Simulations
Louisiana State University
225 B, Nicholson Hall
Baton Rouge, LA  70803-4001
504-388-1112
Fax - 504-388-5855
kalia@bit.csc.lsu.edu

Daniel H. Katayama
Phillips Laboratory
PL/GPID
29 Randolph Road
Hanscom AFB, MA  01731-3010
617-377-5088
Fax - 617-377-7091
katayama@plh.af.mil

John W. Kenney, III
Dept. of Physical Sciences/Chemistry
Eastern New Mexico University
COB 184, MS Sta 33
Portales, NM  88130
505-562-2152
Fax - 505-562-2192
kenneyj@ziavms.enmu.edu

Phillip Kessel
OL-AC PL/RKS
Propulsion Sciences Division
10 E. Saturn Blvd
Edwards AFB, CA  93524-7680
805-275-5591
Fax - 805-275-5471
phil_kessel@ple.af.mil

Kurt S. Ketola
Dept. of Physics
Brown University, Box 1843
Providence, RI  02906
401-863-2854
Fax - 401-863-2024
kurt_ketola@brown.edu

Anatoli Korkin
Dept. of Chemistry
University of Florida
Quantum Theory Project
362 Williamson Hall
Gainesville, FL 32611
352-392-1597
Fax - 352-392-8722
korkin@qtp.ufl.edu

Manchikanti Krishnamurthy
JILA
University of Colorado
Boulder, CO 80303-4400
303-492-7387
Fax - 303-492-5235
mkrism@jila.colorado.edu

Koop Lammertsma
Dept. of Chemistry
University of Alabama at Birmingham
901 S. 14th Street
Birmingham, AL 35294
205-934-0669
Fax -205-934-8955
koop@dali.chem.uab.edu

Peter W. Langhoff
Dept. of Chemistry
Indiana University
Bloomington, IN 47405
812-855-8621
Fax - 812-855-8300
langhoff@indiana.edu

Stephen R. Langhoff
Computational Chemistry Branch
NASA Ames Research Center
Moffett Field, CA 94035
415-604-6213
Fax - 415-604-0350
langhoff@pegasus.arc.nasa.gov

C. William Larson
OL AC PL/RKS
Propulsion Division
10 East Saturn Blvd.
Edwards AFB, CA 93524-7680
805-275-6104
Fax - 805-275-5471
larsonb@lablink.ple.af.mil

William G. Lawrence
Dept. of Chemistry
Emory University
1515 Pierce Drive
Atlanta, GA 30322
404-727-6617/0029 - lab
Fax - 404-727-6586
lawrence@euch4c.chem.emory.edu

Stephen R. Leone
JILA, University of Colorado and NIST
MS 440
Boulder, CO 80309-0440
303-492-5128
Fax - 303-492-5504
srl@jila.colorado.edu

Dale J. Levandier
Orion International Technologies
PL/GPID
29 Randolph Road
Hansom AFB, MA 01731-3010
617-377-2331
Fax - 617-377-8202
levandier@plh.af.mil

Raphael D. Levine
Dept. of Chemistry
Hebrew University
Jerusalem, Israel 91904
972-2-6585260
Fax - 972-2-6573742
rafi@batata.fh.huji.ac.il

Ken Libbrecht
Dept. of Physics
California Institute of Technology
MS 264-33
Pasadena, CA 91125
818-395-3722
Fax - 818-395-3814
kgl@bigbear.caltech.edu

Carl Lineberger
JILA
University of Colorado
Campus Box 440
Boulder, CO 80309-0440
303-492-7834
Fax - 303-492-8994
wcl@jila.colorado.edu

Steven J. Lipson
Phillips Laboratory
PL/GPOS
29 Randolph Road
Hanscom AFB, MA 01731
617-377-7380
Fax - 617-377-8900
lipson@pldac.plh.af.mil

B. Vincent McKoy
Dept. of Chemistry
California Institute of Technology, MS 127-72
Pasadena, CA 91125
818-395-6545
Fax - 818-568-8824
bvm@starbasel.caltech.edu

Donald F. McMillen
SRI International
Molecular Physics Laboratory
333 Ravenswood Avenue
Menlo Park, CA 94025
415-859-4301
Fax - 415-859-6196
mcmillen@mplvax.sri.com

Michel Macler
Hughes STX
OL AC PL/RKS
10 E. Saturn Blvd.
Edwards AFB, CA 93524-7680
805-275-5931
Fax - 805-275-5471

Horia Metiu
Dept. of Chemistry
Unviersity of California
Santa Barbara, CA 93106
805-893-2256
Fax - 805-893-4120
metiu@sbmm1.ucsb.edu

H. Harvey Michels
Dept. of Chemical Sciences
UTRC
411 Silver Lane, MS 129-72
East Hartford, CT 06108
860-727-7489
Fax - 860-727-7909
michelhh@utrc.utc.com

Harold C. Miller
PL/LIDB
Laser and Imaging Directorate
3550 Aberdeen Ave., S.E.
Kirtland AFB, NM 87117-5776
505-853-3119
Fax - 505-846-4807
millerh@plk.af.mil

Roger Miller
Dept. of Chemistry
University of North Carolina, cb 3290
Chapel Hill, NC 27599-3290
919-962-0528
Fax - 919-962-2388
remiller@unc.edu

Steven M. Miller
USAF, Phillips Laboratory
Optical Environment Division, Geophysics
29 Randolph Road, PL/GPOS
Hanscom AFB, MA 01731-3010
617-377-2807
Fax - 617-377-8900
miller@plh.af.mil

Timothy K. Minton
Dept. of Chemistry and Biochemistry
Montana State University
108 Gaines Hall
Bozeman, MT 59717
406-994-5394
Fax - 406-994-5407
tim_m@erc.montana.edu

Keiji Morokuma
Dept. of Chemistry
Emory University
1515 Pierce Drive
Atlanta, GA 30322
404-727-2180
Fax - 404-727-6586
morokuma@emory.edu

Edmond Murad
PL/GPID
Geophysics Directorate
29 Randolph Road
Hanscom AFB, MA 01731
617-377-3176
Fax - 617-377-5571
murad@plh.af.mil

Gilbert M. Nathanson
Dept. of Chemistry
University of Wisconsin, Madison
1101 University Avenue
Madison, WI 53706
608-262-8098
Fax - 608-262-9918
nathanson@chem.wisc.edu

Robert W. Naylor
Alliant Techsystems
Propellant Technology
St Rt 956
Rocket Center, WV 26726
304-726-5405
Fax - 304-726-5125
bnaylor@atk.com

David Nesbitt
JILA
University of Colorado
Boulder, CO 80309-0440
303-492-8857
Fax - 303-492-5235
djn@jila.colorado.edu

Daniel M. Neumark
Dept. of Chemistry
University of California
Berkeley, CA 94720-1460
510-642-3502
Fax - 510-642-6262
neumark@cchem.berkeley.edu

Jeffrey W. Nicholson
Dept. of Physics and Astronomy
University of New Mexico
800 Yale Blvd., NE
Albuquerque, NM 87131
505-277-3100
Fax - 505-277-1520
jeffn@astro.phys.unm.edu

Takeshi Oka
Dept. of Chem, Astronomy, & Astrophysics
University of Chicago
5738 S. Ellis
Chicago, IL 60637
312-702-7070
Fax - 312-702-0805
oka@biovax.ucmicago.edu

Mitchio Okumura
Dept. of Chemistry
California Institute of Technology
1201 E. California Blvd. MS 127-72
Pasadena, CA 91125
818-395-6557
Fax - 818-568-8824
mo@cco.caltech.edu

Leslie S. Perkins
Phillips Laboratory
10 E. Saturn Blvd, Bldg 8451
Edwards AFB, CA 93524-7680
805-275-5623
Fax - 805-275-5471
leslie_perkins@ple.af.mil

Mark A. Petrie
Phillips Laboratory, Hughes STX
Propulsion Science
Edwards AFB, CA 93524-7680
805-275-5759
Fax - 805-275-5471
petriem@lablink.ple.af.mil

Wilson T. Rawlins
Physical Sciences, Inc.
20 New England Business Center
Andover, MA 01810
508-689-0003
Fax - 508-689-3232
rawlins@psicorp.com

Hanna Reisler
Dept. of Chemistry
Univ. of Southern California
MS 0482
Los Angeles, CA 90089-0482
213-740-7071
Fax - 213-746-4945
reisler@chem1.usc.edu

Peter J. Reynolds
ONR, Physical Sciences
800 N. Quincy Street, ONR 331
Arlington, VA 22217
703-696-4205
Fax - 703-696-6887
reynolp@onrhq.onr.navy.mil

Eric E. Rice
ORBITEC
Space Center, 1212 Fourier Drive
Madison, WI 53717
608-827-5000
Fax - 608-827-5050


Stephen L. Rodgers
USAF Phillips Laboratory
PL/RKS
10 Saturn Road
Edwards AFB, CA 93524
805-275-5623
Fax - 805-275-5471
steve@helium.ple.af.mil

John Ross
Dept. of Chemistry
Stanford University
Roth Way, MS 5080
Stanford, CA 94305-5080
415-723-9203
Fax - 415-723-4817
ross@chemistry.stanford.edu

Stephen B. Ross
Dept. of Physics
California Institute of Technology
MS 264-33
Pasadena, CA 91125
818-395-8451
Fax - 818-395-3814
sbr@cco.caltech.edu

James E. Rutledge
Dept. of Physics and Astronomy
University of California, Irvine
Irvine, CA 92717-4575
714-824-5141
Fax - 714-824-2174
jrutledg@uci.edu

Henry F. Schaefer, III
University of Georgia
Ctr for Computational Quantum Chemistry
1001 Cedar Street, Rm 608
Athens, GA 30602-2556
706-542-2067
Fax - 706-542-0406
hfsIII@uga.cc.uga.edu

Robert J. Schmitt
SRI International
Chemistry Laboratory
333 Ravenswood Avenue, PS 281
Menlo Park, CA 94025
415-859-5579
Fax - 415-859-4321
robert_schmitt@qm2.sri.com

Giacinto Scoles
Dept. of Chemistry
Princeton University
Washington Road
Princeton, NJ 08544
609-258-5570
Fax - 609-258-6665
gscoles@princeton.edu

Gustavo E. Scuseria
Dept. of Chemistry
Rice University
6100 Main Street, MS 60
Houston, TX 77005-1892
713-527-4746
Fax - 713-285-5155
guscus@katzo.rice.edu

George M. Seidel
Dept. of Physics
Brown University
Providence, RI 02912
401-863-2584
Fax - 401-863-2024
seidel@physics.brown.edu

Ramesh D. Sharma
Optical Environment Division, PL/GPOS
29 Randolph Road
Hanscom AFB, MA 01731-3010
617-377-4198
Fax - 617-377-8900
sharma@plh.af.mil

Jeffrey A. Sheehy
Phillips Laboratory, Hughes STX
Propulsion Sciences Division
10 E. Saturn Blvd.
Edwards AFB, CA 93524-7680
805-275-5762
Fax - 805-275-5471
sheehy@helium.ple.af.mil

Isaac F. Silvera
Dept. of Physics
Harvard University
Cambridge, MA 02138
617-495-9075
Fax - 617-496-5144
silvera@physics.harvard.edu

Steven M. Singleton
PL/GPOS
29 Randolph Road
Hanscom AFB, MA 01731
617-377-2845
Fax - 617-377-8900
ssinglet@pldac.plh.af.mil

David M. Sonnenfroh
Physical Sciences, Inc.
20 New England Business Center
Andover, MA 01810
508-689-0003
Fax - 508-689-3232
sonnenfroh@psicorp.com

William C. Stwalley
Dept. of Physics, U-46
University of Connecticut
2152 Hillside Road
Storrs, CT 06269-3046
860-486-4924
Fax - 860-486-3346
stwalley@uconnvm.uconn.edu

Peter Taborek
Dept. of Physics
University of California
Irvine, CA 92717-1875
714-824-2254
ptaborek@uci.edu

Donald L. Thompson
Dept. of Chemistry
Oklahoma State University
Stillwater, OK 74078
405-744-5174
Fax - 405-744-6007
dlt@osuunx.ucc.okstate.edu

Thanh N. Truong
Dept. of Chemistry
University of Utah
Henry Eyring Building
Salt Lake City, UT 84112
801-581-4301
Fax - 801-581-8433
truong@chemistry.chem.utah.edu

Randall S. Urdahl
Dept. of Chemistry
Stanford University, MS 19
Stanford, CA 94305-5080
415-723-9862
Fax - 415-723-4817
rsurdahl@d3lmf0.stanford.edu

James J. Valentini
Dept. of Chemistry
Columbia University
3000 Broadway, MS 3120
New York, NY 10027
212-854-7690
Fax - 212-932-1289
jjv1@chem.columbia.edu

Priya Vashishta
Dept. of Physics
Louisiana State University
Nicholson Hall
Baton Rouge, LA 70803-4001
504-388-1342
504-388-5855
priyav@bit.csc.lsu.edu

Albert A. Viggiano
Phillips Laboratory
Ionospheric Effects Divsion, MS GPID
Hanscom AFB, MA 01731
617-377-4028
Fax - 617-377-1148
viggiano@plh.af.mil

Gregory A. Voth
Dept. of Chemistry
University of Pennsylvania
231 South 34th Street, MS 6323
Philadelphia, PA 19104-6323
215-898-3048
Fax - 215-573-2112
voth@a.chem.upenn.edu

14

Stephen P. Walch
Thermosciences Institute
NASA Ames Research Center
MS 230-3
Moffett Field, CA 94035
415-604-6189
Fax - 415-604-0350
walch@pegasus.arc.nasa.gov

Xiao-Qian Wang
Dept. of Physics
Clark Atlanta University
223 James P. Brawley Drive
Atlanta, GA 30314
404-880-8649
Fax - 404-880-8360
wang@hubble.cau.edu

David E. Weeks
Air Force Institute of Technology (AFIT)
Engineering Physics
2950 "P" Street
WPAFB, OH 45433-7765
513-255-3636, ext 4501
Fax - 513-255-2921
dweeks@afit.af.mil

John Raymond Wells
Armstrong Laboratory
Environics Directorate (EQC)
139 Barnes Drive
Tyndall AFB, FL 32403-5323
904-283-6087
Fax - 904-283-6090
ray_wells@ccmail.aleq.tyndall.af.mil

K. Birgitta Whaley
Dept. of Chemistry
University of California, Berkeley
217 Hildebrand Hall
Berkeley, CA 94720-1460
510-643-6820
Fax - 510-643-1255
whaley@holmium.cchem.berkeley.edu

Charles A. Wight
Dept. of Chemistry
University of Utah
2424 Henry Eyring Building
Salt Lake City, UT 84112
801-581-8796
Fax - 801-585-3207
wight@chemistry.utah.edu

Skip Williams
Orion Technologies, International
PL/GPID
29 Randolph Road
Hanscom AFB, MA 01731-3010
617-377-2332
Fax - 617-377-5571

William W. Wilson
Phillips Laboratory
Hughes STX
10 E. Saturn Blvd., Bldg 8451
Edwards AFB, CA 93524-7680
805-275-5194
Fax - 805-275-5471
william_wilson@ple.af.mil

Curt Wittig
Dept. of Chemistry
Univ. of Southern California
Los Angeles, CA 90089-0482
213-740-7368
Fax - 213-746-4945
wittig@chem1.usc.edu

Alec M. Wodtke
Dept. of Chemistry
University of California, Santa Barbara
Santa Barbara, CA 93106
805-893-8085
Fax - 805-893-4120
wodtke@sbmmi.ucsb.edu

E. J. Wucherer
Phillips Laboratory
Propulsion Sciences Division
10 E. Saturn Blvd
Edwards AFB, CA  93524-7680
805-275-5759
Fax - 805-275-5471
wucherere@lablink.ple.af.mil

David R. Yarkony
Dept. of Chemistry
Johns Hopkins University
3400 N. Charles Street
Baltimore, MD  21218
410-516-4663
Fax - 410-516-8420
yarkony@jhuvmx.hel.jhu.edu

Ahmed H. Zewail
Dept. of Chemistry & Chemical Engineering
California Institute of Technology
1201 E. California Blvd., MS 127-72
Pasadena, CA  91125
818-395-6536
Fax - 818-792-8456
ahz@starbase1.caltech.edu

## Conference Administration
## & Registration

*Judy Flory*
*Donna Tinley*
*UES, Inc.*
*4401 Dayton-Xenia Road*
*Dayton, Ohio 45432-1894*
*513-426-6900*
*Fax - 513-429-5413*
*jflory@erinet.com*

# Solid hydrogens doped with atomic and molecular oxygen: Experiment and Theory (HEDM Contractors' Meeting, 1996)

*Z. Li and V. A. Apkarian, Department of Chemistry, University of California, Irvine, CA 92717.*

*Lawrence B. Harding, Theoretical Chemistry Group, Argonne National Laboratory, Argonne, IL.*

## I. INTRODUCTION

We report studies on $O_2$ and O doped solid hydrogens, with the aims of establishing the viability of such solids as HEDM materials. The experiments have allowed the development of practical simulation methods for treating dynamics in systems of large dimensionality which are dominated by zero-point effects. The combination of experiment and simulation now enables a rigorous assessment of various physical and chemical properties of these systems with far more confidence than ever before. We first consider the spectroscopy of molecular oxygen, as a probe of the local structure and energetics of the host, followed by a consideration of the properties of atomically doped solid hydrogens with respect to their stability and reactivity in the various electronically excited states.

## II. QUANTUM VERSUS CLASSICAL HOSTS

We have already reported on the experimental studies of the $A'(^3\Delta_u)-X(^3\Sigma_g^-)$ transition, or the Herzberg III band, of $O_2$ isolated in solid hydrogens.[1] This non-allowed transition, is activated in these solids through orbital mixing in the excited state. It has been shown that the molecule is observable only when pointing along the [111] axis in fcc sites, and accordingly is a good probe of structural transformations in the bulk. While in $D_2$, there is a large enough number of molecules isolated in such sites to enable spectroscopic studies, in $H_2$ the transition is not observable except when a long-range perturbation is induced by overcoating the solid with Xe and after heat cycling to 27 K. We will therefore concentrate mainly on solid $D_2$. The excitation spectra of $O_2$ isolated in $D_2$ show a zero-phonon line, and a broad phonon sideband, on which a librational progression with a spacing of 15 cm$^{-1}$ is distinctly identifiable. The emission is polarized, with a polarization anisotropy of 1.25, which is exactly what would be expected for a $\Delta\Lambda=1$ transition of a non rotating molecule. We had therefore inferred that the molecule, at least in the excited state, cannot rotate. Does this then imply a rigid lattice? Indeed, when the vibrational spectral shifts are used to reconstruct an effective potential for $O_2$ in $D_2$ the caging of the stretched molecule becomes quite evident. Does this imply a stiff lattice? What is the difference between a "classical" and a "quantum" van der Waals solid with

respect to isolated impurities in them? The simulations address this issue most clearly.

We carry out simulations using pseudo-potentials which are constructed by Gaussian convolution of the known pair potentials. The Gaussians are chosen to reproduce the structure of the solid when the effective total potential is minimized with respect to nearest neighbor separation at zero-pressure. The methodology and its tests have already been published.[2] Dynamics using the full width of the determined Gaussian is equivalent to describing a classical solid since all zero-point motion is frozen into the potential of the system. A proper representation of kinetic correlations is obtained when using a Gaussian of half this width, in which case it can be shown that the exact radial distribution function and an acceptable phonon spectrum for the pure solid is retrieved.[2] The contrast between dynamics in classical and quantum solids is then best obtained by these two methods. In figures 1 and 2 we present results of simulations for two extremes: the ground state of $O_2$, which has a bond length of 1.1 Å, in a "classical" solid of $D_2$; and the excited state of $O_2$, which has a bond length of 1.6 Å, in a "quantum" solid of $D_2$. Four properties are plotted, in each case:

a) the time correlation of the molecular orientation, $\theta(t) = \arccos[\mathbf{r}(t)\cdot\mathbf{r}(0)]$,

b) the cage anisotropy as measured by the inter-planar separation along the three cubic axes, $R_{i,j,k}$

c) the mass anisotropy, as given by the principle moments of inertia of the cage measured from the molecular center of mass, $I_{a,b,c}$

d) the correlation between molecular axis and the principle moment: $\phi(t) = \arccos[\mathbf{I}(t)\cdot\mathbf{r}(t)]$.

In the classical solid, in the ground state, the molecule undergoes nearly free rotations. This is verified by noting that the Fourier transform of $\theta(t)$ yields a rotational frequency which corresponds to that of the thermal rotations of the free molecule $I\omega^2/2 = kT/2$. It can be seen in Fig. 1b, that the cage does not distort, as would be expected if the lattice were held together through potential energy alone. There is a small anisotropy in the mass tensor, as observed from the splitting of the moments of inertia, since the cage is not distorted, this is an indication that the molecule remains eccentric in the cage (the center of mass and the center of interaction do not coincide). Finally, it is obvious that the molecular axis and the principle moment of inertia remain correlated. This motion is well described by the rotation-translation coupling model for rotations of an impurity in a classical cavity. The rotation of the molecule is facilitated by its eccentricity.

A very different picture is obtained in the quantum host, as illustrated in figure 2. We show the case of the excited A' state for emphasis. The molecular orientation is completely locked, the cage is distorted by expanding along the molecular axis and contracting along the belt. The mass anisotropy is now split, and shows no dynamic exchange. In effect, in the quantum solid the cavity deforms, to fit the shape of the impurity. This deformation is responsible for halting all rotation. The librational frequency, as extracted from the Fourier transform of $\theta(t)$ is 15cm$^{-1}$, in excellent agreement with experiment. While this agreement may be fortuitous, it is clear that the underlying physics is well reproduced by these simulations.

While not shown here, we discover that in the ground state of $O_2$ isolated in quantum $D_2$, the molecule undergoes rotational hops which are completely correlated with the cage deformation. This then provides the means for excitation of molecules initially trapped along [100] axes, to have Franck-Condon overlap with the librational wavefunction along [111], *i.e.*, excitation with a flip of the molecular orientation. Such a change in molecular orientation was deemed necessary to explain the F-C intensities in the librational progressions.[1] The absence of the spectra in solid $H_2$ can now be understood to result from the larger local deformation in both excited and ground states, and the absence of any intensity in orientation flipping transitions.

## II. ATOMIC OXYGEN IN SOLID HYDROGENS

We have already reported on our experimental studies on solid hydrogens doped with atomic oxygen.[3] In brief, O atoms can be photgenerated by 193 nm irradiation of $O_2$ doped solids. The atoms can be detected by 193 nm induced fluorescence over the $O(^1S) \rightarrow O(^1D)$ transition. Rather surprisingly, the fluorescence does not bleach, indicating that O atoms in any of its term states, $^1S$, $^1D$ or $^3P$, does not react with the host. This is somewhat surprising, because $O(^1D)$ in the gas phase reacts with $H_2$ on every collision. The recombination of O atoms in these solids can be monitored through the thermoluminescence induced over the $A' \rightarrow X$ transition. All attempts at observing recombination under controlled conditions have failed. Depending on the details of the preparation of the solid, and its history, the recombination is observed to occur catastrophically at various temperatures: a sudden burst in temperature, pressure, and luminescence is observed at temperatures varying from 5.5 to 9.5 K. The latter observations lead us to conclude that the recombination is not due to thermal diffusion of O atoms in the lattice, but rather a result of changes in the morphology of the solid and the self-diffusion of the host. We try to rationalize these observations through simulations.

### A) Ab initio Surfaces of O-H2

*Ab initio* calculations of the $O-H_2$ surfaces were carried out by Larry Harding of the Argonne National Labs. The calculations were of the multi-reference, configuration interaction (MR-CI) variety, in which orbitals are first optimized using a state-averaged, multi-configuration, self-consistent field (MCSCF) and then used in a subsequent MR-CI calculation. To optimize the orbitals, separate, singlet and triplet, state averaged, 10 orbital, 8 electron, complete active space self consistent field (CASSCF) calculations were carried out using the MOLPRO[4] program package. For the singlet surfaces, the state averaging was done over the five lowest states (corresponding to the five components of the $O(^1D)+H_2$ asymptote). For the triplet states the state averaging was done over the three lowest states (corresponding to the three components of the $O(^3P)+H_2$ asymptote). In all cases, all states were weighted equally in the averaging. In these calculations the 10 active orbitals consist of the oxygen 2s, $2p_x$, $2p_y$, $2p_z$, 3s, $3p_x$, $3p_y$, and $3p_z$ orbitals and the HH, s and s* orbitals. Tests using smaller

active spaces were found to be unsatisfactory due to problems resolving the 1s, 2s and 2p orbitals and/or to inequivalent p orbitals at large $R_{O-HH}$ separations. For the singlet surfaces the CASSCF wavefunction include as many as 13860 configurations. A more detailed description of these calculations and the resulting 9 surfaces as a function of internuclear separation, R, and $H_2$ orientation, $\theta$, is now being prepared for publication.[5] Global fits to the three distinct manifolds that arise from $^3P$, $^1D$, and $^1S$, were obtained in a diabatic representation limited to $p_x$, $p_y$ and $p_z$ for the $^3P$ state, and $d_{z^2}, d_{xy}, d_{xz}, d_{yz}, d_{x^2-y^2}$ for the $^1D$ state, and used in subsequent simulations. It was verified that in the $^3P$ state the O-$H_2$ interaction does not localize the angular function of the $H_2$. This can be discerned from the 1-dimensional calculations of the vibrational and angular wavefunctions shown in Figure 3. It is therefore assumed that the concept of p-$H_2$(o-$D_2$) is useful in considering even the nearest neighbor shell of the host, and all subsequent calculations were conducted on surfaces generated by taking the rotational average over $\theta$.

## B) Ground State

Using pseudo-potentials, the structure of O($^3P$) doped solid $D_2$ was simulated through molecular dynamics. The O-$D_2$ radial distribution function, and the resulting increase of the molar volume of the doped solid, remain nearly identical to our previous calculations.[2,3] In effect, the nearest neighbor shell is localized, and the density of the solid increases with a linear dependence on the dopant concentration. The activation energy for recombination, or diffusion was also calculated. This was accomplished by calculating the potential of mean force, along the reaction path, by thermally relaxing the solid after each step along the reaction coordinate. An activation energy of 80 cm$^{-1}$ is obtained. This then is consistent with the experimental observation that O atoms may not diffuse in solid $D_2$ prior to self-diffusion of the solid.

O($^3P$) doped solid $H_2$ is stable with respect to chemistry, and mobility of dopants, moreover, doping stabilizes the lattice.

## C) Excited state

The rotationally averaged surfaces for O($^1D$)-$H_2$ can be expanded in three Legendre terms and the many-body interactions can then be expressed as:

$$V_{O-D_2}(r, R_1, R_2, ..., R_n) = \sum_{k=1}^{n} \sum_{L=0,2,4} V_L(r, R_k) P_L(R_k \cdot r)$$

in which the summation over k runs over all host atoms. The three angular terms in the expansion are shown in figure 4. While the isotropic term, $V_0$, is bound, the anisotropic terms are reactive. Note, in $O_h$ symmetry, or any high symmetry site in a cubic lattice, the summation over k completely eliminates $V_2$ (the direct product of $V_2$ with cubic groups does not contain the totally symmetric representation). When limited to $V_0$ and $V_4$, the surfaces along all normal modes remain bound. Thus, in high symmetry sites, the static many-

body surface is not reactive. However, the combination of asymmetric modes, even at 4 K, lead to reaction. This is shown in figure 5, where trajectories of the twelve nearest neighbor atoms are illustrated. Within 1 ps, the axial atoms contract, lock the $d_{z^2}$ orbital, and the atom inserts in one of the $H_2$ molecules.

While in high symmetry sites $O(^1D)$ is stable, lattice fluctuations along asymmetric cage coordinates lead to reaction. This is the result of a subtle interplay between the anisotropic $V_4$ and isotropic $V_0$ potentials of interaction, and the accuracy of the generated surfaces may not be sufficient to reproduce the experimental observation that this state is not reactive at 4 K.

## III. CONCLUSIONS

One of the more important accomplishments has been the introduction of a practical method for dynamical simmulations in solid hydrogens, a feat that was until now thought to not be possible. The simulations have allowed a rigorous description of spectroscopic observables in $O_2$ doped solid $H_2$ and have enabled a realistic assessment of the physical properties of $O(^3P)$ doped solids. All tests of this sytem indicate that they qualify as HEDM materials. The challenge at present is to scale-up the concentraion of the dopant. The refined ab initio surfaces of O-$H_2$ will undoubtedly be useful in understanding the details of chemistry in these systems. Nevertheless, we have not been able to rationalize the experimental observation that $O(^1D)$ is not reactive in solid $H_2$. At present, the source of this discrepancy is not known.

**References:**

1.  Danilychev, A. V.; Bondybey, V. E.; Apkarian, V. A.; Tanaka, S.; Kajihara, H.; Koda, S. J. Chem. Phys. 103, 4292, (1995).
    Photodynamics of Oxygen isolated in solid $D_2$

2.  Sterling, M.; Li, Z.; Apkarian, V. A.; J. Chem. Phys. 103, 5679 (1995).
    "Simulations of quantum crystals by classical mechanicas."

3.  V. A. Apkarian, Proceedings of HEDM conference, (Woods Hole, 1995).
    "Photodynamics of O and $O_2$ isolated in solid $D_2$/($H_2$)".

4.  MOLPRO is a package of *ab initio* programs written by H.-J. Werner and P.J. Knowles, with contributions from J. Almlof, R.D. Amos, M. J.O. Deegan, S.T. Elbert, C. Hampel, W. Meyer, K. Peterson, R. Pitzer, A. J. Stone, and P. R. Taylor. H.-J. Werner and P. J. Knowles, J. Chem. Phys., 82, 5053 (1985); P. J. Knowles and H.-J. Werner, Chem. Phys. Lett. 115, 259 (1985).

5.  Z. Li, L. B. Harding, and V. A. Apkarian, (manuscript in preparation).

**Fig. 1**  $O_2(X)$ / "Classical" $D_2$
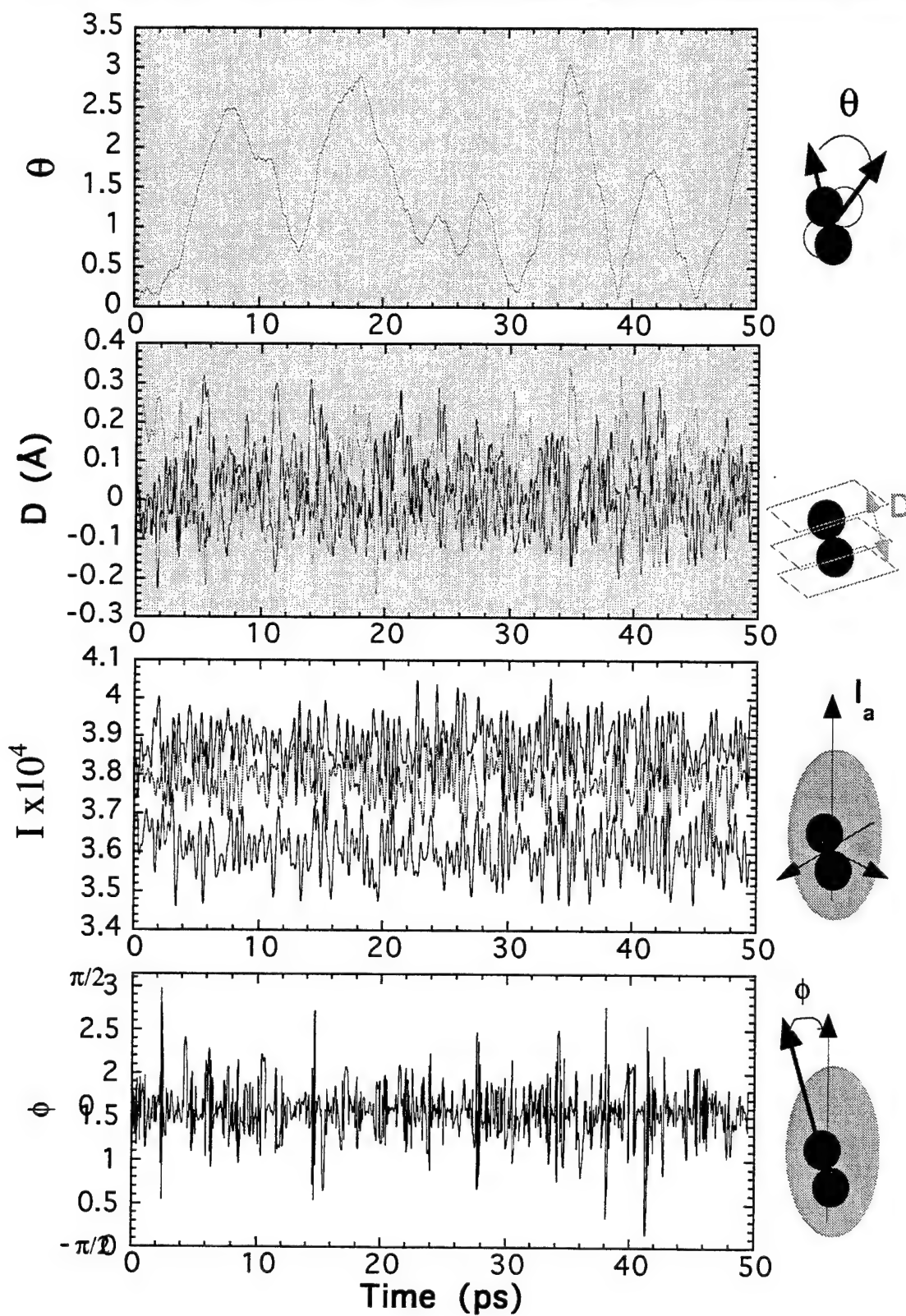
*Fig. 2*                    $O_2(A)$ / "Quantum" $D_2$

# Fig. 3

# $O(^3P) - H_2(j=0)$

O(3P)--H2 (j=0)



v=0

$\omega$=43 cm$^{-1}$

V (cm$^{-1}$)

R (Å)



V (cm$^{-1}$)

$|\psi(\theta)|^2$

$\theta$
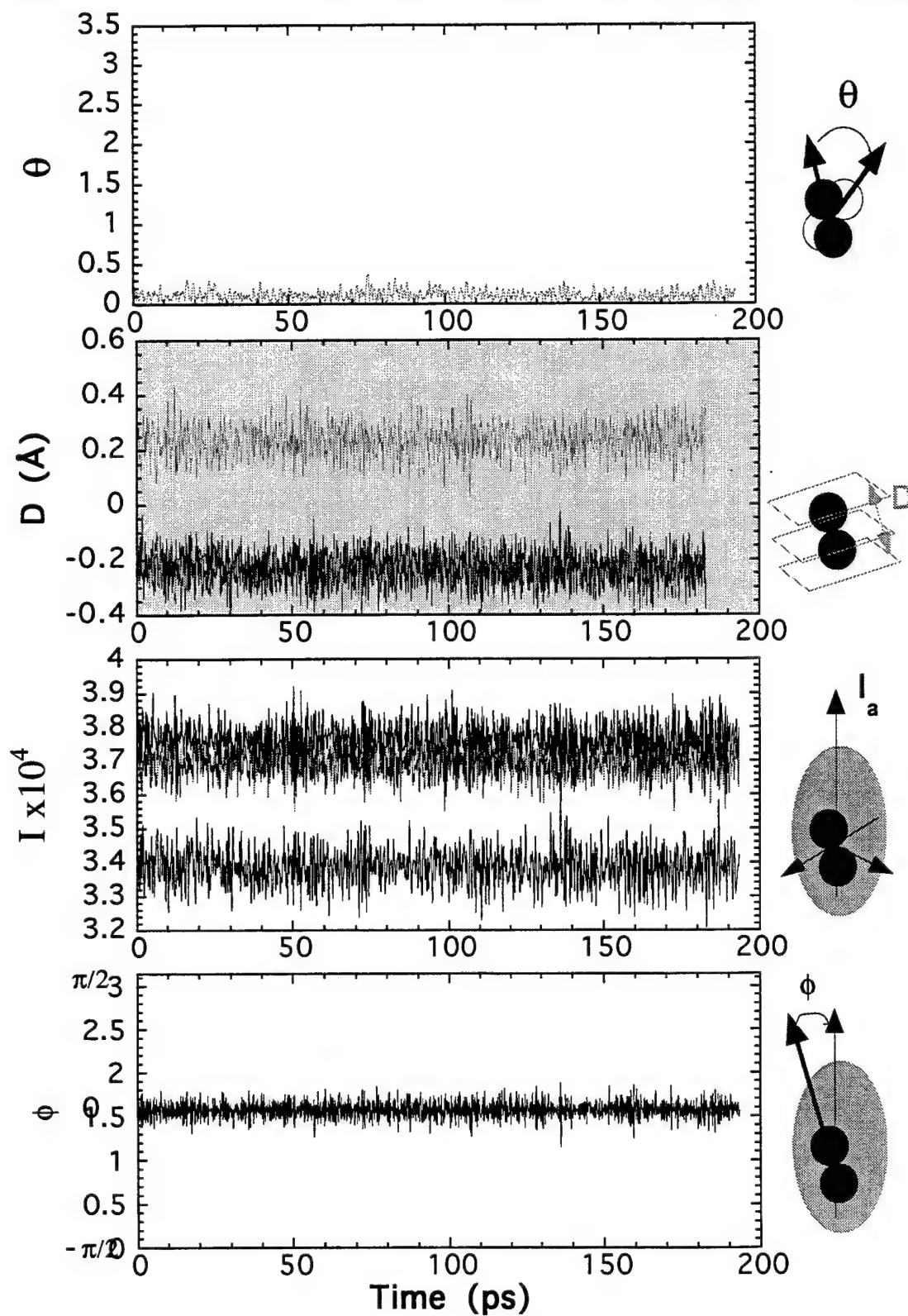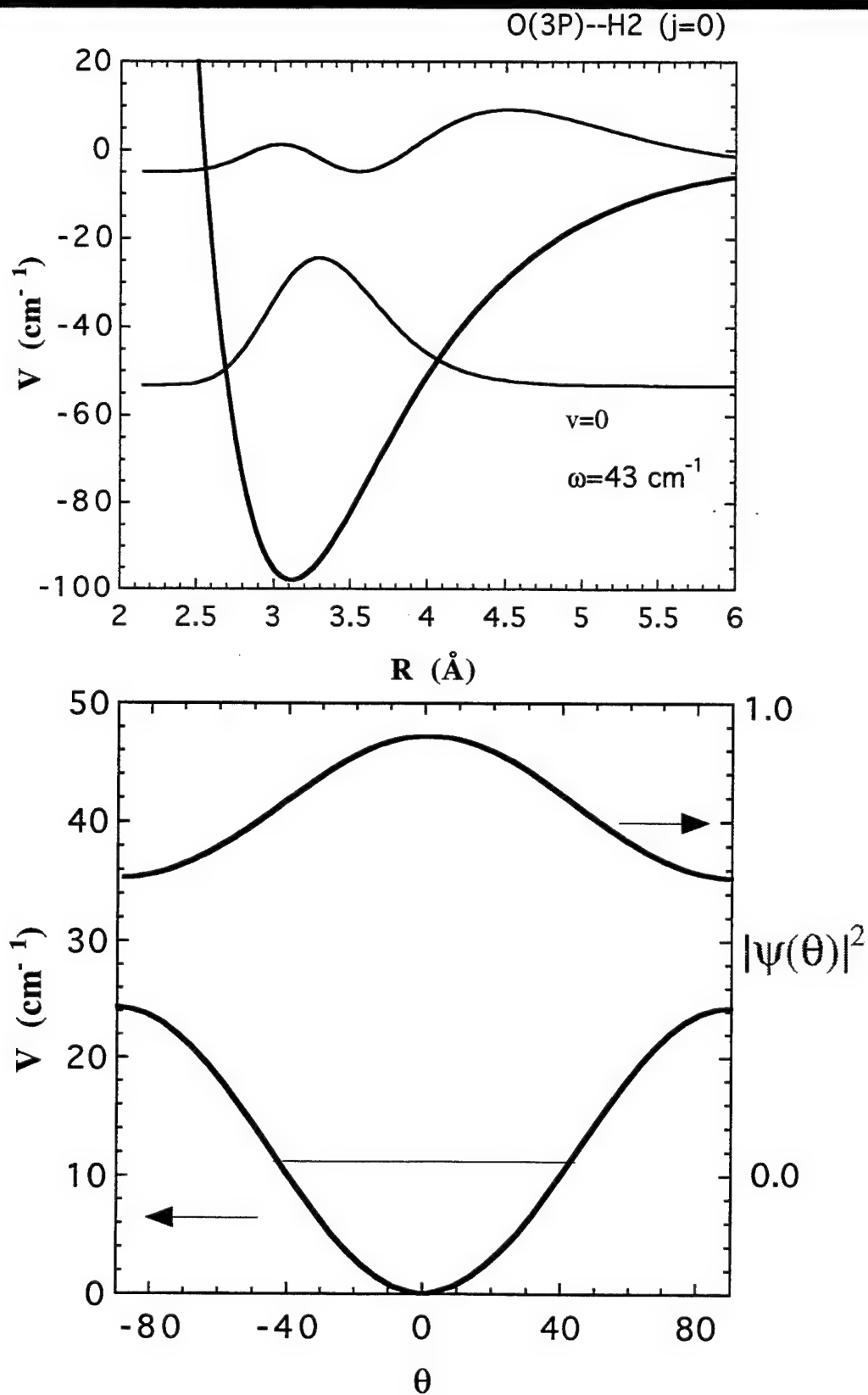
**Fig. 4** $O(^1D) - H_2(j=0)$ potentials
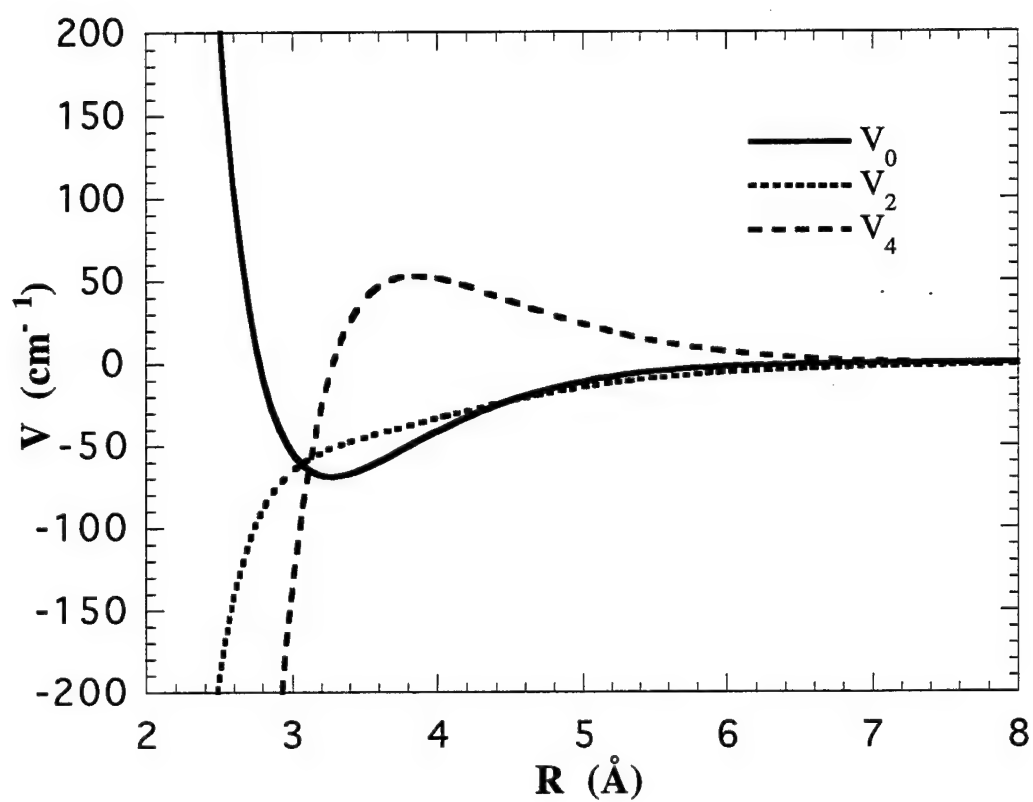
*Fig. 5*    *Reaction of O(¹D) in solid p-H₂*
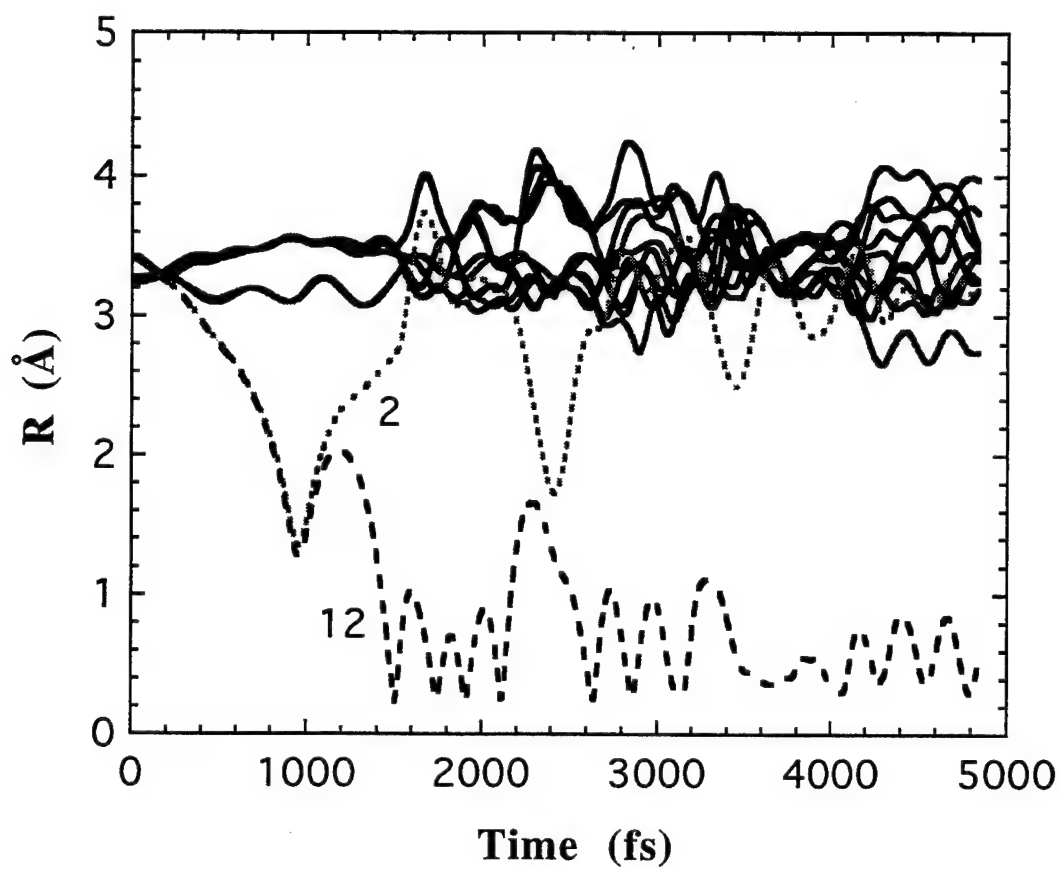
# Mass Spectrometry Studies of Pick-up by Helium Clusters

Berton Callicoatt, Kenneth Janda, V. Ara Apkarian, Peter Taborek and James Rutledge
Advanced Cryogenics Group
University of California, Irvine, CA 92717

We are exploring the use of liquid He clusters for a deposition source to create highly doped hydrogen solids. For instance, if we could pick up an oxygen atom in with the helium cluster, then pick up 20-40 hydrogen molecules, we expect that the hydrogen molecules would diffuse to the oxygen atom, and surround it without reacting, due to the 0.4 K temperature of the helium "solvent". Next we would like to deposit the pre-formed $O-(H_2)_n$ cluster onto the surface of solid $H_2$. We expect that the He will act as both a very efficient heat bath and an efficient shock absorber so that there is some probability that the oxygen and hydrogen do not react during the deposition process.

Characterization of the contents of liquid He clusters is a very recent, and rapidly developing topic.[1-4] A major difficulty is that upon ionization, such a cluster almost completely fragments, so it is difficult to relate the measured mass spectrum to the neutral cluster contents. For instance, Fig. 1 shows the mass spectrum obtained when a pure He cluster containing about 9000 atoms is ionized with 60 eV electrons.
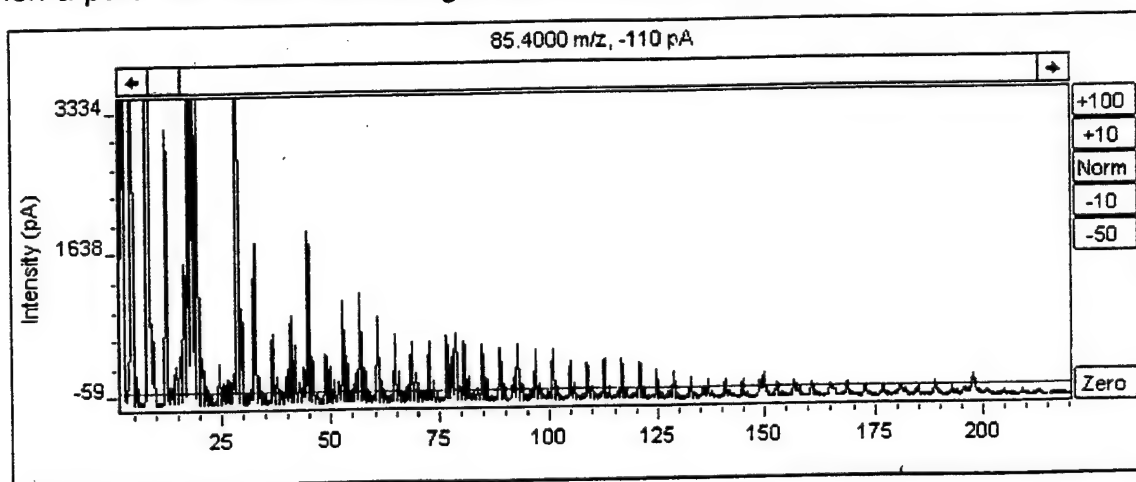


Fig. 1. Mass spectrum of pure He clusters produced with a 5 μm nozzle at 13 K, backed by 300 psi of He. The estimated mean neutral cluster size is 8000 He atoms.

As seen in Fig. 1, ionization of even a large He cluster produces a mass spectrum that has most of its intensity for m/e < 200 amu. Ionization proceeds by excitation of a single He atom in the large cluster since the atoms are very loosely bound to the cluster and the mean distance between atoms is over 3 Å. Some time after the initial ionization event, however, a $He_2^+$ molecular ion is formed, releasing 2.4 eV of energy into the cluster. This energy is sufficient to evaporate most of the other atoms. Indeed, $He_2^+$ is the most intense mass peak observed other than $He^+$, which probably does not originate from large clusters.

**Pressure vs. NO Ion Signal**

Legend:
- ● NO$^+$
- ■ (NO)$_2^+$
- ▲ (NO)$_3^+$
- ▼ (NO)$_4^+$
- ◆ Total He$_N$(NO)$_x$
- ● He$_3^+$ x6

He$_3^+$ x6

Y-axis: Intensity (arb), values 0, 2000, 4000, 6000
X-axis: Pressure (x10$^{-6}$torr), values 0, 5, 10, 15, 20, 25, 30, 35
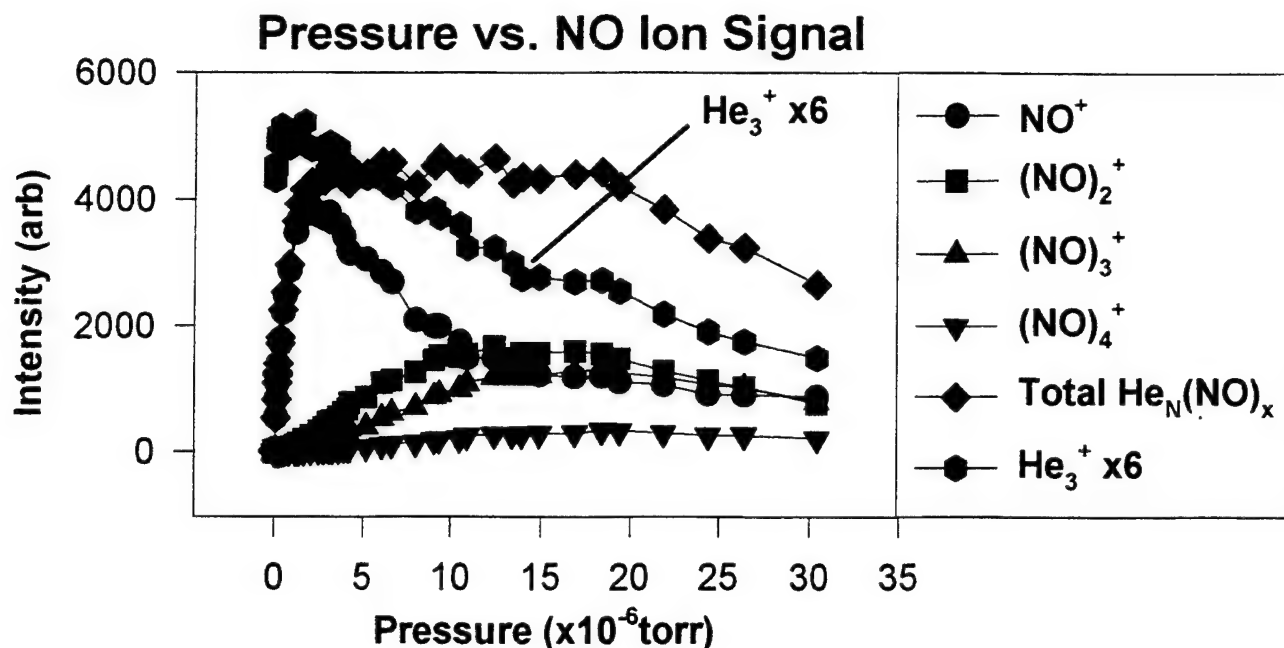
Figure 2. This figure shows how the intensity of mass peaks for different numbers of NO moieties varies with NO pressure in the pick up cell. The most striking result is that the NO$^+$ signal saturates at pressures that have cause very little change in the He$_3^+$ signal. This is clear evidence that often the cluster fragments before the positive charge finds its way on to an NO moiety. Also, the signal for (NO)$_2^+$ maximizes for "pick-up" pressures much large than those for which the NO$^+$ signal saturates. This shows that there is extensive fragmentation of the (NO)$_2$ sub cluster upon ionization. To obtain He cluster with an average of 9000 atoms, 20 bar of He at 13 K was expanded through a 5 μm nozzle.

NO so that their size has decreased due to the fact that He atoms must "boil" off to dissipate the "deposition energy" . Since the ionization efficiency is proportional to the number of He atoms in the cluster, smaller clusters are less efficiently detected. Again, this is a clear signal that the He clusters have all picked up one or more NO molecules. These results are as would be expected based on the work of Toennies and colleagues.

Next, notice the dependence of the He$_3^+$ peak intensity on the NO pressure in the scattering cell. The intensities of this peak is approximately independent of the NO pressure up to 5 x 10$^{-6}$ torr and then gradually decreases for higher NO pressures. The most important thing to notice about this data is that the intensity of mass peaks that only contain He are hardly affected by NO pressures high enough that each He cluster must contain one or more NO molecules. This shows that it is actually fairly rare that the charge on a He$^+$ ion transfers to the NO molecule in a cluster. Once the charge transferred to a NO molecule, it could never go back to a He atom, so no He$_n^+$ peaks could be observed.

Figure 3 shows an expanded view of the low pressure region of Fig. 2. In this Figure, it is seen that the NO$^+$ mass peak goes through it's maximum intensity while the (NO)$_2^+$ and (NO)$_3^+$ peaks are still quite small. Assuming that the pick up process is purely statistical, the intensity of the (NO)$_2^+$ mass peak should approximately equal 1/2 that of the NO$^+$ mass peak, when half the clusters have picked up at least one NO

Toennies and colleagues have published a series of seminal papers on the mass spectrometry of He clusters that contain one or more "dopant" atoms or molecules.[1,2] They suggest that consideration of the following sequence of events would aide the interpretation of mass spectrometry data.  1. Since by far the largest fraction of the electrons in a cluster are in He atoms, the initial ionization step is invariably ionization of a He atom.  2. The ionization center quickly de-localizes throughout the cluster since resonant charge transfer between He atoms takes place on the $10^{-14}$ second time scale, and since trapping of the charge into a $He_2^+$ molecule is relatively slow.  3. Since the any dopant atom or molecule will have a lower ionization energy than He, the dopant atoms efficiently trap the positive charge if the charge center comes within a critical radius of the dopant atom.  At this point, several eV of energy are released, and the cluster fragments leaving behind the charge dopant atom or molecule, perhaps with a few He atoms still attached.  4. If there is more than one dopant molecule in a cluster, they form a dimer, or larger sub-cluster within the He on the nanosecond time scale, before entering the ionizer.  5. Since He has an extremely low boiling point and high thermal conductivity, upon ionization of a sub-cluster any energy released is quickly transferred to the He bath, and the cation of the sub-cluster is observed intact in the mass spectrum.  6. If the dopant is a molecule whose internal degrees of freedom are excited upon ionization, or if a dimer or larger sub-cluster is ionized, energy released from these internal degrees of freedom will "boil-off" any remaining He atoms from the cation before the cation reaches the detector.

We have recently obtained data that allow us to more quantitatively discuss several of the "rules" postulated in the previous paragraph. In particular, we are measuring the branching ratios for various daughter ions that are produced upon ionization of the cluster.  For instance, for medium to large He clusters (4000 atoms or larger)  it is actually fairly rare that charge transfer between the initially ionized He atom and the dopant atom occurs.  For smaller clusters, the transfer is more efficient and we can measure the branching ration between localization of the charge on an $He_2^+$ moiety compared to transfer of the charge to a dopant.  Second, we can estimate probability that "sub-clusters" of dopant molecules fragment upon ionization.   Figure 2 which shows one example of the data that speaks to these issues.

In Figure 2, the intensities of mass peaks m/e =  12 ($He_3^+$); 30 ($NO^+$); 60 (($NO)_2^+$); 90 (($NO)_3^+$); and 120 (($NO)_4^+$) are shown as a function of NO pressure in a 10 cm long pick up region through which He clusters with an average size of 9000 atoms pass as they travel from the source to the mass spectrometer. Notice that the $NO^+$ intensity increases rapidly as the pressure is raised from 0 to $3 \times 10^{-6}$ torr, and then starts to fall.  The rapid rise for such a low pressure is simply due to the fact that the He clusters are large, so the pick-up cross sections are also large.   After the rapid rise, the $NO^+$ intensity falls due to the fact that pick up of more NO shifts the mass spectrum to higher mass peaks.   From this we conclude that for NO pressures in the scattering cell higher than $5 \times 10^{-6}$ torr each He cluster picks up at least one NO molecule, and most of them pick up several NO molecules. If we add the signals for m/e = 30, 60, 90 and 120, the sum  peaks at a NO pressure of approximately $10^{-5}$ torr, and then starts to fall.  The gradual drop off in this integrated intensity at high pressure is due to the fact that the He clusters have picked up enough

# Pressure vs. NO Ion Signal
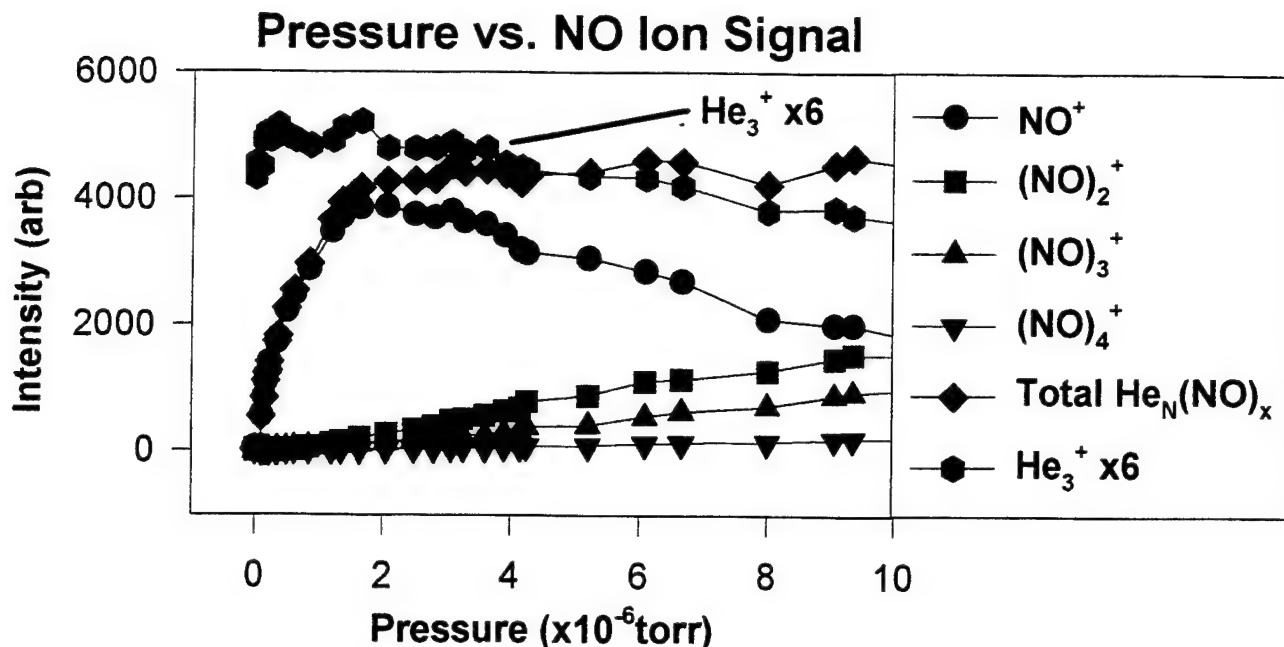


Figure 3: This figure shows an expansion of the low pressure region of Fig. 2. This allows the phenomena discussed in the text to be observed more clearly.

molecule. It is apparent from Fig. 3 that the $(NO)_2^+$ mass peak does not grow as quickly as would be expected if ionization of every cluster that contained two NO molecules resulted in a contribution to the m/e = 60 intensity. This means that either two NO molecules in a cluster do not always form a dimer before ionization, or that the ionization process dissociates the dimer even in the presence of He.

We are in the process of extracting quantitative numbers from data such as that shown in Figs. 2 and 3 by running simulations of the "pick-up" and ionization processes with different sets of assumptions regarding the various fragmentation branching ratios. It should be possible, for instance, to determine quite accurately what the branching ratio is for charge transfer from He to NO compared to the probability of $He_2^+$ formation, as a function of cluster size. There is no reason to believe that the conclusions presented above are limited to NO dopant molecules. They should be quite general.

The results that we will present have specific implications for the application of mass spectrometry to cluster of interest in the "synthesis" of HEDM cryogenic solids. For instance, results that will be presented for pick up of Ar atoms, indicate quite clearly that there will almost certainly not be a significant signal in the mass spectrum at m/e = 12 for He clusters that contain a single C atom nor signal at m/e = 16 for He clusters that contain a single O atom. Instead, such clusters will have to be characterized by laser ionization techniques, or by co-deposition of other impurities that make interpretation of the mass spectrometry more straight forward. We are in the process of developing such techniques.

1. M Lewerenz, B. Schilling and J. P. Toennies, J. Chem. Phys. **102**, 8191 (1996).
2. M. Lewerenz, B. Schilling and J. P. Toennies, Chem. Phys. Letts. **206**, 381 (1993).
3. F. Stienkemeier, W. E. Ernst, J. Higgins and G. Scoles, J. Chem. Phys. **102**, 615 (1995).
4. F. Stienkemeier, W. E. Ernst, J. Higgins and G. Scoles, Phys. Rev. Letts. **74**, 3592 (1995).

# Calorimetric Detection of Oxygen Atoms Produced in a Microwave Discharge

J.E. Rutledge and P. Taborek
University of California, Irvine

Formation of a cryogenic solid doped with a high concentration of free atoms has been a long-standing goal of HEDM research. One plausible method for making this kind of material is to quench a diatomic gas which has been passed through a microwave discharge to form atoms. Although there is considerable spectrographic data on atoms trapped in this way, the atom concentrations are either very low or not readily obtainable from optical measurements.

We have constructed a special-purpose low temperature calorimeter to monitor the heat flux and light emission due to atom recombination when a microwave discharge is quenched onto a cold surface. The calorimeter is equipped with a mechanical heat switch which allows it to be operated in two different modes. With the switch closed, the latent heat of solidification can be removed at low temperature and the heat liberated by atom recombination during growth can be monitored. With the switch open, the sample temperature rises under nearly adiabatic conditions and the heat of recombination can be detected as a function of temperature of the solid sample.The threshold sensitivity of the calorimeter is approximately 10mW, which corresponds to atom concentrations of less than 0.1% for typical sample sizes and growth rates. Atoms are formed in a microwave discharge and conducted into the low temperature calorimeter through metal tubes coated with fluorocarbon wax. A typical calorimetric signal is shown in Figure 1.
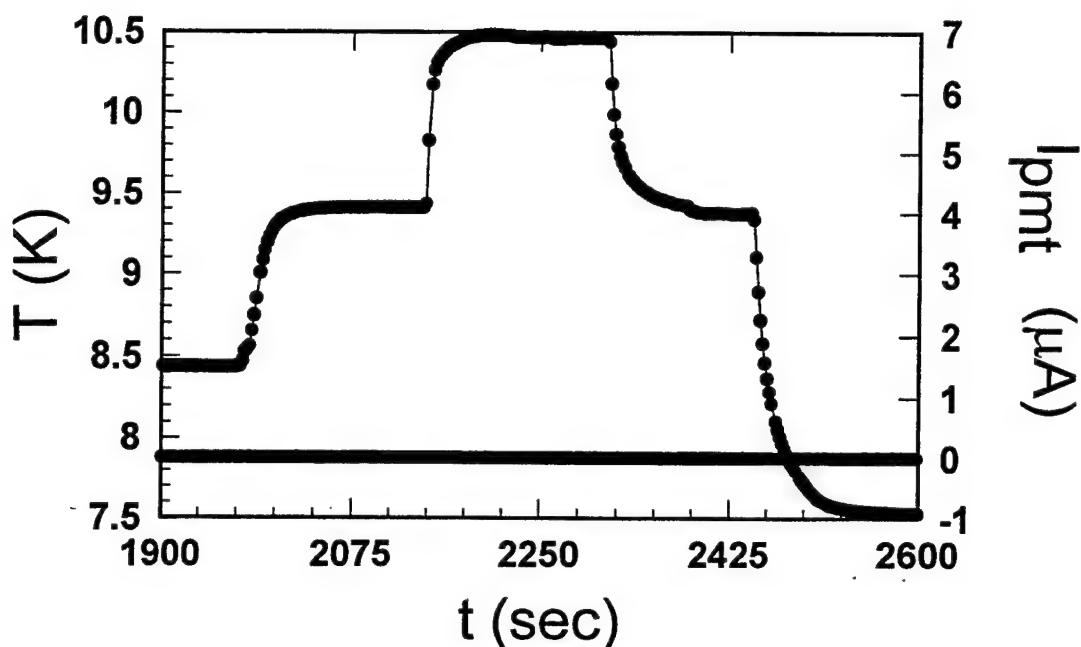
Figure 1. Heat deposited in the calorimeter and the light emitted while an oxygen sample is deposited. 50 sccm of oxygen flows during the time interval between 2000 and 2500 sec. The microwave dissociator is on between 2100 and 2350 seconds. The additional heat corresponds to 2% of the incoming gas recombining as the sample grows. Note that a negligible amount of light is emitted during this process.

Our results with O2 show that the concentration of atoms entering the calorimeter is only 2%, and virtually all of these recombine as the sample is grown. The small atom concentration in the incoming gas is not the result of recombinations in the delivery tube, but is characteristic of the dissociation efficiency of the microwave atom source. Although the cryo solids emit light under some circumstances, the light intensity is a poor measure of the recombination rate.

# STATUS REPORT OF CRYOGENIC SOLID HYBRID ROCKET ENGINE DEVELOPMENT FOR HEDM DEMONSTRATIONS

Eric E. Rice and William H. Knuth
Orbital Technologies Corporation (ORBITEC[TM])
Space Center, 1212 Fourier Drive
Madison, WI 53717
(608)-827-5000

ORBITEC is working under USAF and NASA SBIR contracts and company IR&D to develop test-bed and larger engines/systems that can be used in the future to both demonstrate HEDMs and demonstrate improved performance over conventional space propulsion systems. The purpose of the most recent work to date has been to: perform solid gas formation research and analysis in support of the test-bed engine development; and design, develop, and test small test-bed rocket engines for combustion testing of solid cryogens with gas or liquid propellants. ORBITEC has carried out the following work: developed approaches to allow introduction of gas mixtures into freezer hardware; conducted research on the formation of many solid grains from the gas and liquid phase; determined the temperature gradient through grains; evaluated the freezing process of various gas mixtures; evaluated grain life under a GHe purge; developed freezer simulations and combustion models; developed requirements, operational, and design definitions for engines and systems; conducted engine design and analysis; performed component/prototype testing; and conducted over 30 test-bed engine firings, with the latest firing being held at USAF/PL. A brief summary of results are as follows: freezing of mixtures of gases in the warm wall tube freezer proved that, in oxygen with small amounts of nitrogen, cracks, clear zones, perhaps preferential freezing, and all types of discontinuities in the grain were observed; the freezer model accurately predicts the freezing process and has been verified by experiments; several combustion models were developed and proved useful to predict burn times and performance; a regression model has been developed and is still evolving; successfully fired several engines numerous times, achieving burn times from 2 to 15 seconds at chamber pressures approaching 200 psi; results showed that surface area appears to be the driving factor to the shape of the chamber pressure curve; there appears to be no limit to the possible use of this technology as applied to HEDM-related research, attitude control thrusters, orbit transfer vehicles, high-thrust military ABMs, LVs/boosters, and single-stage-to-orbit vehicles.

HIGH ENERGY DENSITY MATTER CONTRACTORS' CONFERENCE
University of Colorado, Boulder, CO 5 to 7 June, 1996

## Progress Towards Deposition of Velocity Selected Aluminum Atoms into Cryogenic para-Hydrogen Matrices

Mario E. Fajardo, Michel Macler, and Simon Tam

Propulsion Sciences Division, Propulsion Directorate, Phillips Laboratory
(OLAC PL/RKS Bldg. 8451, Edwards AFB, CA 93524-7680)

### ABSTRACT

Most of this past year has been spent making extensive equipment modifications to our laser ablation/matrix isolation experiment. We have combined several experimental techniques in one apparatus in order to determine the matrix deposition conditions which optimize the concentrations of trapped energetic species, both atomic and molecular.

We have previously demonstrated the efficient isolation of Li, B, Na, Mg, and Al atoms in rare gas matrices at 0.001 to 0.1 % molar concentrations via the combined laser ablation/matrix isolation techniques. We had attributed the high atomic isolation efficiency, and the observed formation of novel trapping site structures, to the high kinetic energy of the laser ablated atoms (all comparisons relative to experiments using thermal effusive metal atom sources). However, preliminary attempts at trapping Li and Al atoms in Ar matrices, during which a magnetic field was used to reject any **ions** produced by the laser ablation process, have failed. These results force us to reconsider alternative microscopic models of the matrix deposition process in which the metal ions produced by laser ablation are trapped in the matrix and subsequently neutralized, and are thus responsible for the novel effects we have previously ascribed to fast metal atoms.

Results to date of attempted depositions in hydrogen matrices have been far less illuminating. The presence or absence of the ion deflecting magnets has no obvious effect on the strong Li atom absorptions typically observed in $Li/H_2$ matrices, or on the weak Al atom absorptions typically observed in $Al/H_2$ matrices. We will focus our future efforts on depositions into hydrogen and deuterium matrices, using a variety of matrix diagnostics to determine the ultimate fate of the metal atoms.

## INTRODUCTION

We have previously demonstrated the efficient isolation of Li, B, Na, Mg, and Al atoms in rare gas matrices at 0.001 to 0.1 % molar concentrations via the combined laser ablation/matrix isolation techniques [refs. 1-6]. We also observed novel absorption features in the visible spectra of Li/Ar, Li/Kr, Na/Ar, and Na/Kr matrices prepared using laser ablation metal atom sources (compared to experiments using thermal effusive metal atom sources) which we ascribed to the formation of novel metal atom trapping site structures [refs. 1, 3, 7]. We attributed both the high atomic isolation efficiency, and the formation of novel trapping site structures to the high kinetic energy (typically 1 to 20 eV) of the laser ablated atoms, which we conjectured permits these atoms to penetrate (a few atomic layers) into predeposited matrix structures. We proposed that this process reduces the effects of recombination of the metal atoms at the accreting surface of the matrix (long touted in the matrix isolation literature as the primary mechanism for loss of reactive species during sample preparation) and also causes the formation of tighter trapping site structures [ref. 1].

Depositions of laser ablated atoms into hydrogenic ($H_2$, $D_2$) matrices also produced initially promising results, in that strong Li atom [ref. 2] and Mg atom [ref. 6] absorptions were readily observed. However, the poor quality of the B and Al atom spectra from hydrogenic matrices [ref. 5], and the observation of infrared absorptions of boron-hydrides and aluminum-hydrides [refs. 6, 8] from these samples, raised the spectre of loss of metal atoms to unwanted reactions with the hydrogenic hosts. The energetics of various atom+$H_2$ reactions were reviewed in ref. 5; all such energetic barriers are below the kinetic energies of the fastest laser ablated metal atoms.

Thus began our quest to develop a velocity selected fast metal atom source suitable for matrix isolation depositions. We hoped to find a regime of atomic "implantation" energies which would show improved atomic isolation efficiency by avoiding surface recombination, yet minimize reactions between the fast metal atoms and the hydrogenic host. This effort culminated in the invention of a novel, non-mechanical technique for performing velocity selection on the fast metal atoms produced by laser ablation [refs. 9-12]. This process (described below) relies on the efficient photoionization of those ablated metal atoms with unwanted velocities, and their subsequent rejection from the main atomic beam by a static

magnetic field. As a side effect, the magnets also reject the metal ions produced directly by laser ablation.

We recently combined the two setups used in the laser ablation/velocity selection and matrix isolation experiments into a single deposition apparatus. During our preliminary attempts at trapping Li and Al atoms in Ar matrices (described below), we found that simply inserting the ion-rejection magnets into the ablated atomic beam resulted in the nearly complete loss of the Li and Al atom matrix absorptions. These results force us to discard much of our microscopic model of the matrix deposition process in which the incident kinetic energy of the fast metal atoms is the key factor, and to reconsider models in which the metal ions produced by laser ablation are trapped in the matrix and subsequently neutralized, so that the metal **ions** are thus responsible for the novel effects we have previously ascribed to fast metal **atoms**.

In what follows we describe: (1) the new experimental apparatus and sample preparation conditions, (2) the results of preliminary experiments on depositing Li/Ar, Al/Ar, and Li/$H_2$ matrices, (3) the impact of these observations on our microscopic model of the matrix deposition process, and finally (4) our early speculations on how the apparent initial trapping of metal ions and their subsequent neutralization may be used to maximize the concentrations of trapped metal atoms in future experiments.


## EXPERIMENTAL

A greatly simplified version of the new experimental apparatus is shown in Figure 1. Our new Temporally and Spatially Specific PhotoIonization (TASSPI) Velocity Selected metal atom Source (VSS) has been described in detail in a series of publications [refs. 9-12]. Briefly: pulses of atoms with broad velocity distributions are produced by laser ablation ($\lambda$ = 308 nm) of a metal target in vacuum. A second pulsed laser, delayed by ~ 1 $\mu$s and crossed at a right angle to the atomic beam, is used to photoionize only those atoms with unwanted velocities, i.e.: atoms moving too fast or too slow to be hidden behind an opaque mask placed ~ 1 cm from the ablated surface. The photoions, and any metal ions produced in the initial ablation process, are subsequently deflected from the atomic beam by a static magnetic field. Previously, we have demonstrated velocity selection of Al, Ga, and In atoms, and velocity

selected Al atom fluxes equivalent to $\Phi \sim 10^{11}$ atoms/(cm$^2$-eV-pulse) at a working distance of 10 cm [refs. 11, 12].

The TASSPI VSS module has been attached to the deposition chamber of our liquid helium bath cryostat. The cryostat outer vacuum jacket has been modified for vertical travel of the matrix deposition substrate into and out of the metal atom beam path, allowing for characterization of the beam by a Quartz Crystal Microbalance (QCM), or by an Electrostatic Energy Analyzer/Time-Of-Flight Mass Spectrometer (EEA/TOFMS) system. The QCM gives a measure of the total flux of metal, while the EEA/TOFMS gives directly the kinetic energy distributions (KEDs) of the metal atoms and ions, as well as providing for the detection of metal clusters and/or particles.

The simple straight tube matrix host gas inlet system has been replaced by an ortho-to-para hydrogen convertor (O/P CONVERTOR) consisting of a 1/8 inch O.D. by 1.5 meter long copper tube packed with 1.4 g of APACHI catalyst [ref. 13] and wound onto a copper bobbin which can be cooled to below 20 K by a closed-cycle cryostat. This convertor can provide 99.99% para-hydrogen at 15 K to the matrix deposition substrate, in place of the
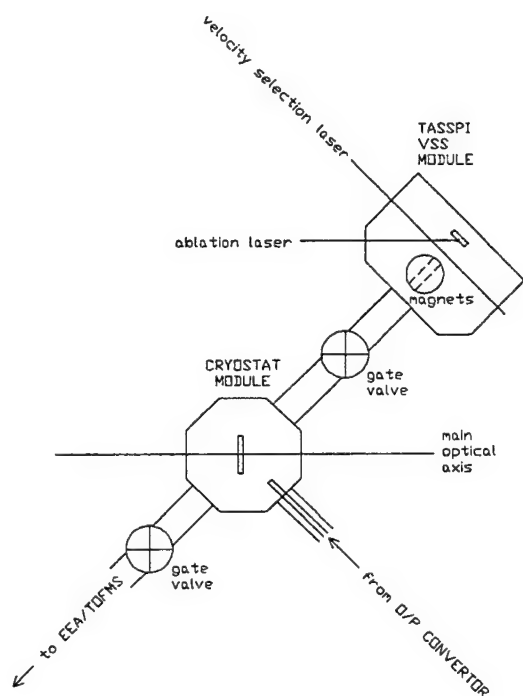


**Figure 1. Experimental Schematic.**
Laser ablation of metal targets in vacuum takes place in the TASSPI VSS MODULE. Metal ions produced by the ablation process ($\lambda = 308$ nm), or generated by photoionization of metal atoms by the *velocity selection laser* ($\lambda = 193$ nm), are deflected by a pair of (removable) *magnets*. The ablation products continue through a *gate valve* and into the CRYOSTAT MODULE where they are codeposited onto a 2 K transparent substrate along with a flow of hydrogen gas from the O/P CONVERTOR. Sample growth rate, and other properties of the deposited film are monitored by a variety of diagnostics aligned along the *main optical axis*. The deposition substrate can be raised out of the ablated beam and the ablation products characterized by a quartz crystal microbalance (not shown) or by the EEA/TOFMS system. See main text for definitions of acronyms and other details.

25:75 para:ortho composition room temperature normal-hydrogen used in our previous hydrogenic matrix experiments [ref. 2]. In the preliminary rare gas matrix host experiments, the Ne or Ar gas was simply passed through the room temperature convertor, although we have recently found that cooling the convertor to $\approx$ 200 K greatly reduces matrix contamination by $H_2O$, $CO_2$ and other residual atmospheric gas impurities adsorbed on the catalyst.

Finally, we have arranged this experiment so as to allow for characterization of the matrix by simultaneous UV/Vis absorption, IR absorption, laser induced fluorescence, and spontaneous Raman scattering. To accomodate the various diagnostics, the majority of the apparatus sits inside a 0.5 $m^3$ polycarbonate box purged with a constant flow of dry $N_2$ gas. In this report, we present only data from the UV/Vis absorption diagnostic.

## RESULTS AND DISCUSSION

Figure 2 shows the results of two attempts at depositing Li/Ar matrices, made with and
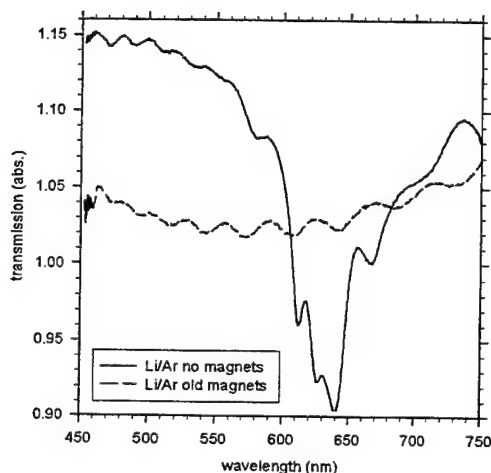


**Figure 2. Li/Ar Matrices.**
Transmission spectra of as-deposited Li/Ar matrices with T = 20 K, $\Phi_{abl} \approx 4 \times 10^7$ W/cm$^2$, 30 mJ/pulse, 10 Hz repetition rate, 15 minute Li deposition time, Ar inlet flow rate = 1.1 mmol/hr. The legend "old magnets" refers to the 0.74 cm spacing used in the original deflection magnet assembly which provides a field of 4.4 kGauss at its center.
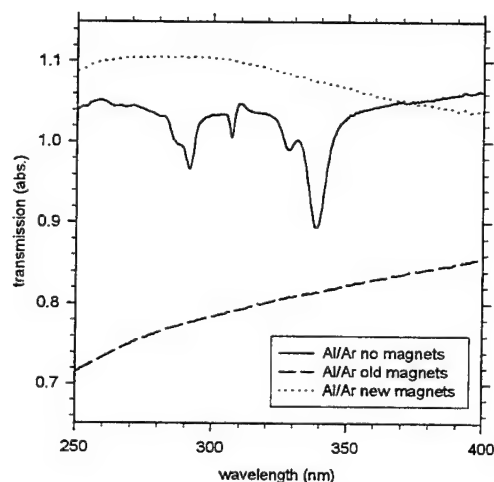
**Figure 3. Al/Ar matrices.**
Transmission spectra of as-deposited Al/Ar matrices with T = 20 K, $\Phi_{abl} \approx$ 1.1x10$^8$ W/cm$^2$, 160 mJ/pulse, 10 Hz repetition rate, 15 minute Al deposition time, Ar inlet flow rate = 1.0 mmol/hr. The legend "new magnets" refers to the 2.0 cm spacing used in the second deflection magnet assembly which provides a field of 1.9 kGauss at its center.

38

without the ion deflection magnets. The spectrum of the sample made without the magnets clearly shows the previously reported [ref. 1] matrix perturbed Li atom 2p←2s "blue triplet" absorption feature between 610 nm and 640 nm, as well as a vestigal "red triplet" absorption peaked at 670 nm. The spectrum of the sample made using the ion deflection magnets shows only a weak progression of transmission interference fringes consistent with the ≈ 5 μm total matrix thickness.

Figure 3 shows similar results from three attempted depositions of Al/Ar matrices. The spectrum of the sample prepared without the magnets shows the well known 4s←3p and 3d←3p Al atom absorptions at 338 nm, and 287 & 292 nm, respectively [ref. 14]. The smaller peak at 328 nm has been previously observed in Al/Ar matrices prepared by laser ablation [ref. 15], but was not commented upon; we tentatively assign it to the 4s←3p transition of Al atoms in a secondary trapping site. The feature at 308 nm is an artifact caused by the inadvertent exposure of the spectrometer's array detector to scattered light from the ablation laser. The spectra of two samples prepared using two different ion deflection magnet assemblies do not show any of these absorption features. The new magnet assembly, with its
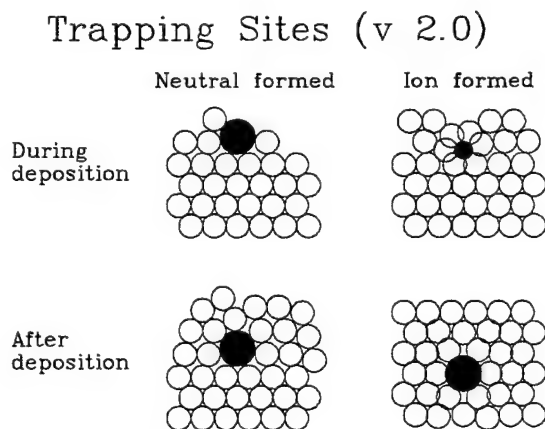


**Figure 4. M/Rg Trapping Site Formation.**
Revised cartoon depicting the differences between final metal atom trapping site structures formed by depostion of metal atoms vs. metal ions.
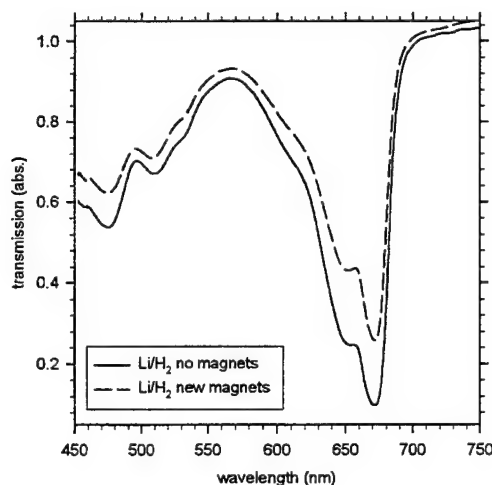


**Figure 5. Li/$H_2$ matrices.**
Transmission spectra of as-deposited Li/$H_2$ matrices with T = 2 K, $\Phi_{abl} \approx 5\text{x}10^7$ W/cm$^2$, 40 mJ/pulse, 10 Hz repetition rate, 15 minute Li deposition time, $H_2$ inlet flow rate through O/P convertor not measured.

larger spacing and hence weaker and more uniform magnetic field, was used to allay fears that inhomogeneities in the magnetic field might be deflecting neutral Al atoms from the beam.

The results shown in Figures 2 & 3 demonstrate that it is the laser ablated Li and Al **ions**, rather than the fast metal **atoms**, which are trapped efficiently in Ar matrices. The ions are subsequently neutralized to yield trapped atoms. Furthermore, the novel spectroscopic features observed in the Li/Ar and Al/Ar experiments reflect the formation of tight trapping sites due to the strong ion/induced-dipole $M^+/^{\delta-}Ar^{\delta+}$ interactions, as depicted in Figure 4. We had begun to suspect the importance of the role of ionic species in the matrix deposition process after observing the "blue" and "violet" triplet absorption features [ref. 3] in Na/Ar matrices prepared with a commercial $Na^+$ ion source [ref. 16]. Finally, recent molecular dynamics (MD) simulations of fast Na atoms incident onto Ar surfaces also dispute our original notion that fast laser ablated atoms can actually penetrate into previously deposited Ar layers [ref. 17].

Surprisingly, the presence or absence of the laser ablated ions seems to make little difference in the spectra of $Li/H_2$ matrices, as is shown in Figure 5. Both spectra show strong $H_2$ matrix perturbed Li atom $2p\leftarrow2s$ absorptions, just as were previously observed in $Li/H_2$ matrices produced using our more primitive apparatus which did not convert the ortho-$H_2$ to para-$H_2$ prior to deposition [ref. 2]. Attempts at depositing Al atoms into para-$H_2$ matrices have so far met with the same meager successes as were observed using the older apparatus [ref. 5].

Finally, all the metal atom absorptions shown in this preliminary study are for matrices containing $\sim 0.01$ % metal atoms (*i.e.* guest:host ratio of 1:10,000). It remains to be seen if the method of initially depositing ions, then subsequently neutralizing them to yield isolated atoms, can be extended to higher concentrations. One might have suspected that space charge limitations would preclude the stability of large matrix regions with ion concentrations of even 0.01 % ($\sim 3\times10^{18}$ ions/cm$^3$, or mean ionic separations of $\sim$ 70 Å). Perhaps, however, the instantaneous concentration of ions themselves never has to actually reach such high levels. Lower concentrations of freshly deposited ions may become mechanically stable due to partial screening by polarization of the host matrix dielectric. These "surface" ions could then be

neutralized by photoelectrons produced in subsequent ablation laser pulses. Ensuing alternating pulses of metal atoms and photoelectrons could fill in the gaps between the trapped metal atoms. Thus, the limiting factor to the achievable atomic concentration would be recombination of the atoms due to thermal energy liberated by the neutralization of the ions.

## CONCLUSIONS AND FUTURE DIRECTIONS

We have demonstrated that laser ablated metal **ions**, and not laser ablated fast metal **atoms**, are responsible for the novel effects observed in our Ar matrix experiments. More work must be done to elucidate the role of metal ions in hydrogenic matrix depositions. If, in fact, the mutual repulsion between metal ions is responsible for their efficient isolation during the hydrogenic matrix deposition process, then our focus in future experiments must turn away from finding deposition conditions which minimize recombination of atoms on the accreting matrix surface, and towards finding mechanisms for the efficient removal of the large amounts of energy released upon the ultimate neutralization of those isolated ions.

## REFERENCES

1. M.E. Fajardo, P.G. Carrick, and J.W. Kenney III, J. Chem. Phys. **94**, 5812 (1991).

2. M.E. Fajardo, J. Chem. Phys. **98**, 110 (1993).

3. S. Tam and M.E. Fajardo, J. Chem. Phys. **99**, 854 (1993).

4. R.A. Corbin and M.E. Fajardo, J. Chem. Phys. **101**, 2678 (1994).

5. M.E. Fajardo, S. Tam, T.L. Thompson, and M.E. Cordonnier, Chem. Phys. **189**, 351 (1994).

6. S. Tam and M.E. Fajardo, unpublished B, Mg, and Al matrix isolation data.

7. J.A. Boatz and M.E. Fajardo, J. Chem. Phys. **101**, 3472 (1994).

8. M.E. Fajardo, S. Tam, and M. Macler, Trapping of Light Metal Atoms in Hydrogen Matrices in Proceedings of the High Energy Density Matter (HEDM) Contractors' Conference held 6-8 June 1993 in Woods Hole MA, ed. T.L. Thompson, PL-TR-93-3041 (Phillips Lab, Edwards AFB, CA, 1993).

9. M. Macler and M.E. Fajardo, MRS Symp. Proc. **285**, 105 (1993).

10. M. Macler and M.E. Fajardo, Appl. Phys. Lett. **65**, 159 (1994).

11. M. Macler and M.E. Fajardo, Appl. Phys. Lett. **65**, 2275 (1994).

12. M. Macler and M.E. Fajardo, MRS Symp. Proc. **388**, 39 (1995).

13. I.F. Silvera, Rev. Mod. Phys. **52**, 393 (1980).

14. R. Grinter and R.J. Singer, Chem. Phys. **113**, 87 (1987).

15. G. Jeong and K.J. Klabunde, J. Am. Chem. Soc. **108**, 7103 (1986).

16. D. Silverman and M.E. Fajardo, unpublished results of $Na^+$ ion matrix depositions.

17. L.S. Perkins, unpublished results of MD simulations of Na/Ar matrix depositions.

## Transport of Model HEDM (The BIG FLUSH)

Mario E. Fajardo, Michelle DeRose, and Amy Pritz

Propulsion Sciences Division, Propulsion Directorate, Phillips Laboratory
(OLAC PL/RKS Bldg. 8451, Edwards AFB, CA  93524-7680)

### ABSTRACT

We have completed a series of three experiments in which gram scale $N/N_2/lHe$ samples ($N:N_2 \sim 1:1000$) have been transported from a 2 K liquid He environment to a room temperature receptacle.  Optical images of the thermoluminescence (TL) from recombining N atoms were recorded using four video cameras placed along the transport path.  In all three experiments, these images showed that the model high energy density matter (HEDM) propellant samples began decomposing and releasing energy immediately upon ejection from the 2 K production/storage chamber, but that the majority of the energy releases took place in the room temperature "combustion" chamber.

### INTRODUCTION

One proposed method of utilizing cryogenic solid propellants based on solid hydrogen doped with energetic species is as a slurry in liquid helium [ref. 1].  The experiments described below seek to elucidate the special storage and handling requirements of gram scale $N/N_2/lHe$ ($N:N_2 \sim 1:1000$) "model" HEDM propellant samples.

### EXPERIMENTAL

The experimental apparatus (Figure 1) is only slightly modified from that described in detail in last year's conference proceedings [ref. 2].  Briefly:  the products emerging from a corona excited supersonic expansion (CESE) of a 1:50 $N_2/He$ gas mixture are deposited onto a "superfluid" liquid He II surface kept below 2 K by continuous pumping on the He vapor ($P_{He} \sim 10$ Torr).  The condensed luminescent solid (which we suspect to be a diffusion limited $N/N_2/He$ aggregate, but has been described by the original investigators as an "Impurity-

stabilized Helium Solid Phase (IHSP)" [ref. 3]) sinks through the liquid He and is collected by a funnel into a 12.7 mm inside diameter by 5 cm tall glass tube.

After several grams of sample have been prepared, the CESE source is shut off, and the excess liquid He is boiled off at $T \approx 4.0$ K. During this process the sample displays only faint green thermoluminescence. The last half-liter or so of liquid He is removed by pumping, which cools the bottom of the chamber back to $T \approx 2$ K. A pneumatically actuated fast plunger then forces the "dry" $N/N_2/He$ sample down through a brass foil burst disk and into the top of a 12.7 mm inside diameter glass tube which leads straight down to a room temperature 50 ml Pyrex beaker situated in a separate evacuated chamber. The bright green
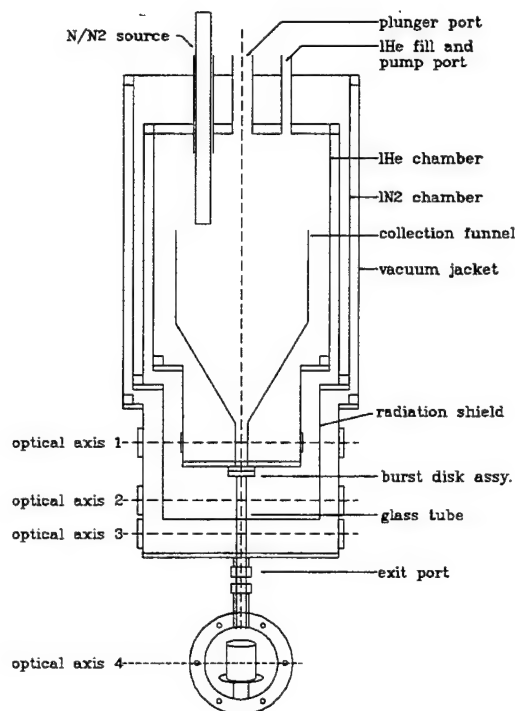


**Figure 1. Experimental Diagram**
New additions from last year include a pneumatically actuated plunger which forces the model HEDM sample through a brass foil burst disk, through a glass delivery tube, and into a room temperature receptacle.
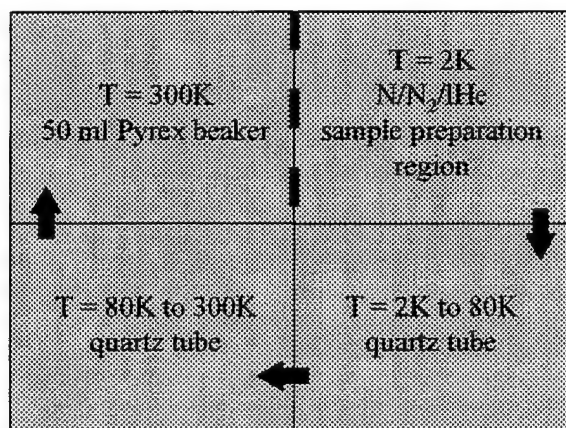


**Figure 2. Quad-Split Screen Legend.**
This figure shows the ordering of the video images in Figs 3(a)-(d) obtained from the four camera views depicted in Fig. 1. The upper right panel shows the liquid He region of the cryostat, the lower right panel shows the glass tube leading from the liquid He region to the liquid $N_2$ cooled radiation shield, the lower left panel shows the glass tube between the radiation shield and the room temperature outer vacuum jacket, and the upper left panel shows the room temperature Pyrex beaker in the evacuated "combustion" chamber. The arrows indicate the sample flow sequence during a "Big Flush."

Fig. 3a

01:13:51:01



Fig. 3b

01:13:51:02

44

Fig. 3c

01:13:51:02



Fig. 3d

01:13:51:03

45

Fig. 4
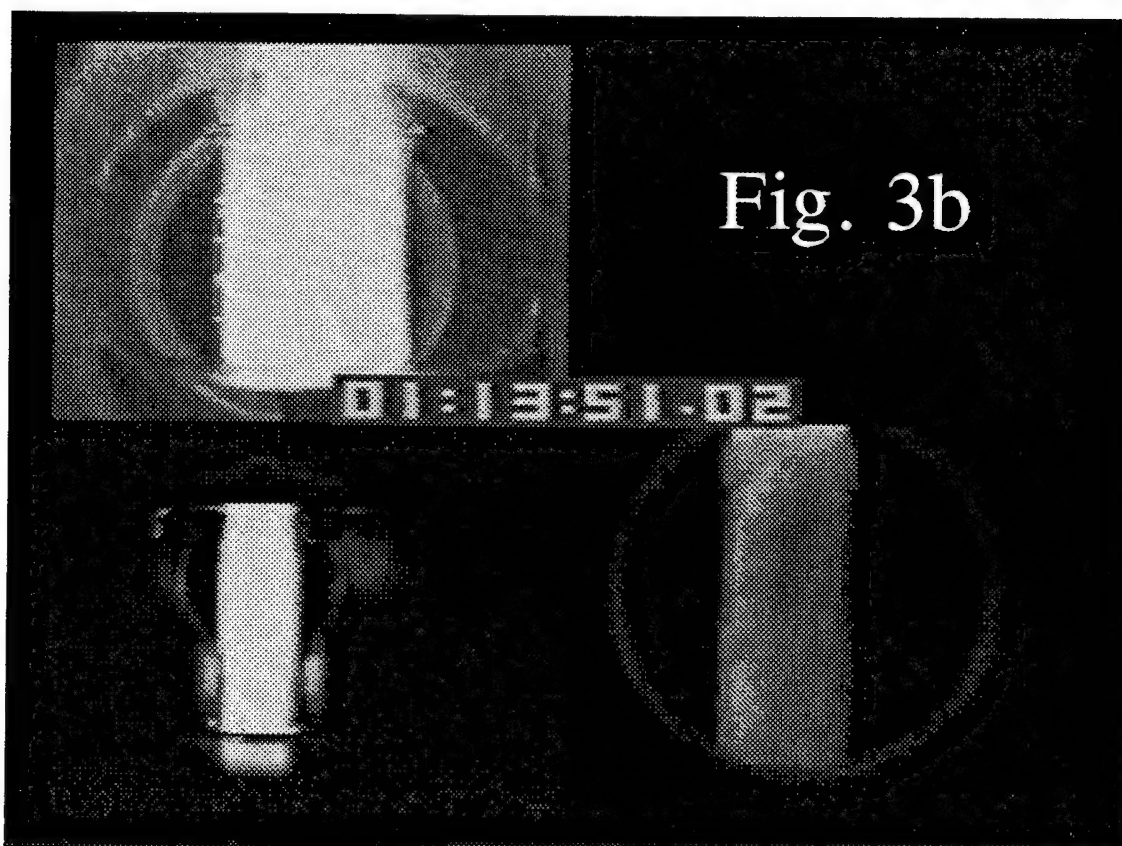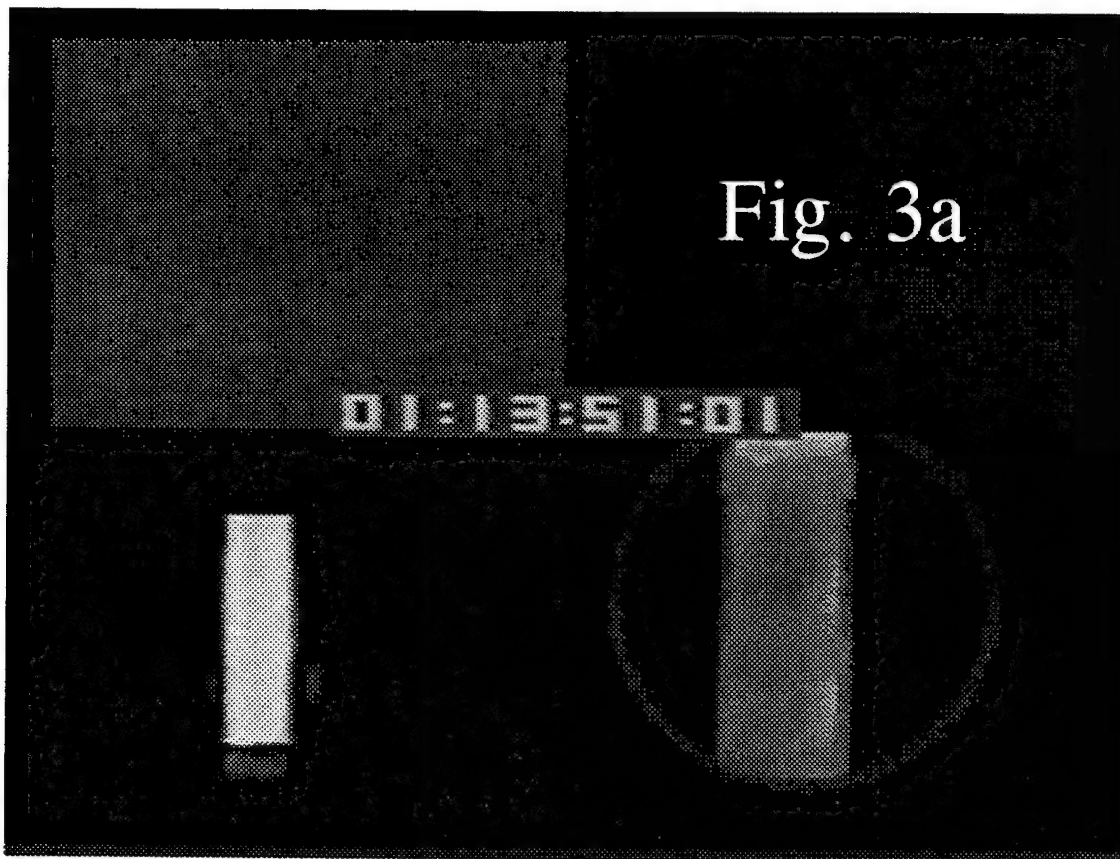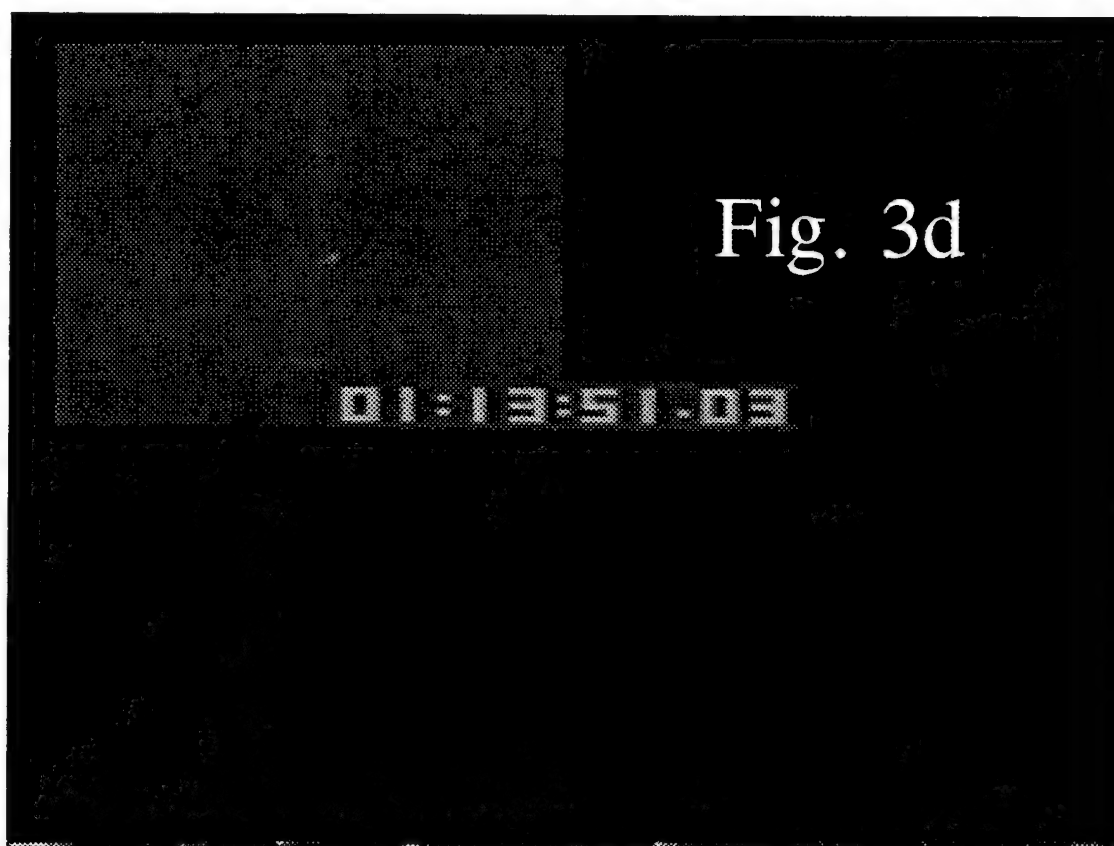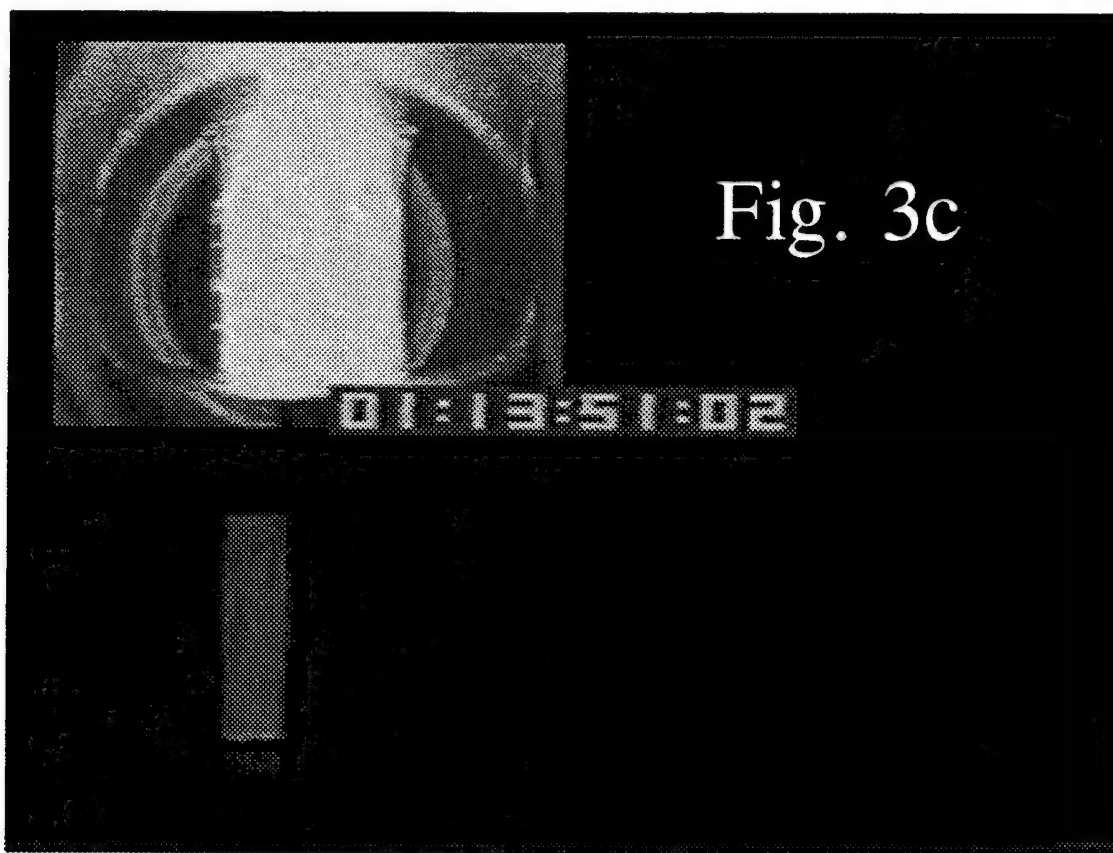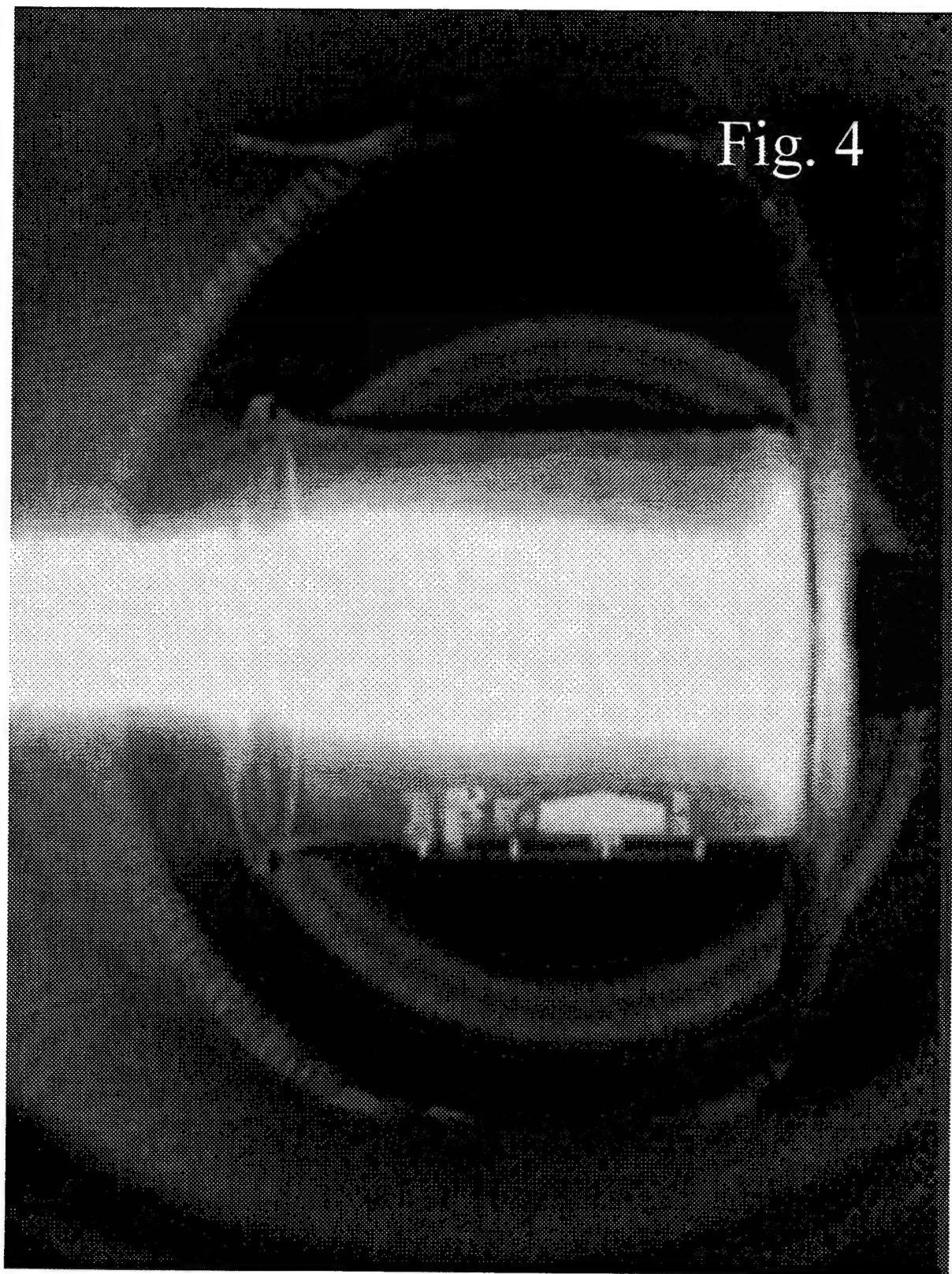
thermoluminescence which accompanies the rapid heating of the sample is recorded with four video cameras placed at the four optical axes shown in Figure 1. Figure 2 describes how the four camera views have been combined into a single "quad-split" screen in Figures 3(a)-(d). Subsequent images in Figure 3 are separated by 16.7 ms from the previous video "sub-frame."

## RESULTS, DISCUSSION, AND CONCLUSIONS

Figure 3 shows the results of the first Big Flush experiment, which were reproduced precisely in the other experiments. Figure 3a shows the first video sub-frame in which any thermoluminescence can be detected. The luminous major energy release in the room temperature Pyrex beaker shows up as the upper left hand panels of Figures 3(b)&(c), and lasts less than 34 ms. The samples are apparently completely vaporized by a combination of heat transport from the room temperature surroundings and the energy released by the recombining N atoms. Figure 4 shows a close-up of the upper left hand panel in Figure 3(c).

The observation of thermoluminescence in the 2 to 80 K section of the glass transport tube does not bode well for the prospects of pumping HEDM doped hydrogen/helium slurries for appreciable distances. These experiments indicate that the entire propellant transport system should remain at liquid helium temperatures to prevent catastrophic recombination of the HEDM species. On the other hand, the absence of visible thermoluminescence from the sample collection region itself (upper right hand panels in Figure 3) during compression of the sample by the pneumatic plunger, shows that the present model HEDM samples are not as delicate as may have been presumed. Further testing of this type should await the production of HEDM samples containing higher concentrations of energetic species.

## REFERENCES

1. R.H. Frisbee, "Systems-level implications of high energy density matter (HEDM) propulsion concepts" in Proceedings of the High Energy Density Matter (HEDM) Contractors' Conference held 12-15 April 1992 in Lancaster CA, M.R. Berman ed., (AFOSR, Bolling AFB, DC, 1992).

2. M.E. DeRose, Y.K. Bae, C.W. Larson, and M.E. Fajardo, "Thermoluminescence studies of $N/N_2$ condensates formed on liquid helium II" in Proceedings of the High Energy Density Matter (HEDM) Contractors' Conference held 6-8 June 1995 in Woods Hole MA, P.G. Carrick and S. Tam eds., PL-TR-95-3039 (Phillips Lab, Edwards AFB, CA, 1995).

3. R.E. Boltnev, E.B. Gordon, V.V. Khmelenko, I.N. Krushinskaya, M.V. Martynenko, A.A. Pelmenev, E.A. Popov, and A.F. Shestakov, Chem. Phys. **189**, 367 (1994).

# Spectral Theory of Weakly Bonded Atomic Aggregates

**Jeffrey A. Sheehy[†], Jerry A. Boatz, and Mario E. Fajardo**

Propulsion Sciences Division
USAF Phillips Laboratory
Edwards AFB, CA   93524-7680

**Peter W. Langhoff[‡]**

Department of Chemistry
Indiana University
Bloomington, IN   47402

## I. Introduction

Research aimed at enhancing the performance of rocket propulsion systems by employing atom- or molecule-seeded cryogenic fuels or oxidizers continues to be an important component of the high energy density matter (HEDM) program [1]. This concept is viewed as a novel yet potentially feasible means of achieving significant improvements in operating characteristics such as the specific impulse, which is the total impulse, or time-integrated thrust force, per unit weight of propellant.  Calculations suggest that the addition of even a few mole percent of selected atomic or molecular species to solid hydrogen may provide specific impulse increases of as much as 25% by comparison with current liquid-hydrogen/liquid-oxygen rocket engines [2]. Consequently, determining structural, spectroscopic, and other properties of doped cryogenic solids remains an important area of HEDM study, with theoretical and computational efforts supporting experimental work.

In the present report, the development, implementation, and application of a new method for constructing adiabatic potential-energy surfaces for aggregates of interacting atomic or molecular species is outlined. Although the spectral theory of binding has recently been described in the literature [3], certain aspects of the development, particularly related to its computational implementation, continue to evolve. Conceptually, the approach is designed to provide a unified quantum-mechanical treatment of both physical and chemical binding, and a new foundation for a class of theories that construct exact many-body adiabatic electronic potential-energy surfaces, including non-pairwise-additive contributions, from information about component fragments. In particular, the spectral theory is shown to generalize and clarify aspects of "diatomics-in-molecules" methods [4,5], giving rigorous and unambiguous prescriptions for their convergent computational implementation.

In Section II, the main features of the theory are indicated, paying specific attention to

---

† Hughes STX Corporation
‡ AFOSR University Resident Research Professor, 1996-1997.

points of comparison with other approximate treatments of non-additive interactions [4-11]. An initial application of the spectral theory to sodium-seeded argon clusters and solids is discussed briefly in Section III. A specific approach to implementing the theory as a computational technique employing information from *ab initio* quantum-chemical calculations of diatomic properties is described, and reference is made to predictions of the structure and optical absorption spectrum of NaAr$_{11}$ based on classical Monte Carlo simulations using potential surfaces provided by the spectral method [12,13]. Finally, future directions for this project are indicated in Section IV.

## II. Theoretical Development

### A. Spectral Representation

The general form of the Hamiltonian operator for an aggregate of $N$ atoms may be written [14,15]

$$\hat{H}(i,j,\ldots) = \sum_{\alpha=1}^{N} \left\{ \hat{H}^{(\alpha)}(i) + \sum_{\beta=1}^{N} (\beta > \alpha) \, \hat{V}^{(\alpha,\beta)}(i;j) \right\}, \tag{1}$$

where the Hamiltonian operator for the $n_\alpha$-electron atom $\alpha$ and the interaction Hamiltonian between the pair of atoms $\alpha$ and $\beta$ are expressed, in the Coulomb approximation, as [16]

$$\hat{H}^{(\alpha)}(i) = \sum_{i}^{n_\alpha} \left\{ -\frac{\hbar^2}{2m} \nabla_i^2 - \frac{Z_\alpha e^2}{r_{i\alpha}} + \frac{1}{2} \sum_{i'}^{n_\alpha} (i' \neq i) \, \frac{e^2}{r_{ii'}} \right\} \tag{2}$$

and

$$\hat{V}^{(\alpha,\beta)}(i;j) = \frac{Z_\alpha Z_\beta e^2}{R_{\alpha\beta}} - \sum_{i}^{n_\alpha} \frac{Z_\beta e^2}{r_{i\beta}} - \sum_{j}^{n_\beta} \frac{Z_\alpha e^2}{r_{j\alpha}} + \sum_{i}^{n_\alpha} \sum_{j}^{n_\beta} \frac{e^2}{r_{ij}}. \tag{3}$$

Here, the notation $(i;j)$ denotes distinguishable groups of electrons, with arbitrary assignment of a particular electron $i$ or $j$ to atom $\alpha$ or $\beta$. Electronic eigenstates of the operator in Eq. (2) may be written as a vector $\mathbf{\Phi}^{(\alpha)}(i)$ of functions $\Phi_{E,\Gamma}^{(\alpha)}(i)$ that are eigenfunctions of energy $(E)$, orbital and spin angular momenta, and parity $(\Gamma \equiv L, M_L, S, M_S, P)$ [17], transforming irreducibly as the totally antisymmetric representation of the permutation group for the electrons labeled $i$ [18]. These atomic spectral states, which include the ionization continua, are quantized in a set of $N$ individual coordinate systems with axes parallel to the laboratory-frame axes, and with the $N$ atomic centers specified in the laboratory frame by the vectors $\mathbf{R}_\alpha$.

Because the atomic spectral states $\mathbf{\Phi}^{(\alpha)}(i)$ form a complete antisymmetric set for representation of square-integrable functions of electron coordinates $i$ [18,19], the ordered direct product spectrum of these states,

$$\mathbf{\Phi}(i;j;k;\ldots) = \left\{ \mathbf{\Phi}^{(\alpha)}(i) \otimes \mathbf{\Phi}^{(\beta)}(j) \otimes \mathbf{\Phi}^{(\gamma)}(k) \cdots \right\}_O, \tag{4}$$

suffices to represent the antisymmetric eigenstates of all the electrons $i,j,k,\ldots$ in the atomic aggregate [6-9]. The notation $\{\cdots\}_O$ denotes an ordering rule on the indices of

the direct product functions; this choice, although arbitrary, must be followed in any manipulations of matrices constructed in the spectral basis.

The product set of Eq. (4) does not constitute a symmetrical representation [18] of the aggregate, and members of the set are not antisymmetric with respect to exchange of electrons between distinct sets, yet this basis can nevertheless be employed to represent totally antisymmetric wave functions. Prior antisymmetrization of the product basis, which has been commonly employed to avoid unphysical solutions corresponding to other irreducible representations of the electron permutation group [4,5,7], can lead to linear dependence, frequently termed "overcompleteness," in the limit of unrestricted closure unless preventative measures are devised [6,8,9]. Although the present formulation, which avoids the use of the overlap matrix that arises with an explicitly antisymmetrized atomic product basis set, is expected to be particularly suitable for aggregates that do not display significant electron delocalization or transfer between atoms, its applicability is not limited to such systems.

## B. Matrix Representation

In a matrix representation the Hamiltonian in the product spectral basis of Eq. (4) has the form

$$\mathbf{H}(\mathbf{R}) = \sum_{\alpha=1}^{N} \left\{ \mathbf{H}^{(\alpha)} + \sum_{\beta=1}^{N} (\beta > \alpha) \, \mathbf{V}^{(\alpha,\beta)}(\mathbf{R}_{\alpha\beta}) \right\}, \tag{5}$$

where $\mathbf{R} = (\mathbf{R}_1, \mathbf{R}_2, \ldots, \mathbf{R}_N)$ gives the position of the $N$ atoms in the laboratory frame, $\mathbf{R}_{\alpha\beta} \equiv \mathbf{R}_\beta - \mathbf{R}_\alpha$ corresponds to the relative positions of atoms $\alpha$ and $\beta$, and $\mathbf{H}^{(\alpha)}$ and $\mathbf{V}^{(\alpha,\beta)}(\mathbf{R}_{\alpha\beta})$ are the matrix representations of the operators in Eqs. (2) and (3). The dimensions of these matrices follow from the size of the complete product basis, with matrix elements determined by the product ordering convention of Eq. (4). Evident from Eq. (5) is the rigorous pairwise-additive nature of the Hamiltonian matrix in terms of interaction matrices constructed in the direct product basis [7]. This feature may be conveniently exploited in the present development which, as indicated in the foregoing, does not require the basis-set overlap matrix that has complicated previous approaches [4,5].

By choosing an ordering convention in Eq. (4) where later indices run to completion prior to earlier indices, the final atomic and atomic-pair matrices of Eq. (5), $\mathbf{H}^{(N)}$ and $\mathbf{V}^{(N-1,N)}(\mathbf{R}_{N-1\,N})$, assume block diagonal forms with repeating matrices constructed in the corresponding atomic and atomic-pair product basis, respectively, on the diagonals. The analogous matrices for an arbitrary pair of atoms $(\alpha, \beta)$ are obtained from similar block diagonal matrices by interchanging rows and columns determined by the relative positions of the indices $\alpha$ and $\beta$ to $N - 1$ and $N$, respectively:

$$\mathbf{H}^{(\alpha)} = \left\{ \begin{matrix} \mathbf{E}^{(\alpha)} & \mathbf{0} & \mathbf{0} & \cdots \\ \mathbf{0} & \mathbf{E}^{(\alpha)} & \mathbf{0} & \cdots \\ \mathbf{0} & \mathbf{0} & \mathbf{E}^{(\alpha)} & \cdots \\ \vdots & \vdots & \vdots & \ddots \end{matrix} \right\}_O \tag{6}$$

50

and

$$
\mathbf{V}^{(\alpha,\beta)}(\mathbf{R}_{\alpha\beta}) = \left\{ \begin{matrix} \mathbf{v}^{(\alpha,\beta)} & \mathbf{0} & \mathbf{0} & \cdots \\ \mathbf{0} & \mathbf{v}^{(\alpha,\beta)} & \mathbf{0} & \cdots \\ \mathbf{0} & \mathbf{0} & \mathbf{v}^{(\alpha,\beta)} & \cdots \\ \vdots & \vdots & \vdots & \ddots \end{matrix} \right\}_{\text{O}} .
\tag{7}
$$

Here, the definitions

$$
\mathbf{E}^{(\alpha)} = \left\langle \mathbf{\Phi}^{(\alpha)}(i) \middle| \hat{H}^{(\alpha)}(i) \middle| \mathbf{\Phi}^{(\alpha)}(i) \right\rangle,
\tag{8}
$$

$$
\mathbf{v}^{(\alpha,\beta)} \equiv \mathbf{v}^{(\alpha,\beta)}(\mathbf{R}_{\alpha\beta}) = \left\langle \mathbf{\Phi}^{(\alpha,\beta)}(i;j) \middle| \hat{V}^{(\alpha,\beta)}(i;j) \middle| \mathbf{\Phi}^{(\alpha,\beta)}(i;j) \right\rangle,
\tag{9}
$$

and

$$
\mathbf{\Phi}^{(\alpha,\beta)}(i;j) = \left\{ \mathbf{\Phi}^{(\alpha)}(i) \otimes \mathbf{\Phi}^{(\beta)}(j) \right\}_{\text{O}'}
\tag{10}
$$

are employed. The subscript O' in Eq. (10) denotes ordering only within the direct product space of the pair of vectors indicated, in accordance with their positions in the full ordered direct product of Eq. (4).

## C. Pair-Interaction Representation

Unphysical solutions arising from the lack of antisymmetrization of the product spectral basis of Eq. (4) are avoided by constructing the pair-interaction matrices in a basis of diatomic functions that can be readily transformed to the atomic-product basis in a procedure reminiscent of the generalized diatomics-in-molecules method [4]. Whereas the atomic product states are a convenient representational basis for the pair interactions, the diatomic wave functions, which can be obtained by conventional quantum-chemical calculations, are a more appropriate computational basis. The diatomic states $\mathbf{\Psi}^{(\alpha,\beta)}(i_r, j_r)$ are solutions of the Schrödinger equation for the pair Hamiltonian in a rotated coordinate system, denoted by the subscript $r$, wherein atoms $\alpha$ and $\beta$ have colinear $z$ axes:

$$
\left[ (\hat{H}^{(\alpha)}(i_r) + \hat{H}^{(\beta)}(j_r) + \hat{V}^{(\alpha,\beta)}(i_r; j_r) \right] \mathbf{\Psi}^{(\alpha,\beta)}(i_r, j_r) = \mathbf{\Psi}^{(\alpha,\beta)}(i_r, j_r) \cdot \mathbf{E}^{(\alpha,\beta)}(R_{\alpha\beta}).
\tag{11}
$$

These states transform irreducibly under the operations of the $C_{\infty v}$ point group and are antisymmetric with respect to interchange of any two electrons within the combined set $i$ and $j$. The transformation matrix between the diatomic basis and the atomic product basis in this coordinate system is given by

$$
\mathbf{\Phi}^{(\alpha,\beta)}(i_r; j_r) = \mathbf{\Psi}^{(\alpha,\beta)}(i_r, j_r) \cdot \mathbf{U}^{(\alpha,\beta)}(R_{\alpha\beta}),
\tag{12}
$$

hence

$$
\mathbf{U}^{(\alpha,\beta)}(R_{\alpha\beta}) = \left\langle \mathbf{\Psi}^{(\alpha,\beta)}(i_r, j_r) \middle| \mathbf{\Phi}^{(\alpha,\beta)}(i_r; j_r) \right\rangle
\tag{13}
$$

describes the mixing of the atomic product states $\mathbf{\Phi}^{(\alpha,\beta)}(i_r; j_r)$ in the diatomic eigenstates $\mathbf{\Psi}^{(\alpha,\beta)}(i_r, j_r)$. Because the set of properly antisymmetrized diatomic wave functions is employed as a projector on the spectral pair states, it is anticipated that unphysical solutions spanned by the latter set will not arise in the present development.

The atomic product states of Eq. (10) are related to the rotated coordinate system of Eqs. (11)-(13) by the transformation

$$\mathbf{\Phi}^{(\alpha,\beta)}(i;j) = \mathbf{\Phi}^{(\alpha,\beta)}(i_r;j_r) \cdot \mathbf{R}^{(\alpha,\beta)}(\phi_{\alpha\beta},\theta_{\alpha\beta}), \tag{14}$$

where

$$\begin{aligned}
\mathbf{R}^{(\alpha,\beta)}(\phi_{\alpha\beta},\theta_{\alpha\beta}) &= \left\langle \mathbf{\Phi}^{(\alpha,\beta)}(i_r;j_r) \middle| \mathbf{\Phi}^{(\alpha,\beta)}(i;j) \right\rangle \\
&= \left\{ \mathbf{D}^{(\alpha)}(\phi_{\alpha\beta},\theta_{\alpha\beta},0) \otimes \mathbf{D}^{(\beta)}(\phi_{\alpha\beta},\theta_{\alpha\beta},0) \right\}_{O'}
\end{aligned} \tag{15}$$

is the appropriate transformation matrix, comprised of an ordered direct product of block diagonal rotation matrices [20].

Now the pair-interaction matrix of Eq. (9) is obtained from the diagonal matrix of diatomic potential-energy curves

$$\mathbf{E}^{(\alpha,\beta)}(R_{\alpha\beta}) = \left\langle \mathbf{\Psi}^{(\alpha,\beta)}(i_r,j_r) \middle| \hat{H}^{(\alpha)}(i_r) + \hat{H}^{(\beta)}(j_r) + \hat{V}^{(\alpha,\beta)}(i_r;j_r) \middle| \mathbf{\Psi}^{(\alpha,\beta)}(i_r,j_r) \right\rangle, \tag{16}$$

in the form

$$\mathbf{v}^{(\alpha,\beta)}(\mathbf{R}_{\alpha\beta}) = \mathbf{H}^{(\alpha,\beta)}(\mathbf{R}_{\alpha\beta}) - \mathbf{E}^{(\alpha,\beta)}, \tag{17}$$

where $\mathbf{H}^{(\alpha,\beta)}(\mathbf{R}_{\alpha\beta})$ is the transform of $\mathbf{E}^{(\alpha,\beta)}(R_{\alpha\beta})$,

$$\begin{aligned}
\mathbf{H}^{(\alpha,\beta)}(\mathbf{R}_{\alpha\beta}) &= \mathbf{R}^{(\alpha,\beta)}(\phi_{\alpha\beta},\theta_{\alpha\beta})^\dagger \cdot \mathbf{U}^{(\alpha,\beta)}(R_{\alpha\beta})^\dagger \cdot \mathbf{E}^{(\alpha,\beta)}(R_{\alpha\beta}) \\
&\quad \cdot \mathbf{U}^{(\alpha,\beta)}(R_{\alpha\beta}) \cdot \mathbf{R}^{(\alpha,\beta)}(\phi_{\alpha\beta},\theta_{\alpha\beta}).
\end{aligned} \tag{18}$$

The separated-atom limit for the $(\alpha,\beta)$ pair is

$$\mathbf{E}^{(\alpha,\beta)} \equiv \mathbf{E}^{(\alpha,\beta)}(R_{\alpha\beta} \to \infty) = \left\{ \begin{matrix} \mathbf{E}^{(\alpha)} & \mathbf{0} \\ \mathbf{0} & \mathbf{0} \end{matrix} \right\}_{O'} + \left\{ \begin{matrix} \mathbf{0} & \mathbf{0} \\ \mathbf{0} & \mathbf{E}^{(\beta)} \end{matrix} \right\}_{O'}, \tag{19}$$

with use of the interaction matrix rather than the total pair potential energy matrix ensuring that the atomic energies $\mathbf{E}^{(\alpha)}$ and $\mathbf{E}^{(\beta)}$ are not multiply counted.

## D. Finite-Basis Development

The mathematical framework set forth in previous sections is formally correct, with pair-interaction matrices constructed from properly antisymmetrized diatomic wave functions. The convergent transformation matrix connecting the diatomic basis with the atomic-product basis [Eq. (13)], however, will generally be arbitrarily large, consequent of the lack of prior antisymmetrization and the infinite sums of atomic spectral states required to properly describe even long-range interactions in this representation. Therefore, a finite-basis-set representation of the spectral method is desirable, as implementing the development in the form outlined to this point would likely result in aggregate representations [Eq. (4)] that are intractably large for the purposes of *ab initio* computational studies.

A conventional optical potential approach [21], wherein the atomic product basis is partitioned into a finite reference space $\mathbf{Q}$ and its complement $\mathbf{P} = 1-\mathbf{Q}$, may be employed. Accordingly, the pair Schrödinger equation in matrix representation [cf. Eq. (11)],

$$\mathbf{H}^{(\alpha,\beta)}(R_{\alpha\beta}) \cdot \mathbf{U}^{(\alpha,\beta)}(R_{\alpha\beta}) = \mathbf{U}^{(\alpha,\beta)}(R_{\alpha\beta}) \cdot \mathbf{E}^{(\alpha,\beta)}(R_{\alpha\beta}), \tag{20}$$

may be partitioned

$$\begin{pmatrix} \mathbf{H}_{QQ}^{(\alpha,\beta)}(R_{\alpha\beta}) & \mathbf{H}_{QP}^{(\alpha,\beta)}(R_{\alpha\beta}) \\ \mathbf{H}_{PQ}^{(\alpha,\beta)}(R_{\alpha\beta}) & \mathbf{H}_{PP}^{(\alpha,\beta)}(R_{\alpha\beta}) \end{pmatrix} \cdot \begin{pmatrix} \mathbf{U}_{Q;\gamma}^{(\alpha,\beta)}(R_{\alpha\beta}) \\ \mathbf{U}_{P;\gamma}^{(\alpha,\beta)}(R_{\alpha\beta}) \end{pmatrix} = E_{\gamma}^{(\alpha,\beta)}(R_{\alpha\beta}) \cdot \begin{pmatrix} \mathbf{U}_{Q;\gamma}^{(\alpha,\beta)}(R_{\alpha\beta}) \\ \mathbf{U}_{P;\gamma}^{(\alpha,\beta)}(R_{\alpha\beta}) \end{pmatrix}, \tag{21}$$

where $E_{\gamma}^{(\alpha,\beta)}(R_{\alpha\beta})$ is one of the energies of the $\mathbf{Q}$-space matrix $\mathbf{E}_{QQ}^{(\alpha,\beta)}(R_{\alpha\beta})$ and the vectors $\mathbf{U}_{Q;\gamma}^{(\alpha,\beta)}(R_{\alpha\beta})$ and $\mathbf{U}_{P;\gamma}^{(\alpha,\beta)}(R_{\alpha\beta})$ are the $\mathbf{Q}$- and $\mathbf{P}$-space components of row $\gamma$ of the full matrix $\mathbf{U}^{(\alpha,\beta)}(R_{\alpha\beta})$. The infinite vector $\mathbf{U}_{P;\gamma}^{(\alpha,\beta)}(R_{\alpha\beta})$ may be eliminated [21], giving

$$\left\{ \mathbf{H}_{QQ}^{(\alpha,\beta)}(R_{\alpha\beta}) + \mathbf{H}_{QP}^{(\alpha,\beta)}(R_{\alpha\beta}) \cdot \left[ E_{\gamma}^{(\alpha,\beta)}(R_{\alpha\beta})\mathbf{I}_{PP} - \mathbf{H}_{PP}^{(\alpha,\beta)}(R_{\alpha\beta}) \right]^{-1} \cdot \mathbf{H}_{PQ}^{(\alpha,\beta)}(R_{\alpha\beta}) \right\}$$

$$\cdot \mathbf{U}_{Q;\gamma}^{(\alpha,\beta)}(R_{\alpha\beta}) = E_{\gamma}^{(\alpha,\beta)}(R_{\alpha\beta})\mathbf{U}_{Q;\gamma}^{(\alpha,\beta)}(R_{\alpha\beta}), \tag{22}$$

with the energy-dependent optical-potential matrix, evaluated at the diatomic eigenvalue $E = E_{\gamma}^{(\alpha,\beta)}(R_{\alpha\beta})$, contained therein as

$$\mathbf{V}_{QQ}^{(\alpha,\beta)}(E) \equiv \mathbf{H}_{QP}^{(\alpha,\beta)}(R_{\alpha\beta}) \cdot \left[ E\mathbf{I}_{PP} - \mathbf{H}_{PP}^{(\alpha,\beta)}(R_{\alpha\beta}) \right]^{-1} \cdot \mathbf{H}_{PQ}^{(\alpha,\beta)}(R_{\alpha\beta}). \tag{23}$$

The optical potential will generally be different for each pair eigenvalue; that is, the lowest $N$ diatomic potential-energy values constituting the matrix $\mathbf{E}_{QQ}^{(\alpha,\beta)}(R_{\alpha\beta})$ are not eigenvalues of a single Hermitian matrix. However, as the dimension of $\mathbf{Q}$ increases, the lowest solutions of Eq. (22) will eventually become insensitive to change with further increase in the extent of $\mathbf{Q}$. In that limit, the upper-left corner of the effective Hamiltonian [Eq. (23)] becomes insensitive to energy,

$$\mathbf{V}_{QQ}^{(\alpha,\beta)}\left( E_{\gamma}^{(\alpha,\beta)}(R_{\alpha\beta}) \right) = \mathbf{V}_{QQ}^{(\alpha,\beta)}\left( E_{\gamma'}^{(\alpha,\beta)}(R_{\alpha\beta}) \right), \tag{24}$$

and

$$\mathbf{E}_{AA}^{(\alpha,\beta)}(R_{\alpha\beta}) = \tilde{\mathbf{U}}_{AA}^{(\alpha,\beta)}(R_{\alpha\beta}) \cdot \left[ \mathbf{H}_{AA}^{(\alpha,\beta)}(R_{\alpha\beta}) + \tilde{\mathbf{V}}_{AA}^{(\alpha,\beta)}(R_{\alpha\beta}) \right] \cdot \tilde{\mathbf{U}}_{AA}^{(\alpha,\beta)}(R_{\alpha\beta})^{\dagger}, \tag{25}$$

where $\mathbf{E}_{AA}^{(\alpha,\beta)}(R_{\alpha\beta})$ is the diagonal matrix comprised of any $E_{\gamma}^{(\alpha,\beta)}(R_{\alpha\beta})$ belonging to the reference space $\mathbf{A}$, a subset of $\mathbf{Q}$. Element $ij$ of the optical potential matrix [Eq. (23)], now becomes

$$\left( \tilde{\mathbf{V}}_{QQ}^{(\alpha,\beta)} \right)_{ij} = \left\{ \mathbf{H}_{QP}^{(\alpha,\beta)}(R_{\alpha\beta}) \cdot \left[ E_{\gamma}^{(\alpha,\beta)}(R_{\alpha\beta})\mathbf{I}_{PP} - \mathbf{H}_{PP}^{(\alpha,\beta)}(R_{\alpha\beta}) \right]^{-1} \cdot \mathbf{H}_{QQ}^{(\alpha,\beta)}(R_{\alpha\beta}) \right\}_{ij}, \tag{26}$$

where $i$ and $j$, and $E_\gamma^{(\alpha,\beta)}(R_{\alpha\beta})$, are in the **A** space. Finally, the product-state Hamiltonian of Eq. (18) is rewritten in the finite-basis representation as

$$\tilde{\mathbf{H}}_{AA}^{(\alpha,\beta)}(\mathbf{R}_{\alpha\beta}) = \mathbf{R}_{AA}^{(\alpha,\beta)}(\phi_{\alpha\beta},\theta_{\alpha\beta})^\dagger \cdot \tilde{\mathbf{U}}_{AA}^{(\alpha,\beta)}(R_{\alpha\beta})^\dagger \cdot \mathbf{E}_{AA}^{(\alpha,\beta)}(R_{\alpha\beta})$$
$$\cdot \tilde{\mathbf{U}}_{AA}^{(\alpha,\beta)}(R_{\alpha\beta}) \cdot \mathbf{R}_{AA}^{(\alpha,\beta)}(\phi_{\alpha\beta},\theta_{\alpha\beta}), \tag{27}$$

with $\tilde{\mathbf{U}}_{AA}^{(\alpha,\beta)}(R_{\alpha\beta})$ determined from Eqs. (25) and (26).

## III. Discussion and Computational Implementation

The foregoing analysis demonstrates that a finite-dimension unitary matrix may be constructed that transforms the lowest $N$ exact diatomic energies into an atomic-product representation of the Hamiltonian matrix. Several features of the development are similar to aspects of diatomics-in-molecule approaches and other methods that have been set forth previously [4-11]. The exact pairwise-additive nature of the many-body interaction Hamiltonian matrix is exploited in a spectral-product representation [7], and diatomic wave functions provide a convenient computational basis set [4,5]. Furthermore, Wigner rotation matrices are employed in a unitary transformation from the diatomic to the atomic-product representation [5].

By contrast with previous approaches, however, the present development employs a complete rather than an overcomplete set of atomic states convergent in the limit of closure [6,8,9]. Accordingly, prescriptions may be devised for unambiguous and completely *ab initio* computational implementation of this method. Additionally, the spectral theory unifies apparently dissimilar theoretical and computational approximations, such as the Balling and Wright method [10,11] and various diatomics-in-molecules models [4,5] within a single rigorous formal development which is seen to contain these other approaches as special cases in appropriate limits.

Certain schemes for computational implementation of the spectral theory can be considered. In one completely *ab initio* formulation, the required spectral states may be constructed directly employing a somewhat extended version of the Stieltjes moment methods [22,23] that have been successfully used to represent attributes of the discrete and continuous spectra of quantum systems in finite spatial regions. A second approach makes use of information on the requisite diatomic pairs derived from quantum-chemical calculations or experiment, with subsequent transformation from the diatomic basis to the atomic-product basis set, as outlined in Section II Part C. This latter method has been pursued in initial applications of the spectral theory [3,13,24], which have focused on alkali metals in rare-gas matrices, prototypical systems that have been thoroughly examined experimentally and theoretically under the auspices of the HEDM program [25-29].

To date the most extensive applications are to sodium-doped argon clusters and solids, where the structures and absorption spectra of variously sized systems of this type are simulated employing classical Metropolis Monte Carlo techniques and many-body potential-energy surfaces constructed via the spectral theory [13]. The vector $\Psi^{(\alpha,\beta)}(i_r,j_r)$

of Eq. (11) is comprised of NaAr wave functions computed expressly for this purpose by accurate *ab initio* quantum-chemical methods [12],

$$\{X\,^2\Sigma^+,\ A\,^2\Pi,\ B\,^2\Sigma^+,\ \dots\},$$

whereas $\Phi^{(\alpha,\beta)}(i;j)$ [Eq. (10)] is formed from the corresponding product states of Na and Ar functions

$$\left\{\,|\mathrm{Na}\,(3s)\,^2S\rangle|\mathrm{Ar}\,^1S\rangle,\ |\mathrm{Na}\,(3p)\,^2P_\pm\rangle|\mathrm{Ar}\,^1S\rangle,\ |\mathrm{Na}\,(3p)\,^2P_0\rangle|\mathrm{Ar}\,^1S\rangle,\ \dots\,\right\}.$$

Dipole- and transition-moment functions connecting the molecular states, obtained from the diatomic calculations [12], are used in construction of the unitary transformation matrix [Eq. (13)] connecting the two representations in a procedure detailed elsewhere [3,13,24]. The argon-argon interaction potential is obtained from the literature [30]. Reference 13 reports radial probability distibution functions and absorption spectra for $NaAr_{11}$ using various dimensions for the expansions of $\Psi^{(\alpha,\beta)}(i_r,j_r)$ and $\Phi^{(\alpha,\beta)}(i;j)$; an examination of the convergence of the spectral theory is a principal goal of these initial studies.

## IV. Summary

A spectral theory of binding that provides exact many-body potential-energy surfaces for aggregates of interacting species is undergoing active development and testing. Through this theory, crystal-field-like methods such as that of Balling and Wright are generalized to higher angular momenta, and long-range and pairwise-additive potential limits are clarified. Extensive computational application of the theory to $Na(Ar)_N$ clusters and solids is in progress, with subsequent studies of other alkali-seeded rare gas systems, as well as atom-doped solid $H_2$, planned for coming months. Concomitantly, the full *ab initio* implementation of the theory is being pursued. Notably, there is nothing in the theoretical framework that limits application of the spectral method to van der Waals or other weakly interacting systems; its ability to give accurate potential surfaces for covalently bonded complexes will also be investigated.

## References

[1] See, for example, *Proceedings of the High Energy Density Matter (HEDM) Contractors Conference*, ed. by P. G. Carrick and S. Tam (Phillips Laboratory, Edwards AFB, CA, 1995), Report PL-TR-95-3039.

[2] P. G. Carrick, *Theoretical Performance of High Energy Density Cryogenic Solid Rocket Propellants*, 31st Joint Propulsion Conference, July 1995, San Diego, CA, AIAA 95-2893.

[3] P. W. Langhoff, *J. Phys. Chem.* 100 (1996) 2974.

[4] F. O. Ellison, *J. Am. Chem. Soc.* 85 (1963) 3540.

[5] J. C. Tully, in *Semiempirical Methods of Electronic Structure Calculation, Part A: Techniques*, ed. by G. A. Segal (Plenum, New York, 1977), pp. 173-200.

[6] R. Eisenschitz and F. London, *Z. Phys.* 60 (1930) 491.

[7] W. Moffitt, *Proc. Royal Soc. London* A210 (1951) 245.

[8] A. T. Amos and J. I. Musher, *Chem. Phys. Lett.* 1 (1967) 149.

[9] J. I. Musher and A. T. Amos, *Phys. Rev.* 164 (1967) 31.

[10] W. E. Baylis, *J. Phys. B* 10 (1977) L477.

[11] L. C. Balling and J. J. Wright, *J. Chem. Phys.* 79 (1983) 2941.

[12] A more detailed discussion of these calculations is given in J. A. Sheehy, *Calculations of van der Waals Molecules Relevant to HEDM Studies*, these proceedings.

[13] More information on this aspect of the project is given in J. A. Boatz, M. E. Fajardo, J. A. Sheehy, and P. W. Langhoff, *Monte Carlo Simulations of the Structures and Optical Absorption Spectra of Na/Ar Clusters and Solids: An Application of Spectral Theory of Chemical Binding*, these proceedings.

[14] H. A. Bethe and E. E. Salpeter, in *Encyclopedia of Physics*, ed. by S. Flügge (Springer-Verlag, Berlin, 1957), Vol. 35, p. 88.

[15] T. Itoh, *Rev. Mod. Phys.* 37 (1965) 159.

[16] J. C. Slater, *Quantum Theory of Matter* (McGraw-Hill, New York, 1968).

[17] E. U. Condon and G. H. Shortley, *Theory of Atomic Spectra* (Cambridge, New York, 1935).

[18] P. A. M. Dirac, *The Principles of Quantum Mechanics (Revised Fourth Edition)* (Oxford, New York, 1958), Ch. IX.

[19] R. Courant and D. Hilbert, *Methods of Mathematical Physics* (Interscience, New York, 1953), Vol. 1.

[20] A. R. Edmonds, *Angular Momentum in Quantum Mechanics* (Princeton, New Jersey, 1960).

[21] P. O. Löwdin, *J. Math. Phys.* 3 (1962) 969.

[22] P. W. Langhoff, in *Computational Chemical Physics*, ed. by G. H. F. Diercksen and S. Wilson (Reidel, Dordrecht, Holland, 1983), pp. 299-334.

[23] P. W. Langhoff, in *Mathematical Frontiers in Computational Chemical Physics*, ed. by D. G. Truhlar (Springer, Berlin, 1988), pp. 85-135.

[24] Ref. 1, pp. 93-113.

[25] J. A. Boatz and M. E. Fajardo, *J. Chem. Phys.* 101 (1994) 3472.

[26] J. A. Boatz and M. E. Fajardo, *Monte Carlo Simulations of the Structures and Optical Absorption Spectra of Na Atoms in Ar Clusters, Surfaces, and Solids: A Detailed Presentation of the Theoretical Methods Used* (Phillips Laboratory, Edwards AFB, CA, 1994), Report PL-TR-94-3024.

[27] M. E. Fajardo and J. A. Boatz, *J. Comput. Chem.*, in press.

[28] M. E. Fajardo, P. G. Carrick, and J. W. Kenney III, *J. Chem. Phys.* 94 (1991) 5812.

[29] S. Tam and M. E. Fajardo, *J. Chem. Phys.* 99 (1993) 854.

[30] R. A. Aziz and M. J. Slaman, *Mol. Phys.* 58 (1986) 679.

# Quantum Molecular Dynamics Simulations of Low Temperature Hydrogen Systems

Gregory A. Voth

*Department of Chemistry, University of Pennsylvania, Philadelphia, Pennsylvania 19104-6323*

## Background

Solid hydrogen doped with energetic impurities may form the basis for high energy density matter (HEDM) to be used in rocket propulsion [1]. A key research priority is therefore the largescale computer simulation of impurity diffusion and recombination in HEDMs in order to better understand the reasons for their stability, or instability, as the case may be. The rate of recombination of two impurities in a low temperature solid can be characterized in terms of their intrinsic recombination rate when they have diffused to within some well-defined distance from one another, and the rate at which the two impurities diffuse into the required proximity with one another. The latter rate is proportional to the impurity self-diffusion constant, and it is a possible limiting factor in the undesirable impurity recombination process. If the intrinsic rate of recombination is very fast compared with the impurity self-diffusion rate, the process will be limited by the impurity self-diffusion.

To put the above discussion in mathematical terms, the rate constant $k_r$ for recombination of two impurities in a low temperature solid can be approximately described by the equation

$$\frac{1}{k_r} \approx \frac{1}{k_{in}} + \frac{1}{k_D} \quad , \tag{1}$$

where $k_{in}$ is the intrinsic recombination rate for the two impurities after having diffused to some distance apart, $r_c$, and $k_D$ is the rate at which the two impurities diffuse to within that distance. The latter diffusion rate is related to the impurity self-diffusion constant $D$ such that $k_D \approx 4\pi r_c D$. It is therefore clear from Eq. (1) that the overall rate of recombination will be limited by the impurity diffusion if it is very slow.

The most immediate goal of this HEDM research program is to calculate directly from largescale computer simulation the relevant parameters in Eq. (1) for the impurity recombination rate. Along these lines, the self-diffusion constant can be obtain from one of two equivalent formulas:

$$D = \frac{1}{6} \lim_{t \to \infty} \frac{d}{dt} \langle |\mathbf{q}(t) - \mathbf{q}(0)|^2 \rangle \tag{2}$$

or

$$D = \frac{1}{3} \int_0^\infty dt \langle \dot{\mathbf{q}}(t) \cdot \dot{\mathbf{q}}(0) \rangle \quad , \tag{3}$$

where the notation $A(t) \equiv e^{iHt/\hbar} A e^{-iHt/\hbar}$ denotes a quantum Heisenberg operator for any operator "$A$". Both of the above functions are quantum dynamical time correlation functions.

## Quantum Dynamical HEDM Simulations

The simulation of impurity mobility in quantum solids represents an extraordinary challenge for the theorist because the solid is so strongly influenced by nuclear quantum effects. Such systems thus require an explicit *quantum dynamical* treatment such as the one our group

has developed termed "Centroid Molecular Dynamics" (CMD) [1]. In the CMD approach, the impurity self-diffusion constant can be obtained through the correlation functions in either Eq. (2) or (3) by running *classical-like trajectories* for the quantum particles on an effective, temperature-dependent classical potential [2-4]. In the "exact" CMD algorithm, the effective potential is calculated "on the fly" by performing equilibrium quantum averaging simultaneously with the time-integration of the CMD equations. In fact, we have recently developed a "hyper-parallel" CMD algorithm [3] which has exhibited near linear performance scaling over 50 or more IBM SP2 nodes in our preliminary simulations of liquid and solid hydrogen (cf. Fig. 1). As an alternative, the quantum centroid potential has been represented by an effective pairwise pseudopotential [4], allowing for *extremely efficient* quantum dynamical simulation of large systems (i.e., once the potential is specified in the pairwise form, the simulation is no more time-consuming than a classical MD simulation). The theoretical breakthrough of CMD is now allowing our group to directly simulate the dynamics of quantum liquids and solids, as well as impurity diffusion and recombination in potential HEDMs and related systems.

## HPCMD of Hydrogen
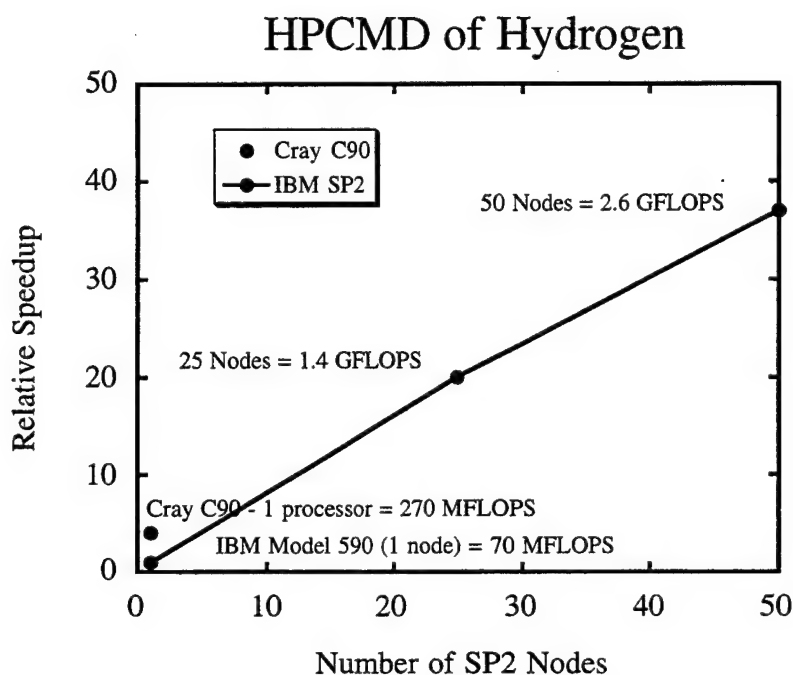


**Figure 1**: A plot of the computational speed-up of the "hyper-parallel" CMD algorithm versus number of nodes on an IBM SP2 [3].

Preliminary results from our CMD studies of liquid and solid hydrogen are shown in Figs. 2 and 3. In Fig. 2 is plotted the quantum velocity autocorrelation function for liquid hydrogen near its triple point at 14 K. The exact CMD-based calculation gives a liquid phase self-diffusion constant via Eq. (3) which is in excellent agreement with the experimental result [3], while the centroid pseudopotential result deviates somewhat due to three- and higher-body quantum correlations which are not described in the pairwise pseudopotential approach. The classical MD result is significantly worse than both CMD results [3,4]. Our calculations on 14 K liquid hydrogen, as well as ones at 25 K exhibiting similar agreement with experiment [3], have helped to establish the validity of both the theoretical and computational CMD methodology.

A very recent calculation is shown in Fig. 3 of the CMD mean-squared displacement function for solid hydrogen at 5 K after a vacancy was instantaneously created at time $t = 0$. The lattice clearly first undergoes a large amplitude reorganization, and then it begins to vibrate in a more stable fashion. No self-diffusion in the solid is evident on this timescale, but a longer CMD run is now in progress. Other simulations presently underway include a calculation of the lithium atom self-diffusion constant in liquid $p$–$H_2$, the recombination of two lithium impurities in the same system, and the dynamics of one and two lithium atoms in solid hydrogen at 5K. The CMD method is also being generalized to include the effects from Bose-Einstein and Fermi-Dirac quantum statistics.

## References

(1) M. E. Fajardo, in *Proceedings of the High Energy Density Matter Conference*, edited by M. E. Cordonnier (USAF Phillips Laboratory, Edwards AFB, CA, 1991); J. Chem. Phys. **98**, 110 (1993).

(2) J. Cao and G. A. Voth, J. Chem. Phys. **99**, 10070 (1993); J. Chem. Phys. **100**, 5106 (1994); J. Chem. Phys. **101**, 6157 (1994); J. Chem. Phys. **101**, 6168 (1994).

(3) A. Calhoun, M. Pavese, and G. A. Voth, Chem. Phys. Lett. (submitted).

(4) M. Pavese and G. A. Voth, Chem. Phys. Lett. **249**, 231 (1996).
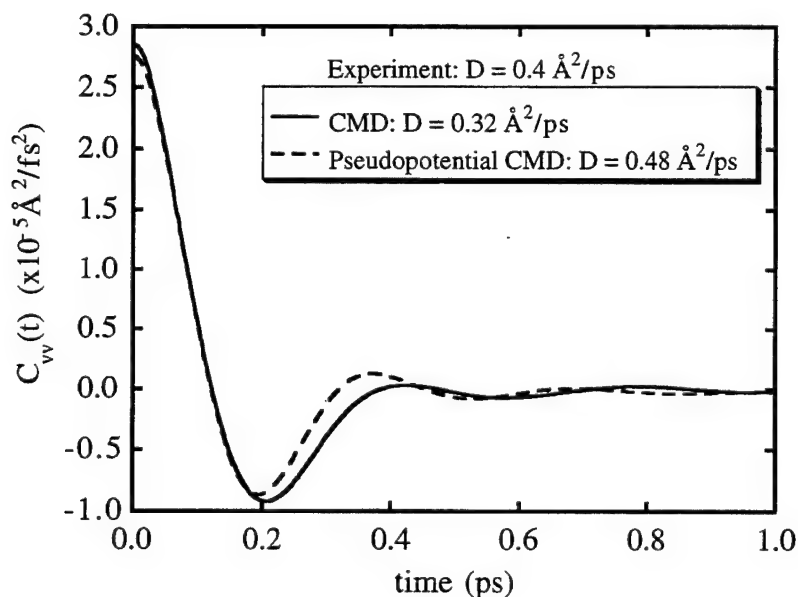
**Figure 2**: Plots of the exact CMD and pairwise pseudopotential CMD velocity autocorrelation functions for liquid $p$–$H_2$ at 14 K [3,4].

60
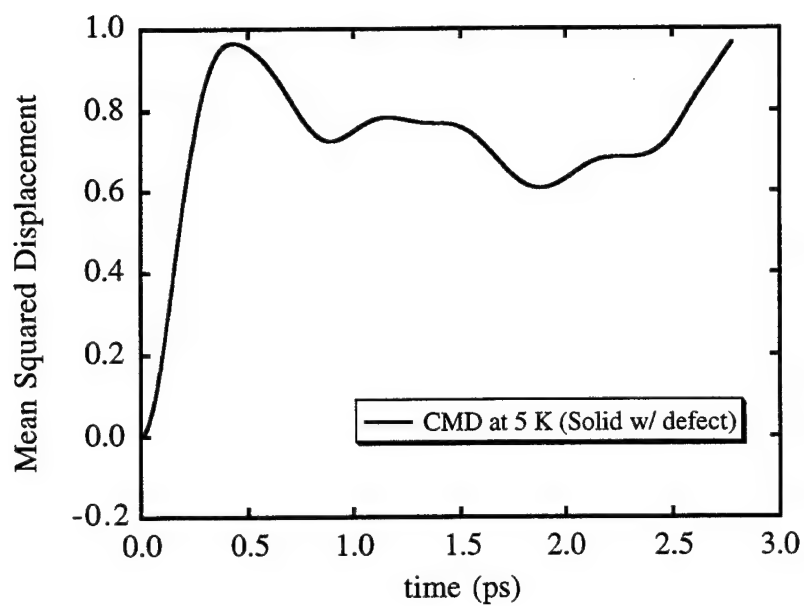
**Figure 3**: A Plot of the CMD mean-squared displacement function for solid $p$–$H_2$ at 5K with a vacancy instantaneously created at time $t = 0$.

# The Interaction of Li Atoms with Large Clusters of $n$-H$_2$, $p$-H$_2$ and $o$-D$_2$ Probed by Laser Spectroscopy

C. Callegari, J. Higgins, F. Stienkemeier, and G. Scoles

*Chemistry Department, Princeton University, Princeton, NJ 08544*

## INTRODUCTION

Seeding with light metal atoms is presently being considered as a way to increase solid hydrogen performance as a rocket propellant. For this purpose, an accurate knowledge of the properties of such mixtures (e.g. melting rate, diffusion and recombination rate of the impurities) is indispensable. Computer modeling of these highly quantum systems is making steady progress, as far as algorithms and computational capabilities are concerned, but still relies on very approximate interaction potentials. Experimental results are at present needed to test the validity of existing theoretical models and to improve our knowledge of interaction potentials. To the best of our knowledge the only experimental measurements on alkali doped hydrogen other than those reported below have been performed in solid hydrogen matrices, for lithium only. Although they provide useful information about the interaction energy scale and the nature of trapping sites these bulk experiments suffer from difficulties in making/doping a reproducibly uniform matrix, and, possibly from the presence of multiple trapping configurations. Finally, these experiments have been carried out exclusively with normal hydrogen, while, as it will be shown later, the $o$-, $p$-H$_2$ relative concentration plays a crucial role in determining the structure of the absorption spectra. One should also remember that since molecules in the J=1 state (the lowest state available to $o$-H$_2$) require extensively more complicated modeling, simulations are in general made for pure J=0 para-hydrogen aggregates.

By using large ($n \approx 1000$) hydrogen clusters as matrices we believe we are able to overcome some of these difficulties. Large clusters are relatively easy to produce and to dope and offer a more homogeneous substrate (the main source of non homogeneity being the cluster size distribution). In addition we can easily change the relative concentration of J=0/J=1 molecules in the cluster, and study its influence on the excitation spectra (hence on the alkali-cluster interaction). We report here progress made in the investigation of the properties of alkali-atom-doped hydrogen clusters since last year's meeting. Since the experimental apparatus is described in the HEDM Contractors Conference Proceedings of the past three years we will give here only a short description of it while presenting also a summary of the previously obtained results.

## EXPERIMENTAL APPARATUS

Beams of H$_2$ clusters are prepared by supersonic expansion through a 10 $\mu$m nozzle. Typical stagnation pressures and nozzle temperatures are 32 atm and 70 K, resulting in an average size of $10^3$ molecules per cluster (this estimate is made by rescaling the value reported in [1] with the formula suggested in [2]). The beam is chopped (for lock-in detection), skimmed and passed through a pick-up cell where a low (on the order of $10^{-4}$ torr) vapor pressure of Li can be established (two collinear pick-up cells containing Na and K have also been used). Depending on this pressure, each cluster picks up (on average) one or more dopant atoms. Optical excitation spectra of the resulting complexes are obtained with two complementary techniques:

- Laser Induced Fluorescence (LIF): the fluorescence emitted by the complexes upon excitation with a tunable dye laser is collected by a set of mirrors and conveyed by fiber optics to a photomultiplier (PMT).

- Beam Depletion (BD): the depletion of the beam induced by the laser is measured with a hot wire surface ionization detector located downstream from the LIF detector.

As an alternative, the collected fluorescence can be dispersed with a monochromator and detected with a liquid-nitrogen-cooled CCD camera, obtaining additional information on the excited states and on the ground state of the complexes. Recently, an ortho-para converter has been installed, in order to control the fraction of J=1 molecules in the beam. This converter consists of an alumina supported transition metal catalyst through which the hydrogen gas supply is passed before reaching the nozzle. Assuming the flux to be slow in comparison to the conversion rate (our case), the ortho-para ratio is determined by the equilibrium thermal distribution at the converter temperature, which can be set to any value from 300 K down to 20 K. The corresponding J=1 fraction changes from 75% to 0.2% for H$_2$ (33% to 2% for D$_2$).

## SUMMARY OF PREVIOUSLY REPORTED RESULTS

Up to the 1995 meeting, the LIF spectra of Li, Na and K attached $H_2$ clusters had been measured. All of the spectra showed a common pattern in the excitation features:"fluorescent" absorption was concentrated at the position of the D lines (broadened due to the interaction with the cluster, but basically unshifted with respect to the gas phase), and under at least two broad peaks shifted to the blue by 200 to 600 $cm^{-1}$. Detailed measurements in the case of Na showed that the unshifted lines intensities and shapes were fairly insensitive to the average size of the clusters, whereas the blue shifted peak showed a tendency to disappear at smaller cluster sizes. In addition, in the neighborhood of the unshifted lines one or more satellite peaks were present, showing a structure whose complexity increases moving from the lighter to the heavier atoms. Finally, a BD spectrum had been taken for K on $H_2$ clusters, showing a totally different absorption profile, since it consisted of several broad (a few hundred $cm^{-1}$) peaks merged together with the maximum absorption showing up at the gas phase lines position. It should be recalled here that no qualitative differences between LIF and BD spectra are observed when using He instead of $H_2$ clusters. Therefore, we decided to have a more detailed comparison between LIF and BD spectra for hydrogen. The integrated intensities of the BD spectra turn out to be of the same order of magnitude as for He clusters, suggesting no substantial change in the pick-up probability if the same average cluster size is assumed. From the LIF spectra, on the contrary, one calculates that, contrary to what happens in the case of He where a 100% fluorescence yield can be estimated, only about 0.1% of the excited K atoms do fluoresce back to the ground state. Lack of fluorescence in other regions of the spectrum convinced us that in the case of $H_2$ most of the excited atoms return to their ground state via non radiative transitions (quenching). This makes BD spectra of great importance to the study of alkalicluster interactions, and suggests that LIF spectra could be a sensitive probe of the trapping site if (as it is natural to assume) the quenching cross section strongly depends on the shape of the atom-cluster potential energy surface. During the past year we have aimed at extending BD spectra to Li and Na, and to study the isotopic effect on all of the spectra we already collected. Also, based on the assumption that the use of pure $p$-$H_2$ or $o$-$D_2$ clusters was likely to simplify the spectra, we have studied the changes produced in the spectral features when the J=1 molecular concentration is reduced.

## LASER INDUCED FLUORESCENCE SPECTRA OF LI ATOMS ATTACHED TO HYDROGEN CLUSTERS

**a) $n$-$H_2$ clusters**

LIF spectra of Li doped $n$-$H_2$ clusters are shown in fig. 2(a). These spectra follow the same pattern of features already observed for K:

- a small absorption is present at the position of the D lines, with a sharp onset at the gas phase resonance frequency and a tail extending about 100 wavenumbers to the blue.

- most of the absorption is concentrated under two bell shaped broad peaks (the first one about twice as high as the second) about 300 and 600 $cm^{-1}$ to the blue of the gas phase lines. In the case of Li, the onset of a splitting of the higher peak into two is evident; as we will see later, this is related to the presence of $o$-$H_2$ in the cluster.

- the excited atoms that yield fluorescence are only a minor fraction of the total (by comparison with beam depletion spectra, for Li one obtains about 7%, while for K (see above) this fraction was of the order of 0.1%).

The same pattern of features has been observed for Na and K attached to $H_2$ and $D_2$ clusters as well, suggesting that a theoretical model based on very general properties of alkali atoms could be devised. However we will only discuss spectra of Li from now on, since other experimental and theoretical results are available for comparison. The blue shifted part of this spectrum shows good agreement with Cheng and Whaley's calculations [3] for Li <u>inside</u> solid $H_2$, (with a Li atom replacing 12 $H_2$ molecules). It should be pointed out that these calculations have been run for pure $p$-$H_2$, rather than $n$-$H_2$. LIF spectra of Li doped $p$-$H_2$ clusters do not exhibit as good of an agreement (see below). Also, simulations calculate the <u>absorption</u> spectra, whereas the LIF technique, by definition, only detects the minor fraction of excited atoms yielding fluorescence, and therefore is not likely to reproduce the absorption spectrum faithfully.

**b) $p$-$H_2$ clusters**

Reducing the percentage of J=1 $H_2$ molecules to less than 1% (fig.2(b)) does not greatly affect the shape of the features close to the D lines, but makes some of the blue shifted peaks disappear. In order to decide on whether the intensity of these features has an abrupt change (which might indicate a phase transition of the clusters) or a smooth change as a function of the ortho-para

concentration, we fixed the excitation laser frequency at 15217.9 cm$^{-1}$ and monitored the total amount of fluorescence collected as a function of the slowly changing (-0.5 K/min) converter temperature (fig.1). As one can see, there seems to be an almost linear relationship between the height of the peak at 15217.9 cm$^{-1}$ and the theoretical $o$-H$_2$ fraction. Unfortunately some fluorescence from the adjacent peaks masks the peak under investigation at low $o$-H$_2$ concentrations.

It is not clear yet whether the difference between the $n$-H$_2$ and the $p$-H$_2$ spectra is due to different atom-cluster potentials (which might also change the quenching probability) or to the excitation of different internal degrees of freedom of the clusters related to the ortho component. Some additional theoretical analysis is needed in order to clarify this issue.

### BEAM DEPLETION SPECTRA OF LI ATOMS IN HYDROGEN CLUSTERS

Beam depletion spectra of Li in H$_2$ are shown in fig. 3. Again they exhibit the same pattern found before for K (and Na as well): namely they are completely different from the LIF spectra (in sharp contrast with the He case), with most of the absorption located under a bell shaped profile, slightly shifted to the red with respect to the gas phase lines, with a long structured tail to the blue. As one can see, these spectra closely resemble Fajardo's spectra of Li in solid hydrogen matrices [4] (dashed line), which are broader and show more intensity in their blue wings. Even if no quantitative analysis has been done yet, both of these facts are consistent with the assumption that Fajardo's spectra are relative to Li atoms inside the bulk of H$_2$, whereas our spectra refer to species sitting on a dimple on the surface of the cluster, as in the model proposed by Ancilotto *et al.* [5]. Finally, the differences between $n$-H$_2$ and $p$-H$_2$ are not so sharp as in the case of LIF spectra. Beam Depletion spectra seem to confirm the onset of two peaks about 180 and 400 cm$^{-1}$ to the blue of the gas phase lines, and the disappearance of the intermediate peak.

### LIF SPECTRA OF LI ATOMS ATTACHED TO DEUTERIUM CLUSTERS

LIF spectra of Li picked up by $o$-D$_2$ (fig. 4) show only a minimal amount of fluorescence at the position of the gas phase lines. If the absorption at the gas phase lines is assigned to surface atoms, and the blue shifted absorption to atoms inside the cluster, according to Cheng and Whaley's calculations [3,6], one would conclude that a larger fraction of Li atoms go inside D$_2$ clusters, compared to H$_2$ clusters, in contrast with the model of Ancilotto *et al.* [5]. The model predicts in fact less stable *internal*

states for alkali atoms in deuterium than in hydrogen, regardless of the alkali-D$_2$ potential used. The possible existance of such states is however a critical function of the well depth.

The peaks to the blue of the D lines are shifted more and are considerably broader than their counterparts in H$_2$, so that they all merge and appear as a single peak. Because of its lower zero point energy, deuterium is denser and more tightly bound than hydrogen. This should contribute to increase the interaction with the Li atom (hence the increased shifts and widths of the peaks).

Differences between $n$-D$_2$ (not shown) and $o$-D$_2$ are not great partly because the J=1 fraction only changes from 33% to $\approx$ 2%.

### BEAM DEPLETION SPECTRA OF LI ATOMS ATTACHED TO DEUTERIUM CLUSTERS

Beam depletion spectra of Li in $o$-D$_2$ (fig. 5) do not differ greatly from their counterparts in H$_2$, except for the fact that the maximum of the absorption is shifted more to the red (the same occurs even more markedly for potassium in H$_2$ and D$_2$). Again, this is consistent with a stronger atom-matrix interaction.

In order to further confirm our assumption that BD spectra are related to Li atoms on the surface of the cluster, we tried to compare them to LIF spectra of Li on He clusters (since the fluorescence yield in He is close to 100% the LIF spectra in this case correspond to the total absorption spectra). Li atoms are known to stay on the surface of the He cluster and their absorption spectra have been successfully modeled with an atom-cluster potential [7]. As one can see from fig. 5 both the shape of the main peak and the shift with respect to the gas phase lines match quite well if the energy scale (x-axis) is expanded by a factor of 20. It is interesting to note that Li-H$_2$ and Li-*bulk liquid H$_2$* interaction energies are about a factor of 10 larger than Li-He and Li-*bulk liquid He* [5].

### CONCLUSIONS

We have measured Laser Induced Fluorescence and Beam Depletion Spectra of Li attached to H$_2$ and D$_2$ clusters with different ortho-para compositions. We have been able to demonstrate that fluorescent transitions are heavily quenched by the presence of hydrogen, and that beam depletion is an excellent way to measure the total absorption spectra of alkalis in hydrogen. We have shown that the ortho-para composition of the cluster plays a major role in determining the shape of the excitation spectra, and in particular that certain features are likely to have a linear dependence on the $o$-H$_2$ ($p$-D$_2$)

concentration. The interpretation of the excitation spectra depends on the future availability of reliable Li-H$_2$ potentials for both the ground and excited states. Experimentally, we hope to further explore the spectroscopy of Li$_2$ on hydrogen clusters. This will hopefully yield information on the mobility on or in the cluster and would provide invaluable information on the interactions and dynamics of alkalis attached to hydrogen clusters.

## ACKNOWLEDGEMENTS

[1] D. Schutt, *Infrared Spectroscopy of molecules solvated in and attached to clusters of helium, hydrogen, and deuterium*; Ph.D. thesis, Princeton University, Princeton, NJ, 1992.

[2] H. Haberland in *Clusters of Atoms and Molecules*, H. Haberland (Ed.), Springer Series in Chemical Physics 52, p. 221.

[3] E. Cheng and K. B. Whaley *J. Chem. Phys.* **104**, 3155 (1996)

[4] M. E. Fajardo *J. Chem. Phys.* **98**, 110 (1993)

[5] F. Ancilotto, E. Cheng, M. W. Cole and F. Toigo *Z. Phys. B* **98**, 323 (1995)

[6] E. Cheng and K. B. Whaley *J. Chem. Phys.* submitted

[7] F. Stienkemeier, J. Higgins, C. Callegari, G. Scoles and S. Kanorsky *Z. Phys. D* submitted
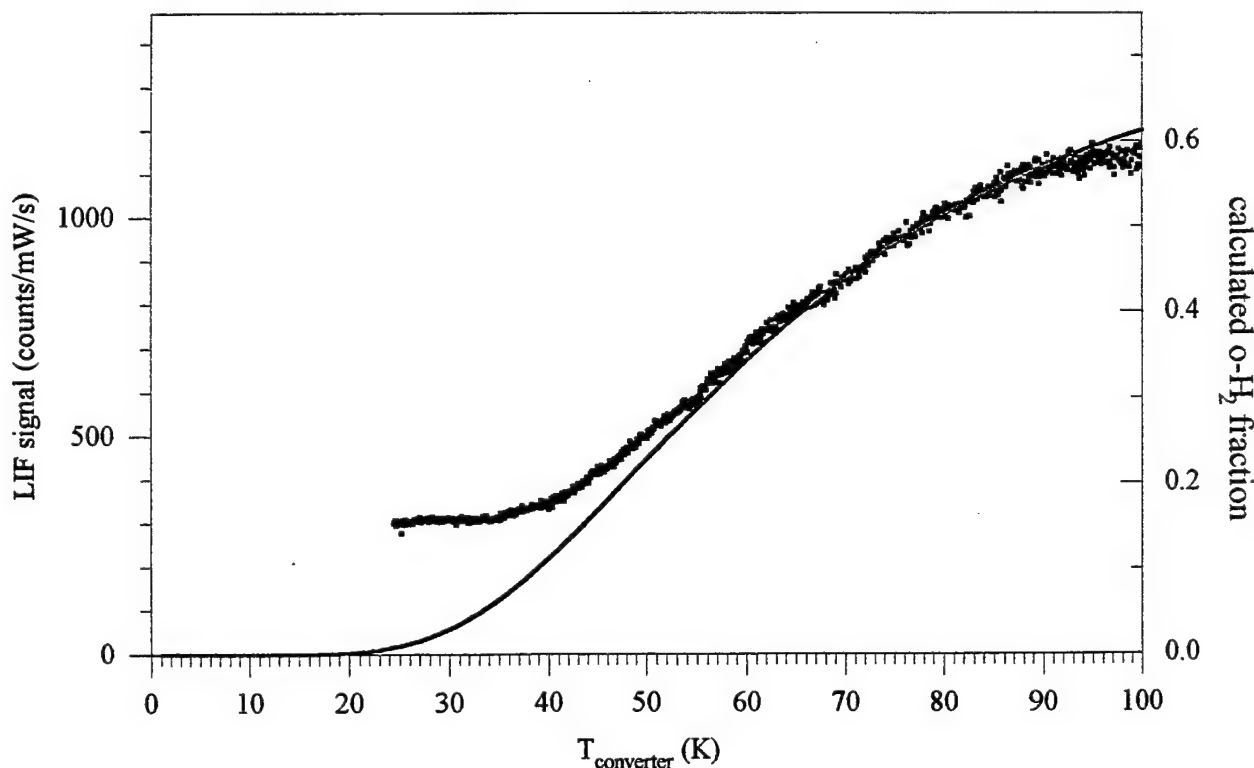
Fig. 1: Laser induced fluorescence intensity of peak (*) (see fig. 2a) for Li attached to H$_2$ clusters, as a function of the ortho-para converter temperature. The excitation laser is set at 15217.9 cm$^{-1}$ and the temperature is ramped at a rate of -0.5 K/min. The solid line is the calculated $o$-H$_2$ equilibrium fraction (right axis) at the corresponding temperature.
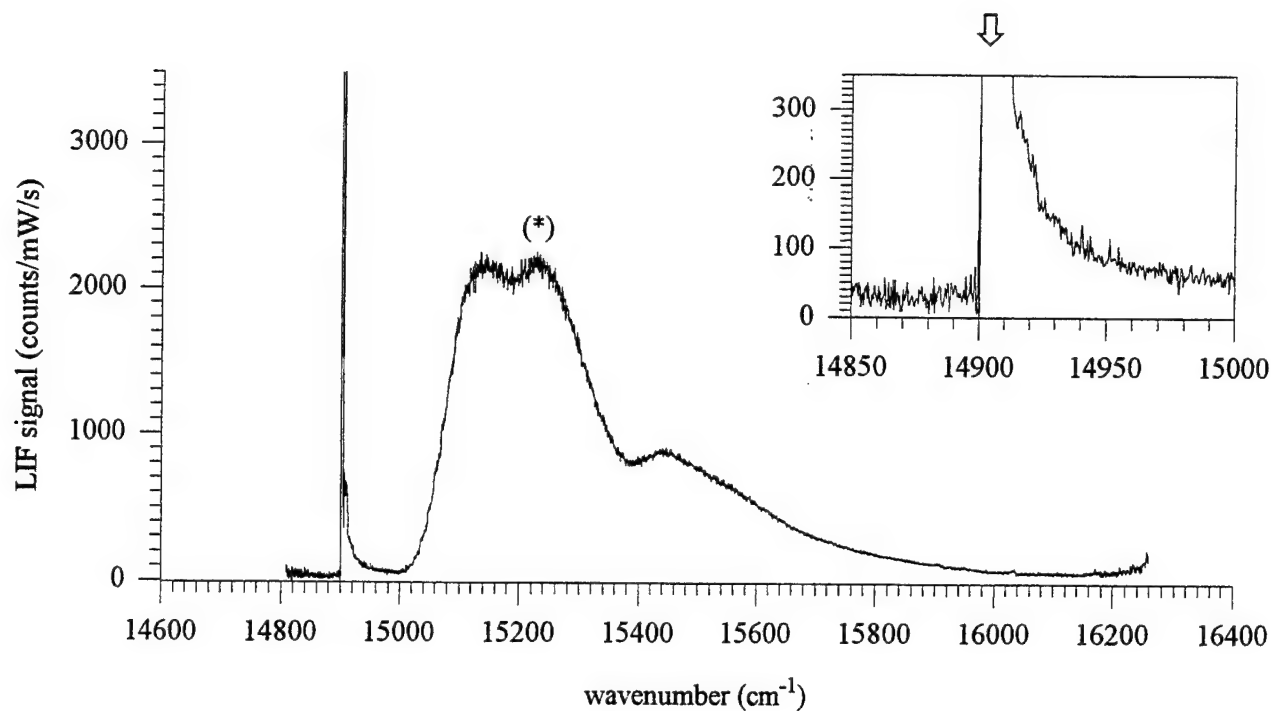
Fig. 2(a): Laser Induced Fluorescence of Li atoms attached to $n$-$H_2$ clusters. The inset panel shows a detail around the position of the gas phase lines (indicated by the arrow). The peak marked with (*) is related to the presence of $o$-$H_2$ (see fig. 1). Source conditions are: $T_{converter}$= 100 K (60 % o-$H_2$), $T_{nozzle}$= 85K, stagnation pressure = 32 atm.



Fig. 2(b): same as fig. 2(a) for $p$-$H_2$ clusters.
Source conditions are: $T_{converter}$= 25 K (1 % o-$H_2$), $T_{nozzle}$= 85K, stagnation pressure = 32 atm.

Fig. 3(a): Beam depletion spectrum of Li attached to $n$-$H_2$ clusters (solid line) compared to absorption spectra of Li in a $n$-$H_2$ matrix (dashed line, from [4]). The vertical line marks the gas phase lines position. Source conditions are: $T_{converter}$ = 100 K (60% o-$H_2$), $T_{nozzle}$ = 85K, stagnation pressure = 32 atm.
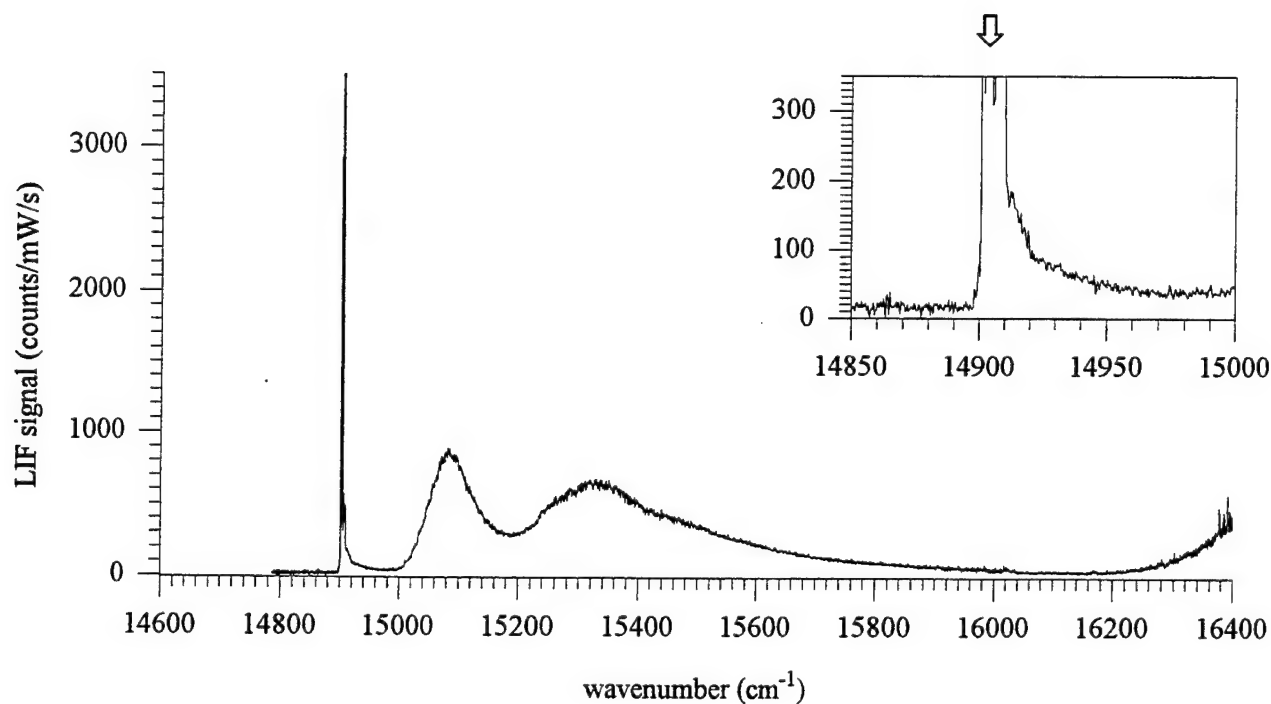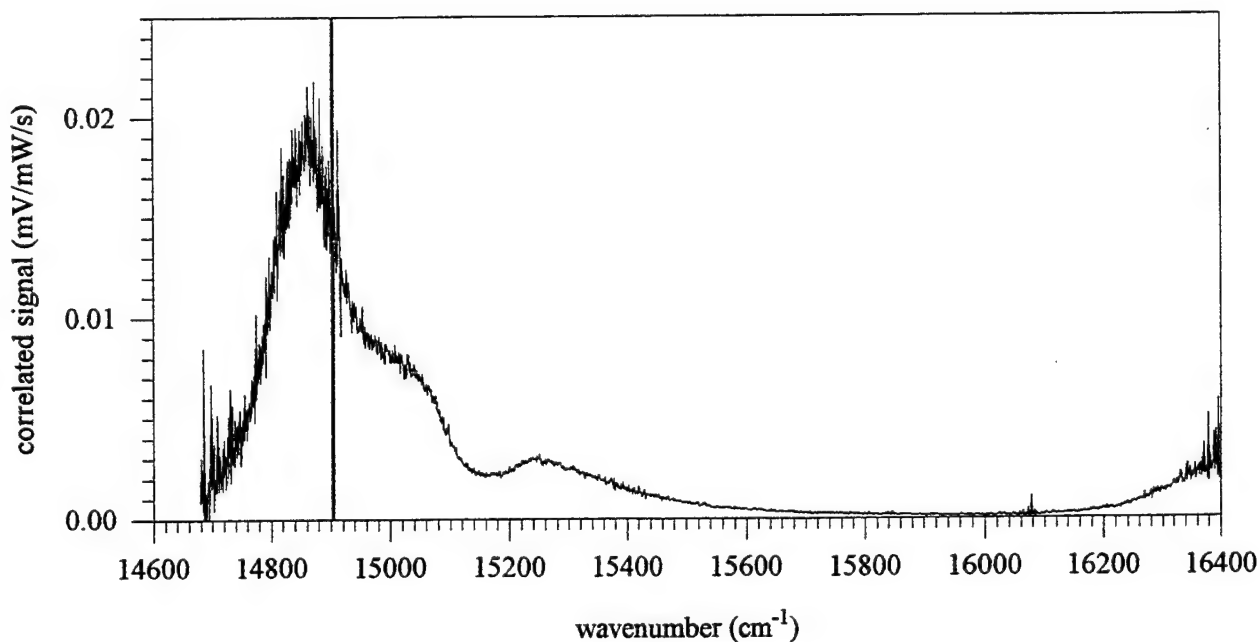


Fig. 3(b): same as fig. 3(a) for $p$-$H_2$ clusters.
Source conditions are: $T_{converter}$ = 25 K (1% o-$H_2$), $T_{nozzle}$ = 85K, stagnation pressure = 32 atm.

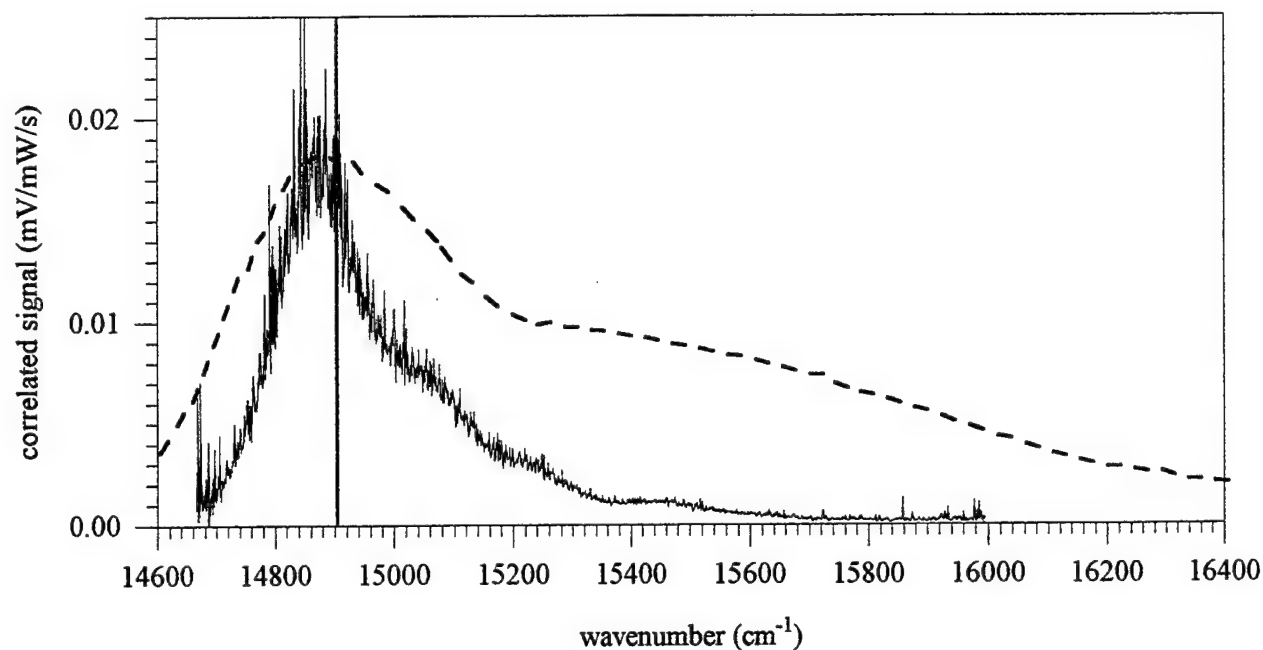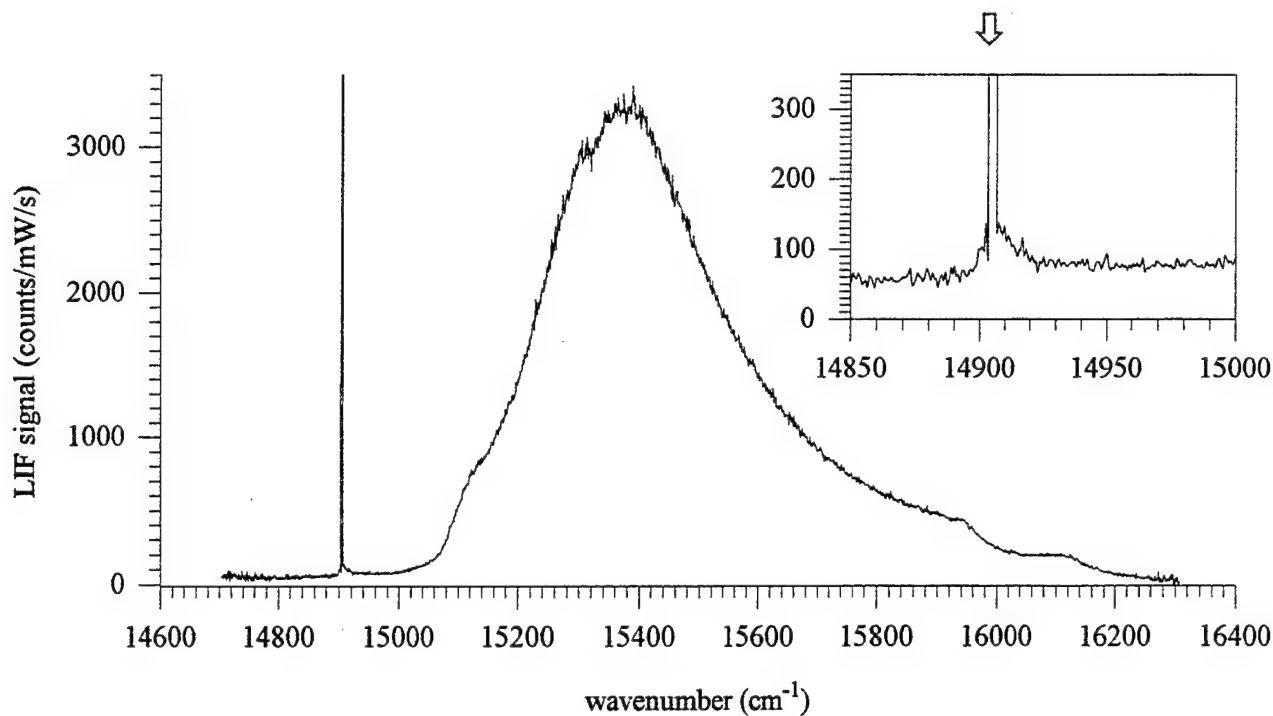Fig 4: Same as fig. 1 for $o$-$D_2$ clusters.

Source conditions are: $T_{converter}$= 24 K (4% p-$D_2$), $T_{nozzle}$= 70K, stagnation pressure = 32 atm.
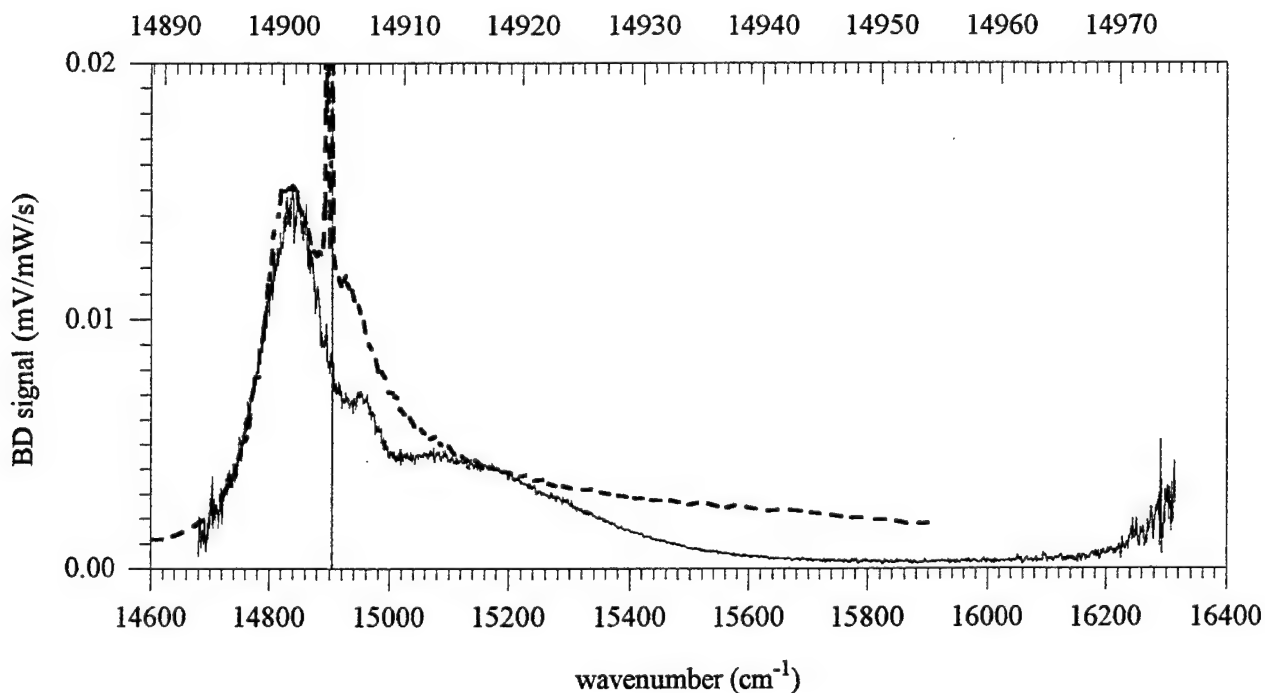


Fig 5: Beam Depletion Spectra of Li atoms attached to $o$-$D_2$ clusters (solid line, bottom axis) compared to LIF spectra of Li atoms **on the surface** of He clusters (dashed line, top axis). The comparison is made by matching the gas phase lines position and expanding the x-scale of the LIF spectrum by an arbitrary factor of 20.

Source conditions are: $T_{converter}$= 24 K (4% p-$D_2$), $T_{nozzle}$= 70K, stagnation pressure = 32 atm.

# Resonant Multiphoton Ionization Spectroscopy of Al(Ar)$_n$ Clusters

James M. Spotts, Chi-Kin Wong, Matthew S. Johnson and Mitchio Okumura

*Arthur Amos Noyes Laboratory of Chemical Physics*
*Mail Code 127-72*
*California Institute of Technology*
*Pasadena, CA 91125*

We have investigated the ultraviolet spectra of Al(Ar)$_n$ clusters to gain insight into the frequency shifts and band assignments of transitions observed for metal atoms trapped in cryogenic matrices. Our approach, 1+1' resonant two-color multiphoton ionization spectroscopy, allowed us to explore how the structure and ultraviolet spectra evolved with cluster size. Three Al(Ar)$_n$ cluster bands were observed around the Al atom $3p \rightarrow 3d$ transition, all of which exhibited electronic band shifts that were strongly dependent upon the degree of solvation.

## Motivation

Previous HEDM studies have predicted that the propellant properties of solid molecular hydrogen can be greatly enhanced by doping Group III atoms such as boron and aluminum into the cryogenic matrix.[1] The properties of doped matrices have been examined extensively by optical spectroscopy, but quantitative analysis in terms of lattice site, Jahn-Teller dynamics, etc. requires highly accurate theory. Recent theoretical models developed within the HEDM program have made great progress in their predictive ability to model the bonding interactions, global structure, electronic spectra, and dynamics of these and related systems. Whereas there exists some ambiguity in the interpretation of bulk systems, a reservoir of accurate, predictive information has accumulated regarding the behavior of sequentially solvated atoms or dopant atoms embedded within finite-sized clusters. As a result, we have pursued a systematic spectroscopic study of aluminum atoms solvated by Ar$_n$ ($n < 55$). Using such a cluster approach, we sought to gain insight into the size dependent behavior of both cluster structure and the electronic band frequency shifts resulting from sequential solvation. Such measurements can provide a stringent benchmark for testing the accuracy and reliabilty of the theories used to describe the bulk doped matrices.

The UV absorption spectrum of aluminum trapped in argon matrices has been extensively investigated,[2,3] along with a number of other HEDM related systems.[4] These studies have concentrated on the spectral region corresponding to the lowest energy Al transitions between 400-240 nm where the matrix bands appear relatively uncongested and therefore assignable. One band of interest is the matrix band assigned to the lowest energy Al transition, namely the $3p \rightarrow 4s$. While the Al $3p \rightarrow 4s$ transition appears at 395 nm, the matrix band assigned to result from the $3p \rightarrow 4s$ transition exhibits a blue shift to roughly 340 nm. Such a large blue shift is rather unusual, and the exact interactions that give rise to this shift are still unquantified. The

next band, a multiplet near 290 nm has been assigned to the $3p \rightarrow 3d$ transition that occurs at 308 nm in the isolated atom.

Size-selective studies of Metal(Solvent)$_n$ clusters can elucidate the interactions involved in matrix band shifts, but such measurements have rarely been undertaken. Recent experimenta on alkali and alkaline earth metals solvated by He$_n$ and Ar$_n$ respectively have focused on very large clusters ($n \sim 100 \rightarrow >10,000$).[5,6] In addition, Whetten and co-workers have studied the Al(Ar)$_n$ cluster ($n < 150$) $3p \rightarrow 4s$ frequency shifts as a function of increasing solvation.[7] However, these authors were unable to infer structural details from merely the solvent shifts. Far more insight could potentially be gained by investigating the matrix band spectral shifts arising from the Al ground state $3p$ manifold to the excited $3d$ mainfold because asymmetries in the Al atom binding site could lift the five-fold degeneracy of the $3d$ states, leading to the possibility of more than one resolvable band. By studying the size dependent frequency shifts and band splittings arising from transitions to the $3d$ manifold, a more complete picture of structure evolution may be inferred. For this reason, we have investigated the UV spectra of Al(Ar)$_n$ clusters ($n < 56$) about the atomic aluminum $3p \rightarrow 3d$ transitions by 1+1' resonant two-color multiphoton ionization spectroscopy (R2MPI).

## Experimental

Al(Ar)$_n$ clusters were generated by a standard laser vaporization techniques. Following the opening of a piezoelectric pulsed valve, the pure Ar carrier gas (~8 atm. stagnation pressure) entered the first of three regions of the laser vaporization source (Figure 1). The first region consisted of a Ø0.040" channel that then opened up at 10° in region 2 to join region 3, a straight Ø0.100" channel. The tripled output of a Nd-YAG laser (Continuum Surelite 1) was focused on the surface of a rotatable 2024 Al rod that was positioned 0.105" after region 2. Following supersonic expansion, the clusters passed through a 3-mm skimmer into the second differential region. The clusters were then ionized by 1+1' resonant two-color multiphoton ionization by crossing the jet with an unfocused pump beam consisting of both the residual fundamental and doubled fundamental of the appropriate laser dye wavelength (DCM, Rhodamine 640/610). The pump laser was the output of a dye laser (Quantel TDL-51) pumped by a Nd:YAG laser (Continuum NY-61) that was doubled to generate the UV beam (1-4 mJ/pulse). Figure 2 shows the ionization scheme employed. The clusters were scanned through the UV region from 330 nm to 296 nm, first exciting the Al atom $3p \rightarrow 3d$ transition with the doubled UV photon, and subsequently ionizating with the visible fundamental dye photon (10-50 mJ/pulse). In the current single dye laser experiments, the UV and visible wavelengths ($\nu_{vis} = \frac{1}{2}\nu_{UV}$) were forced to tune simultaneously. The total photon energy ($\nu_{UV} + \nu_{vis}$) was always within 0.75 eV or less of the ionization threshold of the clusters.[8]

Following ionization, the clusters were extracted perpendicularly and mass-analyzed by a standard 1-m Wiley-McLaren time-of-flight (TOF) spectrometer, and detected by a microchannel plate. TOF mass spectra were collected by a transient digitizer (LeCroy 8818). Individual scans were recorded by gating the mass peak of interest with a gated integrator. S/N was greatly improved by switching the laser vaporization Q-switch at half the rep rate and using the gated integrator to subtract the pump background due to DP oil contaminant fragments (LV off) from from every signal shot (LV on). All spectra were normalized for UV fluence.

# Results

All of the Al(Ar)$_n$ clusters ($n = 4$ - $54$) exhibited two broad principal transitions. We have tentatively assigned them as arising from the Al $3p \rightarrow 3d$ transitions. One band was blue-shifted relative to atomic Al $3p \rightarrow 3d$ transition (308.215 nm), and the other red-shifted.

The blue-shifted bands were generally broad and asymmetric. Figure 3 shows some typical spectra in the 305-297 nm region. For smaller clusters ($n \leq 12$), the peak shifted to the blue as $n$ increased. However, a splitting was observed for larger clusters ($n \geq 18$). At $n = 18$, the peak was more symmetric and a dip started to appear at around 301 nm. The splitting became more pronounced as $n$ increased.

The red-shifted bands were observed in the 325-308 nm region. Some typical spectra are shown in Figure 4. The peaks were also broad and asymmetric, but they showed a monotonic increase in the red-shift relative to the atomic transition with cluster size (Figure 5). Moreover, the band positions varied in a stepwise fashion with $n$, and the changes appeared to coincide with the shell sizes ($n = 12$, and 54) for icosahedral shell closings.[7,9] As shown in Figure 5, the peaks were close to 312 nm for $n \leq 12$, 320 nm for $25 \leq n \leq 40$, and 324 nm at $n = 54$. This result suggested that the observed spectral shifts indeed reflected the structural evolution in the clusters, and that cluster fragmentation was not seriously degrading the size-selectivity of our measurements.

# Discussion

The observed patterns in this experiment resulting from putative Al atom $3p \rightarrow 3d$ transitions as well as those observed by Whetten involving Al transitions between the $3p \rightarrow 4s$ differ significantly from the matrix features. Most notable is the difference in the magnitude of the cluster electronic band shifts relative to those of the matrix. The two resolved bands in the matrix appear at 291 nm and 286 nm have been assigned as $3p \rightarrow 3d$ transitions. In contrast, our R2MPI spectra of Al(Ar)$_n$ ($n < 55$) exhibit a considerably less pronounced blue-shift. With small Al(Ar)$_n$ clusters that form the first icosahedral shell ($n \leq 12$), a strong size dependent blue-shift is observed as the cluster size is monotonically increased (Figure 5). Al(Ar)$_{12}$ shows a significant blue-shift maximum at 299 nm, but no splitting of electronic bands is observed. By Al(Ar)$_{18}$ and for all larger clusters observed, the overall bandwidth and blue-shift remains roughly the same as for Al(Ar)$_{12}$. However, by Al(Ar)$_{18}$ a discernible splitting of the is evident. This splitting increases up to Al(Ar)$_{34}$ at which point the splitting matches that in the matrix, namely 5 nm. Moreover, the dip between the bands remains at the same position for all clusters greater than Al(Ar)$_{18}$. Hence, the increased splitting is due to equal red- and blue-shifts of the two respective bands about the dip wavelength. This data suggests that the maximum blue-shift has been essentially achieved by Al(Ar)$_{12}$, and that those interactions that give rise to the electronic band splitting are present by Al(Ar)$_{34}$. However, the blue shifts are only about +400 cm$^{-1}$ and +1100 cm$^{-1}$ or ~25% and ~44% of the matrix shift, suggesting that even for the large clusters we have not been able to reproduce the bulk behavior.

Whetten and co-workers obtained analogous results in their R2MPI experiment on the Al(Ar)$_n$ clusters ($n < 40$) $3p \rightarrow 4s$ transition.[7] As was the case with the $3p \rightarrow 3d$ electronic bands, the $3p \rightarrow 4s$ band exhibited a strong monotonic blue-shift with increasing cluster size up to Al(Ar)$_{12}$, after which the observed spectral shift leveled off. The maximum extent of the cluster $3p \rightarrow 4s$ blue-shift was +700 cm$^{-1}$, only 17% of the +4200 cm$^{-1}$ matrix shift. These shifts are

proportionally smaller than those in the $3p \rightarrow 3d$ case. Such behavior caused Whetten to likewise conclude that these cluster systems do not yet resemble the bulk.

The other band observed during the course of this study in the wavelength range 330-310 nm has no assigned counterpart in any metal doped matrix study. These broad features are significantly red-shifted relative to the Al atom $3p \rightarrow 3d$ transitions. Similar to the blue-shifted putative $3p \rightarrow 3d$ Al(Ar)$_n$ cluster bands, these red-shifted bands also exhibited a size dependence on the magnitude of the spectral shift. For the smaller clusters corresponding to the first icosahedral shell, the observed red-shifts were all small in magnitude relative to the Al atom $3p \rightarrow 3d$ transitions, and almost exactly the same as the red-shift in the $^2\Delta$ state of AlAr. Moreover, the spectral shifts in the first icosahedral shell did not evolve with increasing solvation. All cluster bands originating from the second icosahedral shell of the Al(Ar)$_n$ clusters ($12 < n \leq 54$), are significantly red-shifted relative to the first shell. A strong, monotonically increasing red-shift from 312 nm to 319 nm is observed in the cluster sizes Al(Ar)$_{13}$ through Al(Ar)$_{25}$. After Al(Ar)$_{25}$, the cluster red-shift levels off for the rest of the clusters in the second icosahedral shell. Another significant red-shift to 324 nm is again observed upon complete solvation of the second shell.

An interesting question arises as to the nature of the structure in the $3p \rightarrow 3d$ case, as well as the origin of the cluster electronic splitting. In particular, it is puzzling that relatively small clusters like Al(Ar)$_{34}$ can on one hand mimic the electronic band splitting of the bulk while on the other failing to achieve bulk characteristics such as the magnitude of the matrix blue-shift. If we examine the singly solvated system, namely AlAr, we find that there are three excited electronic states that arise from the 3d manifold that can be accessed by either $^2\Pi_{1/2}$ or $^2\Pi_{3/2}$ spin orbit ground state, namely $^2\Delta$, $^2\Pi$, and $^2\Sigma^+$. In AlAr, the $^2\Delta$ was observed to exhibit a significant red-shift relative to the Al atom transitions, while both the $^2\Pi$ and $^2\Sigma^+$ were slightly blue-shifted by less than 1 nm.[10] The blue-shift of the $^2\Pi$ and $^2\Sigma^+$ states has been attributed to greater repulsive interactions in the excited state between Ar and the Al $d_{xz}$ and $d_{yz}$ for $^2\Pi$ and $d_{z^2}$ for $^2\Sigma^+$ (assuming z lies along the internuclear axis).[#] With respect to the AlAr $^2\Delta$ state, the $d_{x^2-y^2}$ and $d_{xy}$ orbitals lie perpendicular to the internuclear axis. The $^2\Delta$ red shift, then, can be attributed to the increase in Al atom polarizability upon excitation from the $3p$ to $3d$ orbitals.

The fact that the clusters in the first icosahedral shell exhibit almost the same red-shift as the $^2\Delta$ state in AlAr strongly suggests that this red-shifting band evolves from this state. The question arises, then, whether such a band is observable in the bulk matrix, or ultimately blue-shifts as $n \rightarrow \infty$. The other possibility could be that this red-shifted cluster band continues to red-shift in the matrix to form a $3d$-$4s$ hybrid band at the position currently assigned $3p \rightarrow 4s$ band position at 340 nm. Such a hybridization would be rather novel, but would further illuminate the intricacies involved in metal solvation.

While there is presently no single model that provides a complete interpretation of cluster structure based on the observed data, a potential candidate would place the Al atom always on or slightly above the outermost shell in a "cap site" (Figure 6). Evidence for such solute surface binding has been predicted by Alexander in a recent modified deterministic/stochastic genetic algorithm (DS-GA) study.[11] Alexander found that for the isoelectronic clusters, B(Ar)$_n$ ($n \leq 12$), the B atom prefers to lie on the surface of the cluster occupying a site with the fewest number of

---

[#] Due to uncertainty in the AlAr ground state D$_o$ value, the origin of the $^2\Pi$ blue shift is not definitive.

Ar nearest neighbors when the B-Ar interaction was described by both the attractive $^2\Pi$ state as well as the significantly more repulsive $^2\Sigma^+$ state. Due to similarities between the B-Ar and Al-Ar potentials, it would be reasonable to postulate that $Al(Ar)_n$ clusters may form similar structures.

The cap site model can account for many of the observed electronic band shift trends. In essense, the cap site model preserves much of the same bonding interactions as those of AlAr itself. Therefore, the furthest blue-shifted band can be envisioned as arising from strong repulsive interaction between the $d_{z^2}$ of the Al atom and the cluster. Likewise, the $d_{xz}$ and $d_{yz}$ of the Al atom would be forced to orient into the Ar-Ar bonds that form the cap site, resulting in a lesser but still significant repulsive interaction that drives the band to the blue. Moreover, the observed red-shifting behavior of the putative $^2\Delta$ band can be justified by the cap site model. By occupying a cap site, the Al atom can minimize repulsive interactions between its $d_{x^2-y^2}$ and $d_{xy}$ orbitals while at the same time stabilizing the these orbitals by favorable $\pi$-type interactions with the Ar-Ar bonds that form the edges of the cap site.
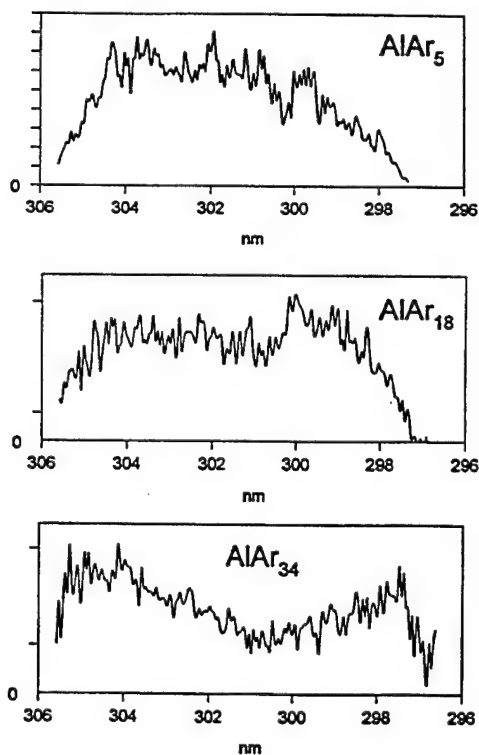
A definitive interpretation of the current results requires accurate calculations addressing the cluster structure as well as the shifts and splittings of the electronic transitions as a function of cluster size. The $Al(Ar)_n$ clusters should serve as important prototypes for metal-doped solids, and will provide a critical test of theoretical efforts to model these HEDM materials.[4,12]
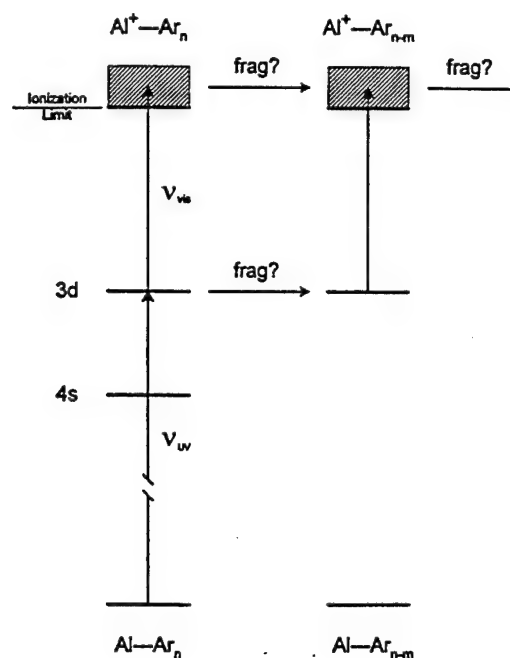
# References

1   *Proceedings of the High Energy Density Materials (HEDM) Conference*, edited by P. G. Carrick and S. Tam (Phillips Laboratory, Edwards AFB, CA, 1996).

2   H. Abe and D. M. Kolb, *Ber. Bunsenges. Phys. Chem.*, **87**, 523-527 (1983).

3   R. Grinter and R. J. Singer. *Chem. Phys.*, **113**, 87-97 (1987).

4   M. E. Fajardo, S. Tam, T. L. Thompson and M. E. Cordonnier, *Chem. Phys.*, **189**, 351-365 (1994); J. A. Boatz and M. E. Fajardo, *J. Chem. Phys.*, **101**, 3472-3487 (1994); R. A. Corbin and M. E. Fajardo, *J. Chem. Phys.*, **101**, 2678-2683 (1994); S. Tam and M. E. Fajardo, *J. Chem. Phys.*, **99**, 854-860 (1993); M. E. Fajardo, *J. Chem. Phys.*, **98**, 119-125 (1993); M. E. Fajardo, *J. Chem. Phys.*, **98**, 110-118 (1993); M. E. Fajardo, P. G. Carrick and J. W. Kenney, *J. Chem. Phys*, **94**, 5182-5825 (1991).

5   F. Stienkemeier, J. Higgins, W. E. Ernst, and G. Scoles, *Z. Phys. B*, **98**, 413-416 (1995), and references therein.

6   A. I. Krylov, R. B. Gerber, M. A. Gaveau, J. M. Mestdagh, B. Schilling, and J. P. Visticot, *J. Chem. Phys.*, **104**, 3651-3663 (1996), and references therein.

7   R. L. Whetten, K. E. Schriver, J. L. Persson and M. Y. Hahn, *J. Chem. Soc. Faraday Trans.*, **86**, 2375-2385 (1990).

8   K. E. Schriver, M. Y. Hahn, J. L. Persson, M. E. LaVilla and R. L. Whetten, *J. Phys. Chem.*, **93**, 2869-2871 (1989).

9   D. A. Estrin, L. Liu and S. J. Singer, *J. Phys. Chem.*, **96**, 5325-5331 (1992).

10  S. A. Heidecke, Z. Fu, J. R. Colt, and M. D. Morse, *J. Chem. Phys.*, **97**, 1692-1710 (1992).

11  S. K. Gregurick, B. Hartke, and M. H. Alexander, *J. Chem. Phys.*, **104**, 2684-2691 (1996).

12  P. W. Langhoff, *J. Phys. Chem.*, **100**, 2974-2984 (1996).
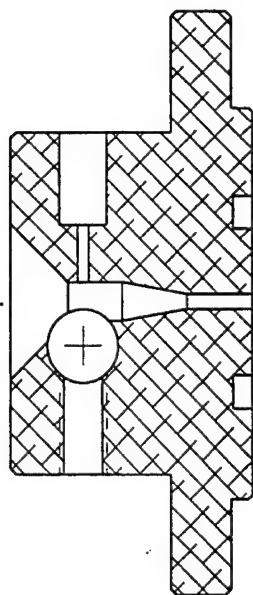
**Figure 1.** Laser vaporization source (x2 magnification)



**Figure 2.** 1+1′ two-color multiphoton ionization scheme



**Figure 3.** R2MPI spectra for Al(Ar)$_n$ in the region of 306 - 296 nm
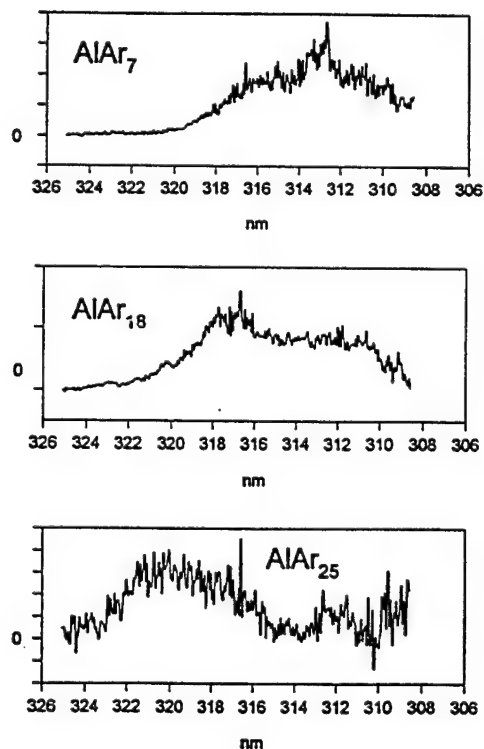


**Figure 4.** R2MPI spectra for Al(Ar)$_n$ in the region of 325 - 308 nm
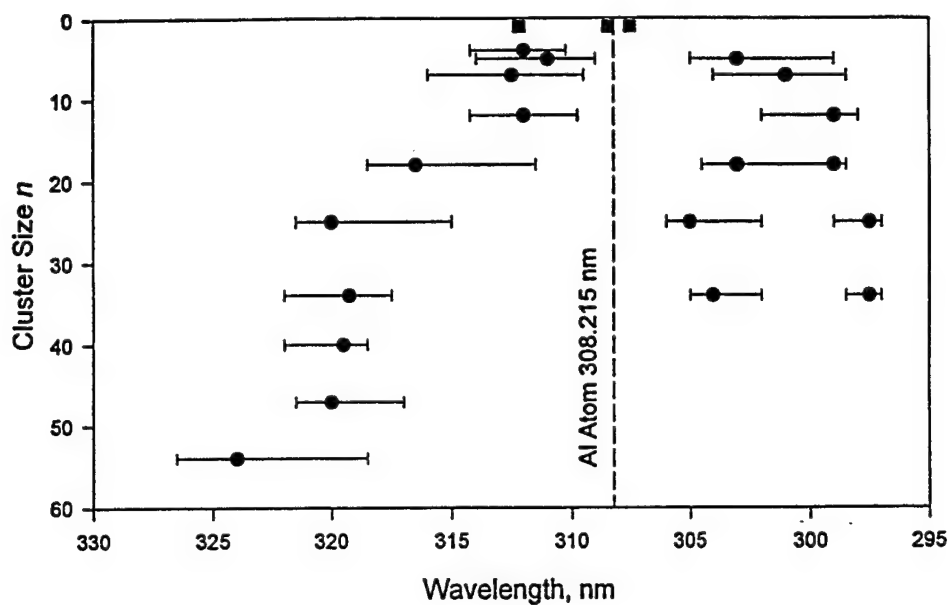
## 3p-3d Band Positions of AlAr$_n$



**Figure 5.** Variation of spectral shift with cluster size $n$



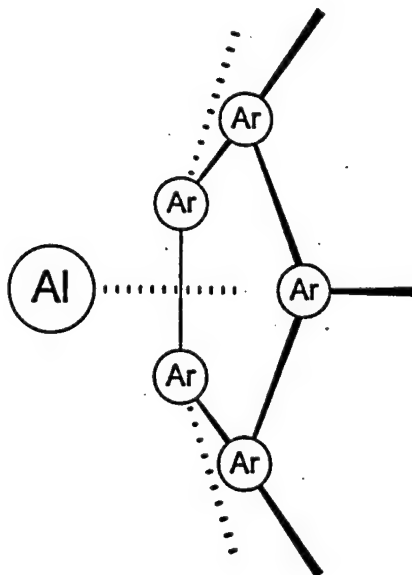**Figure 6.** Possible structure for Al(Ar)$_n$ from the cap site model

# Spectroscopic Characterization of Non-bonding Interactions of the Boron Atom

Paul J. Dagdigian, Xin Yang, and Eunsook Hwang
*Department of Chemistry, The Johns Hopkins University*
*Baltimore MD 21218-2685*

## 1. Introduction

We have previously reported laser fluorescence excitation (FE) spectra of weakly bound complexes of the boron atom built on the $2s^23s\ ^2S \leftarrow 2s^22p\ ^2P$ atomic transition, which occurs at 249.8 nm.[1-5] In intense collaboration with Millard Alexander and his group,[1,2,4-6] these spectra have been interpreted to provide detailed information about non-bonding interactions of the B atom, in its ground $2s^22p\ ^2P$ and Rydberg $2s^23s\ ^2S$ states with the rare gases and $H_2$.

Our experiments have now been extended to the study of electronic transitions of weakly bound complexes of boron atoms correlating with the $2s2p^2\ ^2D \leftarrow 2s^22p\ ^2P$ atomic transition at 208.9 nm. It is notable that the upper level of this transition is an excited *valence* state. We report here our studies of electronic transitions in the BNe, B$\cdots$H$_2$, and BAr complexes which correlate with this atomic transition. In the case of BNe, it was possible to observe by laser fluorescence excitation two electronic states in this energy range.[7] Only one excited BAr state could be observed by fluorescence excitation, while no fluorescence could be observed for B$\cdots$H$_2$. In order to detect transitions to non-fluorescing states of the latter two species, we have implemented a fluorescence depletion (FD) scheme, which is a folded variant of optical-optical double resonance. With this technique, we have been able to observe two electronic transitions in BAr, one of which is the previously observed fluorescing state, as well as transitions in the B$\cdots$H$_2$ complex.[8]

Chemical reaction within the excited B($^2D$)$\cdots$H$_2$ complex is also energetically allowed. We have observed BH chemiluminescence from the decay of B($^2D$)$\cdots$H$_2$. This indicates that chemical reaction is occurring within the excited complex. By contrast, no evidence of chemical reaction was found in our earlier study of the B$\cdots$H$_2$ state correlating with B($2s^23s\ ^2S$) + H$_2$.

The following sections present detailed descriptions of our experimental observations, as well as our inferences on the relevant potential energy curves. The binding energies and decay behavior of BNe, BAr, and B$\cdots$H$_2$ excited states are drastically different and are discussed in terms of our knowledge of the electronic states of these complexes.

## 2. The BNe Complex

The approach of a spherical rare gas perturber to B($2s2p^2\ ^2D$) will lead to 3 molecular electronic states, of $^2\Delta$, $^2\Pi$, and $^2\Sigma^+$ symmetry . Since the Pauli repulsion will be minimized with the electrons on the B atom in $2p\pi$ vs. $2p\sigma$ orbitals, we expect the most attractive of these states to be $^2\Delta$, hereafter denoted $C^2\Delta$. The other states are denoted $D^2\Pi$, and $E^2\Sigma^+$.

Figure 1 presents a low-resolution FE survey spectrum of a supersonic beam of a photolyzed diborane/Ne/He mixture in the region of the B atomic transition of interest. In addition to the strong atomic lines, we observe 6 partially resolved molecular bands assigned to BNe. We have taken high-resolution scans of all the molecular bands. Rotational analyses of the 4 lowest bands show that these all involve transitions to the $C^2\Delta$ state, and their vibrational assignments are given in Fig. 1. In addition, there 2 other bands which we assign as excitation to the $D^2\Pi$ state. Finally, we observe the onset of an unstructured, continuous transition. This onset is assigned as the energy corresponding to excitation of $BNe(X^2\Pi_{1/2}, v'' = 0)$ to the $B(2s2p^2\,{}^2D)$ + Ne dissociation limit.
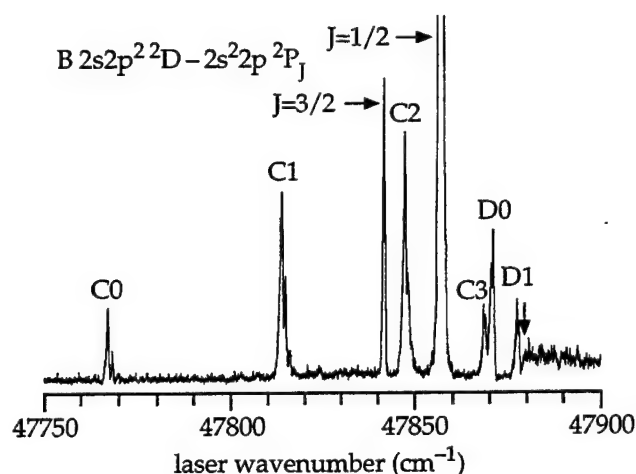


FIG. 1. Laser fluorescence excitation spectrum of BNe. The $C - X$ and $D - X$ (v',0) bands are labeled $Cv'$ and $Dv'$, respectively. The vertical arrow denotes the excitation energy of the $B(2s2p^2\,{}^2D)$ + Ne asymptote.

Table 1 compares the derived dissociation energies for the observed bound BNe electronic states. The binding energy for the ground $X^2\Pi$ state agrees reasonably well with the previously calculated[4] *ab initio* value. There is a significant increase in the binding when the complex is promoted to the $C^2\Delta$ state. Since this transition involves a $2p\pi \leftarrow 2p\sigma$ promotion, the increasing binding can be rationalized as resulting from decreased Pauli

Table 1. Estimated dissociation energies (in cm$^{-1}$) for the observed BNe electronic states.

| Electronic state | $D_0$ |
|------------------|-------|
| $X^2\Pi$ | 21.3(3)[a] |
| $C\,^2\Delta$ | 111.3(4) |
| $D^2\Pi$ | 7.9(3) |

[a] Uncertainties reported in units of the last significant digit.

repulsion by removing electron density along the internuclear axis. We also see that the binding in the $D^2\Pi$ state is very weak. We believe that the accompanying $E^2\Sigma^+$ state is purely repulsive.

### 3. The B⋯H₂ Complex

In order to observe the non-fluorescing excited states of this complex, we have implemented a fluorescence depletion technique, in which two tunable lasers access the same level.[8] This allows the observation of transitions for which the excited state does not fluoresce by monitoring the effect of the depletion laser on fluorescence induced by the probe laser. The application of this technique thus requires that there be one fluorescing electronic trans- ition. In the case of B⋯H₂, we have utilized as the probe transition fluores- cence from the lower-lying $B(2s^23s\ ^2S)$⋯$H_2$ state, which we have previously reported.[5] We first validated the utility of the FD method by observing the BNe bands displayed in Fig. 1 by this method. We find that the relative in- tensities of the bands differ significantly when observed by FE and FD. We have carried out rate equation modeling and have shown that when the ex- cited state decays nonradiatively, *e.g.* by predissociation or chemical reaction, then the FD intensities closely track the relative absorption strengths.

Figure 2 presents the FD spectrum recorded for B⋯H₂. The spectrum covers a broader wavenumber range than for BNe (see Fig. 1). There are broad, unstructured features, arbitrarily labeled *A*, *B*, and *C* in Fig. 2. No B⋯H₂ FE features corresponding to these FD transitions have been observed. Formation of BH in several electronic states is energetically allowed for the $B(2s2p^2\ ^2D)$⋯$H_2$ complex. As we describe below, we have observed BH chemiluminescence from the formation of radiating excited states.

There five BH₂ potential energy surfaces (three in linear geometry)
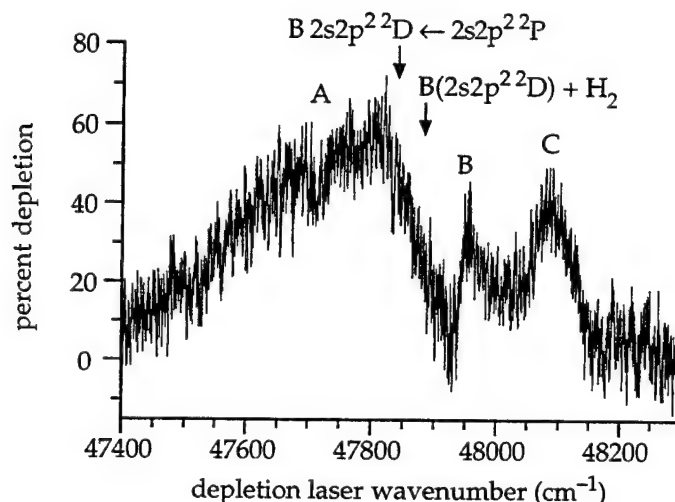


FIG. 2. Laser fluorescence depletion spectrum of B⋯H₂. The observed features are labeled *A*, *B*, and *C*, in order of increasing wave number. The wave number of the B atomic transition and the excitation energy to the $B(2s2p^2\ ^2D)$ + H₂ dissociation asymptote are indicated. The pulse energies of the depletion and probe lasers were 200-250 and 25 $\mu J$, respectively.

emanating from the $B(2s2p^2\,{}^2D) + H_2$ asymptote. The FD spectrum in Fig. 2 extends both to the red and blue of the excitation energy of the $B({}^2D) + H_2$ dissociation asymptote. This suggests that there are both attractive and repulsive surfaces in the Franck-Condon region ($T$-shaped geometry, with ~6 bohr equilibrium $B-H_2$ separation[6]). As with BNe, we expect for the most attractive excited surfaces (corresponding to feature $A$ in Fig. 2) that the B $2p$ orbitals whose lobes are perpendicular, rather than parallel, to the $B-H_2$ axis are occupied. Unlike the $B(2s^23s\,{}^2S) + H_2$ state,[5,6] this will facilitate chemical reaction from a favorable overlap with the antibonding $H_2\,1\sigma_u$ orbital.

We have also observed BH chemiluminescence, in the $b^3\Sigma^- \rightarrow a^3\Pi$ and $A^1\Pi \rightarrow X^1\Sigma^+$ band systems, from the reactive decay of the $B(2s2p^2\,{}^2D)\cdots H_2$ complex and from bimolecular $B(2s2p^2\,{}^2D)-H_2$ collisions, as we previously observed in $B(2s^24p\,{}^2P)-H_2$ collisions.[9] For both the $b \rightarrow a$ and $A \rightarrow X$ band systems, the emission from $B({}^2D)\cdots H_2$ is observed mainly with excitation of feature $A$. From comparison of the spectra with simulations, we find that only v' = 0 and 1 vibrational levels are produced in $BH(b^3\Sigma^-)$, with the reaction of v' = 1 increasing with increasing excitation wavenumber.

## 4. The BAr Complex

In contrast to the BNe FE spectrum, we observe only one electronic band system in the FE spectrum of BAr. The BAr FD spectrum shows two transitions, one to a weakly bound excited state, observed by FE, and a second transition to a strongly bound state. Figure 3 presents the FD spectrum recorded for $^{11}$BAr. We assign the two observed band systems as the $C^2\Delta \leftarrow X^2\Pi$ and $D^2\Pi \leftarrow X^2\Pi$ transitions. The v' quantum numbers were assigned (to ±1) with the help of the observed $^{11,10}$BAr isotope shifts. It has been possible to record the FD spectrum of the isotopomers separately by appropriate choice of the monitoring transition employed by the probe laser.
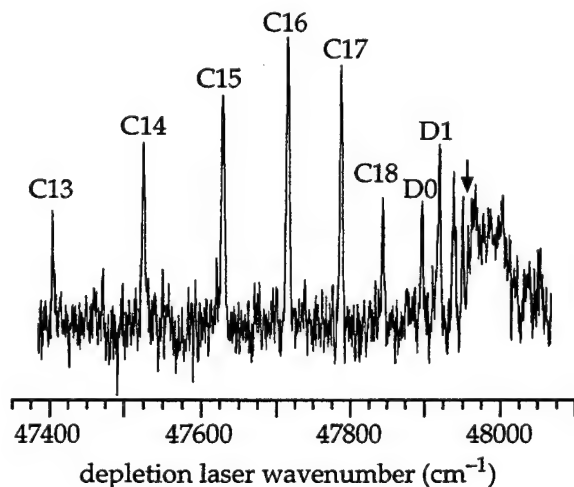


FIG. 3. Laser fluorescence depletion spectrum of $^{11}$BAr. The $C - X$ and $D - X$ (v',0) bands are denoted Cv' and Dv', respectively. The vertical arrow denotes the excitation energy of the $B(2s2p^2\,{}^2D) + Ar$ asymptote.

We find that the binding energy of the $BAr(C^2\Delta)$ state is substantial ($\sim 3500$ cm$^{-1}$), in sharp contrast to the weak binding found for $BNe(C^2\Delta)$ [see Table 1]. Similarly, a large binding energy ($D_0 = 1186 \pm 6$ cm$^{-1}$) was found for the $BAr(B^2\Sigma^+)$ state,[1] while the $BNe(B^2\Sigma^+)$ is purely repulsive.[4]

It is striking that both the $C^2\Delta$ and $D^2\Pi$ states of BNe decay radiatively, while only the latter does so in BAr. From our knowledge of the B–rare gas potential energy curves, we believe that the $BAr(C^2\Delta)$ state is decaying nonradiatively, through predissociation mediated by a crossing with a repulsive quartet state correlating with $B(2s2p^2\,{}^4P) + Ar$, which lies $\sim 28000$ cm$^{-1}$ above the ground atomic asymptote. This suggestion is being pursued in collaborative theoretical work by David Yarkony and his group.[11]

### 5. Additional Experiments

We have been attempting to record the FE spectrum of other B-molecule complexes. Recently, we have successfully observed the electronic transition of the B–N$_2$ complex built upon the B atomic $2s^2 3s\,{}^2S \leftarrow 2s^2 2p\,{}^2P$ transition. The relevant BN$_2$ potential energy surfaces have been computed by Millard Alexander and his group[12] and are being employed to generate theoretical predictions of the spectrum, for comparison with our experimental spectrum.

We have also observed BH in its low-lying $a^3\Pi$ electronic state by FE detection in its $b - a$ band system.[10] Decay lifetimes of a number of $BH(b^3\Sigma^-$, $v' = 0 - 4$.) rotational/fine-structure levels were measured. This electronic state is predissociated by the repulsive $1^3\Sigma^+$ state. Our measured lifetimes compare very well with radiative and nonradiative rates calculated by Yarkony and Pederson.[10]

1.  E. Hwang, Y.-L. Huang, P. J. Dagdigian, and M. H. Alexander, J. Chem. Phys. **98**, 8484 (1993).

2.  E. Hwang, P. J. Dagdigian, and M. H. Alexander, Can. J. Chem. **72**, 821 (1994).

3.  E. Hwang and P. J. Dagdigian, Chem. Phys. Lett. **233**, 483 (1995).

4.  X. Yang, E. Hwang, P. J. Dagdigian, M. Yang, and M. H. Alexander, J. Chem. Phys. **103**, 2779 (1995).

5.  X. Yang, E. Hwang, M. H. Alexander and P. J. Dagdigian, J. Chem. Phys. **103**, 7966 (1995).

6.  M. H. Alexander, J. Chem. Phys. **99**, 6014 (1993); M. H. Alexander and M. Yang, *ibid.* **103**, 7956 (1995).

7.  X. Yang, E. Hwang, and P. J. Dagdigian, J. Chem. Phys. **104**, 599 (1996).

8.  X. Yang, E. Hwang, and P. J. Dagdigian, J. Chem. Phys. **104**, 8165 (1996).

9.  X. Yang and P. J. Dagdigian, J. Phys. Chem. **97**, 4270 (1993).

10. X. Yang, L. Pederson, D. R. Yarkony, and P. J. Dagdigian, J. Phys. Chem. **100**, 5649 (1996).

11. D. R. Yarkony, abstracts *AFOSR 1996 HEDM Contractors Meeting*, Boulder, CO.

12. M. H. Alexander, abstracts *AFOSR 1996 HEDM Contractors Meeting*, Boulder, CO.

# (a) Structure and Energetics of $B(Ar)_n$ and $B(N_2)$ Clusters
# (b) Hibridon 4 program package

Millard H. Alexander, Andrew Walton, and Moonbong Yang
*Department of Chemistry and Biochemistry*
*University of Maryland, College Park, MD 20742-2021*

## I. Introduction

We have continued our investigation of weakly-bound clusters involving atomic B, carrying out additional work on clusters with Ar and initiating a new investigation of the $BN_2$ cluster. Close contact continues with Dagdigian's group, who are reporting[1] related experimental investigations of $B(Ar)_2$ and $BN_2$.

In addition we report development of a new version (4.0) of our Hibridon™ code for the study of scattering, photodissociation, and weakly-bound complexes.

## 2. $B(Ar)_n$ clusters

We are continuing work on our previously introduced, deterministic/ stochastic genetic algorithm (DS-GA) for the determination of minimum energy structures of weakly-bound clusters.[2] In conventional GA methods[3] the coordinates of a particular cluster, the "individual," are encoded into a binary string, the "genome". Pairs of individuals are selected as parents, one chosen for high "fitness" (low potential energy) and the other chosen randomly. Offspring clusters inherit genomes which are random crosses of those of each parent.

We have shown[2] that determination of the minimum energy cluster can be accelerated significantly by adding, after each mating, a coarse, conjugate gradient optimization. This repositions the children closer to local minima or saddle points. Recently, Niesse and Mayne[4] have suggested that this procedure can be further improved by the use of genomes which are base-10 (decimal) strings of the *space-fixed* coordinates of each atom rather than base-2 (binary) strings of the *relative* coordinates.

We are currently testing the Niesse-Mayne[4] algorithm for $B(Ar)_n$ clusters. Since the B atom has an open shell, the effective PES is obtained as the root of a $3 \times 3$ Hamiltonian.[5, 6] In our initial study[2] we neglected the spin-orbit splitting in the B atom($16$ cm$^{-1}$ [7]). This may not be insignificant compared to the BAr well depth of $95$ cm$^{-1}$. With inclusion of spin-orbit coupling, the electronic states occur in three sets of degenerate pairs and are roots of the $6 \times 6$ Hamiltonian.

$$V(R) = T(\theta, \phi) \; H(R) \; T(\theta, \phi)^T \,, \tag{1}$$

where $H(R)$ is a $6 \times 6$ matrix and $T(\theta, \phi)$ is the product of the two rotations which define the position of the Ar atom. In an uncoupled basis $(l, m_l, s, m_s)$ $H(R)$ contains the spin-orbit constant in both diagonal and some off-diagonal positions and the electrostatic BAr BAr $X^2\Pi$ and $A^2\Sigma^+$ potential curves[8] on the diagonal.

Fig. 1 compares these potential curves with the roots of the $H(R)$ matrix.
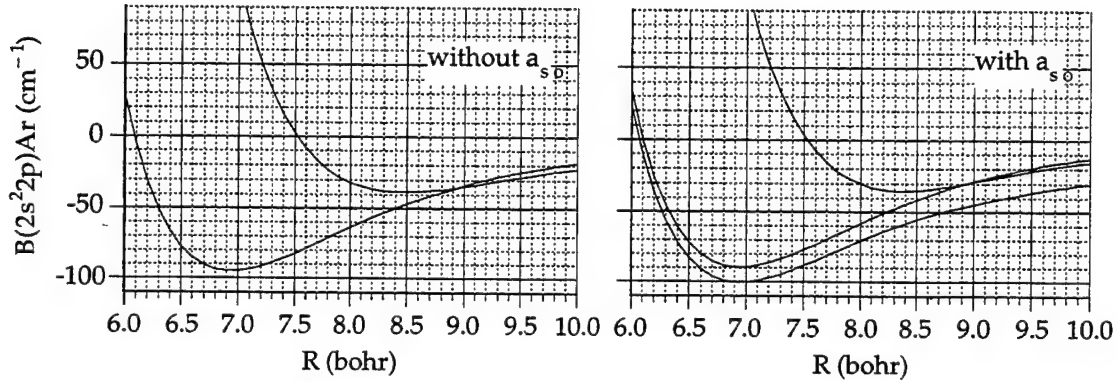


Fig. 1. $B(2s^2 2p)$Ar potential curves. The left panel displays the $X^2\Pi$ and $A^2\Sigma^+$ potential curves from Ref. [8], while the right panel displays the roots of the $H(R)$ matrix [Eq. (1)].

Following Balling and Wright[5] and our earlier paper,[2] we then describe the interaction of $n$ Ar atoms with a single B atom by a $6 \times 6$ Hamiltonian which is a pairwise sum of $n$ $V(R)$ matrices plus the $\frac{1}{2}n(n-1)$ Ar–Ar interactions. The lowest root of this Hamiltonian then defines the potential energy of the $B(Ar)_n$ cluster. This we minimize using our DS-GA.

Although the lowest curve in the right panel of Fig. 1 (with spin-orbit coupling) is lower than that in the left panel (without spin-orbit coupling), the actual binding energy of the dimers are quite similar. Table I (next page) lists the minimum cluster energies, with and without the inclusion of spin-orbit splitting. These are also compared to those we predict using just the $V_\Pi$ potential (lower curve in the left panel of Fig. 1) to describe the BAr interaction. As can be seen in the Table, inclusion of the spin-orbit splitting apparently allows a slightly more attractive interaction. Since the BAr and $Ar_2$ potentials are so similar,[2] this may imply that inclusion of the spin-orbit splitting may allow B to insert more readily into larger $Ar_n$ clusters.

Table I. Minimum energies of B(Ar)$_n$ clusters

| $n$ | without $H_{so}$ | without $H_{so}$; just $V_\Pi$ [a] | with $H_{so}$ |
|---|---|---|---|
| 1 | −96.02 | −96.03 | −101.60 |
| 2 | −289.85 | −289.87 | −301.01 |
| 3 | −532.38 | −581.53 | −592.42 |
| 4 | −828.33 | −879.65 | −896.98 |
| 5 | −1133.85 | −1224.10 | −1240.41 |
| 6 | −1497.48 | −1586.00 | −1613.89 |
| 7 | −1842.96 | −1897.60 | −1930.32 |
| 8 | −2211.61 | −2303.75 | −2333.53 |
| 9 | −2612.33 | −2707.53 | −2659.37 |
| 10 | −3025.89 | −3113.35 | −3135.71 |

a. Ref.[2].

## 3. B(Ar)$_2$ trimer

Stimulated by new work in Dagdigian's laboratory,[1] we are involved in a simulation of the fluorescence spectrum of the B(Ar)$_2$, trimer subsequent to excitation in the vicinity of the atomic $(2s^2 3s \leftarrow 2s^2 2p)$ transition. We use the classical expression for the total absorption cross section, namely[9]

$$\sigma(w) \propto \sim \hbar\omega \int dR |\psi_g(R)|^2 \delta\left[V_e(R) - E_g - \hbar\omega\right] \ . \tag{2}$$

Here $R$ designates, collectively, the 3 internal coordinates of the B(Ar)$_2$ complex, $E_g$ is the energy of the lowest bend-stretch state of the complex in its electronic ground state, and $V_e(R)$ is the excited state PES. Since the electronic transition is localized on the B atom, we take the electronic transition moment to be constant

In our simulation, we are using, initially, the diffusion Monte-Carlo (DMC) technique[10, 11] to determine the energy, and, approximately, the square of the ground state vibrational wavefunction. We[12] (and others) have previously applied, with success, the DMC technique to weakly bound clusters. Since the B($2s^2 3s$) excited state is nondegenerate, the B($2s^2 3s$)Ar$_2$ PES is expressed as a simple pair-wise additive function, involving the B($2s^2 3s$)Ar diatomic potential, which we determined previously, in prior collaborative work with Dagdigian.[8, 13]

## 4. BN$_2$ complexes

In a continuation of our earlier work on the BH$_2$ complex,[12, 14-16] we have initiated the *ab initio* study of the BN$_2$ complex. This work is motivated by LIF investigation of this complex by Dagdigian and co-workers.[1]

Approach of the $N_2$ molecule leads to a mixing of the two electronic states corresponding to the two in-plane orientations of the B $2p$ orbital. We then reverse this mixing to transform the three *adiabatic* states into an electronically *diabatic* representation, defined by the three possible orientations of the $2p$ orbital along $\boldsymbol{R}$. To do so, we use[14, 15] either matrix elements of the electronic orbital angular momentum $\boldsymbol{l}$ or the coefficients in the CI expansion of the wavefunction.

In contrast to the $BH_2$ complex, the minimum energy geometry corresponds to a linear geometry, with $D_e \geq 150$ cm$^{-1}$. The behavior of the two diabatic PES's is illustrated by the following figure.
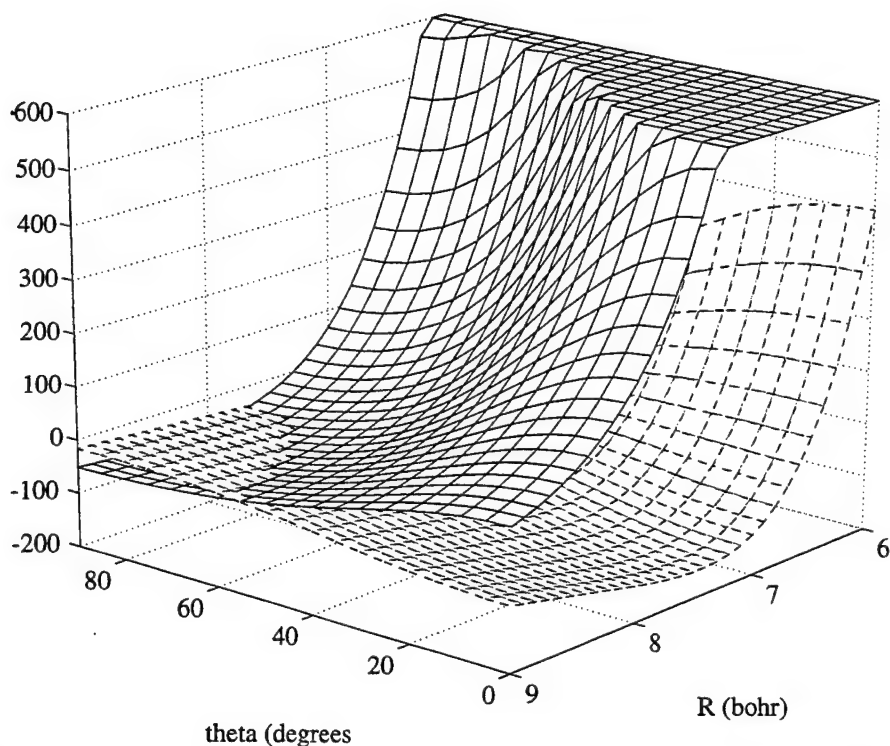


Fig. 2. $B(2s^2 2p)N_2$ electronically diabatic potential energy surfaces (PES, cm$^{-1}$) as a function of the $B \cdots N_2$ distance $R$ and orientation $\theta$. The upper PES (solid lines) corresponds to an orientation of the $2p$ orbital $/\!/$ to $R$, while the lower PES (dashed lines) designates the average of the PES's corresponding to the two possible orientations of the 2p orbital $\perp$ to $R$. A conical intersection occurs in perpendicular geometry at $R \cong 7.5$ bohr.

The description of the excited state of the $BN_2$ complex is more involved. The $B(2s^2 3s)N_2$ state displays a barrier at long range with a substantial minimum farther in. This state is crossed by, and mixes with, a strongly attractive state which corresponds to the $^2\Delta(A')$ component of the $B(2s 2p^2)N_2$ state. The

determination of the excited states PES's is complicated by the large size of the reference space associated with these (and other) electron occupancies.

## 5. Hibridon™ code, version 4

Over the past decade, in collaboration with D. Manolopoulos and H.-J. Werner, we have developed the Hibridon™ package for the investigation of inelastic scattering and photodissociation. This code combines two fast and numerically stable propagation algorithms. Helped by support from AFOSR, we have extended this package to allow the determination of collisional or photo-dissociation fluxes and (in Version 4.1, to be released soon) the determination of bend-stretch levels of weakly-bound complexes. An html-based documentation and help facility is also available.

Hibridon™ 4 is now available for use by the community. More information, as well as instructions for downloading and automatic installation on various platforms (AIX, HPUX, SunOS, Irix, OSF) is available at the Hibridon web site:

http://www-mha.umd.edu/~mha/hibridon

## References

1.   P. J. Dagdigian, E. Hwang, and X. Yang, abstracts *AFOSR HEDM Contractors Conference,* Boulder, CO, 1996, p. .
2.   S. K. Gregurick, M. H. Alexander, and B. Hartke, J. Chem. Phys. **104**, 2684 (1996).
3.   D. E. Goldberg, *Genetic Algorithms in Search, Optimization, and Machine Learning* (Addison-Wesley, Reading, MA, 1989).
4.   J. A. Niesse and H. R. Mayne, J. Chem. Phys. **XX**, yyyy (1996).
5.   L. C. Balling and J. J. Wright, J. Chem. Phys. **79**, 2941 (1983).
6.   J. A. Boatz and M. E. Fajardo, J. Chem. Phys. **101**, 3472 (1994).
7.   C. E. Moore, *Atomic Energy Levels, NSRDS-NBS 35* (U. S. Government Printing Office, Washington, 1971).
8.   E. Hwang, Y.-L. Huang, P. J. Dagdigian, and M. H. Alexander, J. Chem. Phys. **98**, 8484 (1993).
9.   R. Schinke, *Photodissociation Dynamics* (Cambridge University Press, Cambridge, UK, 1992).
10.  J. B. Anderson, J. Chem. Phys. **63**, 1499 (1975).
11.  M. A. Suhm and R. O. Watts, Phys. Repts. **204**, 293 (1991).
12.  A. Vegiri, M. H. Alexander, S. Gregurick, A. McCoy, and R. B. Gerber, J. Chem. Phys. **100**, 2577 (1994).
13.  E. Hwang, P. J. Dagdigian, and M. H. Alexander, Can. J. Chem. **72**, 821 (1994).
14.  M. H. Alexander, J. Chem. Phys. **99**, 6014 (1993).
15.  M. H. Alexander and M. Yang, J. Chem. Phys. **103**, 7956 (1995).
16.  X. Yang, E. Hwang, M. H. Alexander, and P. J. Dagdigian, J. Chem. Phys. **103**, 7966 (1995).

# Cryogenic Solid Combustion

K. L. Pfeil, M. E. DeRose, P. G. Carrick and C. W. Larson
Phillips Laboratory
Edwards AFB, CA 93524-7680

## ABSTRACT

We investigated combustion of solid cryogenic hydrocarbon fuels as models for rockets that would utilize the hybrid geometry. Ported fuel cylinders were prepared, (15.2-cm long, 2.28-cm diameter, 0.95-cm diameter ports, about 52-cm$^3$) by condensation of gaseous and liquid hydrocarbons into a mandrel at 77K. Combustion with gaseous oxygen was carried out in a tube burner at pressures up to 800-psia and oxidizer mass flow rates up to 30-grams per second. The pressure achieved during the burns was selected by variation of the area of a converging sonic nozzle at the discharge end of the burner. In this paper we focus on an analysis of combustion of solid n-pentane.

All the hydrocarbons burned in this work produced soot. In the case of sooty pentane burns, the $c^{*2}$ combustion efficiency indicated that a maximum of 90% of the fuel mixes and combusts to the equilibrium state during a 15-ms residence time of combustion gases within the burner. Oxidizer to fuel ratios (O/F) increased from ~0.5 to ~2 during the 2.5- to 3.5-second burns. Within this range, the calculated equilibrium soot mass fraction from O/F ~ 0.5 to ~ 1.1 drops from ~ 0.45 to zero. Higher pressure produced higher $c^{*2}$ efficiency.

Fuel regression rates (r') were analyzed in terms of a simplified, 1-dimensional contraction of the Marxman-Altman (MA) model. In the MA model r' is independent of pressure and proportional to the 0.8 power of the mass flux in the port, and to the 0.32 power of the mass transfer number, or blowing coefficient. In sooty burns, regression rates appear to be proportional to a higher power of the mass flux in the port. Energy transfer to the fuel surface by radiation from hot, optically thick soot may contribute to this behavior. The regression rate increased slightly with increasing pressure and the pressure effect was stronger at low pressure. The high regression rates of cryogenic solids are a consequence of their high blowing coefficients, which are about twenty times larger than conventional fuels.

## INTRODUCTION

The use of high energy density matter (HEDM) for propulsion promises to improve rocket performance.[1] Difficult engineering problems need to be solved before the quintessential HEDM, solid hydrogen at 4 degrees Kelvin, seeded with up to 8% atomic additive, may become useful. One approach envisions burning cryogenic HEDM in the hybrid rocket configuration. To demonstrate this feasibility, and to further understanding of combustion in hybrid rockets, we carried out laboratory scale experiments to evaluate combustion of cryogenically solidified lightweight hydrocarbons, fuels that are gases or liquids at ambient temperature and pressure.

Compared to conventional hybrid fuels, cryogenic solids are expected to have much faster burning rates because they require ten to twenty times less energy to vaporize into the oxidizer stream. Whereas conventional fuels must be pyrolyzed and vaporized, the cryogenic solids need only be melted and vaporized. If the thermal diffusivities of cryogenic solids are similar to conventional polymer fuels, around 0.001 cm$^2$/sec, then the time scale for melting to a depth where liquefied fuel would slough off would be long compared to the burning rate, thus precluding the loss of the cryogenic solid's integrity and premature melting during burning.

Previously,[2] we used a low pressure tube burner (100 psia) to burn cryogenic (77K) solid ethylene and n-pentane fuel grains and compared burning rates with polymethylmethacrylate (Plexiglas). The cryogenic solids burned fuel rich with considerable sooting. Plexiglas was fully oxidized and its measured burning rate and oxidation efficiency agreed with previous studies. This paper extends our investigation to 800 psia. We focus on a more comprehensive analysis of the combustion of solid n-pentane.

## BACKGROUND

The history of the hybrid rocket was described recently by Altman.[3] Marxman and co-workers,[4] in a series of seminal papers published in the early sixties, described a two-dimensional model in which the instantaneous radial regression rate of the fuel, r'(t,x,r) = dr(t,x)/dt, in the axisymmetric hybrid rocket geometry was:

(1)     $r'(t,x,r) = (0.036/\rho_f) \, [G(t,x,r)]^{0.8} \, (\mu/x)^{0.2} \, B^{0.32}$,     for 5 < B < 100.

In the Marxman-Altman Equation[5], the port mass flux is $G(t,x,r) = [m'_f(t,x,r) + m'_{ox}]/\pi[r(t,x)]^2$. The ratio of the free stream viscosity, $\mu$, to the distance from the fuel's oxidizer entrance port, $x$, has dimensions of mass flux, so the numerical constant is dimensionless. B is the blowing coefficient, $B = \Delta h/h_v$, where $h_v$ is the energy required to pyrolyze and vaporize unit mass of fuel, and $\Delta h$ is the enthalpy difference between a unit mass of fuel and unit mass of the hot, fully oxidized free stream gas. We estimate the blowing coefficient for solid n-pentane to be about 100. Sutton's textbook[6] summarizes this and other approaches for modeling the regression rate.

The "uniform burn" approximation reduces the Marxman-Altman Equation to a 1-dimensional approximation in which r'(t,r) is independent of x, and where the $(\mu/x)^{0.2}$ term is combined with the other constants:

$$(2) \qquad r'(t,r) = a_n \left[ \frac{\frac{1}{2} m'_f(t) + m'_{\infty}}{\pi \{r(t)\}^2} \right]^n .$$

In equation 2, the bracketed quantity is the mass flux in the port at the mid-point ($x = L/2$) of the fuel cylinder, $G_{mid}(t)$. The multiplier, $a_n$, is a property of the fuel, a measured constant having dimensions of (mass flux)$^{1-n}$ per unit density; n is another property of the fuel. Behaviors of fuels with n values of 1/2, 3/4, and 1 are examined below.

Substitution of the mass balance, $m'_f(t) = 2\pi L \rho_f r(t) r'(t,r)$ into equation (2) produces

$$(3) \qquad r'^{\frac{1}{n}} - a_n^{\frac{1}{n}}(\rho_f L)\left[\frac{r'}{r}\right] - a_n^{\frac{1}{n}}(\frac{m'_{\infty}}{\pi})\left[\frac{1}{r^2}\right] = 0 .$$

Solutions to equation (3) beginning at $r_0 = 0.48$-cm and burning for 5-seconds were computed with n = 1/2, 3/4, and 1 for constant $m'_{ox}$ of 5-, 10-, 20-, 40-, and 80-g/s. Boundary conditions embodied in $a_n$ appropriate for pentane, $a_n = [0.2\text{-cm/s}]/[7.5\text{-g/cm}^2 \text{ s}]^n$, and our fuel cylinder length, L = 15.2-cm, were used. Figure 1a shows O/F(t) as a function of the port radius for the 15 cases considered. For the "ideal burn" case where n = 0.5, the fuel burns at constant $m'_f(t)$, so that the O/F(t) ratio is constant throughout the burn. In practice, ideal burns occur in experiments that involve small changes in fuel cylinder port radius, such as large scale experiments with slower burning fuels. Fuels that burn with n = 1/2 may be burned at the optimum constant O/F with constant $m'_{ox}$ over the entire range of change of the port radius. When n = 3/4, O/F(t) increases during the burn and larger $m'_{ox}$ produces larger O/F(t). If n = 1, O/F(t) increases with time, but the fuel burns at the same O/F(t) regardless of $m'_{ox}$. The O/F(t) of the burn depends only on the geometry (L and r) and properties ($a_n$ and $\rho_f$) of the fuel grain. Shorter fuel cylinders produce burns with proportionately higher O/F.

The evaporation flux from the surface of the fuel is $G_f(t) = \rho_f r'(t,r)$. The surface temperature of the evaporating thin film of liquid fuel, $T_S(t)$, may be related to the surface evaporation flux by application of the detailed balance principle to the liquid-vapor equilibrium[7]: $G_f(t) = \rho_{gas} c_{av}/4 = [1/4] [p_v/R_2 T_S(t)] [8kT_S(t)/\pi m]^{1/2}$. The Clausius-Clapeyron[7] equation gives the vapor pressure as a function of temperature: $p_v = p_{v,o} \exp[-h_v/R_1 T_S(t)]$. Thus, $G_f(t) \propto [T_S(t)]^{3/2}\exp[-\text{ constant}/T_s(t)]$, and measurements of $G_f(t)$ may be used to infer an effective instantaneous temperature at the surface of the evaporating fuel. Use of the uniform burn approximation produces the upper limit to $T_s(t)$ because the surface area is the minimum surface area, without consideration of departures from a smooth cylindrical surface. Table 1 summarizes values of computed variables at the midpoint of the burn, after one-half of the fuel has burned, at which point $r(t_{mid}) = 0.88$-cm.

We carried out calculations[8] to determine the properties of equilibrium mixtures produced when solid pentane and gaseous oxygen react at constant enthalpy; results are summarized in Table 2. The total chemical energy release is $\Delta H^o_{equil,0}$, the difference between the standard heat of formation at 0 K of unit mass of reactants and unit mass of equilibrium mixture. The temperature of the equilibrium mixture, $T_{adiab}$, is given by $\Delta H^o_{equil,0} = \int_0^{T_{adiab}} \sum_i C_{p,i}(T)dT$, where the sum is over the i species of the mixture and $C_{p,i}(T)$ is the heat capacity of the ith species. Figure 1b shows equilibrium composition as a function of O/F. Below O/F ~ 1.1, the soot mass fraction, $\Phi_{soot}$, rises to a maximum around 0.5.

Table 1. Calculated quantities at midpoint of the burn[a]

| n | $m'_{ox}$ g/s | $m'_f$ g/s | O/F | $t_b$ s | $t_{mid}$ s | $r'$ cm/s | $T_s$ K |
|---|---|---|---|---|---|---|---|
| 1 | 80 | 94.4 | 0.85 | 0.42 | 0.14 | 1.44 | 239 |
| 1 | 40 | 47.2 | 0.85 | 0.84 | 0.29 | 0.72 | 229 |
| 1 | 20 | 23.6 | 0.85 | 1.67 | 0.58 | 0.36 | 221 |
| 1 | 10 | 11.8 | 0.85 | 3.34 | 1.17 | 0.18 | 213 |
| 1 | 5 | 5.9 | 0.85 | 6.68 | 2.34 | 0.09 | 205 |
| .75 | 80 | 50.5 | 1.58 | 0.80 | 0.35 | 0.76 | 230 |
| .75 | 40 | 31.2 | 1.28 | 1.29 | 0.57 | 0.47 | 224 |
| .75 | 20 | 19.5 | 1.03 | 2.06 | 0.90 | 0.29 | 219 |
| .75 | 10 | 12.3 | 0.81 | 3.25 | 1.41 | 0.18 | 213 |
| .75 | 5 | 7.9 | 0.63 | 5.10 | 2.17 | 0.12 | 208 |
| .5 | 80 | 30.8 | 2.60 | 1.33 | 0.67 | 0.46 | 224 |
| .5 | 40 | 22.6 | 1.77 | 1.82 | 0.91 | 0.34 | 220 |
| .5 | 20 | 16.8 | 1.19 | 2.44 | 1.22 | 0.25 | 217 |
| .5 | 10 | 12.7 | 0.79 | 3.22 | 1.61 | 0.19 | 214 |
| .5 | 5 | 9.9 | 0.50 | 4.12 | 2.06 | 0.15 | 211 |

(a)  $r_o$ = 0.48-cm, $r_{max}$ = 1.14-cm, L = 15-cm, $\rho_f$ = 0.85 g/cm$^3$,
$a_n$ = [(0.2 cm/s)/(7.5 g/cm$^2$/s)]$^n$.

Table 2. Properties of equilibrium oxygen/pentane mixtures, P = 500 psia[a]

| (O/F) | $c^*$ m/s | $T_{adiab}$ K | $M_{mole}$ g/mole | $\Delta H^o_{equil,0}$ kJ/Kg | $\Delta H^o_{equil,0}/c^{*2}$ | $\Phi_{soot}$ |
|---|---|---|---|---|---|---|
| 0.2 | 967 | 953 | 21.11 | 505 | 2.26 | 0.465 |
| 0.3 | 1060 | 1052 | 19.38 | 577 | 2.15 | 0.490 |
| 0.4 | 1132 | 1123 | 18.09 | 618 | 2.02 | 0.472 |
| 0.5 | 1189 | 1177 | 17.12 | 644 | 1.91 | 0.430 |
| 0.6 | 1236 | 1224 | 16.38 | 661 | 1.81 | 0.372 |
| 0.7 | 1277 | 1269 | 15.80 | 675 | 1.73 | 0.304 |
| 0.8 | 1312 | 1312 | 15.35 | 686 | 1.67 | 0.231 |
| 0.9 | 1345 | 1358 | 14.99 | 698 | 1.62 | 0.156 |
| 1.0 | 1375 | 1409 | 14.71 | 712 | 1.57 | 0.079 |
| 1.1 | 1404 | 1465 | 14.50 | 729 | 1.55 | 0.002 |
| 1.2 | 1442 | 1596 | 14.52 | 789 | 1.59 | 0 |
| 1.3 | 1512 | 1844 | 15.09 | 904 | 1.66 | 0 |
| 1.4 | 1583 | 2092 | 15.74 | 1017 | 1.70 | 0 |
| 1.5 | 1642 | 2324 | 16.38 | 1119 | 1.74 | 0 |
| 2.0 | 1808 | 3171 | 19.35 | 1453 | 1.86 | 0 |
| 2.5 | 1829 | 3513 | 21.56 | 1527 | 1.91 | 0 |
| 3.0 | 1792 | 3591 | 23.13 | 1485 | 1.94 | 0 |
| 3.5 | 1747 | 3586 | 24.36 | 1419 | 1.95 | 0 |

(a) reactants are gaseous oxygen at 298 K and solid n-pentane at 77 K,
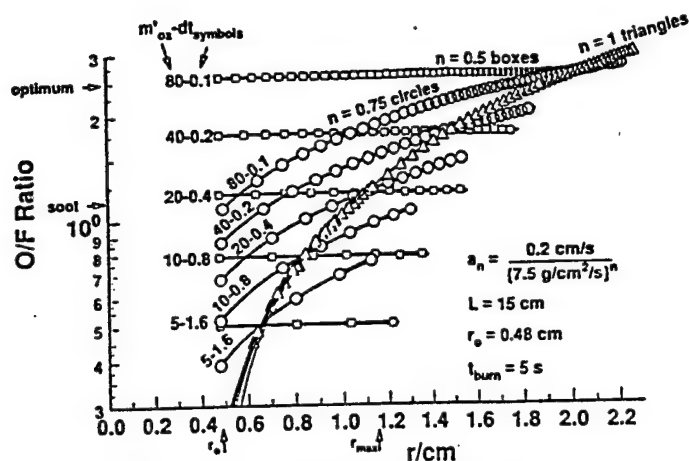$\Delta H^o_{f298}$ = - 242 kJ/mole

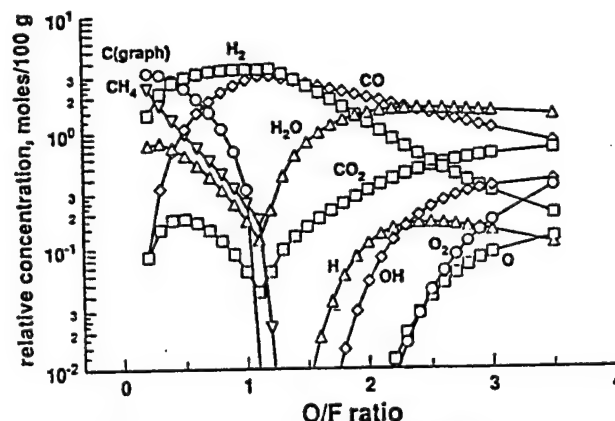Figure 1a. Calculated O/F vs r for 5-second burns.

Figure 1b. Equilibrium composition at 500 psia.

## EXPERIMENTAL - TUBE BURNER

Previously,[2] we described an axisymmetric laboratory scale experiment to measure the overall average burning properties of conventional and cryogenic solid hybrid rocket fuel. The current tube burner has about one-third the head space, and produced smooth burns compared to the noisy burns and low frequency instabilities of the previous burner. It was fabricated from 0.049-inch wall stainless steel tube, 14.3-inches long, 1-inch outside diameter.

Burner chamber pressure, $P_c(t)$, was measured during combustion of a solid n-pentane fuel cylinder of known mass and dimensions ($V_f$ = 51.8-cm³, L = 15.2-cm, initial port radius $r_o$ = 0.48-cm, outside radius $r_{max}$ = 1.14 cm, density of solid n-pentane $\rho_f$ = 0.85 ± 0.02-g/cm³, $m_{f,total}$ = 42.9-g) with a constant oxidizer mass flowrate ($m'_{ox}$ ~ 10 or 20 g/s) in a tube burner with a converging sonic nozzle of area, $A_n$. $P_c(t)$ was measured at 100 Hertz to ± 1% with a diaphragm pressure transducer that had a frequency response around 300 Hertz.

Two nozzles, with 59-degree converging half-angles, were used: $A_n$ = 0.100±0.001 and 0.206±0.002-cm². The oxidizer mass flow rate was metered with one of two sonic chokes that had throat diameters of 0.0696 ± 0.0002-inch and 0.0466 ± 0.0002-inch. At 1000-psia upstream pressure they metered ~ 44- or ~20-g/s of oxygen.

Temperatures were measured with type K thermocouples (TC) that were clamped to the outside of the tube at three locations: TC1 measured temperature about 3-cm above the nozzle, TC2 measured temperature 3-cm above the fuel grain bottom, and TC3 measured temperature 3-cm below the fuel grain top.

No effort was made to condition the oxidizer flowfield prior to entering the fuel grain port. The tube burner's head space was minimized to enable a good close-up, "down the tube" views of the fuel grain through a window mounted 10-cm above the top of the fuel grain. Oxygen entered the combustion chamber at room temperature through a 0.95-cm diameter tube, at right angles to the combustion tube, 5-cm above the top of the fuel grain. Tangential injection that would impart swirl to the oxidizer flow was avoided as much as possible. At $m'_{ox}$ of 10-g/s, the Reynolds number was 650,000 at the top of the fuel grain, based on the tube burner diameter of 2.24-cm and room temperature oxygen.

Video recordings (30-frames per second) of the burning fuel surface were acquired from two angles, a straight down the tube view, and a high oblique view to enhance perspective. Occasionally, high speed video was acquired at 1000- to 3000-frames per second from the high oblique view. By reviewing this data, it was possible to obtain an estimate of the fuel fraction burned as a function of time to within about ± 20%. Close up video of the exhaust plume and a wide angle view of the apparatus were also acquired.

A vacuum Dewar was fabricated around the tube burner that enabled a 15-cm length of tube to be maintained at 77K. A polycrystalline solid n-pentane fuel cylinder was produced using a mandrel to shape the centerline port. The Dewar was filled with liquid nitrogen at the rate of about 0.5-cm per minute. Liquid n-pentane was measured into the mandrel with a calibrated long-needle syringe where it froze simultaneously with the raising of the liquid nitrogen. About 69±2-cm³ of liquid n-pentane condensed into a 52-cm³ solid.

The fuel was ignited by a small methane/oxygen torch (0.015-cm diameter) and a staged increase of oxygen flow to the final $m'_{ox}$ of the experiment. The microtorch contributed enough energy to melt and vaporize a small amount of fuel, which mixed with the initial slow flow of oxygen (0.02-g/sec) and provided a smooth "soft" start to the

burning of the fuel. After about 1-second of slow oxygen, the main oxygen valve was opened. The time required to reach steady $m'_{ox}$ was about 70-ms.

## RESULTS AND DISCUSSION

Table 3 summarizes values of the fixed experimental variables of a 4-burn test matrix with pentane. The maximum chamber pressure of the burn, $P_{c,max}$, and the chamber pressure at the end of the burn, $P_{c,cold}$, are also listed. The measured discharge coefficient with room temperature oxygen was $C_D = 0.90$ for both nozzles. $P_{ambient} = 13.2$ psia.

Table 3. Pentane test matrix.

| RUN | $m'_{ox}$ g/s | $A_n$ cm$^2$ | $P_{c,max}$ psia | $P_{c,cold}$ psia |
|-----|------|-------|--------|--------|
| 100 | 11.8 | 0.206 | ~200 | 37.1 |
| 101 | 22.6 | 0.206 | ~400 | 67.7 |
| 102 | 10.5 | 0.100 | ~400 | 66.9 |
| 103 | 19.0 | 0.100 | ~800 | 121 |

Figure 2 shows the $P_c(t)$ data. The pressure ratio, $P_c(t)/P_{ambient}$, is plotted in figure 2a. In figure 2b, a reduced parameter is plotted, the apparent c* of the burn, defined by

$$(4) \qquad c^*_{app}(t) = P_c(t)\left[\frac{A_n C_D}{m'_{ox}}\right],$$

which is independent of any knowledge about the fuel. $C^*_{app}(t)$ is a hypothetical quantity that describes the performance of tube burner combustion as if only energy, not energy plus mass, were added to the input oxidizer. The $c^*_{app}(t)$ summarized by figure 2b show that pressure does not influence burning rate. Runs 100 and 102 ($m'_{ox} \sim 10$-g/s) had about same burning rate although the pressure differed by a factor of two; the same finding applies to runs 101 and 103 ($m'_{ox} \sim 20$-g/s). However, within each pair of burns, $c^*_{app}(t)$ is slightly larger for the higher pressure burns. At the end of the burns $c^*_{app}(t) \sim 420$-m/s, near the room temperature value for oxygen, 406-m/s at 298K. After all fuel is burned, significant cooling of oxygen takes place in the 15-cm cold section of tube, to about 255K. Before discharge, the cold gas is reheated by the hot nozzle/tube assembly to slightly above room temperature. The actual experimental c* of the burn may be determined if the mass flow rate of fuel, $m'_f(t)$, is available:

$$(5) \qquad c^*_{exp}(t) = c^*_{app}(t)\left[\frac{m'_{ox}}{m'_f(t) + m'_{ox}}\right].$$
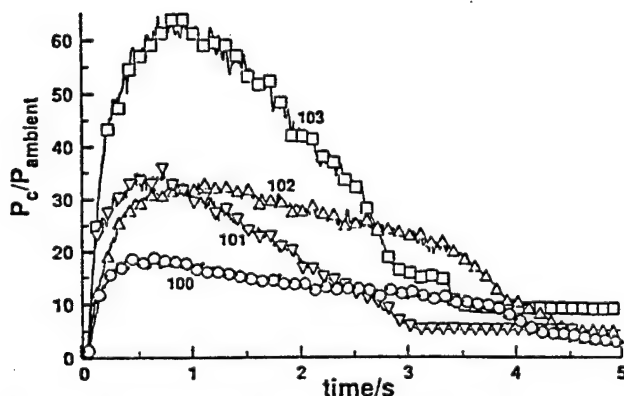


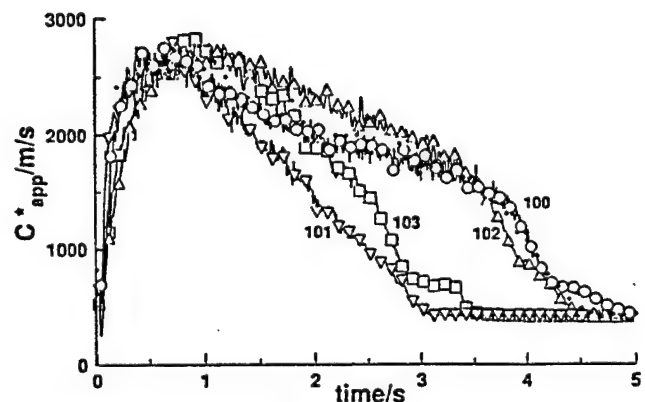Figure 2a. Experimental chamber pressure traces,.



Figure 2b. Experimental c*$_{app}$ vs time.

90

The excess chamber pressure is $P_{ex}(t) = P_c(t) - P_{c,cold}$, where $P_{c,cold}$ is the chamber pressure maintained at the end of the burn when only oxygen flows. Excess pressure is produced only when fuel flows, which suggests that $P_c(t)$ itself may be codified into a metric of $m'_f(t)$. If $m'_f(t) \propto [P_{ex}(t)]^m$, then

$$(6) \qquad m'_f(t)/m_{f,total} = N^{-1}[P_{ex}(t)]^m, \text{ where } N = \int_0^{t_b}[P_{ex}(t)]^m dt.$$

Figure 3a shows $m'_f(t)$ calculated with m = 1 to 2 in increments of 0.2 for run 100. Experimental noise is suppressed by plotting the 0.1 second running average of $m'_f(t)$. Use of m = 1 provides equal weighting for the excess pressure produced per unit $m'_f(t)$, which is reasonable for clean burning fuel at constant O/F. A value of m > 1 assigns greater weight to $P_{ex}(t)$ during the early times of the burn where $P_{ex}(t)$ is largest. If O/F increases during the burn and improves combustion efficiency, then more excess pressure would be produced by unit $m'_f(t)$ later in the burn, and use of m > 1 would be appropriate.

In sooty burns, only the gaseous combustion products contribute to $P_{ex}(t)$. If the soot fraction is $\Phi_{soot}(t) = m'_{f,soot}(t)/m'_f(t)$, where $m'_{f,soot}(t)$ is the mass flowrate of fuel that produces soot, then $m'_f(t)$ could be determined from

$$(7) \qquad m'_f(t)/m_{f,total} = N^{-1}\frac{P_{ex}(t)}{1 - \Phi_{soot}(t)}, \quad \text{where} \quad N = \int_0^{t_b}\frac{P_{ex}(t)}{1 - \Phi_{soot}(t)}dt.$$

The equilibrium soot mass fraction over the range 0.5 < O/F < 1.1 (Table 2) may be represented by:

$$(8) \qquad \Phi_{soot,equil}(O/F) = 0.825 - 0.75 \, O/F.$$

To determine $m'_f(t)$ in the current pentane test matrix, we iterated equation (7) with equation (8), beginning with $\Phi_{soot}(t) = 0$ in equation (7). Equation (8) made use of $m'_f(t)$ from the first iteration to generate $\Phi_{soot,equil}(t)$ for use in the second iteration of equation (7). The process converged to unchanging $m'_f(t)$ after about six iterations.

Figure 3b shows results of each iteration applied to run 100. Use of equation (6) with m = 2 produces $m'_f(t)$ similar to the sixth iteration with equilibrium soot. As the number of iterations increases, more fuel mass becomes assigned to the beginning of the burns where the O/F is lowest and the soot fractions are highest. In figure 3b noise is suppressed by plotting the 0.1 second running average of $m'_f(t)$. Whereas noise in the original $P_c(t)$ signal is greatly magnified as the number of iterations with soot increases, noise generated by equation (6) increases only slightly as m increases. The $m'_f(t)$ from the sixth soot iteration, which is an upper limit of $m'_f(t)$ based on attainment of equilibrium, is used in subsequent analysis.
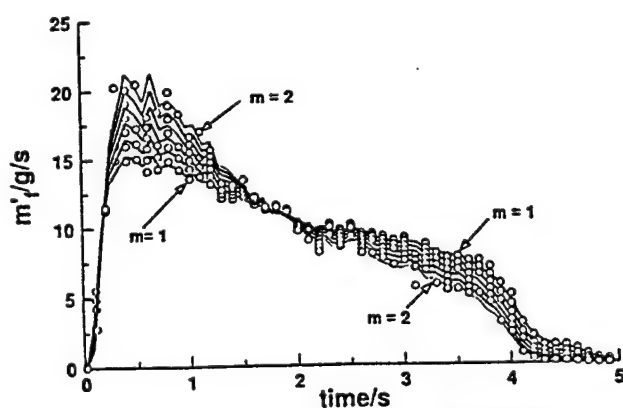


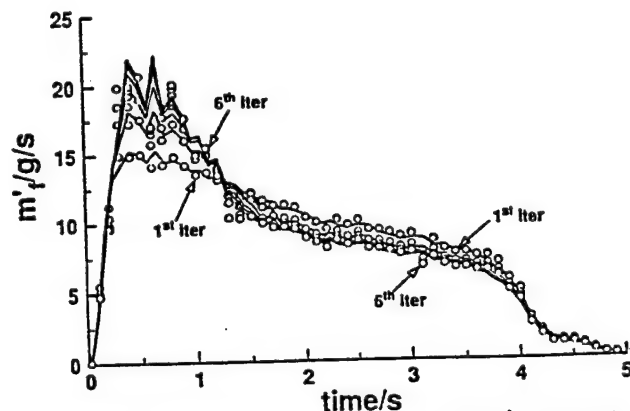Figure 3a. Run 100 $m'_f$ from $P_{ex}^m$, 0.1 s running average.



Figure 3b. $m'_f$ from Iteration with soot, 0.1 s running average.

Figure 4 shows O/F(t) as a function of r(t). Comparison with calculated results shown in figure 1 suggests that n for pentane is less than 1 because O/F increases with increasing $m'_{ox}$. The regression rate, $r'(t,r)$, may be calculated from $r(t) = [F_f(t) \, V_{f,total}/\pi L + r_o^2]^{1/2}$, where $V_{f,total}$ is the initial volume of the fuel, and where $F_f(t)$ is the fraction of the fuel burned: $F_f(t) = 1/m_{f,total} \int_0^t m'_f(t)dt$. Figure 5 shows $r'(t,r)$ as a function of $G_{mid}(t)$ for each burn of the current test matrix. To simplify the figure, only the data from the middle third of the burn are plotted. The figure shows that higher pressure produces slightly higher regression rate and that the effect is more pronounced at lower pressure. Model $r'(t,r)$ from equation (3) are also shown for a burn at $m'_{ox} = 20$-g/s for $n = 1/2$, 3/4, and 1. The data indicate that n for pentane is around 0.9 to 1.
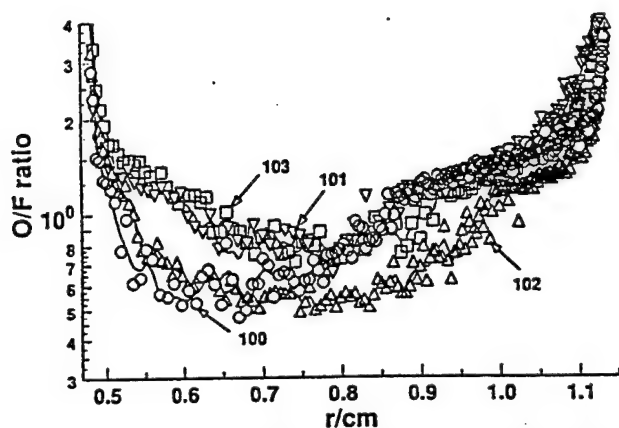


Figure 4. Experimental O/F vs r, symbols at 0.02 second intervals.


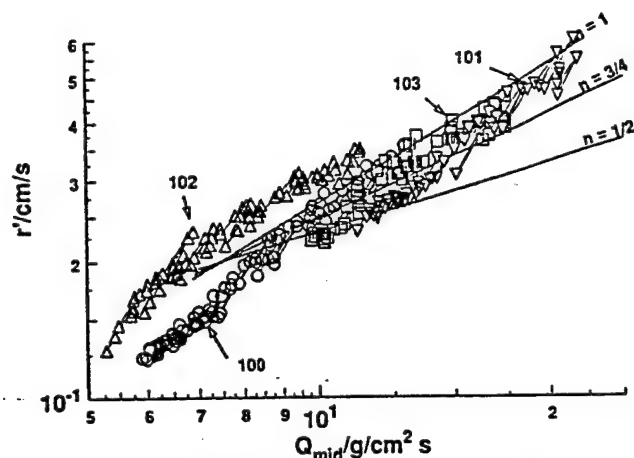
Figure 5. Experimental r' vs Q_mid from middle third of burns.

The sonic nozzle approximation, equations (4) and (5), enables computation of $c^*_{exp}(t)$. Departures from the approximation are quantified by an overall discharge coefficient, $C_D < 1$. The measured overall $C_D$ with room temperature oxygen were around 0.90. As described in detail by Zucrow and Hoffman[9], the failure of the 1-dimensional aspect of the approximation causes the sonic plane to bulge out beyond the nozzle geometric exit plane, and $C_D$ becomes pressure dependent up to $P_c(t)/P_{ambient} \sim 6$. Figure 2a shows $P_c(t)/P_{ambient} > 10$ during the time when more than 90% of the fuel was burned; therefore we carried out this analysis with use of $C_D$ independent of $P_c(t)$ and temperature.

Figure 6 shows $c^*_{exp}(t)$ as a function of the O/F(t) ratio, and compares these results to the $c^*_{equil}(O/F)$ from the equilibrium calculation. Cancellation of noise in figure 6 occurs because the single noisy signal [$P_c(t)$] appears in both numerator and denominator of $c^*_{exp}(t)$ and because the variables plotted contain the same noise, exactly synchronized in time. The figure shows that higher pressure burns have slightly higher $c^*_{exp}(t)$.

Energy loss to the apparatus, $H_{loss}$, occurred from heating the lower 13-cm of the burner tube (92 grams of stainless steel) and nozzle assembly (188 grams); the loss was measured by temperature rise of TC1, which generally rose a few hundred degrees centigrade and closely tracked the combustion process.

$$(9) \qquad H_{loss} = \int_0^{t_b} \left[ C_P \cdot m_{app} \cdot \frac{dT(t)}{dt} \right] dt,$$

where $m_{app}$ is the mass of the apparatus that undergoes temperature rise $dT(t)/dt$. The heat capacity, $C_p$, of the stainless steel heat sink is about 0.51 J/g/C. Table 4 summarizes quantities of interest in the current test matrix. $H_{loss}$ for the two runs with $m'_{ox} \sim 10$ g/s was about 40 kJ, and for the two runs with $m'_{ox} \sim 20$ g/s was about 50 kJ.

A hypothetical c* that would have been realized from an adiabatic burn with no losses, $c^*_{adiab}(t)$, may be computed. The adiabatic chemical enthalpy release of the burn of the burn is $H^o_{adiab,0} = H_{loss} + H^o_{exp,0}$, where

$$(10) \quad H^{o}_{exp,0} = \int_{0}^{t_b} \{[m'_f(t) + m'_{ox}] \, \Delta H^{o}_{exp,0}(t) - m'_{ox} (H^{o}_{298} - H^{o}_{0})_{ox}\} dt,$$

In equation (10), $\Delta H^{o}_{exp,0}(t)$ is the apparent experimental standard enthalpy change between unit mass of reactants and unit mass of the combustion mixture at 0 K, and $(H^{o}_{298} - H^{o}_{0})_{ox}$ is the enthalpy content of room temperature oxygen at 298K.

The equilibrium characteristic velocity is related to $\Delta H^{o}_{equil,0}$, the difference between the standard enthalpy of formation of unit mass of reactants and unit mass of equilibrium mixture at 0 degrees Kelvin: $\Delta H^{o}_{equil,0} = k_{equil}(c^*_{equil})^2$. The equilibrium calculation (Table 2) revealed that $k_{equil} = 1.7 \pm 0.2$ over the O/F range from 0.5 to 3.5.

If the experimental combustion mixture is approximated to be a two component mixture, i.e., unmixed and unreacted reactants, and fully mixed and equilibrated reactants, and if the mixed and unmixed mass have the same O/F ratio, then $\Delta H^{o}_{exp,0}(t) \approx k_{exp} [c^*_{exp}(t)]^2$, $\Delta H^{o}_{adiab,0}(t) \approx k_{adiab} [c^*_{adiab}(t)]^2$, $k_{exp} \approx k_{adiab} \approx k_{equil}$ and

$$(11) \quad c^*_{adiab}(t) \approx c^*_{exp}(t) \left[1 + \frac{H_{loss}}{H^{o}_{exp,0}}\right]^{\frac{1}{2}}.$$

Figure 7 compares $H_{loss}(t)$ to $H^{o}_{exp,0}(t)$, where the accumulated energy quantities at time $t$ were computed from equations (9) and (10) with use of $t$ as the upper limit in the integral. Table 4 shows that $H^{o}_{exp,0}$ for the two runs with $m'_{ox} \sim 10$ g/s was about 150 kJ, and for the two runs with $m'_{ox} \sim 20$ g/s was about 210 kJ. Table 4 lists average properties of the burns in the current test matrix. Variables were averaged over the middle third of the burned fuel mass, i.e., between $F_f(t_{1/3})$ and $F_f(t_{2/3})$: $Y_{average} = \frac{1}{m_{f,total}} \int_{t_{1/3}}^{t_{2/3}} Y(t) m'_f(t) dt$. The average $c^*_{adiab} \approx 1.11 \, c^*_{exp}$, and the overall average combustion efficiency, $\eta = H^{o}_{adiab,0}/\Delta H^{o}_{equil,0} = (c^*_{adiab}/c^*_{equil})^2$ ranges from 0.67 to 0.87.
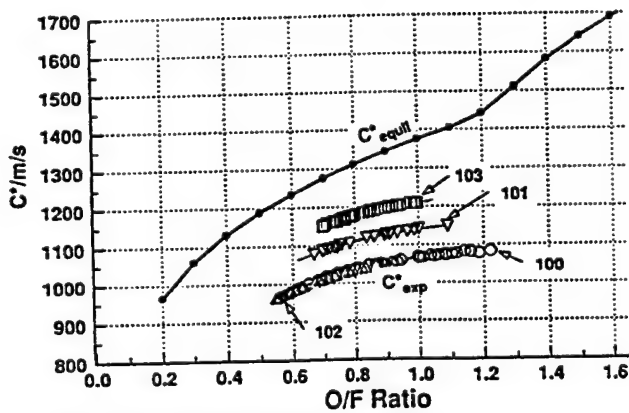


Figure 6. Comparison of $c^*_{exp}$ to $c^*_{equil}$.
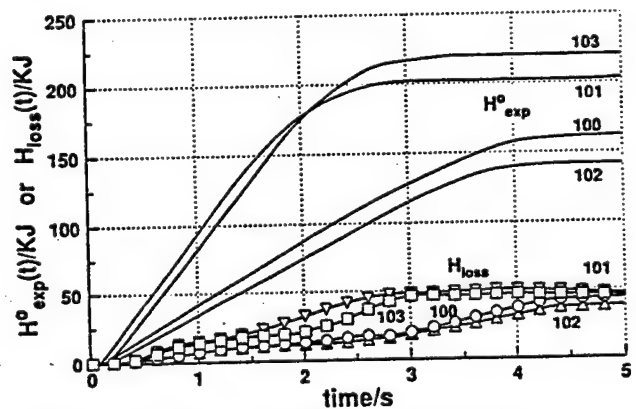


Figure 7. Experimental energies and energy losses.

Table 4 - Burn parameters of pentane 4-test matrix

| RUN | $H_{loss}$ KJ | $H^{o}_{exp}$ KJ | ave $c^*_{exp}$ m/s | ave $\eta$ | ave $\tau_{res}$ ms | ave V' cm³/s | ave x'$_{port}$ m/s |
|---|---|---|---|---|---|---|---|
| 100 | 44 | 162 | 1060 | 0.67 | 6.7 | 8200 | 43 |
| 101 | 51 | 202 | 1150 | 0.76 | 5.9 | 9300 | 39 |
| 102 | 38 | 142 | 1020 | 0.78 | 13.7 | 4000 | 16 |
| 103 | 46 | 220 | 1210 | 0.87 | 11.5 | 4800 | 20 |

93

The volumetric flowrate in the post combustion chamber is $V'(t) = [R_2/P_c(t)] [T_c(t)/M_{mole}(t)] [m'_f(t)+m'_{ox}]$, and for the calorically ideal gas (heat capacity independent of temperature), the second term in brackets may be deduced from $c^*_{exp}(t) = \{\gamma[2/(\gamma+1)]^{(\gamma+1)/(\gamma-1)}\}^{-1/2} [R_1 T_c(t)/M_{mole}(t)]^{1/2}$. Use of $\gamma = 1.3$ enabled estimation of the average residence time in the post combustion chamber of volume $V_{post} = 55$ cm$^3$: $\tau_{res}(t) = V_{post}/V'(t)$. The average gas velocity in the bottom of the port, $x'_{port}(t)$ based on $V'(t)$ from above is also tabulated.

## CONCLUSIONS

High speed video at 3000-frames per second revealed coherent luminous structures, flamelets, within the turbulent flow with lifetimes of several milliseconds during the end of the burns. During intense burning coherent structures in the port were poorly resolved. Residence times in the post combustion chamber were $\tau_{res} \sim 10$ ms and in the fuel port were smaller. Thus, it appears that mixing is more complete during intense burning than at the end of the burn. We estimate the Damköhler number, $\tau_{res}/\tau_{kinetics}$, to be at least 100, which would indicate that the efficiency of the tube burner is limited by incomplete mixing and not by chemical kinetics. This conclusion is consistent with the higher combustion efficiencies measured in higher pressure burns where residence times are longer.

Video recordings showed that the top edge of the fuel grain was preserved throughout the burns. Also, more than 90% of the fuel mass burned before the grain burned to the wall, thus validating the uniform burn approximation. Video showed that the surface of the fuel was not smooth after partial burns and that the area of the evaporating fuel surface is larger than given in the uniform burn approximation, so the $T_s$ summarized in Table 1 are higher than the actual $T_s$

Extrapolation to higher $m'_{ox}$ with figure 1 shows that more than 80 g/s oxidizer would be required to reach the optimum O/F ratio for pentane of around 2.4 (Table 2) with the current fuel geometry and burner. Burn times would be less than 500 ms, shorter than burner fill times, 0.5- to 1-second, so interpretation of experimental data would be complicated. However, experiments with smaller L/D would enable burns with proportionately higher O/F.

## LIST OF SYMBOLS, DEFINITIONS

| | |
|---|---|
| $r'(t)$ | instantaneous radial regression rate, cm/s |
| $r(t)$ | instantaneous fuel cylinder center port radius, cm |
| $\rho_f$ | density of the solid fuel, g/cm$^3$. $\rho_{solid\,pentane}$ at 77 K $\sim 0.85 \pm 0.02$ g/cm$^3$. |
| $G(t,x,r)$ | instantaneous mass flux in Marxman-Altman equation, g/cm$^2$/s |
| $\mu$ | free stream viscosity of combustion gases in port in Marxman-Altman equation, g/cm/s |
| $x$ | distance from oxidizer entrance port in Marxman-Altman equation, cm |
| $B$ | blowing coefficient in Marxman-Altman equation |
| $C_f$ | skin friction coefficient |
| $\Delta h$ | enthalpy difference between unit mass of solid fuel and unit mass of hot, free stream gas, J/g |
| $h_v$ | specific energy required to pyrolyze and/or vaporize fuel per unit mass, J/g |
| $m'_f(t)$ | instantaneous fuel mass flow rate, g/s |
| $m'_{ox}$ | mass flow rate of gaseous oxygen, g/s |
| $t_b$ | total burn time to $m'_f(t) = 0$, s |
| $m_{f,total}$ | total mass of fuel grain, g |
| $F_f(t)$ | fraction of fuel burned at time t, dimensionless |
| $a_n$ | empirical constant in contracted MA equation, dimensions (mass flux)$^{1-n}$ per unit density |
| $G_{mid}(t)$ | instantaneous mass flux in fuel port at the mid-point of the fuel cylinder, g/cm$^2$/s |
| $G_f(t)$ | instantaneous mass flux of fuel from fuel surface, g/cm$^2$/s |
| $A_f(t)$ | instantaneous area of evaporating fuel surface, cm$^2$ |
| $T_s(t)$ | instantaneous temperature of the evaporating liquid fuel surface, K |
| $\rho_{gas}$ | density of vapor in equilibrium with liquid at $T_s$, g/cm$^3$ |
| $c_{av}$ | average velocity of Maxwellian gas, cm/s |
| $m$ | molecular mass, g/molecule |
| $k$ | Boltzman constant, $1.38 \times 10^{-16}$ erg/K/molecule |
| $p_v$ | vapor pressure, atm |
| $R_1$ | universal gas constant in thermal energy units, 8.31 J/K/mole |
| $R_2$ | universal gas constant in mechanical energy units, 82.05 cm$^3$ atm/K/mole |

$P_{ambient}$ ambient pressure, 13.2 psia
$O/F(t)$ instantaneous oxidizer to fuel mass ratio
$L$ length of fuel cylinder, 15.2 cm
$V_{tube}$ volume of tube burner, 152 cm³
$r_{max}$ radius of combustion chamber (tube burner), 1.14 cm
$r_0$ initial radius of fuel cylinder port, 0.48 cm
$P_c(t)$ instantaneous combustion chamber pressure, psia
$P_{ex}(t)$ instantaneous excess pressure, psia
$P_{cold}(t)$ chamber pressure at end of burn, psia
$T_c(t)$ instantaneous combustion chamber temperature, K
$M_{mole}(t)$ instantaneous mole fraction weighted average molecular weight of combustion gases, g/mole
$A_n$ area of nozzle, $0.100 \pm 0.001$, or $0.206 \pm 0.002$ cm²
$c^*_{exp}(t)$ instantaneous experimental characteristic velocity of exhaust gasses, m/s
$c^*_{app}(t)$ instantaneous apparent characteristic velocity of exhaust gasses, m/s
$c^*_{adiab}(t)$ instantaneous adiabatic characteristic velocity of exhaust gasses, m/s
$c^*_{equil}(t)$ instantaneous equilibrium characteristic velocity of exhaust gasses, m/s
$\gamma$ heat capacity ratio, $C_p/C_v$
$C_D$ nozzle discharge coefficient, dimensionless
$H_{loss}$ total energy loss to apparatus, kJ
$H^{\circ}_{exp,0}$ total experimental chemical energy release within tube burner referenced to 0 K, kJ
$H^{\circ}_{adiab,0}$ total adiabatic chemical energy release within tube burner referenced to 0 K, kJ
$\Delta H^{\circ}_{equil,0}$ standard enthalpy difference at 0 K between unit mass of reactants and unit mass of equilibrium mixture

## REFERENCES

1. Carrick, P. G., "Theoretical Performance of High Energy Density Cryogenic Solid Rocket Propellants", AIAA 31st Joint Propulsion Conference, July 1995, San Diego, CA; and USAF Technical Report PL-TR-93-3014.

2. Carrick, P. G., and Larson, C. W., "Lab Scale Test and Evaluation of Cryogenic Fuel Grains," AIAA 31st Joint Propulsion Conference, July 1995, San Diego, CA, Paper No. AIAA 95-2948.

3. Altman, D., "Hybrid Rocket Development History," AIAA/SAE/ASME/ASEE 27th Joint Propulsion Conference, June 24-26, 1991, Sacramento, CA, Paper AIAA 91-2515, American Institute of Aeronautics and Astronautics.

4. Marxman, G. A., "Boundary Layer Combustion in Propulsion," 11th International Symposium on Combustion, The Combustion Institute, August 1966, p. 269.

5. Recently, D. Altman stated, during discussion following presentation of Ref 2, that the exponent of B had been recalculated from a least squares fit to original data and found to be 0.32, not 0.23 as published throughout the literature.

6. Sutton, G. P., "Rocket Propulsion Elements," Sixth Edition, (John Wiley, New York, ©1992) Chapter 15.

7. Moelwyn-Hughes, E. A., "Physical Chemistry," The Macmillan Company, New York, ©1961.

8. Selph, C., et. al., "Phillips Laboratory Isp Code", 1963.

9. Zucrow, M. J., and Hoffman, J. D., "Gas Dynamics," Volume 1, (John Wiley, New York, ©1977), p 277ff. ; and Welty, J.R., Wicks, C.E., and Wilson, R.E., "Fundamentals of Momentum, Heat, and Mass Transfer," (John Wiley, New York, ©1969), Chapter 11.

# GENERATION OF ENERGETIC SPECIES IN SOLID OXYGEN WITH TUNABLE ULTRAVIOLET LIGHT

Richard A. Copeland, Christian G. Bressler, and Mark J. Dyer
Molecular Physics Laboratory, SRI International, Menlo Park, California 94025

## INTRODUCTION

"Energized" cryogenic solids are being considered as the next generation rocket fuels that may enhance rocket performance. Storing reactive atoms and molecules in a solid fuel, composed of either hydrogen or oxygen, is one method of increasing the available energy in the propellant. At SRI International, we are investigating this process of "energizing" solid oxygen with tunable ultraviolet laser light. We generate $O_x$ species that have more available chemical energy than $O_2$ itself, and trap them in the cryogenic solid. The production photophysics, relative concentration, stability, and identity of these species are examined in order to evaluate their potential as high energy materials and performance enhancers.

## EXPERIMENTAL APPROACH

SRI has set up a new cryogenic facility for the growth and spectroscopic investigation of macroscopic (5x5x5 mm$^3$) oxygen crystals. Details of this setup are described in last year's extended abstract [1]. We have grown optically clear bulk $O_2$ samples for investigation. In the course of earlier work, fluorescence and Raman measurements have been successfully undertaken on liquid and solid oxygen bulk samples [1]. This compact setup has been recently upgraded to allow growth of thin matrices of solid oxygen. The technique is widely utilized in matrix isolation spectroscopy [2] and proves to be an experimentally convenient method to study photochemical reactions in solids. This abstract will focus on our recent matrix work.

At the SRI cryogenic facility we use a gold-coated Cu-block (10 mm diameter), thermally connected with indium to the cooling finger on the second stage of the closed-cycle He refrigerator, as the substrate. A Cr/Au thermocouple mounted on the second stage measures the temperature of the sample and a heater/controller stabilizes the temperature anywhere between 10 and 300 K. The base pressure of the chamber is in the $10^{-8}$ mbar range. Oxygen is sprayed onto the substrate using a sensitive needle valve to control the flow. Isotopic mixtures and layered "sandwiches" of $^{16}O_2$ and $^{18}O_2$ are also investigated. Deposition rates can be estimated through the amount of gas admitted into the chamber. Typically, we use a flow rate of 3.5 mmol/h for 20 min. From our past experience, we estimate the thickness of the oxygen matrices to be ~ 10 μm. Apparatus improvements are underway to measure the thickness directly [3]. After deposition and prior to irradiation the matrix is annealed to 30 K in order to reduce the number of defect sites. The defect site density is considerably larger than for the case of macroscopic crystal-growth due to the extreme non-equilibrium conditions existing from room-temperature molecules landing on the cold substrate.

The UV light source (210 - 250 nm) for most studies is an excimer-pumped, frequency-doubled dye laser. Pulse energies of 100 μJ are typical with the beam expanded to about 1 cm$^2$ in order to illuminate the whole sample surface. The photoproducts are analyzed with a Fourier-transform infrared (FTIR) spectrometer in the 600 - 4000 cm$^{-1}$ range operating in the reflection mode (double pass absorption) with an ultimate resolution of 0.5 cm$^{-1}$.

# PHOTOGENERATION OF OZONE IN OXYGEN MATRICES

Recent $O_2$ matrix studies by Schriver-Mazzuoli et al. [4] have shown significant $O_3$ production utilizing a medium pressure mercury arc lamp ($\lambda \geq 245$ nm) for photolysis, indicating ozone formation at energies insufficient to dissociate an isolated $O_2$ with one photon ($\lambda_{diss} \cong 242.5$ nm) [4]. They observe doublets for each fundamental vibrational mode, with the higher energy peak ascribed to $O_3$ monomers and the lower energy feature to a complex $O \cdots O_3$ [4]. In the present work, a set of $O_2$ matrices are prepared under very similar conditions. Each matrix is irradiated with discrete fluence doses of one single wavelength, while we monitor the $O_3$ IR absorption bands until they no longer increase with further irradiation. Figure 1 contains a close-up of the observed absorptions following irradiation at 232 nm. Good agreement is found with the limited number of features of Ref. [4], shown as vertical tick marks below the spectrum. We observe additional features, especially clear in the $\nu_3$ region, not seen in Ref. [4]. The weakest ozone fundamental band belongs to the symmetric stretch mode $\nu_1$ with a frequency around 1100 $cm^{-1}$. Our experiments show an absorption distinguishable from the background at 1100.0 $cm^{-1}$ in accordance with Ref. [4], but their reported second band at 1104.2 $cm^{-1}$ cannot be unambiguously recognized in our spectrum. In the region around 700 $cm^{-1}$ lies the absorption of the bending mode $\nu_2$ of ozone, and our spectrum reveals both bands previously reported [4]. We measure an intensity-distribution of $\nu_1:\nu_2:\nu_3 = 0.07:1:14$ for the higher frequency bands (called "free" molecule in Ref. [4] with their value of 0.07:1:13) and $\nu_1:\nu_2:\nu_3 = 0.12:1:10$ for the lower frequency bands (called "$O \cdots O_3$" in Ref. [4] with 0.11:1:5). Looking over the higher frequency region up to 4000 $cm^{-1}$ we observe an additional new absorption around 2100 $cm^{-1}$, consisting again of two dominant absorptions at 2107.8 $cm^{-1}$ and at 2096.5 $cm^{-1}$, respectively, and additional features near 2100 $cm^{-1}$. The absorption is about an order of magnitude weaker than $\nu_3$, and can be assigned to the combination band, $\nu_1 + \nu_3$. This band has been previously reported only in the gas phase [5] and in ozone-doped Ar and $N_2$ matrices [6].
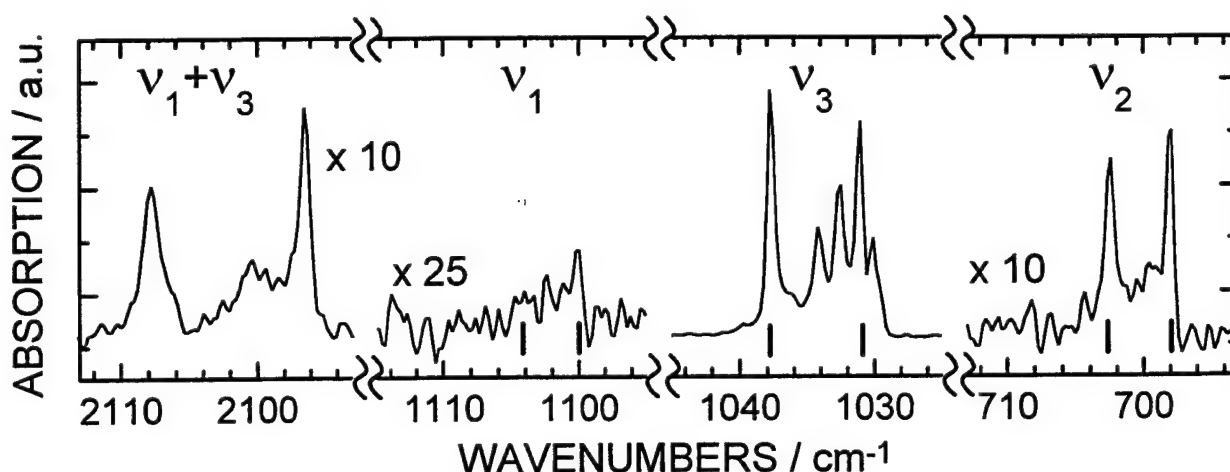


**Figure 1:** Infrared absorptions in an $^{16}O_2$ matrix after long time exposure to monochromatic UV laser light at 232 nm. The vertical ticks below the spectrum denotes the previously reported absorption bands from Ref. [4] for longer wavelength mercury lamp irradiation ($\lambda \geq 245$ nm).

Fig. 2 compiles the absorption spectra in the $v_3$ region of $^{16}O_3$ of 6 different $^{16}O_2$ matrices after irradiation with the indicated UV wavelength. With 248 nm light we could not distinguish any significant $O_3$ absorption from the background. At 244 nm, we observe the same two absorption bands in the 1040 cm$^{-1}$ region as reported by Ref. [4], which they have assigned to be the matrix-isolated $v_3$ vibration of ozone (1037.8 cm$^{-1}$) and to a proposed $O \cdots O_3$ complex
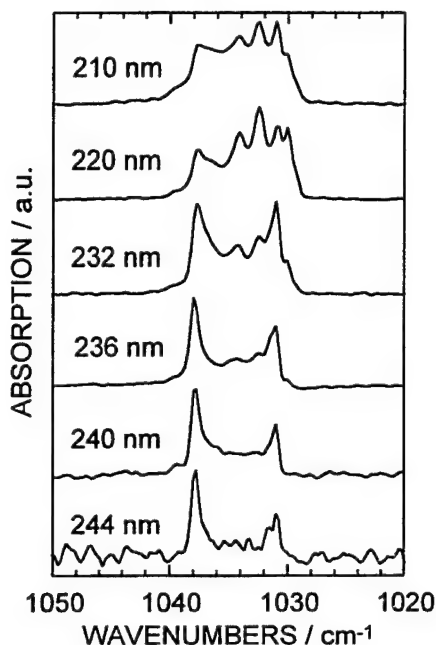


**Figure 2:** Infrared absorptions in the $v_3$ region of $^{16}O_3$ photogenerated each in an annealed $O_2$ matrix with the indicated UV wavelengths.
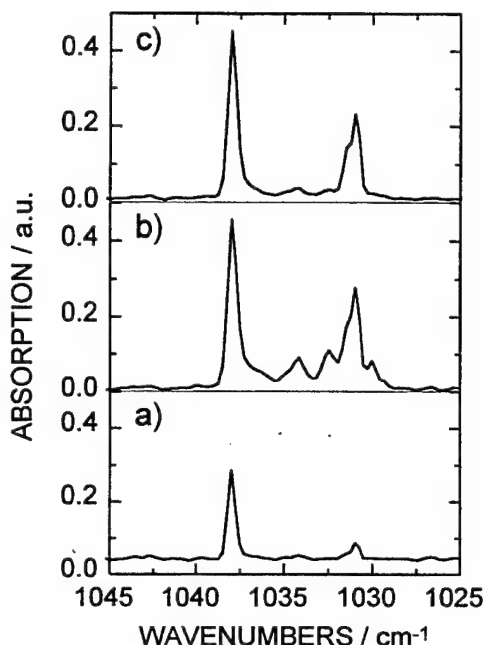
**Figure 3:** A photogenerated $O_3/O_2$ (with 240 nm laser light) before (a) and after (b) irradiating with 232 nm light, finally (c) after subsequent treatment with 240 nm.

(1030.9 cm$^{-1}$). When we use higher photon energies we observe new absorption features with increasing intensity relative to the aforementioned ones and the absolute absorption intensity increases with decreasing wavelength. We attribute this signal increase, in part, to the increasing $O_2$ absorption cross section of the Herzberg-continuum as the wavelength decreases from 250 to 210 nm. Equally important, the $O_3$ absorption cross section of the Hartley-continuum decreases when lowering the wavelength in this range causing fewer $O_3$ molecules to get photodissociated, thus shifting the equilibrium matrix value towards higher $O_3$ concentrations.

Figure 3 shows the result of processing a matrix with light at two UV wavelengths. A photoirradiated matrix containing both absorption features at 1037.8 cm$^{-1}$ and 1030.9 cm$^{-1}$ (Fig. 3a) due to previous processing with 240 nm light is irradiated with 232 nm light. A previous annealing cycle to 30 K during 240 nm irradiation is responsible for the different intensity-ratios of the two dominant bands in Fig. 3a compared to Fig. 2. An absolute increase of both features is observed as well as the appearance of the new IR absorptions between them. (Fig. 3b). When this sample is again irradiated with 240 nm light the 232 nm-created bands disappear and the initial two absorption bands remain with higher intensity (Fig. 3c). This demon-

strates that solid oxygen contains different species of $O_x$ which are not equally stable against the longer wavelength UV light, an extremely interesting observation. The production of additional, photophysically different, $O_x$ sites at shorter wavelengths implies that we should reexamine the results of Ref. [4], especially the $O\cdots O_3$ assignment, in light of the new observations.

## FORMATION KINETICS OF $O_x$ SPECIES

The observation of two groups of ozone-like species photogenerated in oxygen matrices was investigated in more detail. We measured growth curves of the bands in the $\nu_3$ region by measuring the absorption spectrum after selected irradiation doses for two wavelengths: 210 nm and 232 nm. Fig. 4 presents six selected spectra for the 232 nm irradiated sample. Spectra 4a and 4b show no production of the aforementioned two prominent bands at 1037.8 and 1030.9 $cm^{-1}$ while the other bands at 1036.5, 1034.1, 1032.5 and 1030.0 $cm^{-1}$ are already present. With continued irradiation the 1037.8 and 1030.9 $cm^{-1}$ bands appear, and for larger irradiation doses (Fig. 4d, 4e and 4f) they are the strongest absorption bands, as has been shown in Fig. 2 for this wavelength. Clearly, different production processes are occurring for the two groups of features.
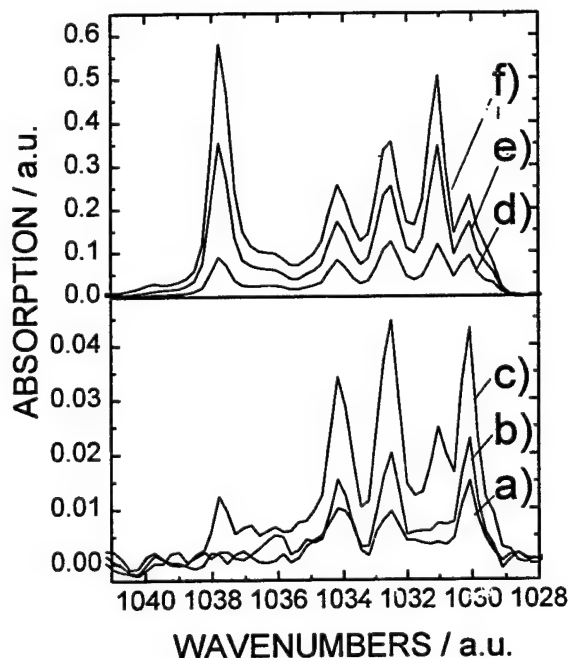


**Figure 4:** Absorption spectra in the $\nu_3$ spectral region of $O_3$ as a function of the incident irradiation dose (increasing from a to f).
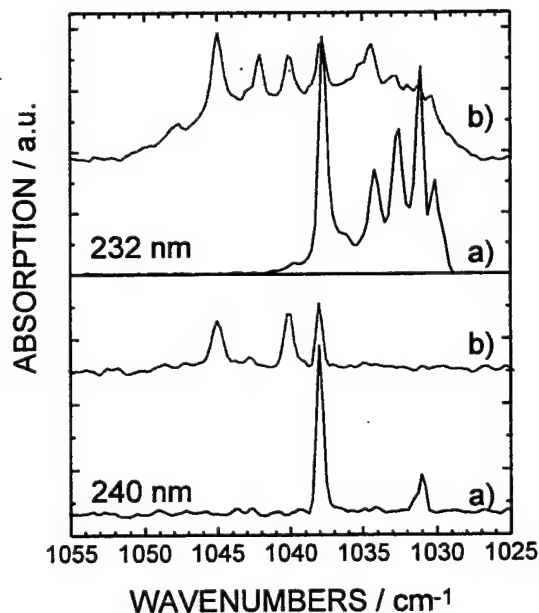


**Figure 5:** Effect of annealing on the $\nu_3$ features of $^{16}O_3$ for two differently photogenerated ozonic oxygen samples The a) spectra have been irradiated at 12 K, the b) spectra are the result of a) heated to 30 K and cooled back down to 12 K.

A quantitative analysis shows that we observe, in contrast to the linear increase with exposure in Ref. [4], an S-shaped growth curve for both the 1037.8 $cm^{-1}$ and the 1030.9 $cm^{-1}$ bands, while the other bands exhibit a linear dose-dependence for small irradiation doses. A study of growth curves at other wavelengths is underway, but our results already indicate two and probably even more distinctly different $O_x$ sites.

## EFFECTS OF TEMPERATURE OF $O_x$ SPECIES

When the sample containing the different ozone-species at 12 K is warmed up to 30 K, the oxygen matrix undergoes a phase transition from $\alpha$-$O_2$ to $\beta$-$O_2$ [7] and the isolated ozone-species rearrange to accommodate this new symmetry. This phase transition changes the $O_x$ spectra significantly (Fig. 5). For a sample containing only both bands at 1037.8 cm$^{-1}$ and 1030.9 cm$^{-1}$ (lower Fig. 5a), anealing to 30 K completely diminishes the latter band while the 1037.8 cm$^{-1}$ line and two new features (attributed to $O_3$ dimers and polymers in Ref. [4]) are red shifted by ca. 1 cm$^{-1}$ relative to their positions after recooling to 12 K (lower curve b) in Fig. 5.). This change is also observed for a 232 nm irradiated sample. However, due to the greater number of absorption bands in the $\nu_3$ region, more features appear on the blue side for this annealed sample (upper Fig. 5b). Irradiation of the annealed spectra (curves b) in Fig. 5) with UV light removes the peaks generated by raising the temperature and recreates the a) spectra in Fig. 5. The origin of these bands is still ambiguous and isotopic studies are underway to aid in the identification of the $O_x$ species.

## CONCLUSIONS

We have generated with tunable UV light and analyzed via FTIR spectroscopy matrix-isolated ozone in oxygen matrices. We observe for the first time the $O_3$ combination band $\nu_1 + \nu_3$ in solid oxygen and the tunability of our photolytic source allowed us to extend the present knowledge to more new features in the $\nu_3$ region. Once generated, these energized species remain stabilized in the solid environment; even a one week old energized sample showed no intensity-change within the experimental accuracy. The UV production and photostability of the formed ozonic species changes drastically within the wavelength region from 210 - 250 nm and further work is necessary to determine the most favorable wavelength with respect to the maximum achievable density. For our understanding of the production mechanisms it is necessary to develop a detailed picture including the photogeneration process on a molecular scale. New experiments using isotopic oxygen and multiple wavelengths are underway which will allow a more detailed interpretation. Other spectral regions and multiphoton effects using tunable picosecond lasers are envisioned.

## REFERENCES

[1]    M. J. Dyer, H. Helm, R. P. Saxon and D. L. Huestis, Proc. of the HEDM Contractor's Conf. (1995).

[2]    N. Schwentner, E. E. Koch, J. Jortner, *Electronic Excitations in Condensed Rare Gases*, Springer Tracts in Modern Physics, Vol. 107, Springer, Berlin, Heidelberg, New York (1985).

[3]    C. Bressler and N. Schwentner, Phys. Rev. Lett. **76**, 648 (1996).

[4]    L. Schriver-Mazzuoli, A. de Saxcé, C. Lugez, A. Schriver, J. Chem. Phys. **102**, 690 (1994).

[5]    A. Barbe, J.-J. Plateaux, S. Bouazza, J.-M.Flaud, and C. Camy-Peyret, J. Mol. Spectrosc. **150**, 255 (1991).

[6]    L. Schriver-Mazzuoli, A. Schriver, C. Lugez, A. Perrin, C. Camy-Peyret, and J.-M. Flaud, J. Mol. Spectrosc. **176**, 85 (1996).

[7]    R. D. Etters, A. A. Helmy and K. Kobashi, Phys. Rev. **B28**, 2166 (1983).

# The Overtone Qv(0) Transitions in Solid Para Hydrogen

Takeshi Oka

Department of Chemistry and
Department of Astronomy and Astrophysics
The University of Chicago

## 1.  *Sharpness of the $Q_3(0)$ Transitions*

The pure vibrational transitions Qv(0) (v←0, J=0←0) are Raman-type transitions which require an extra electric field of induction in addition to the laser radiation for spectroscopy.[1] We here discuss the case where the extra field is due to the electric quadrupole moments of J=1 ortho $H_2$ which remains randomly distributed in the nearly para $H_2$ crystal as the result of incomplete ortho to para conversion of $H_2$ by the catalyst. Since the impurity breaks down the translational symmetry of the crystal, the vibron momentum selection rule $\Delta k=0$ is violated. Thus, for v=1, the broad vibron band with hwhm of ~0.4 cm$^{-1}$ resulting from the hopping of vibrons in the crystal is fully manifested as a broad spectral line.

As the vibrational quantum number increases, however, the width of the vibron band decreases rapidly. The order of magnitude of the intermolecular interaction term which causes the v vibron hopping

$$V_v(q_1q_2) = \frac{1}{(v!)^2} \frac{\partial^{2v}Vdisp}{\partial q_1^v v q_2^v} (q_1q_2)^v \tag{1}$$

decreases by a factor of ~100 as v increases by 1. Therefore, while the width is 0.4 cm$^{-1}$ for v=1, it is ~1 MHz for v=3 and the vibron may well be regarded as localized, leading to the sharp spectrum shown in Fig. 1. The sharpness of the spectral lines enables us to see all details of the fine structure produced from intermolecular and crystal field interaction. Some magnified fine structures are shown in Fig. 2.[2] A Ti:sapphire laser was used as the tunable infrared source, and tone burst modulation was used to increase the sensitivity of detection. The intensity of the $Q_3(0)$ transition is about four orders of magnitude weaker than that of the $Q_1(0)$ transition.
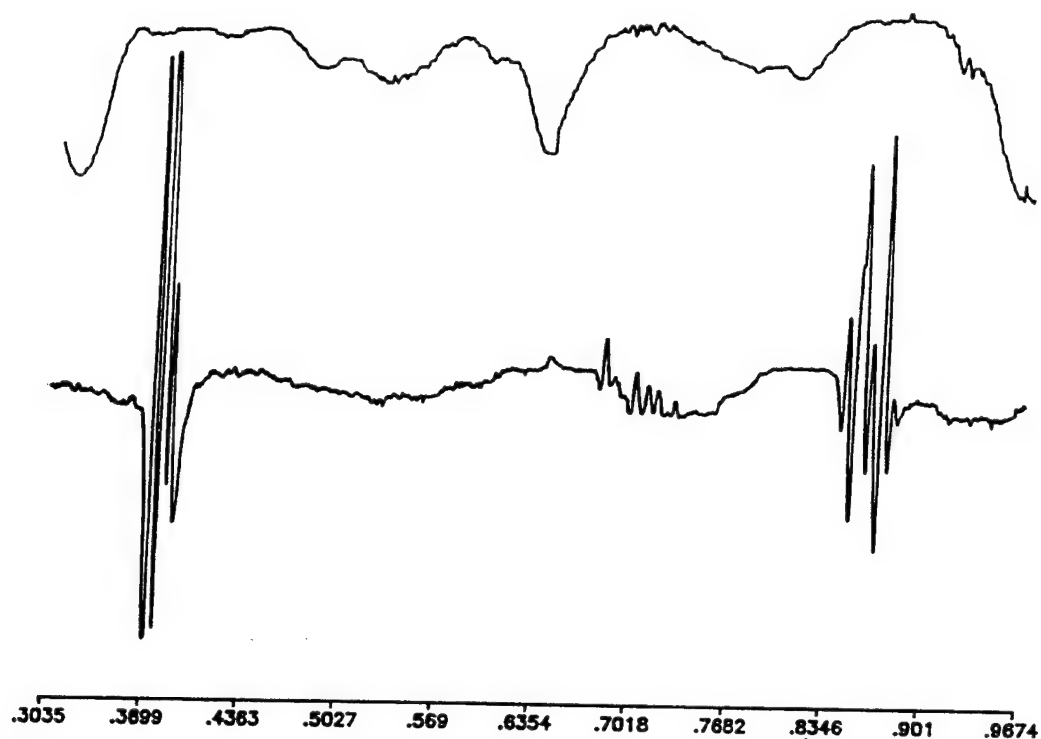
Fig. 1. The entire $Q_3(0)$ spectrum recorded with toneburst modulation for the laser polarization parallel to the C-axis. The wave number scale is 11758.0000 cm$^{-1}$ plus the indicated number.
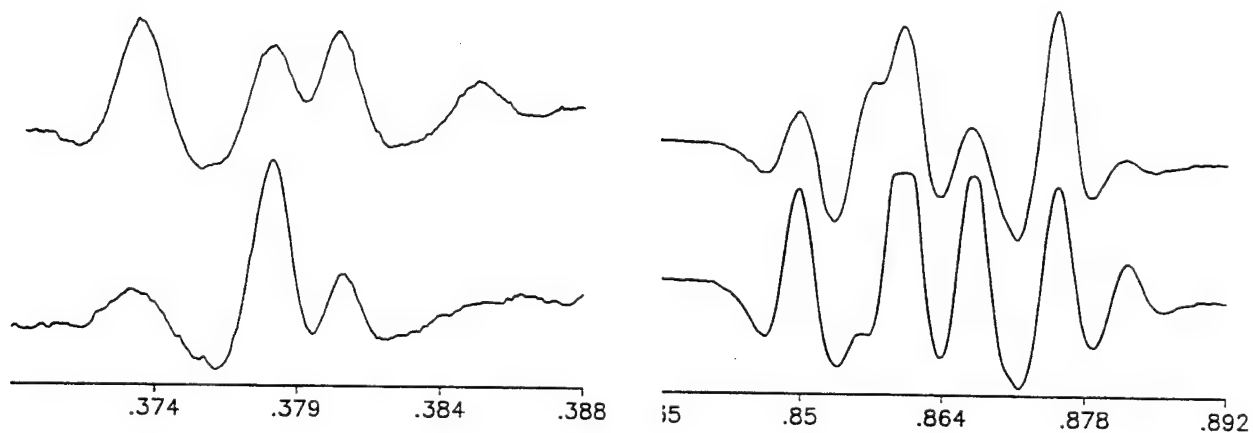


Fig. 2. The expanded recording of the lowest (left) and highest (right) spectral structures in Fig. 1.

## 2.  *Transition Mechanism and Analysis*

The $Q_3(0)$ overtone transition is induced by the same mechanism which causes the $Q_1(0)$ transition worked out by Sears and VanKranendonk[3] except that the third off diagonal vibrational matrix element of the isotopic polarizability $<3|\alpha|0>$ is involved rather than the first off diagonal element $<1|\alpha|0>$. The magnitude of $<3|\alpha|0>$ is $1.5 \times 10^{-3}$ Å which is three orders of magnitude less than that of the isotopic polarizability, $\alpha = 0.802$ Å.[3] The J=1 $H_2$ molecule whose quadrupolar electric field induces the transition is also involved in the transition and the resultant simultaneous transitions of the two molecules causes the intricate structure shown in Figs. 1 and 2. In the ground state the J=1 molecule is surrounded by J=0 $H_2$ molecules, and the system retains the $D_{3h}$ crystal symmetry. Under such symmetry, the M= $\pm$ 1 levels are degenerate and the splitting between the M=0 and M= $\pm$ 1 levels is very small due to the cancellation of the field effect among nearest and next nearest neighbors. When one of the surrounding molecules is excited to the v=3 state, however, the $D_{3h}$ symmetry is broken; the splitting between the M=0 and M= $\pm$ 1 level is greatly amplified from less than 0.01 cm$^{-1}$ to approximately 0.5 cm$^{-1}$, and this is the cause of the large splitting between the fine structures in Fig. 1. The degeneracy of the M= $\pm$ 1 levels is lifted, and this and the small difference between in-plane and out-of-plane nearest neighbors, together with the small crystal field splitting in the ground state, causes the observed intricate structure.

The observed spectrum was analyzed using a simple Hamiltonian[4]

$$V(\omega) = \varepsilon_{2c}C_{20}(\Omega) + \Delta BC_{20}(\omega) \qquad (2)$$

where the first term represents the interaction between the J=1 $H_2$ and the crystal field and the second term represents the pair interaction between the J=1 $H_2$ and the vibrationally excited J=0 $H_2$. $\Omega$ and $\omega$ are angle variables of the J=1 $H_2$ with respect to the crystal C–axis and the pair axis, respectively. Such analysis, together with theoretical relative intensities and the observed polarization dependencies has led us to the complete assignment of the observed structures. The energy levels of the in-plane and out-of-plane nearest neighbors and the next nearest neighbors are shown in Fig. 3.
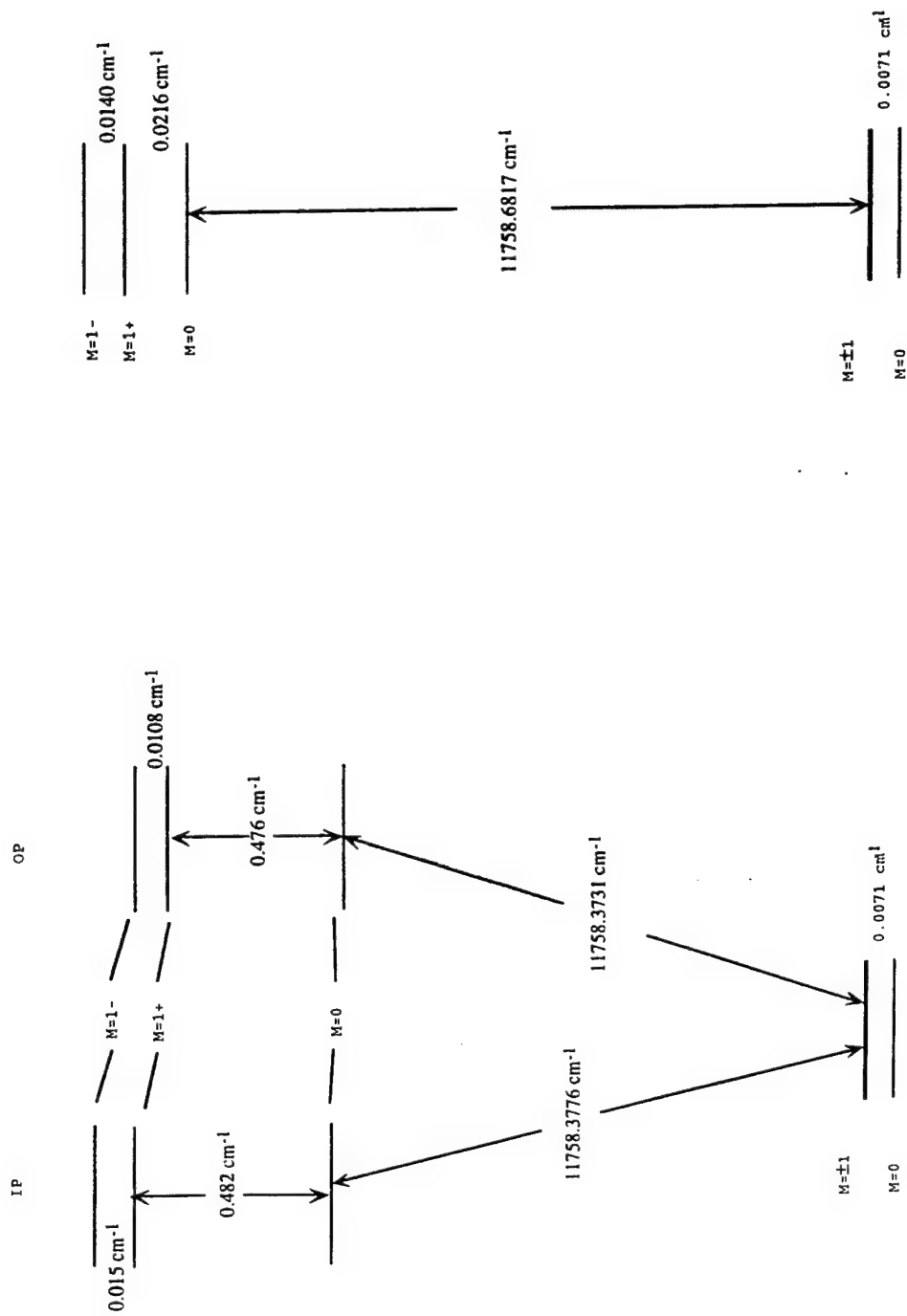
**Fig. 3.** Energy level diagrams of the $Q_3(0)$ transition for in-plane and out-of-plane nearest neighbors (left) and next nearest neighbor (right).

## 3. *Variation of Intermolecular Interaction and Local Lattice Distortion upon Vibrational Excitation*[5]

When a hydrogen molecule in a para $H_2$ crystal is excited to a high vibrational overtone state v=3 or 4, its electronic properties, such as the polarizability and the electric quadrupole moment, vary significantly since the energies of vibration (1.46 eV for v=3 and 1.89 eV for v=4) are a sizable fraction of the energies of excited electronic states. Thus the vibrational excitations lead to a significant variation of the intermolecular potential and resultant local distortion of the crystal lattice. Such effect is sensed by the variation of the splitting of M sublevels of the J=1 $H_2$ impurity which causes the transition. The accurate splitting parameters determined from the spectral structure of Fig. 1 provide the quantitative information. They are summarized in Table 1, together with theoretical values.

Theoretical values were calculated by using the *ab initio* anisotropic intermolecular potential reported by Mulder, van der Avoird and Wormer[6] which was slightly modified by VanKranendonk.[7] When the J=0 $H_2$ is excited to the v=3 state, the isotopic polarizability $\alpha$ increases 27% from 5.414 a.u. to 6.878 a.u.,[8] and the ionization potential decreases by 9.4%, from 15.4 eV[4] to 13.97 eV, resulting in the overall increase in the dispersion energy by 22%. The electric quadrupole moment increases 31.4% from 0.4841 a.u. to 0.6362 a.u.[9] The 22% increase of the isotropic dispersion increases the attraction between the v=3 J=0 $H_2$ and the surrounding molecules and tends to contract the local lattice. There is a reverse effect due to the increased molecular size and mean amplitude of vibration upon the vibrational excitation which, with the repulsive part of the potential, tends to repel the surrounding $H_2$ away from the vibrationally excited $H_2$. The experimentally determined values of the crystal field parameter $\epsilon_{2c}$ and the theoretically calculated variation of $\Delta\epsilon_{2c}$ allow us to discriminate the contraction and expansion of the local lattice and give contraction to be 0.368%. The results are given in Table 1.

The radial contraction of the local lattice is shown schematically in Fig. 4 where the magnitude of the contraction is exaggerated by two orders of magnitude.

Table 1. Calculated pair and crystal field interaction parameters (in cm$^{-1}$)

**Undistorted Lattice**

| | $\varepsilon_{2c}$ | $\Delta B^{nn}$ | | $\Delta B^{nnn}$ |
|---|---|---|---|---|
| Dispersion | -0.0112 | -1.008 | | -0.089 |
| Induction | -0.0002 | -0.027 | | -0.001 |
| EQQ | -0.0001 | -0.009 | | -0.000 |
| Total | -0.0115 | -1.044 | | -0.090 |
| Experimental | -0.0118 | -0.800 (ip) | -0.770 (op) | -0.078 |

**Slightly Distorted Lattice in Excited State**   r/R = 0.00368 assumed

| | $\varepsilon_{2c}^{nn}$ ip | $\varepsilon_{2c}^{nn}$ op |
|---|---|---|
| Dispersion | 0.0384 | -0.0405 |
| Induction | 0.0008 | -0.0008 |
| EQQ | 0.0003 | -0.0005 |
| Total | 0.0395 | -0.0418 |
| Experimental | 0.0368 | -0.0444 |
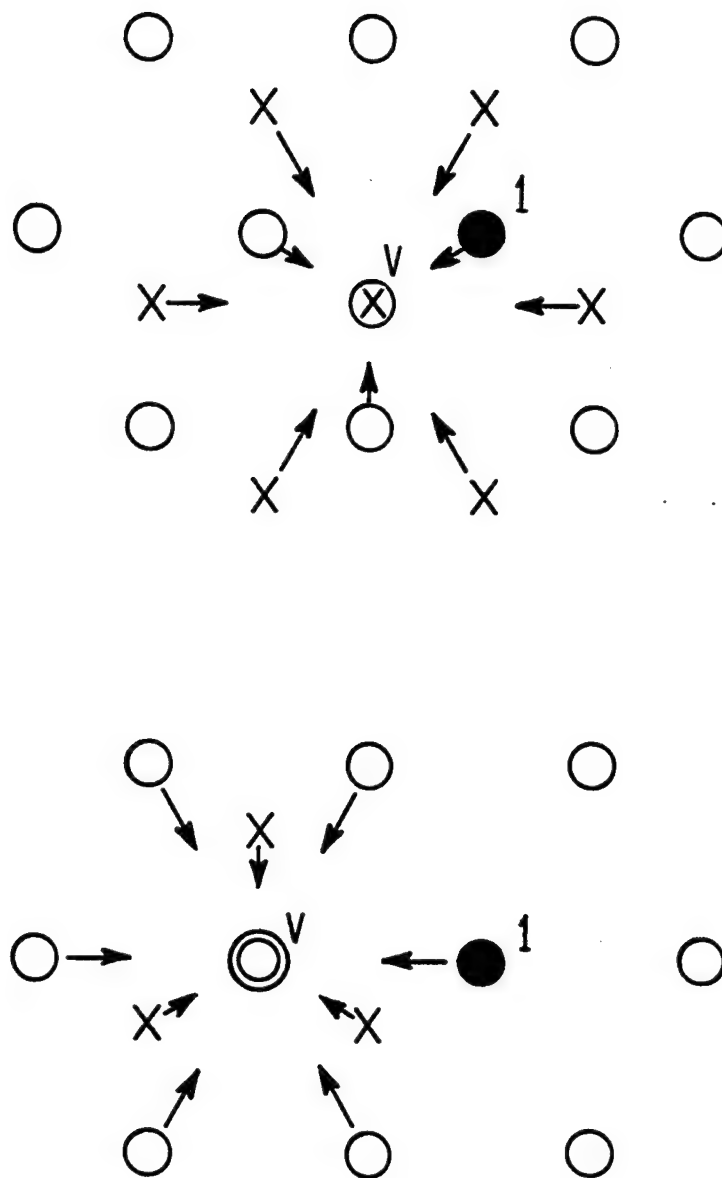
**Fig. 4.** Schematic diagram showing the assumed local lattice contraction upon the vibrational excitation. Molecules in the same hexagonal plane as the J=1 $H_2$ (indicated by a black circle with 1) are shown with white circles, while molecules above and below the plane are shown by X. When a J=0 $H_2$ is vibrationally excited (shown with a circled X and a double circle with V)[12] nearest neighbor molecules are attracted radially by the same amount. The top figure shows op configuration while the bottom figure shows ip configuration. The pair fixed axes are chosen such that z axis is along the pair axis and y axis is along the $C_2$ axis. The magnitude of contraction is exaggerated by two orders of magnitude.

## 4. *Possibility of HEDM through Vibrational Excitation*

Vibrational excitation has hardly been considered as an effective means to energize condensed phase matter although the vibrational excitation of $N_2$ has been very effectively used in the gaseous plasma media of $CO_2$ and $CO$ lasers. This is because (a) the absolute value of vibrational energy is very low and (b) the vibrational excitation relaxes very rapidly in solids in the sea of phonons. These do not apply to solid hydrogen. As is seen clearly from the energy diagram shown below, the v=3 and v=4 states which are above the ground state by 1.46 eV and 1.89 eV, respectively, which are sizable fractions (33% and 42%) of the dissociation energy $D_o$ = 4.478 eV.
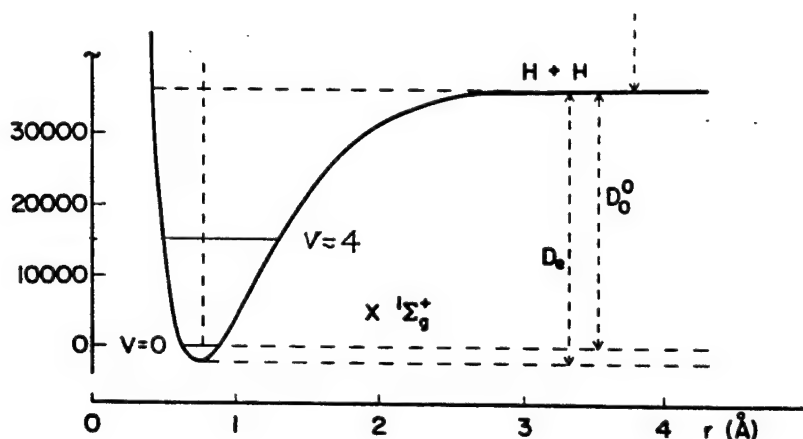


Since the initial report by Jones et al. in 1958[10] it has often been argued that atomic hydrogen is the most efficient chemical fuel because the reaction

$$H + H \rightarrow H_2 + 4.5 \text{ eV} \quad (220 \text{ kJ g}^{-1})$$
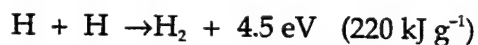
has by far the highest exothermicity per unit mass. It is 15 times higher than the usual fuel reaction

$$H_2 + \tfrac{1}{2}O_2 \rightarrow H_2O + 2.5 \text{ eV} \quad (13 \text{ kJ g}^{-1})$$

$$\tfrac{1}{2}H_2 + \tfrac{1}{2}F_2 \rightarrow HF + 2.8 \text{ eV} \quad (14 \text{ kJ g}^{-1})$$
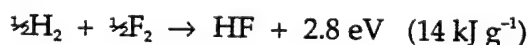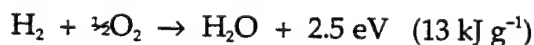
Indeed, one practical aim of producing spin polarized atomic hydrogen has been to realize such a fuel. The vibrational energy releases

$$H_2 \,(v=4) \;\rightarrow\; H_2(v=0) \;+\; 1.9 \text{ eV} \quad (90 \text{ kJ g}^{-1})$$

$$H_2 \,(v=3) \;\rightarrow\; H_2(v=0) \;+\; 1.5 \text{ eV} \quad (70 \text{ kJ g}^{-1})$$
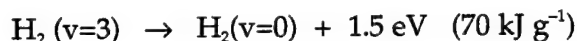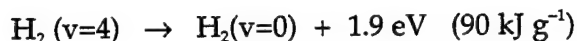
are five times higher than the latter two reactions in terms of energy per mass and, in this regard, much higher than those of metal impurities in cryogenic solids.

Furthermore, the volume of the solid stays the same upon vibrational excitations. The vibrational excitation, if anything, tends to decrease the volume, as discussed in Section 3. In short, vibrational excitation is a very effective and clean way to increase the energy of hydrogen crystals without increase of mass and volume. The question then is, how efficient can we excite molecules in the solid and how long does the excitation stay in the solid? Following estimates are based on our experiments.

## 5. *Efficiency of Vibrational Excitation*

The actual operation of the vibrational excitation is envisaged to proceed as follows. A bulk of solid para-$H_2$, which contains an adjustable fraction of ortho-$H_2$, is produced in a container (diameter ~ 1 m), and it is irradiated through optical windows with high power lasers with wavelengths of 0.85 $\mu$m (v=3) or 0.66 $\mu$m (v=4). I first show below that by properly adjusting ortho-$H_2$ concentration we can make the condition that the laser power is practically used up in the vibrational excitation v=4←0 and the excitation is contained in the solid for up to ~1 min for certain concentration, x, of the excited $H_2$. I do not know this concentration x, but I plan to determine it experimentally.

The electric quadrupole moment of a J=1 ortho-$H_2$ produces an electric field of

$$E \;\sim\; \sqrt{3}\,Q/R^4 \;\sim\; 1.5 \text{ MV/cm,}$$

at the nearest neighbor sites. (I shall ignore the angular dependence and use angle averages throughout) The electric field generates transition moments of

$$<v\,|\,\mu\,|\,0> \;\sim\; <v\,|\,\alpha\,|\,0>E,$$

which is ~55$\mu$D (55x10$^{-6}$ Debye) for v=3 and ~6$\mu$D for J=4. These are extremely small transition dipole moments, and the weakness of the transition is essential in the following discussion. The cross section of absorption is calculated by

$$\sigma = \frac{8\pi^2 v}{hc\Delta v} \, |<v|\mu|0>|^2$$

where $\Delta v$ is the halfwidth at half maximum of the spectral line, which is assumed to be 0.05 cm$^{-1}$. The values of $\sigma$ are $2.8 \times 10^{-22}$ cm$^2$ for v=3 and $3.7 \times 10^{24}$ cm$^2$ for v=4. The mean free path of resonant radiation in the crystal is calculated by

$$\ell = \frac{1}{n\sigma} = \frac{1}{12n_1\sigma}$$

where $n=12n_1$ is the number density of J=0 $H_2$ located at nearest neighbor sites of J=1 $H_2$ whose number density is $n_1$. In order for the mean free path to be ~50 cm, the required ortho-$H_2$ fraction is 0.02% for v=3 and 1.7% for v=4. The former is impractical but the latter is quite feasible and also in accord with the assumed linewidth value of 0.05 cm$^{-1}$. Hereafter I will limit our discussion to v=4. We see that practically all radiation power is absorbed by the crystal and that the excitation reaches deep into the core of the solid.

## 6. Loss of Vibrational Excitation

Three loss mechanisms of the v=4 vibrational excitation (vibron) are considered: (a) diffusion of vibrons to the wall of the container by hopping, (b) spontaneous emission of photons leading to cascading transitions v=4→3→2→1→0, and (c) relaxation of the vibron to phonons of the crystal. The first process is calculated to be very slow and negligible. This is because the v=4 vibron cannot break into smaller vibrons due to energy mismatch caused by the vibrational anharmonicity. The order of magnitude for v=4 vibron hopping is estimated to be ~0.1 MHz. With this slow rate it takes 10 years (!) for the vibron to travel from the core to wall of the container by random walk.

The second mechanism of spontaneous emission is more serious. The Einstein formula

$$A = \frac{4\omega^3\mu^2}{3\hbar c^3}$$

gives the rate of 0.76 sec$^{-1}$, i.e., the spontaneous lifetime for the v=4→3 transition to be 1.3 sec for a vibron which is located at one of the nearest neighbor sites of J=1 $H_2$. The rate gets lower as v is reduced due to the v+1 dependence of $\mu^2$ (which is partly compensated by increase in $\omega$)

and is 0.36 sec⁻¹ for v=1→0. Since the vibron hopping frequency of 0.1 MHz is much faster than these rates, the effective lifetime of spontaneous emission is longer by a factor $n/12n_1$ ~5 for $n_1/n$ of 1.7%. I, therefore, estimate the overall lifetime of spontaneous emission to be 15 sec. By reducing the J=1 $H_2$ concentration by 4, it will be 1 min.

Finally, the rate of the third process, that is, the vibron-phonon relaxation, is not known at all at this stage. Two experiments[11,12] reported the lifetime of vibron $T_1$ to be on the order of 10μ sec. If, indeed this is the case, the vibrational energy deposition will never work; crystal will melt long before appreciable number of $H_2$ are excited. However, in view of the fact that the vibrational relaxation of $N_2$ is extremely slow (~ 50 sec) even in liquid, I believe there is a chance that relaxation of $H_2$ in solid is even slower and limited by the radiative relaxation. Since the energy of the v=4→3 vibron, 3459 cm⁻¹, is ~50 times higher than the Debye temperature of solid hydrogen, the relaxation requires extremely nonlinear many phonon process. (Note that this ratio is higher in $H_2$ than in $N_2$.) I will conduct experiments to measure this rate.

The speculations given above gloss over many practical difficulties that may arise in actual operation. Is it feasible to make a solid of this size which is transparent? What about relaxation due to O transitions (the v=4→3 J=0→2)? What about the radiative relaxation via stimulated emissions due to inverted population? Aren't there underlying broad transitions due to simultaneous transitions and phonon bands? These and many other questions (including those I must have missed) are not addressed here. I just have presented the bone of the idea in simplest form. Nevertheless, there is this bottom issue which cannot be avoided. Even for the 1 min lifetime and 1% of vibrational excitation, we need fairly monochromatic visible lasers with total power of ~ 250 K Watt. Perhaps 25 diode lasers each with 10 kW output power? Currently, commercially available quasi CW stacked array diode lasers have output of 2.5 kW with duty factor of 4% (SDL Optics Inc.).

# References

1.  D. P. Weliky, T. J. Byers, K. E. Kerr, T. Momose, R. M. Dickson, and T. Oka, *Appl. Phys. B.* **59**, 265 (1994)

2.  R. M. Dickson, T. Momose, T. J. Byers and T. Oka, *Phys. Rev. B*, submitted.

3.  V. F. Sears and J. VanKranendonk, *Can. J. Phys.* **42**, 980 (1964)

4.  D. P. Weliky, K. E. Kerr, T. J. Byers, Y. Zhang, T. Momose, and T. Oka, *J. Chem. Phys.*, in press.

5.  R. M. Dickson and T. Oka, *Phys. Rev. B*, submitted.

6.  F. Mulden, A. van den Avoird, and P.E.S. Wormes, *Mol. Phys.* **37**, 157 (1979)

7.  J. VanKranendonk, *Solid Hydrogen*, Plenum Press, New York (1983).

8.  W. Kolos and L. Wolniewicz, *J. Chem. Phys.* **46**, 1426 (1967)

9.  G. Karl and J. D. Poll, *J. Chem. Phys.* **46**, 2944 (1967)

10. J. T. Jones, Jr., M. M. Johnson, H. L. Mayer, S. Katz, and W. S. Wright, *Aeronutronic System, Inc.*, Publication V-216 (1958)

11. C. Delalande and G. M. Gales, *Chem. Phys. Lett.* **50**, 339 (1977)

12. C.-Y. Kuo, R. J. Kerl, N. D. Patel and C.K.N. Patel, *Phys. Rev. Lett.* **53**, 2575 (1984)

13. S.R.J. Brueck and R. M. Osgood, *Chem. Phys. Lett.* **39**, 568 (1976)

14. D. W. Chandler and B. E. Ewing, *J. Chem. Phys.* **73**, 4904 (1980)

# Search for Metallic Hydrogen in the Extended Infrared

Isaac F. Silvera

Lyman Laboratory of Physics, Harvard University, Cambridge, MA 02138

We have developed a unique apparatus which enabled us to extend earlier measurements in the near IR to 10 microns. We have studied broad band absorption in hydrogen to 190 GPa, above the transition pressure to the A-phase in order to determine if the samples displayed Drude behavior, characteristic of a metal. Within the range of our study we find no evidence of metallic behavior. Earlier reports were most likely due to misinterpretation of vibron absorption as a Drude edge. We observe the already studied vibron in the 4000 cm$^{-1}$ region, as well as a new mode identified as a phonon, at much lower frequencies. The pressure dependence of these mode frequencies indicates a crossing at higher pressures which may well be the pressure for the Wigner-Huntington transition to atomic metallic hydrogen.

In the past several years there have been reports of metallization of hydrogen based on optical studies [1-7]. Much of this effort arose when it was realized that a unique new phase existed at pressures above 150 GPa [8], called the hydrogen-A (deuterium-A) phase, believed to be the molecular metallic phase of hydrogen. Although the most rigorous method of identifying a metal is to measure the dc electrical conductivity and establish that this remains finite in the limit that temperature goes to zero, such measurements are experimentally challenging and have not yet been carried out on hydrogen in a diamond anvil cell (DAC). Experimenters have relied on optical properties to identify the conducting state. In particular, experiments have concentrated on measuring the optical response and interpret this on the Drude free electron model. In this case for decreasing frequencies below the plasma frequency, reflectivity and absorption of light increase from low values at higher frequencies. A definitive measurement requires a study over a broad range of frequency below the plasma frequency. Since hydrogen is expected to be an indirect band overlap metal with a low carrier density the plasma frequency should be in the near infrared or lower. Using IR data to a low frequency limit of 4000 cm$^{-1}$, hydrogen was reported to be metallic by an electronic band overlap mechanism above 150 GPa [4-5]. We have extended the measurement range to 1000 cm$^{-1}$ and show that there is no evidence that hydrogen becomes metallic at a pressure of 150 GPa.

We have built a new spectroscopic system which extends measurements to 1000 cm$^{-1}$, and studied solid para-hydrogen down to liquid helium temperatures. The spectroscopic system is shown in Fig. 1. The radiation source is a thin
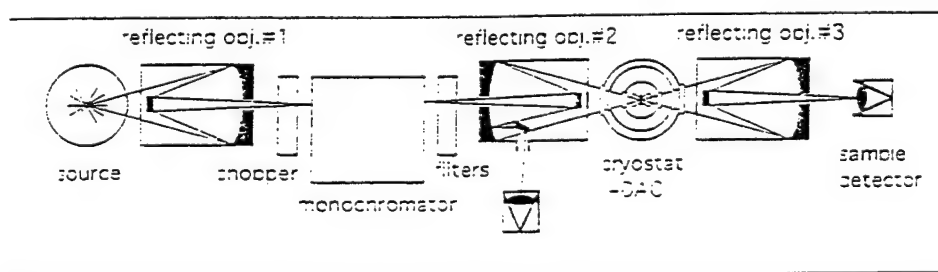


Figure 1. The spectroscopic system to extend studies to 1000 cm$^{-1}$, described in the text.

walled graphite tube in a one atmosphere nitrogen environment, which operates at ~2500K (determined from its gray-body spectrum) when heated with a current of about 45 amperes [9]. This is approximately a factor of 2 hotter than the traditional glowbar sources. The radiation is collected by a large Schwarzschild reflective objective and focused down onto the slits of an ISA HR-320 spectrometer, where it is chopped for detection purposes and filtered to isolate the first order of the grating. A second objective collects this light and focuses it down onto the sample, and a third Schwarzschild collects the transmitted light and images it onto a cooled mercury cadmium telluride detector. A small part of the beam entering the DAC is deflected onto a second reference detector used to normalize out fluctuations of the source. Both detector signals were preamplified and fed into lock-in amplifiers. In order to optimize the Schwarzschild objectives to our system we designed and built them ourselves [10-11]. Since the Drude spectrum does not require high resolution we used a 50 line/mm grating blazed at 6 microns, to enhance our signal, and all spectra shown are low resolution. Although the source has a low intensity per unit frequency as compared to a tunable laser [12], the large bandwidth falling on the detector results in a comparable signal-to-noise ratio. The entire optical system, including the tail of the cryostat, was in a nitrogen atmosphere to eliminate absorption due to water vapor. The spectrometer was computer controlled using a program written in Lab View which sampled spectra at equal intervals in frequency and optimized the signal-to-noise ratio. All data shown are for fixed slit widths.

Spectra for several pressures, shown in Fig. 2, were normalized to a spectrum at 137 GPa
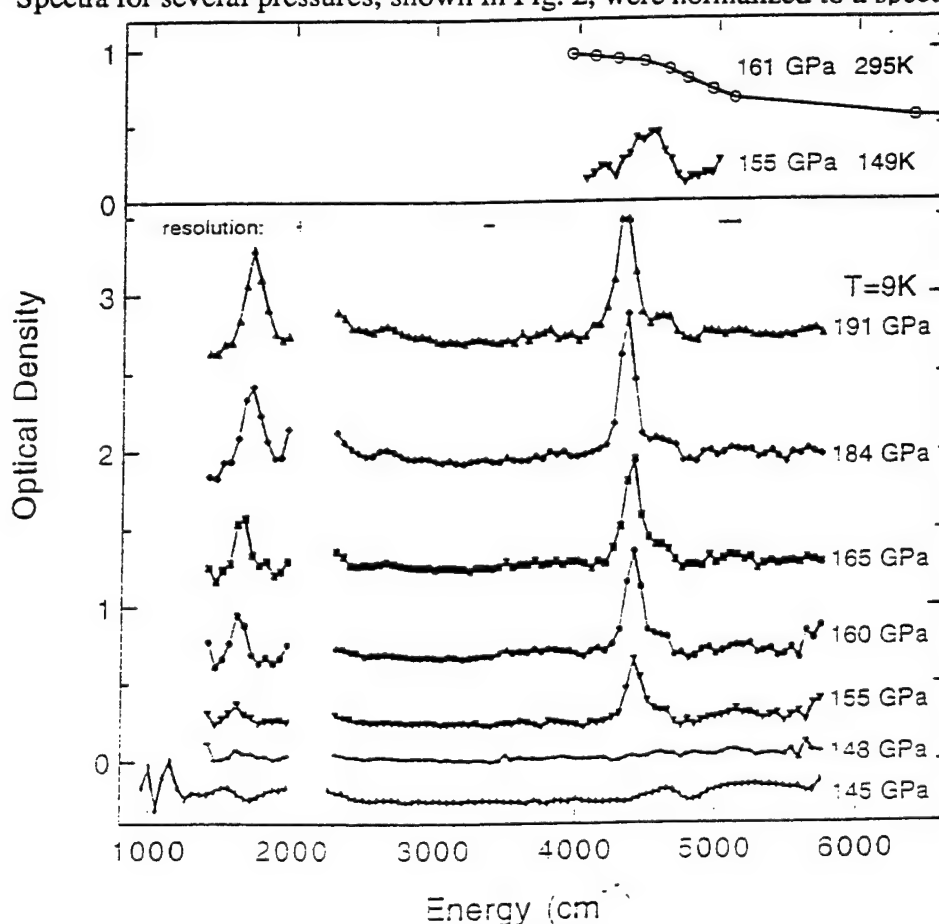


Figure. 2. Absorption spectra of hydrogen to 191 GPa. No evidence of Drude absorption was found. The high frequency vibron and low frequency phonon appear as sharp peaks in the A phase above 150 GPa. An earlier spectrum shown in the top curve, from Hanfland et al, and interpreted as a Drude edge, is believed to be due to vibron absorption at room temperature.

and 9 K, below the A phase pressure. This normalization procedure effectively removes the absorption due to diamond, as described in detail elsewhere [7]. All samples were held at 9K for a minimum of 24 hours before measuring, to insure that they were completely converted to equilibrium ortho-para concentration, which should be almost 100% para. We observed no Drude edge absorption in our measurements up to 191 GPa. Therefore, our experiment does not support previous conclusions based on optical measurements that hydrogen exhibits metallic behavior in the H-A phase [4-5].

The spectra in Fig. 2 show two strong absorption peaks, one at about 4300 cm$^{-1}$ and the other at about 1600 cm$^{-1}$. The high frequency peak represents absorption due to excitation of a vibron mode. The low frequency peak is somewhat low in frequency to be a vibron and is most likely a phonon. The frequency is consistent with the absorption identified by Hanfland et al [13] as a phonon sideband in hydrogen. Its frequency increases with pressure as might be expected in the quasi-harmonic approximation for intermolecular potentials which increase with decreasing lattice constant. No evidence of the low frequency peak was found below 150 GPa, so we do not believe that it is associated with hydrogen diffusing into the diamond anvils, resulting in an impurity mode. An interesting observation [14] is that hydrogen will become atomic metallic when a phonon and vibron of the proper symmetry become degenerate.

Although in the future we can continue these studies to higher pressures, it will be difficult to extend the long wavelength range in search of a Drude edge due to diffraction limits set by gasket hole dimensions. In particular, to achieve higher pressures, smaller holes must be used. In conclusion, our results are consistent with the A phase of hydrogen being non metallic, i.e. the band gap remains open.

1.   J.H. Eggert, K.A. Goettel, and I.F. Silvera, Europhys. Lett. **11**, 775 (1990).
2.   J.H. Eggert, K.A. Goettel, and I.F. Silvera, Europhys. Lett. **12**, 381 (1990).
3.   H.K. Mao and R.J. Hemley, Science **244**, 1462 (1989).
4.   H.K. Mao, R.J. Hemley, and M. Hanfland, Phys. Rev. Lett. **65**, 484 (1990).
5.   M. Hanfland, R.J. Hemley, and H.K. Mao, Phys. Rev. B **43**, 8767 (1991).
6.   J.H. Eggert, F. Moshary, W.J. Evans, H.E. Lorenzana, K.A. Goettel, I.F. Silvera, and W.C. Moss, Phys. Rev. Lett. **66**, 193 (1991).
7.   L. Cui, N.H. Chen, and I.F. Silvera, Phys. Rev. Lett. **74**, 4011 (1995).
8.   H.E. Lorenzana, I.F. Silvera, and K.A. Goettel, Phys. Rev. Lett. **63**, 2080 (1989).
9.   J.B. Burkholder, P.D. Hammer, and C.J. Howard, J. Phys. Chem **91**, 2136 (1987).
10.  P. Erdös, J. Opt. Soc. Am. **49**, 877 (1959).
11.  We thank R. Boehler for a useful suggestion on how to make these objectives.
12.  L. Cui, N.H. Chen, S.J. Jeon, and I.F. Silvera, Phys. Rev. Lett. **72**, 3048 (1994).
13.  M. Hanfland, R.J. Hemley, H.K. Mao, and G.P. Williams, Phys. Rev. Lett. **69**, 1129 (1992).
14.  N.W. Ashcroft, Physical Review B **41**, 10963 (1990).

# Reactions of Laser-Ablated Boron Atoms with $NH_3$, $CH_3NH_2$ and NO to Form Novel Boron Insertion Products

Lester Andrews, Gary P. Kushto, Dominick V. Lanzisera and Craig A. Thompson

Department of Chemistry

University of Virginia

Charlottesville, VA 22901

## Abstract

The major reaction products of laser-ablated B atoms with $NH_3$ are iminoborane, $H-B\equiv N-H$, formed by B insertion and H elimination, and BNBH, formed by a second B insertion and H elimination. These novel molecules were identified by isotopic substitution and comparison to *ab initio* calculated frequencies [1].

Reactions of B with $CH_3NH_2$ give the same $HB\equiv NH$ and BNBH products and both methyliminoborane isomers $CH_3B\equiv NH$ and $HB\equiv NCH_3$. The methyliminoborane molecules are isoelectronic with methylacetylene. It appears that B inserts into the C-N and N-H bonds with comparable facility, but there is little evidence for insertion into C-H bonds in these experiments. The reaction mechanism is illustrated in Scheme 1.

**SCHEME 1**

$$H_2\overset{\cdot}{C}\text{-}B\equiv N\text{-}H$$

$$\uparrow \quad \text{-H(C)}$$

$$H_3C\text{-}B\equiv N\text{-}H$$

$$\uparrow \quad \text{-H(N)}$$

$$H_3C\text{-}N\equiv B^{\cdot}$$

$$\uparrow \quad \text{-H(B)}$$

$$H_3C\text{-}N\equiv B\text{-}H$$

$$\uparrow \quad \text{-H(N)}$$

$$H_2C\text{=}B\text{=}NH_2 \xleftarrow{\text{-H(C)}} \quad \xrightarrow{+B} \quad \overset{\cdot\cdot}{N} \quad \xrightarrow{+B} \quad \xrightarrow{\text{-CH}_3} H\text{-}N\equiv B\text{-}H$$

(trace HBCBH)

$$+B$$

The spectra are analyzed by identifying boron isotopic doublets for new species containing a single B atom. Strong isotopic band pairs were observed at 2001.1-1940.2 cm$^{-1}$, 1975.5-1949.2 cm$^{-1}$, and 1798.5-1743.5 cm$^{-1}$. All of these are, more or less, B-N stretching vibrations, but what else is present in these molecules? The $^{10}$B/$^{11}$B isotopic frequency ratio defines the normal mode. Table 1 shows that these frequency ratios differ, which indicates coupling with other vibrations in the molecule.

Calculations were done for the predicted $CH_3B\equiv NH$, $CH_3N\equiv BH$ and $CH_2=B=NH_2$ product molecules at the MP2 level using the D95$^*$ basis set in Gaussian 94. These molecules have very strong bands calculated at slightly higher frequencies than the observed values. Note the OBS/MP2 ratios (commonly called "scale factors") in Table 1. Of much more importance is comparison of the observed and calculated $^{10}$B/$^{11}$B frequency ratios, which clearly show that observed and calculated

117

molecules are one and the same. Note that the observed anharmonic ratios are slightly lower than the calculated harmonic ratio as expected.

**TABLE 1.** Observed and Calculated Vibrational Frequencies ($cm^{-1}$) for new Iminoborane Species.

(up 22 kcal/mol)

| $CH_2=B=NH_2$ | | MP2 | D95* | OBS/MP2 | |
| --- | --- | --- | --- | --- | --- |
| $^{10}B$ | $^{11}B$ | $^{10}B$ | $^{11}B$ | $^{10}B$ | $^{11}B$ |
| 1798.5 - | 1743.5 | 1881.5 - | 1822.3 | 0.956 - | 0.957 |
| 1.03155 | | 1.03249 | | | |

(up 15 kcal/mol)

| $CH_3N\equiv BH$ | | MP2 | D95* | OBS/MP2 | |
| --- | --- | --- | --- | --- | --- |
| $^{10}B$ | $^{11}B$ | $^{10}B$ | $^{11}B$ | $^{10}B$ | $^{11}B$ |
| 1975.5 - | 1949.2 | 1985.3 - | 1957.6 | 0.995 - | 0.996 |
| 1.01349 | | 1.01415 | | | |

(lowest energy)

| $CH_3B\equiv NH$ | | MP2 | D95* | OBS/MP2 | |
| --- | --- | --- | --- | --- | --- |
| $^{10}B$ | $^{11}B$ | $^{10}B$ | $^{11}B$ | $^{10}B$ | $^{11}B$ |
| 2001.1 - | 1940.2 | 2068.5 - | 2003.6 | 0.967 - | 0.968 |
| 1.03139 | | 1.03239 | | | |

Note in Scheme 2 that the effect of methyl substitution on H-B≡N-H is essentially the same as for the isoelectronic molecule H-C≡C-H. Imminoborane is more reactive than acetylene: HBNH trimerizes readily to form borazine, which is isoelectronic with benzene, whereas the analogous trimerization of HCCH to form benzene is a much slower reaction.

**SCHEME 2**

CH₃-C≡C-CH₃ $\quad$ CH₃-B≡N-CH₃

$CH_3\text{-}C\equiv C\text{-}CH_3$

$2313 \text{ cm}^{-1}$

$176 \text{ cm}^{-1}$

$CH_3\text{-}C\equiv C\text{-}H$

$2137 \text{ cm}^{-1}$

$H\text{-}C\equiv C\text{-}H$

$163 \text{ cm}^{-1}$

$1974 \text{ cm}^{-1}$

$CH_3\text{-}B\equiv N\text{-}CH_3$

$2059 \text{ cm}^{-1}$

$114 \pm 5 \text{ cm}^{-1}$

$CH_3\text{-}B\equiv N\text{-}H \qquad CH_3\text{-}N\equiv B\text{-}H$

$1940 \text{ cm}^{-1} \qquad\qquad 1949 \text{ cm}^{-1}$

$H\text{-}B\equiv N\text{-}H$

$1789 \text{ cm}^{-1}$

$156 \pm 5 \text{ cm}^{-1}$

$H_2C=C=CH_2$

$1956 \text{ cm}^{-1}$

$H_2C=B=NH_2$

$1744 \text{ cm}^{-1}$
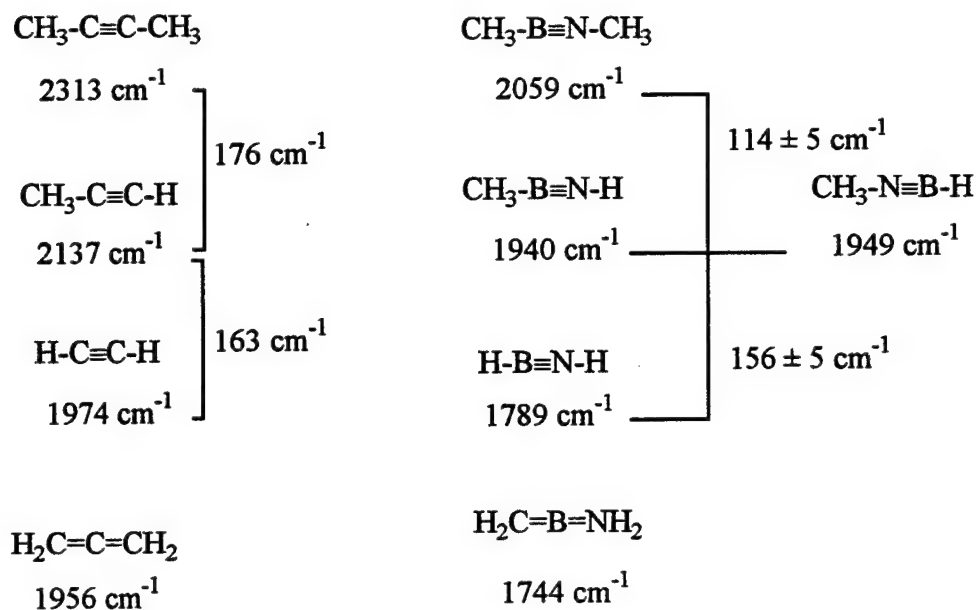
The major B atom reaction with NO is insertion to form triplet NBO which is identified from B-O stretching and NBO bending modes at 1996.8 and 493.5 cm$^{-1}$, respectively, through isotopic substitution and MP2 frequency calculations. Triplet NBO is a high energy density matter candidate. A second B atom adds to give BNBO also identified by 2068.2 and 500.9 cm$^{-1}$ absorptions in the same regions.

Two conclusions must be emphasized here. Since pulsed laser ablated metal atoms contain excess kinetic/electronic energy, these atoms can undergo reactions that require activation energy and produce new molecules for spectroscopic study. Quantum chemical calculations predict frequencies for new molecules, but calculated and observed isotopic frequencies are required to describe the normal modes. The fingerprint match of calculated and observed isotopic frequencies, and thus normal modes, adds another dimension of confidence to the identification of new matrix isolated molecules.

**REFERENCE**

1. L. Andrews and C. A. Thompson, *J. Am. Chem. Soc.*, *117* (1995) 10125.

# EXTENDED ABSTRACT

# Excited States for Molecules and Clusters

**Rodney J. Bartlett, Anatoli Korkin, and Marcel Nooijen**

*Quantum Theory Project*

*University of Florida*

*Gainesville, Florida 32611–8435*

### ABSTRACT

This presentation will discuss the new equation-of-motion (EOM) coupled-cluster (CC) methods for excited states. Specific topics will include application of the electron attached (EA) variant to describe the multiple potential energy surfaces for several excited states of the $Li + H_2$ system to assist modeling a $Li$ atom embedded in an $H_2$ matrix. Surfaces for all states $<5$ ev have been determined at a grid of points. Oscillator strengths between all relevant states are also obtained. In addition, we have considered the characteristic electronic spectra for $Li$ atoms at certain locations in $H_2$ clusters.

A potential high energy density material (HEDM) consists of unbonded atoms embedded in cryogenic solids, such as $H_2$. A particular prototype is $Li$ embedded in $H_2$. The reason for interest, is that a light metal atom provides a much greater energy/mass ratio when burned with oxygen than does most molecules. For $Li + O_2$ the energy/mass ratio is about 19% greater than $H_2 + O_2$ for gas phase products, and 125% more if $Li_2O$ forms in a condensed phase. Obviously, to pursue such a scenario for HEDM, requires documentation that $Li$ can be embedded into solid $H_2$, and we need to know its concentration. These questions can be answered if we can use spectroscopic techniques to establish and characterize the existence of the atom embedded species. Two spectroscopic studies have been made of this prototype, one as an embedded solid [1] and the other as a $(H_2)_N$ cluster with $Li$ attached [2]. The spectra differ considerably. (See Fig. 1)

It is of interest to provide a theoretical study to offer a third voice to help understand the spectra and structure of such embedded atom species. Such a study requires a coupling of electronic structure with molecular dynamics.

The electronic structure component can, in principle, provide the potential energy surfaces for all relevant electronic states, which in this example means all that would correlate with a $Li$ atom with the unpaired electron in a 2s, 2p,3s, 3p, 3d or 4s orbital. The range is up to about 4.5 eV.

Given such potential energy surfaces, dynamics methods can be used to average over all the various orientations of the $(H_2)_N$ cluster molecules relative to the embedded $Li$ atom. Such a study has been done by Whaley [3], using MCSCF/CI potentials for $Li + H_2$ obtained by Konowalow [4] for the lowest $Li + H_2$ surfaces . These calculations were limited as the only states considered corresponded to the $Li$ electron in the 2s or 2p orbital. Here we provide highly correlated results for all excited states through the 4s orbital.

The tool we have recently developed that is ideally suited to providing multiple potential
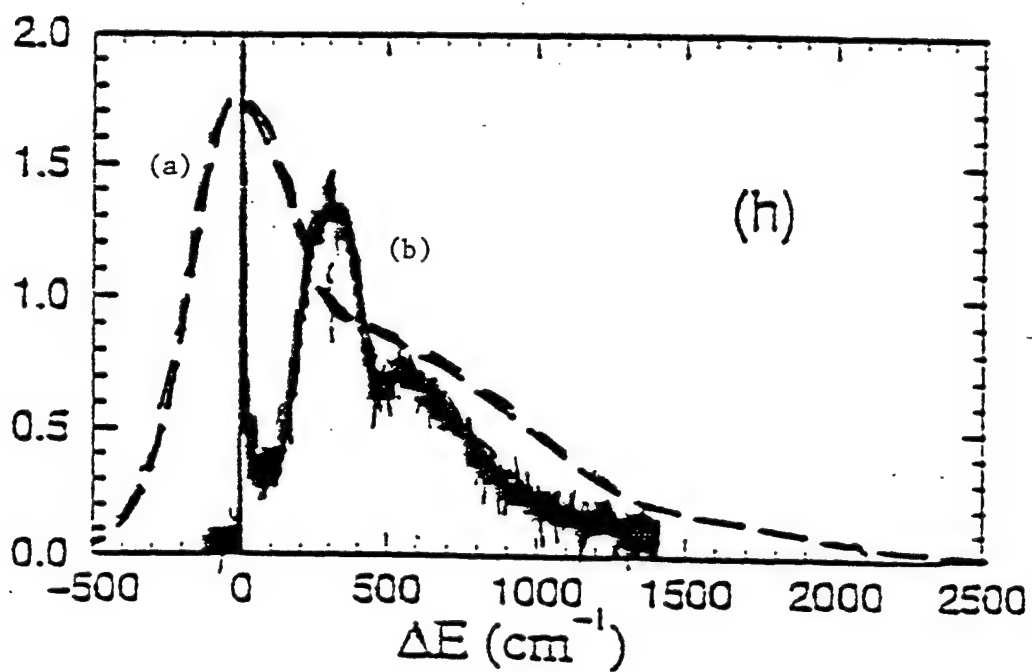
Figure 1: Experimental Spectrum

(a) - - - - -    M.E. Fajardo, JCP (1993)

(b) _____    F. Stienkemeier, J. Higgins, C. Callegari and G. Scoles

energy surfaces for $Li + (H_2)_N$ is our electron-attached equation-of-motion (EOM) coupled-cluster (EA-EOMCC) method [5].

The idea of the EOM-CC method is quite simple. Consider the Shrödinger equation for the ground and a final (excited, electron attached or ionized) state,

$$H\psi_o = E_o\psi_o \tag{1}$$

$$H\psi_f = E_f\psi_f \tag{2}$$

Without approximation, we can write

$$\psi_f = \hat{R}_f\psi_o, \tag{3}$$

where $\hat{R}_f$ is some suitably chosen operator. Inserting this into the second equation, multiplying the first by $\hat{R}_f$ from the left and subtracting, gives

$$\left(H_f\hat{R}_f - \hat{R}_fH\right)\psi_o = \left(E_f - E_o\right)\hat{R}_f\psi_o \tag{4a}$$

$$[H, \hat{R}_f]\psi_o = \omega_f\hat{R}_f\psi_o \tag{4b}$$

which is the EOM.

Coupled-cluster theory comes from $\psi_o = \exp\left(\hat{T}\right)\Phi_o$, and since $[\hat{R}_f, \hat{T}] = 0$ we can rewrite Eq. (4) as

$$[\bar{H}, \hat{R}_f]\Phi_o = \omega_f\hat{R}_f\Phi_o \tag{5}$$

$$\bar{H} = \exp(-\hat{T})H\exp(\hat{T}) \tag{6}$$

The choice of $\hat{R}_f$ depends upon the process of interest. For an electronic excited state,

$$\hat{R}_f^{EE} = r_o + \sum_{i,a} r_i^a \hat{a}^\dagger \hat{i} + \sum_{isj} r_{ij}^{ab} \hat{a}^\dagger \hat{i} \hat{b}^\dagger \hat{j} + \dots$$

123

where $\hat{i}, \hat{j}, \hat{k}$ etc. indicates orbitals and operators occupied in $\Phi_o$ while $\hat{a}, \hat{b}, ...$indicates unoccupied orbitals. For an ionized state,

$$\hat{R}_f^{IP} = \sum_j r_j \hat{j} + \sum_{j>i,a} r_{ij}^a \hat{j} \hat{a}^\dagger \hat{i} + ...$$

and for an electron attached state,

$$\hat{R}_f^{EA} = \sum_b r^b \hat{b} + \sum_{b>a,i} r_i^{ba} \hat{b}^\dagger \hat{a}^\dagger \hat{i} + ...$$

Electronic states can be accessed in different ways. For example, we can determine $\hat{T}$ for the CC ground state and use $\hat{R}_f^{EE}$ to create an excited state. We can also access certain excited states by determining $\hat{T}$ from the CC state for a cation, $M^+$ ,and then look at some $M$ excited states by using the $\hat{R}_f^{EA}$ operator that adds an electron into each unoccupied virtual orbital, $b$. The latter EA approach has the advantage that there are only $\sim n_{occ} N_{virt}^2$ coefficients to determine in the single and double excitation approximation shown, compared with $\sim n_{occ}^2 N_{virt}^2$ for the same level approximation in the EE approach. Assuming that the cation reference is a closed shell, the EA solution is also an exact spin eigenfunction, unlike the EE solution for an open shell ground state.. The EA approach is ideally suited to studying $Li + (H_2)_N$ as we have one electron outside a closed shell.

The first element in the study is to assess the accuracy of the EA-EOMCC method for the $Li$ atom. Table 1 shows results as a function of basis set. The especially optimized excited state basis (XB) provides spectacular agreement with experiment. The PBS basis we often use for excited states is too poor for the high lying 2s →4s transition, so we added an extra s and p diffuse function. Although not as spectacular as the results in the XB basis, the PBS* are good. Recognizing that we are not just describing a $Li$ atom, but one embedded in a cluster of $H_2$ molecules, basis set performance for small molecules like $LiH$, and for other properties like structure, dissociation energies, vibrational frequencies, etc. are also pertinent. In particular,

## Table 1: Excited States of Li atom

|  | PBS 10s6p4d/ 5s4p2d] | WMR [14s9p4d3f/ 7s6p4d3f] | Exp. | XB [12s5p2d/ 6s3p2d] | PBS* [11s7p4d/ 6s5p2d] |
|---|---|---|---|---|---|
| 2s->2p | 14830 | 14860 | 14904 | 14906 | 14830 |
| 2s->3s | 27058 | 27145 | 27206 | 27206 | 27028 |
| 2s->3p | 30781 | 31125 | 30926 | 30938 | 30779 |
| 2s->3d | 32628 | 31913 | 31283 | 31278 | 32628 |
| 2s->4s | 47985 | 36507 | 35012 | 35123 | 35635 |

## Table 2: Comparison of basis sets for LiH

|  | PBS* | XB | Exp. |
|---|---|---|---|
| Dipole | 5.390 | 5.921 | 5.88 |
| R(LiH), Å | 1.6070 | 1.6074 | 1.5953 |
| D($H_2$) - D(LiH), kcal/mol | 42.3 | 48.4 | 47.2 |
| $S_0$ - $S_1$, $cm^{-1}$ | 26139 | 25617 | 26516 |

the PBS* basis does better than XB for the lowest excitation energy, bond length and dipole moment of $LiH$ as shown in Table 2, but is poorer for the dissociation energy. Consequently, we provide two sets of PES's using the XB and the PBS* basis. If the final results are sensitive to the very small differences, we can further refine our numerical results. If the final results are insensitive, then we have the confidence that further refinement is likely to be unimportant.

We have computed the ground and excited states of $Li - H_2$ as a function of $\alpha$, the angle between $Li$ and the midpoint of the $H_2$ bond, and a function of R, the distance between $Li$ and $H_2$. We compute the energies for the ground and 14 excited states as a function of $\alpha$ from $0°$ to $90°$ and R from 3.4 to 6.0 Å. Besides the excitation energies, we provide dipole moments for all states, and the oscillator strengths between all excitations.

The above combined with the Monte Carlo dynamics calculations to be done by Whaley, will enable us to do the following:

1.  Directly compute the shift and splitting of the $Li$ atom excited states, as a probe of $Li's$ interaction with solid state hydrogen;

2.  Estimate the validity of perturbation theories based on $Li - H_2$ pair interactions.

3.  Go beyond Balling and Wright [6] perturbation theory, by virtue of having excited state surfaces beyond those that correlate with $L^*(2p)$; the weakest element in the earlier analysis.

4.  To begin to assess (1), (2) and (3), we have also constructed models for $Li$ in a cube of eight $H_2$ molecules, and investigated its excited states. The model allows us to observe the shift and splitting in the $Li$ spectra as a function of distance and a function of one or two $H_2$ molecules compared to eight. These results are summarized in Figs. 2 and 3.

The same procedure can be applied for multiple PES's for $Li, Na, K + H_2, He, Ne$, etc. In this way, we can provide the fundamental information required to help analyze the interesting cluster experiments of Scoles, et. al.

# Figure 2: Computational Models
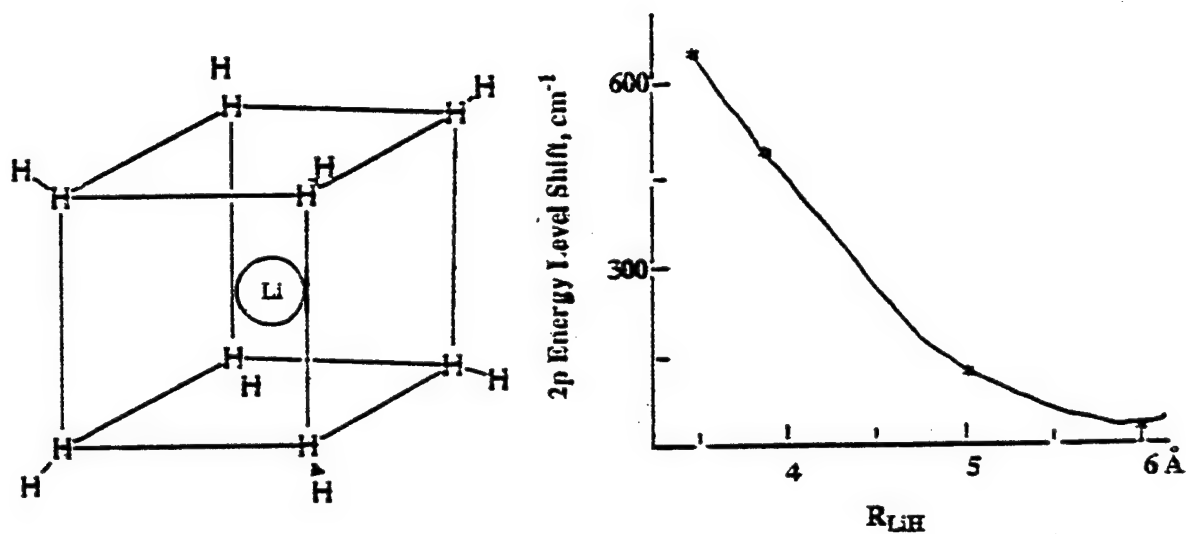


Li atom in $8H_2$ ($O_h$); Li...H-H linear orientation
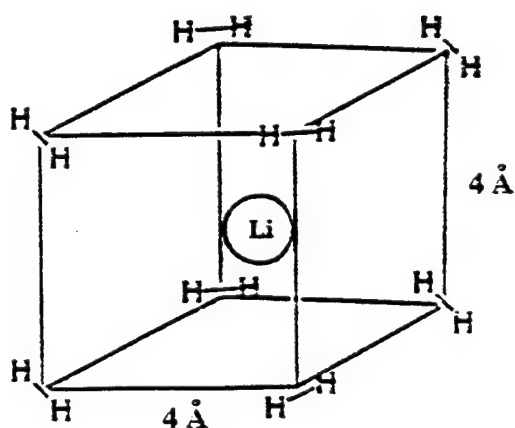


R(Li-H) = 3.48 Å

2s -> 2p:

14288 cm$^{-1}$ x 2
15446 cm$^{-1}$

$\Delta = 1158$ cm$^{-1}$

Li atom in $8H_2$ ($D_{4h}$); Li...$H_2$ perpendicular orientation

# Figure 3: How the number of $H_2$ molecules in Li-$nH_2$ cluster affects 2s->2p excitation energies?



Li—  —  —  —  H
                H
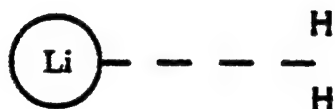
14751 cm$^{-1}$
14785 cm$^{-1}$     $\Delta = 271$ cm$^{-1}$
15039 cm$^{-1}$

R(Li-H) = 4.91 Å

H
—  —  —  —  Li—  —  —  —  H
H                              H
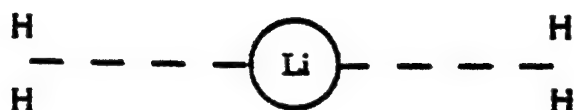
14673 cm$^{-1}$
14741 cm$^{-1}$     $\Delta = 560$ cm$^{-1}$
15267 cm$^{-1}$

8 Å

4 Å
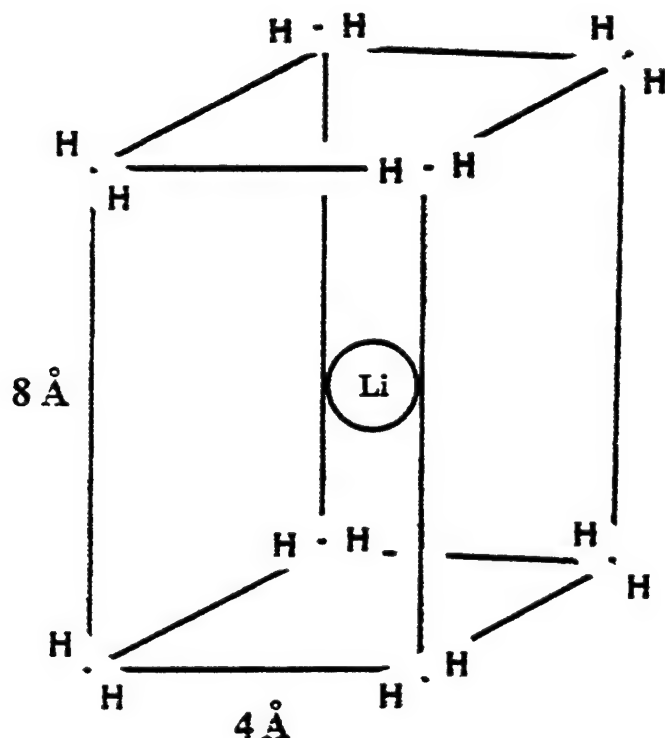
14739 cm$^{-1}$ x 2     $\Delta = 1080$ cm$^{-1}$
15819 cm$^{-1}$

Li atom in gas phase:
E (2s -> 2p) = 14830 cm$^{-1}$ at CCSD/PBS

128

# References

[1]. M.E. Fajardo, J.Chem. Phys. **98**, 110 (1993).

[2]. F. Stienkemeier, J. Higgins, C. Callegari and G. Scoles, to be published.

[3]. E. Cheng and K. B. Whaley, J. Chem. Phys. **104**, 3155 (1996).

[4]. D. D. Konowalow, Technical Report, Phillips Laboratory.

[5]. M. Nooijen and R. J. Bartlett, J. Chem. Phys. **102**, 3629 (1995).

[6]. L.C. Balling and J. J. Wright, J. Chem. Phys. **79**, 2941 (1983).

# Theoretical Studies of Nonadiabatic Processes Relevant to the Stability and Detection of Energetic Species

David R. Yarkony
Department of Chemistry
Johns Hopkins University
Baltimore, MD 21218

## I.  Conical intersections as pathways to energetic materials

### Motivation

Conical intersections can provide efficient pathwiays for the production of ground state products from photochemically prepared reactants.  Relevant in the present context are the cis-trans isoomerization in polyenes and photochemical Diels-Alder (cyclization) reactions.

Recently Chaban *et al.* have identified an isomer of fluorine azide  as a potential high energy density material (HEDM).[1]  This isomer, referred to as cyclic fluorine azide, $N_3F$, consists of a 3-member nitrogen ring with a fluorine bonded to one of the nitrogens, and can be described as an $NF(a^1\Delta)$ moiety bonded to ground state $N_2$.  It is energetic by approximately 15kcal/mol relative to fluorine azide, which has a quasi linear, chain,  structure NNNF.  $N_3F(X^1A')$ is stable with respect to both spin-allowed and spin-forbidden radiationless decay[1] but has yet to be synthesized.  We are in the process of accessing whether conical intersections between the $1,2\,^1A$ potential energy surfaces can provide a photochemical pathway for the production of cyclic $N_3F$ from the chain isomer.

### Computational  Studies

To date we have located points on the surface of conical intersection with the following approximately planar structure
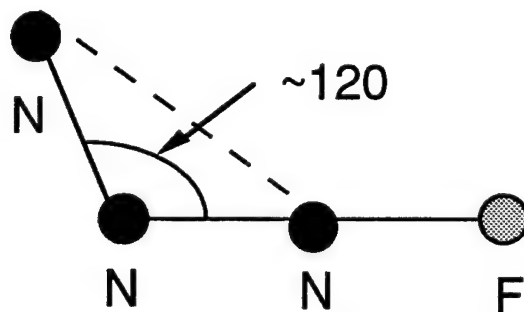


and are considering the possibility of photochemical process

$$NNNF(X^1A') + h\nu \rightarrow NNNF(2^1A) \rightarrow N_3F(1^1A')$$

130

in a buffer gas. To this end we consider whether quasi reaction paths originating near a conical intersection on the $1^1A'$ potential energy surface lead to cyclic $N_3F$ and whether quasi reaction paths on the $2^1A$ potential energy surface originating in the Franck-Condon region of $NNNF(X^1A')$ can lead to the region of the conical intersections. As discussed in the oral presentation the choice of paths near the conical intersection exploits our analysis of g-h paths circumscribing the point of conical intersection.

We intend to perform a similar analysis to see whether cyclic ozone, which has yet to be observed, can be formed from the open structure photochemically.

## II. Quantitative Detection of $BH(a^3\Pi)$ via $BH(a^3\Pi)$ - $BH(b^3\Sigma^-)$ LIF

### Motivation

Benard and coworkers have suggested $BH(a^3\Pi)$ as a possible energy source in an energy transfer chemical laser.[2] The metastable $a^3\Pi$ state stores approximately 1.3 eV of energy for use in a collisional energy transfer chemical laser system analogous to the oxygen-iodine laser system. Quantitative detection of $BH(a^3\Pi)$ is desirable in design of this laser and can be accomplished through $BH(a^3\Pi)$ - $BH(b^3\Sigma^-)$ laser induced fluorescence. The $BH(b^3\Sigma^-)$ state however can be predissociated by a spin-orbit induced interaction with a repulsive $1^3\Sigma^+$ state (see figure below). Thus quantitative detection of $BH(a^3\Pi)$ requires knowledge of the vibrational level dependence of the $BH(b^3\Sigma^-)$ predissociation rate. As part of a joint experimental/theoretical collaboration with P. J. Dagdigian studies were undertaken to determine both the radiative and radiationless decay rates of the $b^3\Sigma^-$ state.[3]

### Experimental/Computational Studies

Lifetimes of rotational/fine-structure levels of electronically excited $BH(b^3\Sigma^-)$, in vibrational levels $v' = 0 - 4$, were determined from fluorescence decay waveforms with laser excitation on isolated rotational lines in the $b^3\Sigma^- - a^3\Pi \Delta v = 0$ sequence. The measured lifetimes were compared with values obtained from a theoretical treatment of the excited state dynamics, in which both radiative decay to the $a^3\Pi$ state, and nonradiative decay through the repulsive $1^3\Sigma^+$ state, were considered. The spin-orbit coupling was determined within the Breit-Pauli approximation using MCSCF/CI wave functions.[3] The relevant potential energy curves and spin-orbit interaction are presented below.
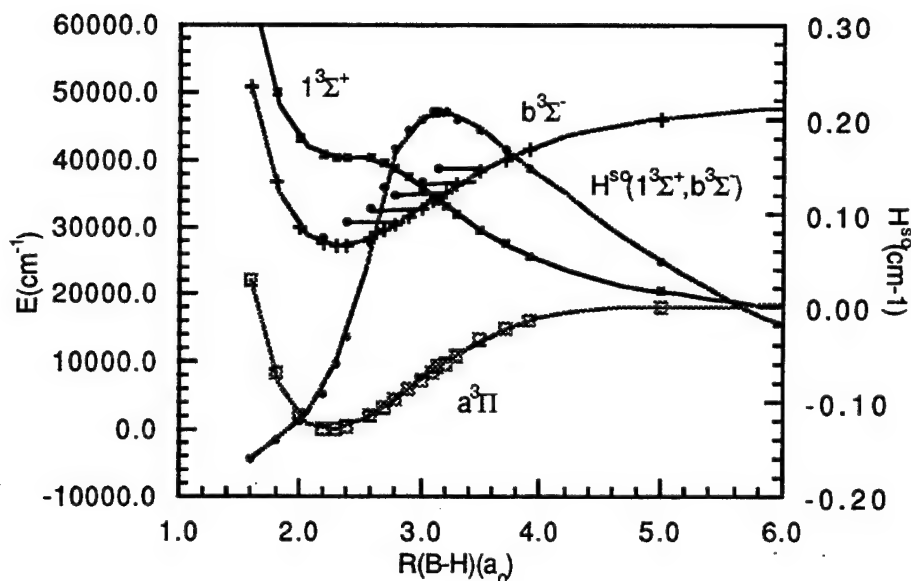
The experimental and theoretical lifetimes agree very well. The comparison shows that the low $b^3\Sigma^-$ rotational levels for $v' = 0 - 2$ decay purely radiatively, with a rate decreasing as $v'$ increases. These rates are virtually independent of the fine-structure level. However the lifetimes of the higher vibrational levels exhibit significant fine-structure level dependence, with the shortest values obtained for the $F_2$ levels. This behavior was shown to be attributable to predissociation induced by $b^3\Sigma^- \sim 1^3\Sigma^+$ spin-orbit coupling.

## III. Detection of BRg

### Motivation

The importance of atomic boron as a potential fuel dopant has lead M. H. Alexander and P. J. Dagdigian to study the interaction of atomic boron with rare gases and molecular hydrogen.[4,5] Spectroscopic probes of these molecules involve the molecular states originating from boron $2s2p^2\ ^2D$ and $2s^22p\ ^2P$ states. Recently Dagdigian has reported that one such transition, the $C^2\Delta \rightarrow X^2\Pi$ transition, is observed in BNe but not in BAr. We have undertaken studies to determine whether the $C^2\Delta$ state in BAr is predissociated by spin-orbit induced coupling to a repulsive $^4\Pi$ state

### Computational Studies

We are in the process of developing atomic orbital, and configuration state function, bases that can describe the $C^2\Delta$ and $^4\Pi$ states of BAr. The description of the $^4\Pi$ state is comparatively straightforward. On the other hand the description of the $^2\Delta$ state is complicated by near degeneracy effects attributable to the atomic boron electron configuration $2s^23d$. Our preliminary results are encourging. Using first order CI wavefunctions and a nonrotating molecule approximation potential energy curves for, and spin-orbit interactions between, the $^4\Pi$ and $C^2\Delta$ states, have been determined. Using these data the folowing preliminary results have been obtained:
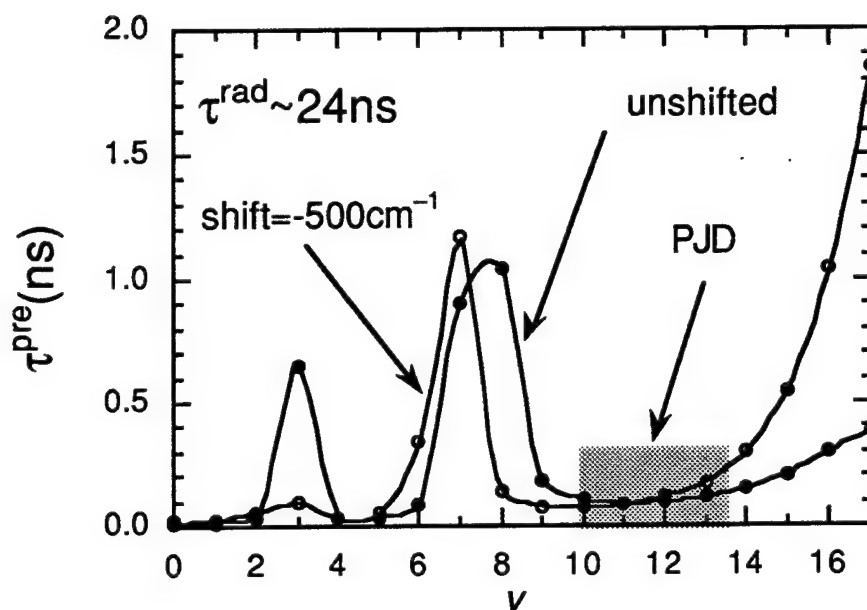


The region labelled PJD corresponds to the vibrational levels of the the $C^2\Delta$ state believed to be probed in the experiments of Yang and Dagdigian. The results indicate that the predissociation rate is much too fast for the $C^2\Delta$ state to be observed in fluorescence.

We are in the process of refining these preliminary studies and intend to extent this work to consider BNe and BKr. The Ne and Kr studies should enable us to quantify the 'heavy atom effect' on 'the spin-orbit coupling in these nonchemically bonded systems.

## REFERENCES

1    G. Chaban, D. Yarkony, and M. Gordon, *J. Chem. Phys.* **103,** 7983 (1995).

2    D. J. Benard, in *Abstracts of the High Energy Density Materials Contractors Meeting* (Air Force Office of Scientific Research, Cal-Neva Lodge, Nevada, 1993).

3    X. Yang, L. Pederson, D. R. Yarkony, and P. J. Dagdigian, *J. Phys. Chem.* **100,** 5649 (1996).

4    X. Yang, E. Hwang, P. J. Dagdigian, M. Yang, and M. H. Alexander, *J. Chem. Phys.* **103,** 2779 (1995).

5    X. Yang, E. Hwang, and P. J. Dagdigian, *J. Chem. Phys.* **104,** 599 (1996).

# POTENTIAL ENERGY SURFACES AND DYNAMICS FOR HIGH ENERGY SPECIES

## EXTENDED ABSTRACT FOR HEDM MEETING, JUNE 5-7, 1996
## BOULDER, COLORADO
## MARK S. GORDON
## DEPARTMENT OF CHEMISTRY
## IOWA STATE UNIVERSITY

Theoretical studies of the potential energy surfaces and dynamics of high energy species has progressed considerably in recent years[1-6]. Identification of such species is frequently aided by recognizing isoelectronic relationships; that is, by (for example) taking well known organic compounds such as bicyclobutane and replacing $CH_2$ groups by isoelectronic NH or O groups. Analysis of the resulting compounds using accurate (i.e., correlated) wavefunctions frequently reveals interesting and potentially useful compounds. High energy species studied in our group recently have included $N_2O_2$ (isoelectronic with bicyclobutane)[1], inorganic prismanes (isoelectronic with benzene and its high energy isomer prismane)[2], $FN_3$ (isoelectronic with bicyclobutane)[3], $NH_4^-$ and $PH_4^-$ [4], tetrasilabicyclobutanes[5], and metal doped clusters of $H_2$[6]. The present report focuses on new features of the $N_2O_2$ potential energy surfaces, as well as on some new studies of silicon analogs of cubane.

### *Heterocubanes*

Using the isoelectronic model noted above, one can imagine a variety of hetero-substituted cubanes, constructed by replacing a "corner" CH group by N or Si, yielding formally neutral species, or by NH, OH, B, C, O, F, BH, NH, yielding formally charged species. This has led to the suggestion of such cubane analogs as $C_4N_4H_4$ (Engelke) and $N_8$ (Bartlett). Indeed, as shown by MP2/6-31G(d) calculations summarized in Table 1, these and other substitutions lead to highly energetic potential energy minima. One interesting species is the cubic tetramer of CO, $(CO)_4$. This species, isoelectronic with $N_8$, is a potential energy minimum, as verified by the SCF/6-31G(d) positive definite hessian and is highly energetic: 358 kcal/mol higher in energy than 4 CO. However, such a large exothermicity should raise a red flag, since the Hammond postulate would suggest a very small barrier for such an exothermic reaction. Indeed, the barrier for the unimolecular decomposition of $(CO)_4$ is only 0.002 kcal/mol! Clearly, this compound is not a viable HEDM species. Comparison of this result with the analogous calcultions on $N_8$ (exothermic by 467 kcal/mol) suggests that the latter species will also

by unstable to unimolecular decomposition. The barrier for $N_8$ decomposition will be reported in a later report.

Note that, starting from cubane, one can systematically replace CH groups with N groups. Replacement of four CH's with four N's changes the unimolecular decomposition energetics from 97.4 endothermic to 83.6 exothermic. This suggests that one can design effective HEDM species by selective substitutions.

An obvious substitution is Si for C, since Si is in the same group as C in the periodic table. Of course, such Si compounds should be thought of primarily as additives, in view of the mass of silicon. Unlike many potential HEDM species, a substituted version of octasilacubane, t-butyl-octasiliacubane (TBOSC), has already been synthesized[7]. Furthermore, the X-ray crystal structure is available, indicating "normal" Si-Si distances, the density is known, and the compound is stable to 250°C in vacuum. So, the questions we set out to answer are: (1) Is TBOSC stable to unimolecular decomposition? Most certainly, the answer to this question is yes, since the compound exists as a stable species; (2) Is TBOSC stable with respect to reactions with $H_2$?; (3) How large is the heat of combustion, as measured by the reaction

$$TBOSC + 58 \; O_2 + 8 \; SiO_2 + 32 \; CO_2 + 36 \; H_2O \qquad ?$$
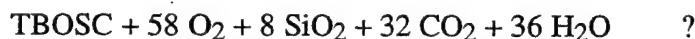
To answer the first question requires consideration of both isomerization and unimolecular decomposition. A recent paper by Versteeg and Koch[8] has examined the relative atabilities of 22 isomers of $X_8H_8$, for X = C, Si, using MP2/6-31G(d) energies. As one would expect, there are striking differences between the relative stabilities of the Si isomers and those of the analogous C isomers. For C, the most stable isomer is semibulvalene, while cubane is 76 kcal/mol higher in energy. In contrast, the cubane structure is the most stable Si isomer. So, clearly octasilacubane (OSC) is stable to isomerization.

With regard to unimolecular decomposition, we have calculated the energy of OSC relative to several possible products. One can imagine extruding a disilyne, whose minimum energy structure has a double hydrogen bridge. This leaves behind a prismane species, and the reaction is endothermic by 104 kcal/mol. This is the *least* endothermic reaction we have found. Dissociation to two $Si_4H_4$ molecules is endothermic by 154 kcal/mol, and decomposition to four disilynes is uphill by 257 kcal/mol. It therefore appears that OSC is stable to unimolecular decomposition

Reacting OSC with a molecule of $H_2$ ultimately leads to a partially open $Si_8H_{10}$ species, with an energy release of about 24 kcal/mol. Although this reaction is exothermic, this two step process through a high energy intermediate has a net energy barrier of 54.5 kcal/mol. So, at "normal" temperatures, OSC is expected to be stable to attack by $H_2$.

We now turn our attention to the potential that OSC or TBOSC may be useful HEDM species. The heats of combustion for several high energy species, including OSC and TBOSC, are listed in Table 2. Both OSC and TBOSC have very high heats of combustion. Because it is so light, $H_2$ wins easily on a cal/g basis, but not when the densities (cal/cm$^3$ are taken into account. Then, for an air-breathing (ramjet) system, the winners are RJ-4 and cubane, although the latter is difficult to synthesize. For a self-contained system, for which the oxygen must be carried internally, TBOSC becomes quite competitive, especially since there is a known synthetic route. In addition, note that the heat of combustion for TBOSC assumes that $SiO_2$ is formed in the gas phase. If $SiO_2$ is formed in a condensed phase, the heat of combustion of TBOSC becomes much more exothermic.

### $N_2O_2$

We have previously identified five isomers of $N_2O_2$ that are candidates for high energy species, **1 - 5** in Figure 1. Of these, isomer **1** is unstable to nonadiabatic pre-dissociation via a low-lying triplet state. In order to obtain a consistent picture of the potential energy surfaces for the remaining four isomers, it is necessary to use multi-configurational wavefunctions in which 14 electrons in 12 orbitals are included in the active space, CASSCF(14,12). The final energies are then obtained by incorporating dynamic correlation via multi-reference second order perturbation theory, CASPT2.

At the CASPT2 level of theory, the barrier to decomposition of $D_{2h}$ isomer **1** to 2 NO molecules is a large 39.4 kcal/mol. The exothermicity of this reaction is nearly 50 kcal/mol. As shown in Figure 2, the lowest triplet state does cross the singlet before the transition state, but the crossing occurs at an energy of more than 35 kcal/mol, still a substantial barrier. So, isomer **1** may be a viable HEDM candidate.

The planar $C_{2v}$ isomer **3** also dissociates exothermically to 2 NO, with a CASPT2 exothermicity of 45 kcal/mol and a barrier height of 19 kcal/mol. In this case, the

repulsive triplet state crosses the singlet surface behind the barrier, so non-adiabatic coupling is not expected to play an important role. Once again, we can conclude that isomer **3** is a potential HEDM species.

The potential energy surface for the bicyclo isomer **2** is more complex. This potential energy surface is still under investigation at the CASSCF(14,21) level of theory, but CASSCF(10,10) calculations already provide interesting insights. At the CASPT2/CASSCF(10,10) level of theory, there is a 20 kcal/mol barrier leading from **2** to isomer **5**. This reaction is exothermic by 26 kcal/mol. However, CASPT2/CASSCF(14,12) calculations show that isomer **5** dissociates to 2 NOwith a barrier of only 8 kcal/mol. The triplet state crosses this surface only after the barrier is traversed, so it appears that non-adiabatic coupling again is unimportant. Nonetheless, the small barrier separating **5** from 2 NO suggests that this isomer may not be a viable HEDM candidate, except at very low temperatures.

**REFERENCES**
1. K.A. Nguyen, M.S. Gordon, J.A. Montgomery, and H.H. Michels, J. Phys. Chem., 98, 10072 (1994).
2. N. Matsunaga and M.S. Gordon, J. Am. Chem. Soc., 116, 11407 (1994).
3. G. Chaban, D.R. Yarkony, and M.S. Gordon, J. Chem. Phys., 103, 7983 (1995).
4. N. Matsunaga and M.S. Gordon, J. Phys. Chem., 99, 1277 (1995).
5. J.A. Boatz and M.S. Gordon, Organomet., 15, 2118 (1996).
6. G. Chaban and M.S. Gordon, J. Phys. Chem., 100, 95 (1996).
7. K. Furukawa, M. Fujino, N. Matsumoto, Appl. Phys. Lett., 60, 2744 (1992)
8. U. Versteeg and W. Koch, J. Comp. Chem., 15, 1151 (1994).

**Table 1.** Unimolecular dissociations of some substituted cubanes (kcal/mol)
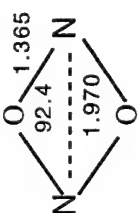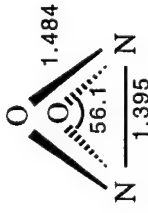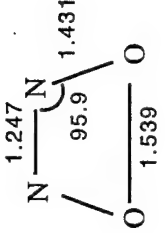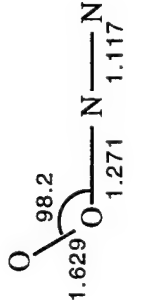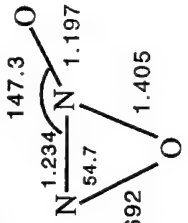
| REACTION | RHF/6-31G(d) | MP2/6-31G(d) |
|---|---|---|
| $C_8H_8 \rightarrow 4\ C_2H_2$ | 76.9 | 97.4 |
| $H_4C_4N_4 \rightarrow 4\ HCN$ | -99.8 | -83.6 |
| $N_8 \rightarrow 4\ N_2$ | -518.7 | -466.9 |
| $B_4N_4H_8 \rightarrow 4\ HBNH$ | 141.4 | 157.4 |
| $H_4B_4O_4 \rightarrow 4\ HBO$ | 83.1 | 84.3 |
| $C_4N_4H_4 \rightarrow 4\ CNH$ | -198.3 | -155.3 |
| $C_4O_4 \rightarrow 4\ CO$ | -409.4 | -358.0 |

**Table 2.** Heats of Combustion at 298K

| COMPOUND | $\Delta H_c$ kcal/mol | AIR BREATHING cal/g | cal/cc | SELF-CONTAINED cal/g | cal/cc |
|---|---|---|---|---|---|
| $H_2(l)$ | -57.8 | -28,670 | -2,030 | -3,208 | -1,360 |
| $H_2(s)$ | -57.8 | -28,670 | -2,466 | -3,208 | -1,542 |
| RJ-4 | -1,674 | -10,190 | -9,374 | -2,363 | -2,553 |
| $C_8H_8$ | -1,133 | -10,875 | -14,030 | -2,671 | -3,134 |
| $Si_8H_8$ | -986 | -4,235 | | -1,783 | |
| $Si_8Me_8$ | -2,083 | -6,038 | | -1,986 | |
| TBOSC | -4,953 | -7,267 | -7,325 | -1,952 | -2,150 |

# N$_2$O$_2$ HIGH ENERGY ISOMERS

MCSCF(10,10)/6-31G(d) geometries (A,deg.) and relative energies (kcal/mol) with reference to 2NO



| Relative energy, kcal/mol | 1. D$_{2h}$ | 2. C$_{2v}$ | 3. C$_{2v}$ | 4. C$_s$ | 5. C$_s$ |
|---|---|---|---|---|---|
| MCSCF/6-31G(d) | 71.0 | 71.2 | 41.6 | 60.3 | 66.0 |
| CASPT2/6-31G(d) | 49.0 | 77.3 | 47.7 | 79.3 | 53.0 |
| MCSCF/6-311+G(2d) | 71.7 | 73.2 | 47.0 | 57.1 | 68.4 |
| CASPT2/6-311+G(2d) | 48.7 | 81.9 | 53.1 | 75.5 | 55.7 |

141

# Quantum Mechanical Study of the Energetics of C8H8 Hydrocarbons

E. J. Wucherer & Jerry Boatz
Phillips Laboratory
Edwards AFB, CA 93524

The current laboratory synthesis of cubane entails 6-8 steps, numerous purifications, solvents and generates significant wastes. A conceptually attractive and much shorter synthesis would be the 2+2 closure of tricyclo[4.2.01,6.02,5]octa-3,7-diene (Fig. 1). This route has been demonstrated for CF3- and CH3- substituted cubanes, but not for the parent C8H8. Three reasons have been cited for the failure of the formally allowed photochemical ring closure: 1) generation of excessive ring strain during the closure, making the process thermodynamically "up hill"[1], 2) the large (ca 3.0A) separation of the two olefins in the starting material, making the concerted ring closure kinetically unfeasible[1], and 3) through-space interaction of the $\pi$ bonding orbitals with the sigma framework resulting in a reordering of the energies of the frontier orbitals making the process "disallowed"[2].

Previous experimental and calculational effort has focused on the singlet potential energy surface. The methyl- and perfluoromethyl- compounds were synthesized in degassed inert solvents without added sensitizers. A common rule of thumb is that if a photochemical reaction does not proceed as you intend, a triplet sensitized photochemical reaction may give the desired transformation. This is based on the characterization of singlet photochemical reactions as fast concerted processes while triplet sensitized reactions are often best described as slower, step-wise, biradical processes. We therefore began to look both theoretically and experimentally at the transformation of the diolefin to cubane via a sensitized photochemical reaction. This report will cover the theory portion of our effort.

Our initial focus was on determining the appropriate basis set to use for the study. The geometry of the biradical olefin was optimized first using the PM3 method in the GAMESS program package. Subsequent geometry optimizations with 6-31G, 6-31G(d,p), 6-31++G(d,p), 6-311G(d,p), 6-311++G(d,p) and aug-CC-vdz basis sets under C1 symmetry revealed that beyond 6-31G(d,p) the geometry showed little variation. We opted to include diffuse s and p functions based on the assumption that these would give a better description on the molecules later in the study when solvent, electrostatic and pressure effects would be addressed. Consequently, 6-31++G(d,p) was chosen as the basis set for the study. This results in a total of 200 functions to describe the molecules under C1 symmetry.

The geometries of six minima and five transition states were optimized using Unrestricted Hartree Fock (UHF) after the Restricted Open-Shell Hartree Fock (ROHF) approach failed to provide reasonable results for two of the transition state geometries. While UHF provided reasonable geometries, the $S^2$ values at the transition states often exceeded 2.2 vs. the expected value of 2.0 of a pure triplet (and as obtained at the minima). This indicated that the

UHF wavefunctions were significantly spin contaminated and that more sophisticated multi-reference or coupled-cluster methods were needed to accurately characterize the molecules. The Hessian was calculated at each stationary point to verify it as a local minimum or transition state. Intrinsic Reaction Coordinate (IRC) calculatons were performed to trace the minimum energy pathway from each saddlepoint to the corresponding reactants and products - confirming that the transitions state did in-fact connect the intended minima. The energies of each of the stationary points was calculated at MP-2, the resultant map of the potential energy surface is shown in Fig. 2.

The starting material, a biradical olefin, exhibits the expected geometry with a short 1.32 A double bond distance, a 1.51A distance between the two radical centers and 3.05A non-bonded distance from the radical carbon to one of the olefinic carbons - the bond we would like to close. Initial studies with ROHF and UHF revealed 3 conformers for this species, differing by their relative geometries at the biradical centers. MCSCF studies (see below) showed that the "twisted" conformer shown in Fig. 3 was the most stable minimum energy structure - although it was not the lowest energy species at the ROHF and UHF calculations.

The transition state connecting the starting material with the cubyl triplet target molecule exhibits a lengthening of the former olefinic bond to 1.41A and the nascent formation of a new carbon-carbon bond with a distance of 2.15A. At this level (UHF), there is no significant energy difference (Fig. 4) between this desired path-way to a cubyl radical and the other two undesired pathways - a twisting ring closure toward cuneane type products and a ring-opening pathway to a bicyclic decomposition product.

A potential decomposition pathway away from the cubyl radical was also explored. This rearrangement route lead to cuneane product. The energy barriers around the cubyl radical are larger than those found around the biradical-olefin, but they could still be small enough to allow significant rates of decomposition of a cubyl triplet before it collapses to the desired cubane singlet. Thus, one possible scenario would be that the cubyl intermediates are formed photochemically, but that they are unstable under real reaction conditions and only the more-stable cuneane product is isolated.

A more plausible explanation of the previous experimental observations emerges when the starting material and the three transition states are examined with multi-reference methods. The transition state energy barrier for the ring-opening decomposition route steadily decreases relative to the other two bond-forming transition states as MCSCF 4e-/4orbital, MRCI 4e-/4orbital and MCSCF 6e-/6orbital treatments are applied and the geometries optimized (Figs. 5-7). These limited multi-reference treatments do not correlate the same sets of orbitals for each geometry so the comparison of energies is not rigorously correct. Computer limitations however, prohibit us from a full multi-reference or correlated treatment of all carbon bonding electrons (24e-/24orbitals). At this point the emerging differences in energy between the various reaction paths and the low symmetry of the species (C1) lead us to predict that inclusion of further reference states would not dramatically change

the relative energy picture nor contradict the conclusion that the ring-opening decomposition route is the favored reaction pathway.

One further task remains, we hope to take a more extensive look at the relative energies of the olefin triplet and the cubyl triplet in order to address the thermodynamic postulate about the failure of this reaction route. If the cubyl radical is indeed more thermodynamically stabile than the olefin biradical, then it may still be possible to find experimental routes or conditions which produce cubane by avoiding the kinetically preferred reaction route which we have identified here.

REFERENCES:

1) E. Osawa, J. Org. Chem., 42, 2621, 1977

2) R. Gleiter, K. Pfeifer & W. Koch, J. Comp. Chem., 16, 31, 1995

# Figure 1. Photochemical Routes to Cubanes

$R_8 =$
(a) $H_8$
(b) $(CH_3)_8$
(c) $(CF_3)_8$
(d) $(C_3H_6)_4$

$R_8 =$
(b) $(CH_3)_8$
(c) $(CF_3)_8$
(d) $(C_3H_6)_4$
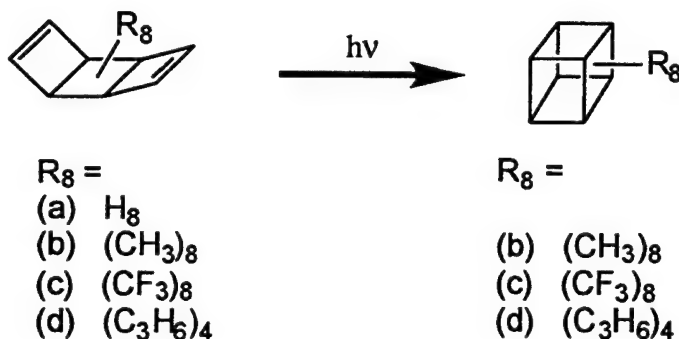
a) H. Iwamura, K. Morio & H. Kihara, Chem. Lett., 457, 1973 - unsuccessful

b) R. Gleiter & S. Brand, Tett. Lett., 4969, 1994 - traces, degassed pentane

c) L. Pelosi & W. Miller, JACS, 98, 4311, 1976

d) R. Gleiter & M. Karcher, Angew. Chem. Int. Ed. Engl., 27, 840, 1988 - 7%, degassed pentane

Figure 2. UMP2/6-31++G(d,p)//UHF/6-31++G(d,p) Relative Energies of Triplet C8H8's



Figure 3. Geometry of Starting Material (Å)

|        | C3 - C7 | C4 - C8 |
|--------|---------|---------|
| Upper: UHF/6-31++G(d,p) | 2.948 | 3.051 |
| Lower: MCSCF(6e⁻/6o)/6-31++G(d,p) | 2.945 | 3.046 |

145
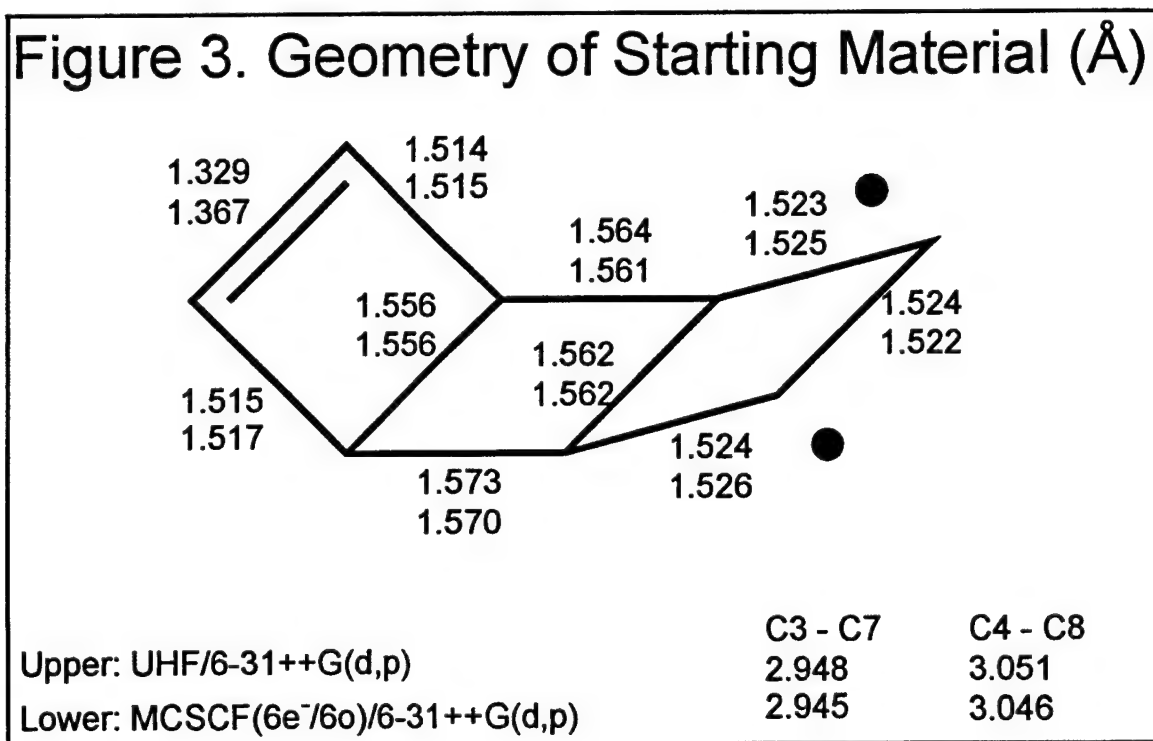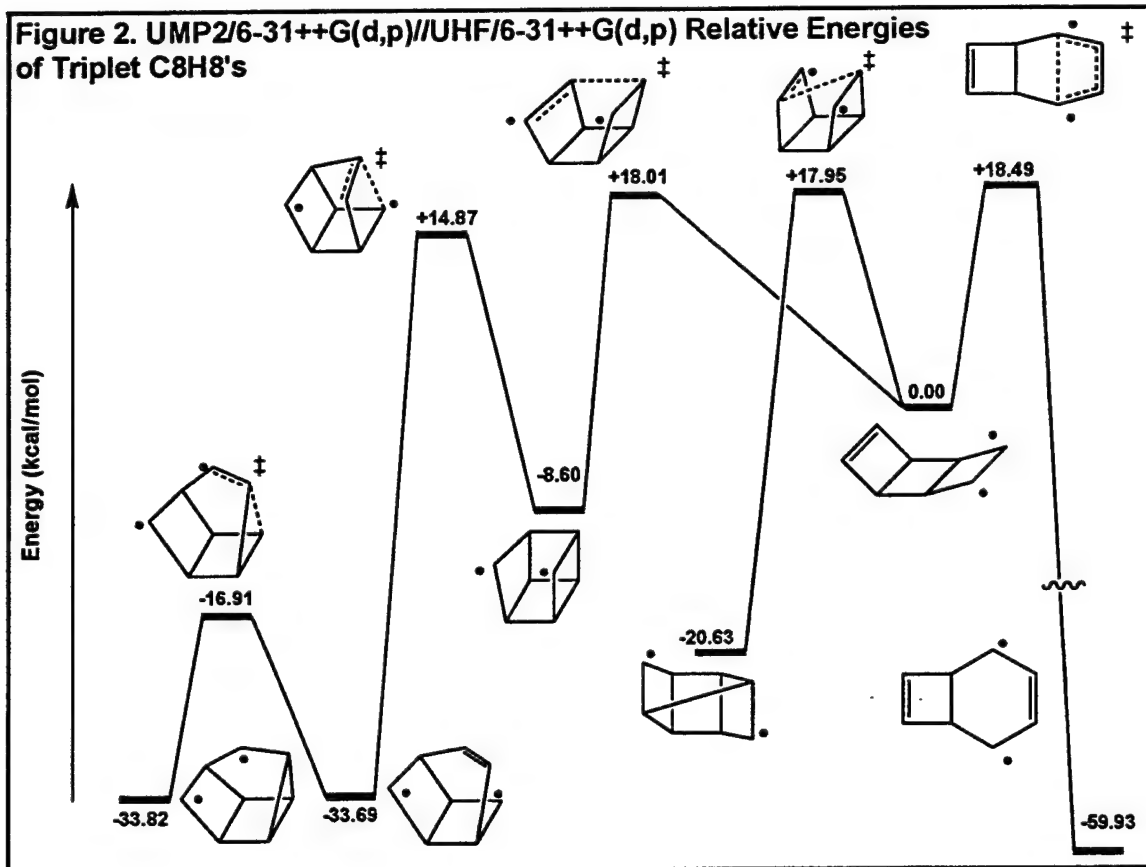
Figure 4. UMP2/6-31++G(d,p)//UHF/6-31++G(d,p) Relative Energies of Triplet C8H8's



Figure 5. CASSCF(4e⁻/4o)/6-31++G(d,p) Relative Energies of Triplet C8H8's

146

Figure 6. MRCI/6-31++G(d,p)//CASSCF($4e^-$/4o)/6-31++G(d,p) Relative Energies of Triplet C8H8's
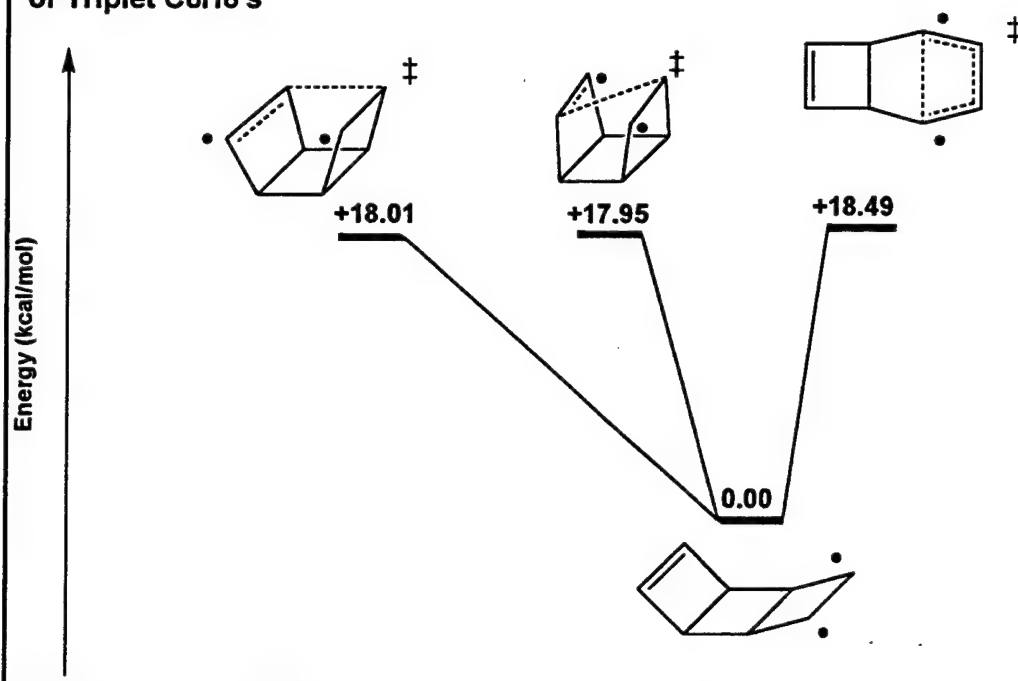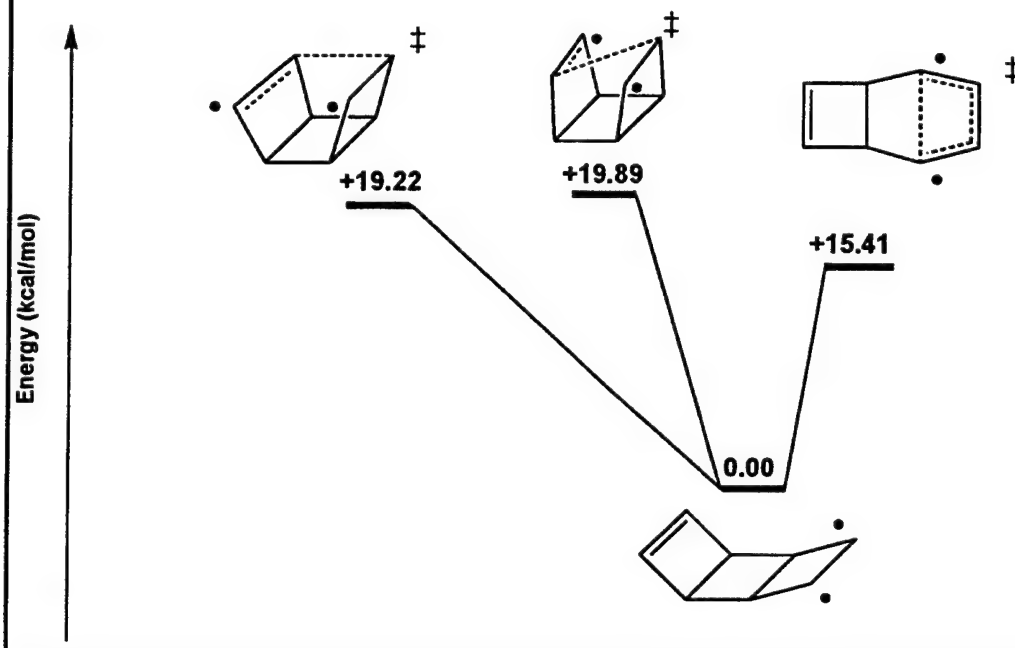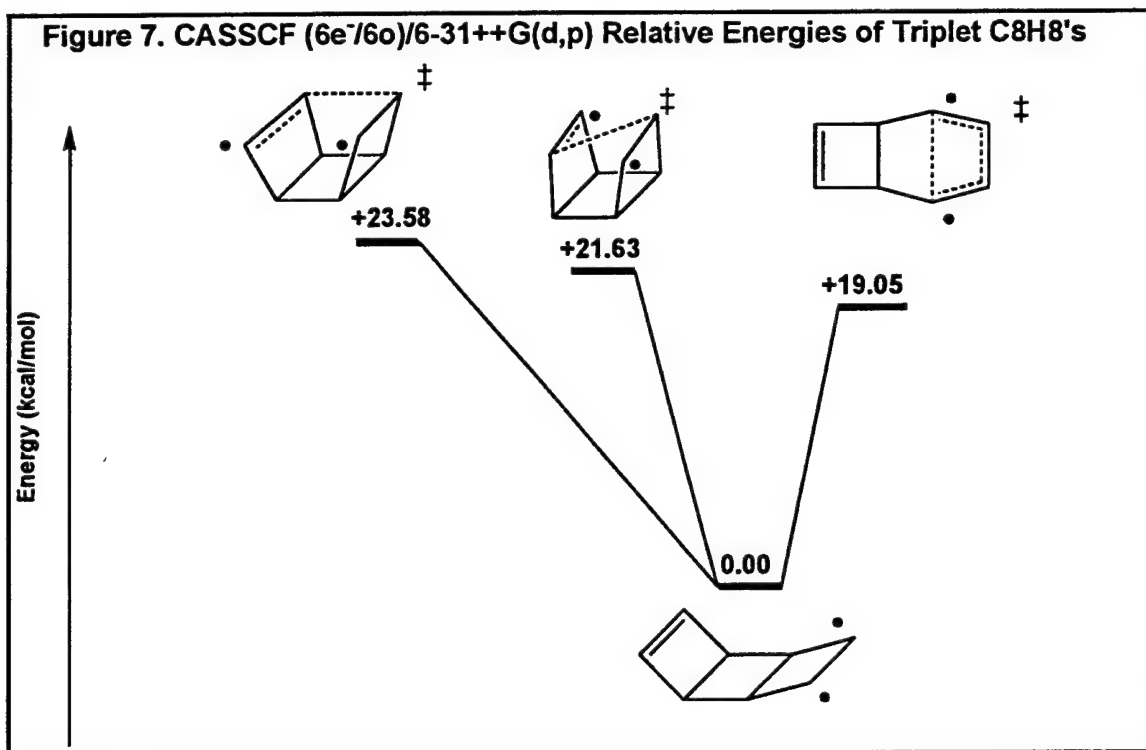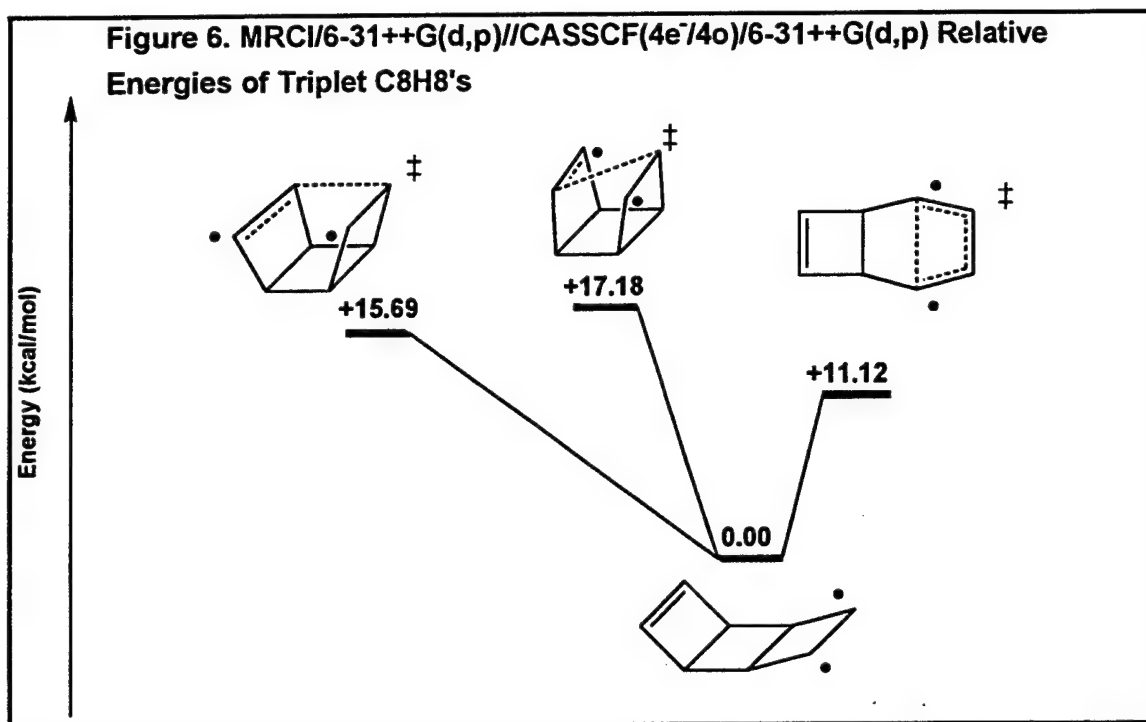


Figure 7. CASSCF ($6e^-$/6o)/6-31++G(d,p) Relative Energies of Triplet C8H8's

# SYNTHESIS OF HIGH-ENERGY DENSITY MATERIALS BASED ON STRAINED-RING COMPOUNDS

William P. Dailey
Department of Chemistry
University of Pennsylvania
Philadelphia, PA  19104-6323

We have been investigating the synthesis of new strained-ring hydrocarbons as potential high energy fuels and fuel additives. Cyclobutane contains almost exactly the same amount (26.5 kcal/mol) of strain energy as cyclopropane (27.5 kcal/mol) yet four membered rings are chemically and thermally much more stable than cyclopropane derivatives. We have investigated two different areas this past year which focus on the synthesis of molecules that contain multiple four membered rings.

The first area involves efforts toward the preparation of an unknown prismane, hexaprismane (**4**), a formal face-to face dimer of benzene. Prismane (**1**), cubane (**2**), and pentaprismane (**3**) have already been prepared but the synthesis of hexaprismane has not yet been achieved. Hexaprismane is predicted to have 175 kcal/mol of strain energy and a calculated Isp of 313 sec. We have made good progress towards the synthesis of hexaprismane and have recently prepared bishomohexaprismanedione (**5**).[1] We believe that hexaprismane can be prepared using similar chemistry.



**1**     **2**     **3**     **4**     **5**
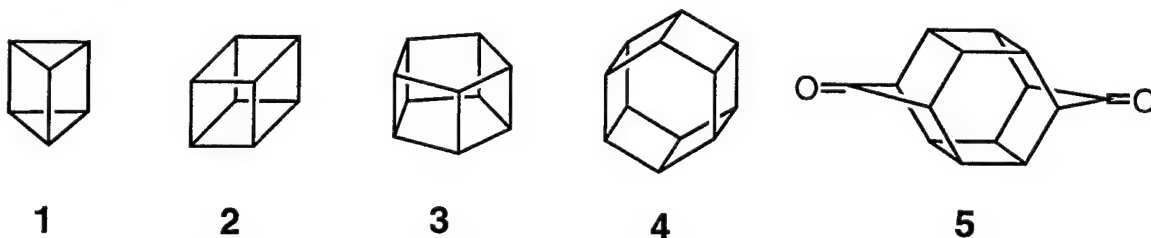
The starting point for our synthesis of **5** was bishomosecoheptaprismanedione **6** which is conveniently available in 8 steps[2] and without resort to any chromatography starting with the Diels-Alder adduct between 5,5-dimethoxycyclopentadiene and benzoquinone. Conversion of the bishomosecoheptaprismane system of **6** to the bishomohexaprismane system can be accomplished in the following manner (Scheme I). Dione **6** was converted to diol **7** using $NaBH_4$, and this was converted to dimesylate **8**. Dimesylate **8** was converted to diiodide **9** as a mixture of diastereomers which when treated with Na/K alloy produced diene **10** in good yield via Grob fragmentation. Diene **10** was converted to the highly water soluble tetraol **11** in quantitative crude yield using catalytic $OsO_4$. Treatment of crude tetraol **11** with periodic acid leads to formation of **12**, the doubly ring contracted product, in 60% yield. The hydroxyl groups in **12** were protected as the acetates to give **13**, and the aldehyde groups were oxidized with $KMnO_4$ to produce diacid **14**.

The carboxylic acid groups were converted to bromides via Hunsdiecker reaction to give **15**. Treatment of **15** with lithium dispersion in *t*-BuOH/THF solution resulted not only in reductive debromination as we had anticipated but also reductive fragmentation to form diene **16** in 25% overall yield. Hydrolysis of **16** produced dienedione **17** which also underwent photochemical ring closure to the highly sought-after norbornadienone dimer **5**.

## Scheme I.
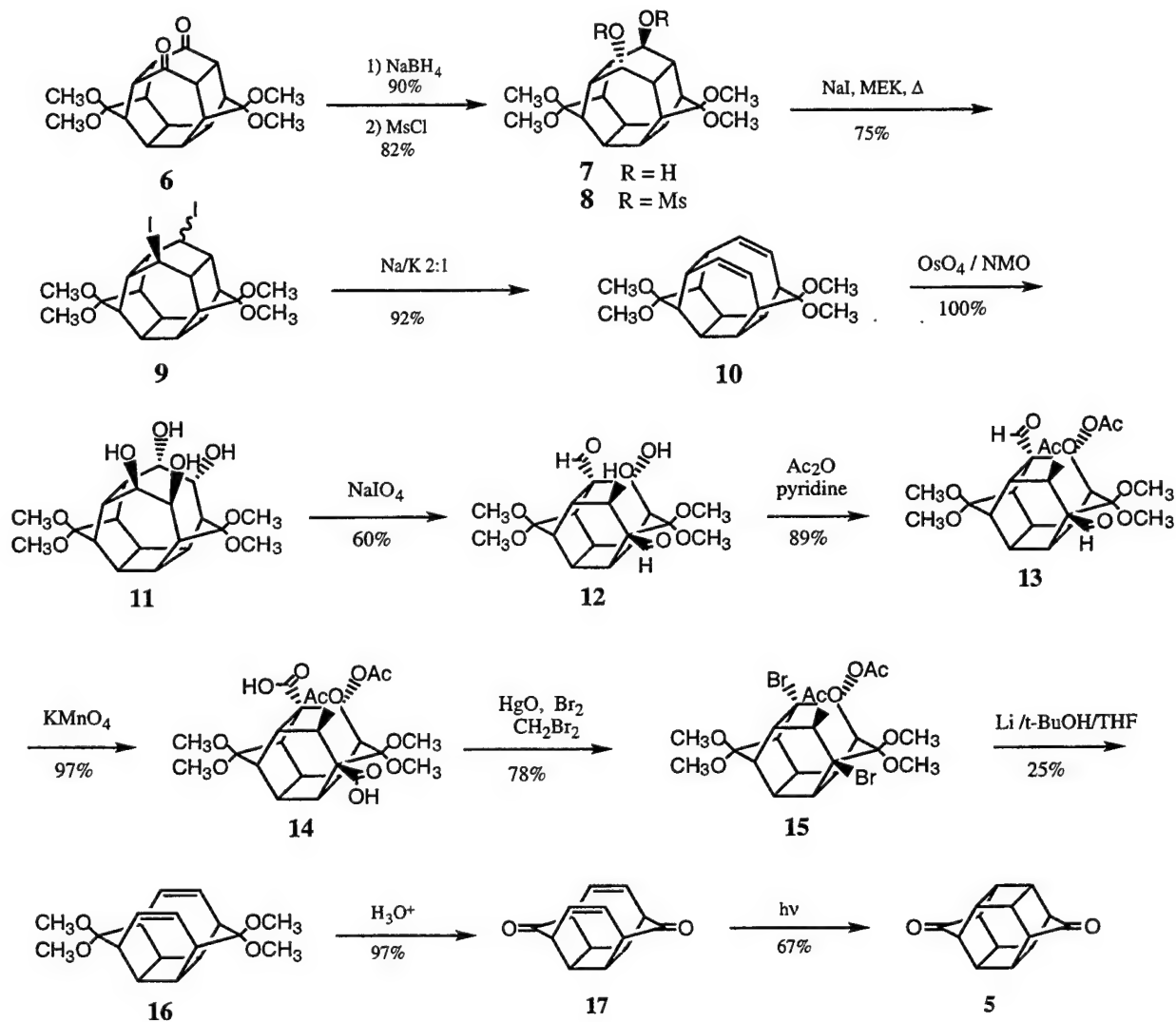


The structure of **5** was determined by single crystal x-ray analysis and some of the results are compared with those obtained from geometry optimized ab initio calculations at the HF/6-31G* level (Table I). The agreement is outstanding. Efforts to prepare hexaprismane using variation of this chemistry are in progress.

Table I.     Comparison of Bond Lengths in **2** .

| Bond | X-ray(Å) | HF/6-31G* |
|------|----------|-----------|
| C1*- C4 | 1.546 | 1.546 |
| C3-C4 | 1.530 | 1.538 |
| C3-C7 | 1.535 | 1.536 |
| C4-C5 | 1.574 | 1.569 |
| C7-O1 | 1.206 | 1.183 |
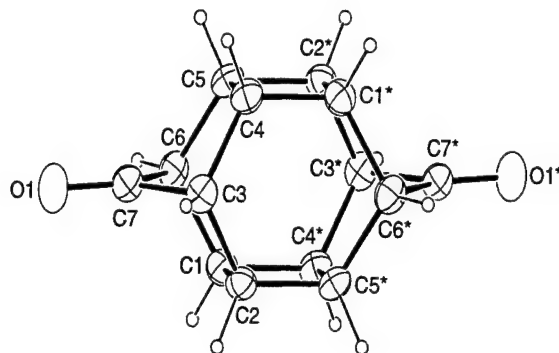


A second area of study concerns the conversion of [1.1.1] to stable high energy materials. The remarkably direct Szeimies synthesis[3] of [1.1.1]propellane (**18**) has allowed the investigation of many reactions of this compound on a preparative scale. The Szeimies method involves addition of dibromocarbene to commercially available 3-chloro-2-(chloromethyl)-1-propene (**19**) followed by methyl lithium induced ring closure of 1,1-dibromo-2,2-bis(chloromethyl)cyclopropane (**20**).
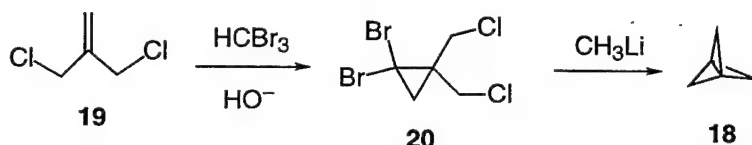


While this method is brief, literature yields for the dibromocarbene addition reaction are modest (30% of recrystallized material), and the work-up is time-consuming due to emulsions. Additionally, 3-chloro-2-(chloromethyl)-1-propene is expensive. We have developed procedures[4] that allow the preparation of large quantities of **19** and **20** in good yields.

The synthesis of 3-chloro-2-(chloromethyl)-1-propene (**19**) can be accomplished by the direct chlorination of methallyl chloride but the yields are low and purification involves a tedious spinning band distillation. A much more satisfactory method is described in our recent report[4] starting with pentaerythritol (**21**). Pentaerythritol is converted to a 2.8:1 mixture of trichloride **22** and tetrachloride **23** using 3.08 equivalents each of pyridine and thionyl chloride. Without purification, the crude mixture of chlorides is oxidized with hot nitric acid. Unreacted tetrachloride **23** may be recovered unchanged from the oxidation while the trichloride **22** is converted to the carboxylic acid **24**. The overall yield of crude acid **24** is 55% from **21**. Heating the crude acid **24** to 210 º C allows for smooth decarboxylation and elimination of HCl and gives a virtually quantitative yield of pure alkene **19**.



150
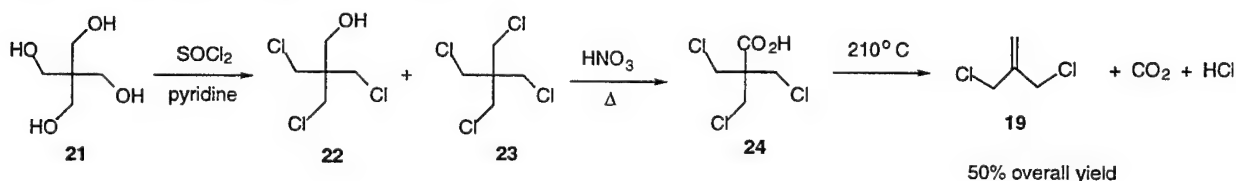
Optimization of the conditions for the dibromocarbene addition to alkene **19** required many trials. Finally a set of conditions were found that afforded high yields of **20** with easy workup.[4] These conditions involve the combination of a catalytic amount of pinacol and dibenzo-18-crown-6 together with bromoform and 50% aqueous sodium hydroxide solution at 40 °C. In this way pure crystalline cyclopropane can be obtained in yields of up to 80%.
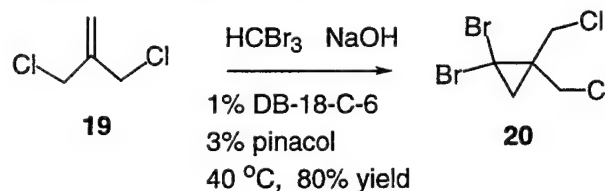


While [1.1.1]propellane shows modest stability, it is sensitive to Lewis acids, strong bases and moderate temperatures. We are interested in developing methods that will allow the conversion of the high energy [1.1.1]propellane system to more kinetically stable species that still have high energy. These will be useful as high energy fuel candidates. Cleaving the central carbon-carbon bond in [1.1.1]propellane produces bicyclo[1.1.1]pentanes which are kinetically very stable, yet have 68 kcal/mol of strain energy. One attractive candidate as a high energy fuel additive is 1-t-butylbicylo[1.1.1]pentane (**25**) which is available by reaction of propellane with t-butyl lithium followed by protonolysis.[5] This molecule is a liquid at room temperature and has a boiling point of 90 °C. It is a very stable compound that is unaffected by moderate temperatures or acids or bases. Geometry optimized ab initio calculations at the 6-31G* level predict a heat of formation of 26 kcal/mol. This translates to an $I_{sp}$ of 308 sec when used as a monopropellant with liquid oxygen. We are in the process of optimizing conditions for the preparation of 1-t-butylbicyclo[1.1.1]pentane so that substantial amounts can easily be prepared. A great advantage of this preparation is that it does not involve any photochemistry and only requires three synthetic steps from commercially available material.
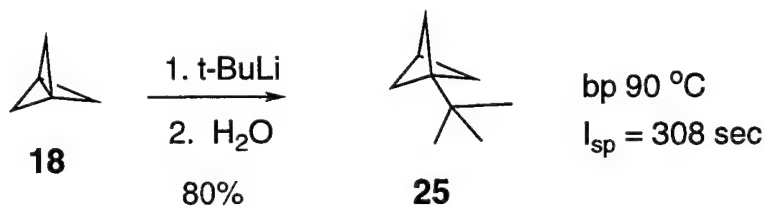


## References

1   Golobish, T. D.; Dailey, W. P. *Tetrahedron Lett.* **1996**, *37*, 3239.
2   Forman, M. A.; Dailey, W. P. *J. Org. Chem.* **1993**, *58*, 1501
3   Semmler, K.; Szeimies, G.; Belzner, J. *J. Am. Chem. Soc.* **1985**, *101*, 6410.
4   Lynch, K.M.; Dailey, W. P. *J. Org. Chem.* **1995**, *60*, 4666.
5   Della, E. D.; Taylor, D. K.; Tsanaktsidis, J. *Tetrahedron Lett.* **1990**, *31*, 5219.

# Recent Progress in the Theory and Synthesis of Novel High Energy Density Materials

*Karl O. Christe, William W. Wilson, Mark A. Petrie and Edward J. Wucherer*
Hughes STX and Propulsion Science Division, Edwards Air Force Base, CA
93524-7680

In collaboration with H. Michels, R. Gilardi and J. Bottaro, the $N(NO_2)_2^-$ anion was characterized by theoretical calculations, x-ray diffraction and vibrational spectroscopy. The crystal structures of $NH_4^+$, $K^+$ and $Cs^+$ dinitramides were determined and compared to the structures calculated at the HF/6-31G*, MP2/6-31+G* and NLDF/GGA/DZVPP levels of theory. The best agreement between experimental and theoretical values was found at the MP2 level. In the salts, the $NO_2$ groups are twisted with respect to each other. The anion is fluxional and easily deformed due to a very small $N-NO_2$ rotational barrier of less than 3 kcal/mol. Even in solution, solvation effects are sufficient to lower its symmetry from the calculated $C_2$ symmetry to $C_1$, based on Raman polarization data.

The $NF_4^+N(NO_2)_2^-$ salt was synthesized by low temperature metathesis, and its decomposition products were studied by ^{19}F NMR spectrtoscopy and IGLO calculations in collaboration with S. Prakash and G. Rasul. Preliminary results indicate that the $FN(NO_2)_2$ molecule is formed as an unstable intermediate. We have also studied the reaction chemistry of the dinitramide anion. Its usefulness for the controlled stepwise replacement of fluorine by oxygen was demonstrated for $BrF_5$ and $ClF_5$ and resulted in a novel and safer synthesis of $ClOF_3$. Previous

syntheses for $ClOF_3$ involved low-temperature fluorinations of shock sensitive materials, such as $Cl_2O$ or $ClONO_2$ and were hazardous. In collaboration with G. Rasul, the stabilities of $N(NO_2)_2^-$, $N(NO_2)_3$ and $N(NO_2)_4^+$ were evaluated by LDF calculations. It was shown that the stability decreases with increasing positive charge and that the $N(NO_2)_4^+$ cation is vibrationally unstable. Attempts to prepare either $N(NO_2)_3$ or $(NO)N(NO_2)_2$ by low temperature metathesis were unsuccessful.

The chemistry of the $C(N_3)_3^+$ cation, which was discovered in 1966 by Dehnicke and Mueller but not further exploited, was studied by theory and synthesis. In collaboration with D. Dixon and G. Rasul, the structures and energies of the $C(N_3)_3^+$ and the corresponding mixed azido-nitro-carbenium cations were calculated. It was found that all these cations are vibrationally stable, but that the trinitrocarbenium ion is tetracoordinated (through formation of a C-O bond with an oxygen atom from a nitro group) because the nitrogen atom of the nitro group does not possess a free valence electron pair which can stabilize the carbenium ion through backdonation. In collaboration with G. Rasul, we have also calculated the corresponding carbanions. Whereas the carbocations are stabilized by azido groups and are destabilized by nitro groups, the opposite holds true for the carbanions. Thus, the $C(NO_2)_3^-$ anion is very stable, while the $C(N_3)_3^-$ anion is vibrationally unstable and decomposes to $(N_3)_2CN^-$ and $N_2$. The novel, extremely energetic compounds $C(N_3)_3^+BF_4^-$, $C(N_3)_3^+N(NO_2)_2^-$ and $C(N_3)_3^+ClO_4^-$ were synthesized by metathetical reactions and characterized by vibrational and NMR spectroscopy.. The heat of formation of the $C(N_3)_3^+$ cation was estimated from ab initio calculations and isodesmic reactions as +418 kcal/mol. From this value, the

heat of formation of solid $C(N_3)_3ClO_4$ was estimated as +465 kcal/mol which translates into an endothermicity of 1.96 kcal/g making it one of the most, if not the most, endothermic compound ever prepared. If the heat of combustion of carbon to carbon dioxide is included, the energy release increases to 2.35 kcal/g. Therefore, it is not surprising that this compound is extremely shocksensitive and a highly energetic explosive. The $[NH_3OH \cdot NH_2OH]^+$ $C(NO_2)_3^-$ salt was also prepared and its crystal structure was determined at USC by Prof. Bau. This energetic compound was found to be insensitive to shock and, therefore, to be of considerable interest. Surprisingly, the $C(NO_2)_3^-$ anion was found to exhibit a structure with two coplanar groups and one perpendicular $NO_2$ group and not the expected propeller-like geometry. Ab initio calculations showed both structures to be vibrationally stable and to differ by only 0.4 kcal/mol in energy.

In collaboration with Dr. Dixon, $F^-$ affinities were calculated for more than 100 compounds by ab initio methods. From these data, a quantitative $F^-$ affinity scale was calculated which, when combined with our previously calculated oxidizer strength scale and lattice energy estimates, will permit stability predictions for ionic oxidizers. The $F^-$ affinity scale should also be useful to measure the relative strength of Lewis acids. At the present time, there are no good criteria on how to judge or quantitatively measure the strength of Lewis acids.

In collaboration with Prof. Schrobilgen, the elusive $POF_4^-$ anion was prepared and characterized by low temperature NMR spectroscopy and its dismutation mechanism to $PO_2F_2^-$ and $PF_6^-$ was established. This dismutation

occurs at temperatures as low as -90°C and explains why all previous attempts to observe it had failed.

In the area of high coordination number chemistry, the novel $IF_5^{2-}$ and $IO_2F_5^{2-}$ anions were synthesized and characterized by theory and vibrational spectroscopy. The $IF_5^{2-}$ anion is only the second known example of a pentagonal planar $XY_5$ species, the first example beeing $XeF_5^-$ which had been discovered by us several years ago. The $IO_2F_5^{2-}$ anion is the first known example of an $XO_2Y_5$ species and was the missing link in the series of pentagonal bipyramidal heptacoordinated compounds. In connection with the synthesis of $IO_2F_5^{2-}$, the $N(CH_3)_4IO_4$ salt was needed as a starting material. It was prepared from $N(CH_3)_4OH$ and periodic acid and characterized by x-ray diffraction and vibrational spectroscopy. It is a shock-sensitive material which explodes when approaching its melting point.

# Synthesis of Highly Energetic Cations and Oxidizer Salts

*Mark A. Petrie, Karl O. Christe and Edward J. Wucherer*
Hughes STX and Phillips Laboratory, Edwards AFB, CA 93524-7680

The synthesis of oxidizing salts with extremely energetic cations is being explored. The triazidocarbonium ion, $C(N_3)_3^+$ was utilized to prepare extremely high energy HEDM solid oxidizer candidates. The literature synthesis[1,2] of $C(N_3)_3^+ SbCl_6^-$ has been improved and the new $C(N_3)_3^+ BF_4^-$ salt obtained. These precursor materials were used to combine the $C(N_3)_3^+$ cation with energetic oxidizing anions. In this manner the dinitramide salt, $C(N_3)_3^+ N(NO_2)_2^-$ was prepared and found to decompose slowly at ambient temperature. The extremely energetic and sensitive perchlorate salt, $C(N_3)_3^+ClO_4^-$ was also prepared. All new $C(N_3)_3^+$ salts were characterized by mass balance, and Raman and FT-IR spectroscopy. The perchlorate salt, $C(N_3)_3^+ClO_4^-$ was found too sensitive to characterize except by mass balance.

The $NO^+$ and $NO_2^+$ salts of dinitramide have been proposed to be stable species by theoretical calculations[3,4] and accessible to synthesis. We attempted to prepare these species by different routes. The reagents $NOBF_4$ or $NO_2BF_4$ react with $KN(NO_2)_2$ as solids or in MeCN (-39°C) and $SO_2$ (-126°C) to give the decomposition products, $K^+NO_3^-$, $N_2O$, or $NO_2$. Liquid $FNO_2$ in excess does not react with $KN(NO_2)_2$ up to -78°C. In contrast, FNO reacts with $KN(NO_2)_2$ at -126°C giving an unstable species whose Raman lines are not yet assigned. Other routes to these interesting salts are being investigated.

Over-oxidized $[HONH_3]^+[N(NO_2)_2]^-$ (HADN) is a candidate for use as a liquid oxidizer or monopropellant (alcohol solution). The melting range of HADN is 18-23°C as reported by the Russians (O.A. Luk'yanov). SRI (R. Schmitt and J.

Bottaro) report HADN as a liquid at ambient temperature. We have synthesized anhydrous HADN to establish a baseline of properties and performance. We obtained a compound of substantially higher melting point (38-40°C) than reported. The compound was characterized by DSC, TGA, and Raman and FT-IR spectroscopy. Unfortunately, both dry and wet solids were found to be *extremely* sensitive to impact.

The sensitivity of the $[HONH_3]^+[N(NO_2)_2]^-$ salt led to studies of nitroformate, $C(NO_2)_3^-$ salts. We have prepared $H_3NOH^+ C(NO_2)_3^-$ (HANF) by an anhydrous acid-base reaction. Reactions between the sensitive alkali salts $M^+C(NO_2)_3^-$ and $H_3NOH^+Cl^-$ were not efficient. The $H_2NOH$ adduct of HANF, $H_3NO \cdot H_3NOH^+ C(NO_2)_3^-$ was obtained by two methods; the addition of $H_2NOH$ to $HC(NO_2)_3$ in a two to one ratio or dissociative evaporation of HANF. Evidence for dissociation of HADN has not been observed perhaps owing to the less basic nature of the dinitramide anion. Crystals for an X-ray structure of the adduct were grown by the latter method. In the high quality crystal structure of the adduct there are two complete adduct salts in the asymmetric unit and the form of the neutral $H_2NOH$ is amine oxide "$H_3NO$". There are two short and one long C-N distances in the $C(NO_2)_3^-$ anions suggesting delocalization of the negative charge over only two of the $-NO_2$ groups. The density of the adduct is 1.850 $Mg/m^3$. In addition, both HANF and its adduct are suprisingly insensitive to impact and friction. The salts were fully characterized by DSC, TGA, and Raman and FT-IR spectroscopy. They are distinguished by melting points and $\nu$(N-O) stretches in the infrared.

1) U. Muller, K. Dhenicke, Angew. Chem. Int. Ed. **5**, 841, 1966.

2) A. Schmidt, Chem. Ber. **100**, 3725, 1967.

3) H.H. Michels, B.N. Cassenti, D.D. Tzeng, and E. Lee, HEDM Conference, Woods Hole, 1995.

4) G. Rasul (USC) private communication.

# Rotational Ordering in Solid Deuterium and Hydrogen: A Path Integral Monte Carlo Study

T. Cui, E Cheng, B. J. Alder, and K. Birgitta Whaley

Department of Chemistry, University of California, Berkeley, California 94720

## 1    Introduction

The search for a possible metallic phase in molecular hydrogen and its isotopes has been a continuously pursued field ever since the inception of the idea by Wigner and Huntington more than sixty years ago. [1] Such a metallic phase would be an outstanding HEDM candidate, with an extremely high specific impulse. Renewed interest was spurred recently by a reported observation of high electrical conductivity in shock compressed liquid $H_2$ and $D_2$. [2] Meanwhile, continued progress in the experimental realization of ultra-high pressure diamond anvil cells that are capable of subjecting solid $H_2$ and $D_2$ samples to pressures up to 200 GPa is being made, [3, 4, 5] and there emerges a consensus phase diagram for solid $D_2$ over a wide range of pressure $P$ and temperature $T$. A remarkably similar diagram has also been proposed for $H_2$, although some controversy still exists at high pressures. [3]

It thus poses a challenge to theorists to model and reproduce the phase diagrams from our understanding of these highly quantum solids. Many recent investigations have been made, employing various levels of the existing Quantum Monte Carlo (QMC) technology. However, success so far has been limited by the various restrictive approximations made, particularly in "freezing out" some degrees of freedom in order to maintain the computational feasibility. [3] In this extended abstract, we report our latest effort in advancing the theoretical frontier by applying the Path-Integral Monte Carlo (PIMC) method with a constant-pressure (NPT) ensemble, to treat simultaneously the translational and rotational motion of the $H_2$ and $D_2$ molecules. Only the boson systems of para-$H_2$ and ortho-$D_2$ are studied, and we henceforth neglect the prefixes for simplicity. Although the intramolecular bond fluctuation is still neglected, we are able to arrive at a phase diagram consistent with experiment for both $H_2$ and $D_2$ for $P < 130$ GPa, and for $H_2$ also at higher pressure, as will be shown below. A detailed account of this work will be published elsewhere. [6]

## 2    Theoretical Models and Methods

Within the approximation that only (effective) pair-wise interactions are important, a quantum molecular solid with translational and rotational degrees of freedom is described by the Hamiltonian:

$$H = -\frac{\hbar^2}{2m} \sum_i^N \nabla_{R_i}^2 + \frac{\hbar^2}{2I} \sum_i^N \mathbf{L}_i^2 + \frac{1}{2} \sum_{i \neq j}^N V(\mathbf{R}_{ij}, \mathbf{\Omega}_i, \mathbf{\Omega}_j), \tag{1}$$

where $\mathbf{R}_i$ is the center-of-mass position of the $i$-th molecule, $\mathbf{\Omega}_i$ its orientation direction, $\mathbf{L}_i$ its angular momentum operator, and $\mathbf{R}_{ij} \equiv \mathbf{R}_i - \mathbf{R}_j$ is the intermolecular separation vector. The molecular mass and moment of inertia are denoted by $m$ and $I$, respectively. With the intramolecular bond length fixed, and for a linear molecule, $I$ is a simple constant. We use the values of $m = 3676$ and $7352$ (atomic units) for $H_2$ and $D_2$, respectively, and rotational constants $B \equiv \hbar^2/2I = 84.98$ and $42.92$ K for $H_2$ and $D_2$, respectively. [6]

A common and convenient way to express the multi-dimensional potential $V(\mathbf{R}_{ij}, \mathbf{\Omega}_i, \mathbf{\Omega}_j)$ is through a spherical harmonic expansion, the leading term of which is the familiar isotropic interaction potential. This term has been extensively studied in the past, and a few analytical forms exist. In this work, we adopt the phenomenological model of Silvera-Goldman (SG), suitable for the solid environment: [3]

$$V_{SG}(R) = e^{\alpha - \beta R - \gamma R^2} - f(R) \left\{ \frac{C_6}{R^6} + \frac{C_8}{R^8} + \frac{C_{10}}{R^{10}} - \frac{C_9}{R^9} \right\}, \tag{2}$$

$$f(R) = \begin{cases} e^{-(1.28 R_m/R - 1)^2} & \text{if } R < 1.28 R_m, \\ 1 & \text{otherwise}, \end{cases} \tag{3}$$

plus the short-range correction proposed by Hemley, et al.: [3]

$$V_{SR}(R) = \begin{cases} a_1 (R - R_c)^3 + a_2 (R - R_c)^6 & \text{if } R \leq R_c \\ 0 & \text{otherwise}. \end{cases} \tag{4}$$

The parameter values are tabulated in references. [3, 4, 6]

Of the anisotropic terms, it has been identified that only the long-range electronic quadruple-quadruple (EQQ) and the socalled "atom-diatom scattering" terms contribute significantly to $V$. [3] Here, we use the tabulated results of a quantum chemical calculation by Schaefer, et al., [7] which consists of the five leading anisotropic terms in the spherical harmonic expansion. Their data have been previously tested by Runge, et al., in the solid environment and a scaling correction was found necessary to soften the repulsion at high pressure. [8] We tested both unscaled and scaled potentials in this work and found the scaled ones yield phase diagrams in closer agreement with experimental data.

The path-integral method solves for the quantum statistical density matrix by expanding this as a convolution of $M$ density matrices at a higher temperature $MT$:

$$\begin{aligned} \rho(x, x'; \beta) &= \langle x | e^{-\beta H} | x' \rangle, \\ &= \int \dots \int dx_1 \dots dx_{M-1} \rho(x, x_1; \tau) \rho(x_1, x_2; \tau) \dots \rho(x_{M-1}, x'; \tau). \end{aligned} \tag{5}$$

Here $x \equiv \{\mathbf{R}_1, ..., \mathbf{R}_N, \mathbf{\Omega}_1, ..., \mathbf{\Omega}_N\}$, $\beta \equiv 1/kT$ and we have defined $\tau \equiv \beta/M$. When $M$ is large enough, the high temperature density matrix $\rho(x, x'; \tau)$ can be well approximated by an analytical solution. We adopt here the standard "primitive approximation" . [9] This multi-dimensional integration, although computationally time consuming, is now readily performed by the standard Metropolis Monte Carlo sampling method. [6]

The extended solid is modeled by a simulation cell of a finite size, with periodicity and long-range corrections handled in the standard fashion. [6] Most of our calculations are performed with $N = 96$ and a cell with two basis vectors ($\mathbf{a}$ and $\mathbf{b}$) forming a 60 degree angle and the third one ($\mathbf{c}$) perpendicular to both $\mathbf{a}$ and $\mathbf{b}$. This choice, with the proper length ratio $a : b : c = 1 : 1 : 6^{1/2}/2$, has the advantage of accommodating both the FCC and HCP lattice structures. Extensive testing with different $N$ and cell geometries have also been made.

In order to minimize the bias of a restrictive cell geometry, particularly to avoid influencing possible phase transitions, we perform most of our calculations in the constant-pressure ($NPT$) ensemble, instead of the simpler constant-volume ensemble ($NVT$) in which the simulation cell remains fixed. The implementation of the $NPT$ ensemble is achieved by an

extra Metropolis move of the cell size and geometry, which generates a Markov chain of states having a limiting distribution proportional to

$$\exp\left[-\beta PV - \beta E(s) + N \ln V\right], \qquad (6)$$

where $P$ is the given pressure, $V$ the (variable) cell volume and $E$ is the energy $\langle H \rangle$ of the configuration $s$ (with a scaled coordinate system). [10] A new state is generated by independent random walks of the three basis vectors of the simulation cell, altering both the volume and the shape of the cell. We tested the NPT PIMC code by performing a classical calculation of the structural transformations in solid nitrogen under pressure. Excellent agreements with previous molecular dynamics results were achieved. [6, 11]

## 3    Results

As a test of our model and the intermolecular potentials, we first study the equation of state (EOS) for both solid $D_2$ and $H_2$. At a given temperature $T$, we perform PIMC at a constant pressure $P$ and measure the average cell volume $V$, thus yielding the (P-V) EOS. The results are directly compared to the experimental data of Ref. [4]. As expected, we find the EOS is dominated by the isotropic part of the potential alone, and the SG potential corrected in short-range, Eqs. (2) and (4), yields the best agreement with experimental data. Indeed, our results from this potential are almost identical with experiments for $P < 25$ GPa, where direct measured data are available, and also overlap with the extrapolated experimental data for larger $P$. [6]

In order to monitor the correlations in molecular orientations, we define the two-body correlation function, $O(R)$:

$$O(R) = \left\langle \frac{\sum_{i<j} P_2(\cos\theta)\delta(R_{ij} - R)}{\sum_{i<j} \delta(R_{ij} - R)} \right\rangle. \qquad (7)$$

Here $\theta$ is the angle between the molecular orientation vectors $\mathbf{\Omega}_i$ and $\mathbf{\Omega}_j$. This function measures the two-body orientation correlation at the intermolecular distance $R$, normalized by the number of molecules at that distance. If the molecular orientations are completely disordered in a solid, $\theta$ has a uniform distribution between 0 and 180 degrees (Note the intramolecular boson symmetry) and $P_2(\cos\theta)$ averages to zero. This is true for all intermolecular distances and yields $O(R) = 0$ everywhere. On the other hand, ordered molecular orientation phases produce finite correlations according to specific intermolecular distances, and thus definitive patterns in $O(R)$. Schematic $O(R)$ illustrations for a few proposed ordered $D_2$ and $H_2$ phases are shown in Ref. [6], whose distinct features allow us to identify phases through our sampled $O(R)$.

Fig. 1 shows the $O(R)$ signature of a typical molecular orientational ordering phase transition. For a given temperature $T$, the molecular orientation is completely disordered in the solid at low pressure $P$, below the values shown here, as evidenced by the fact that $O(R)$ averages to approximately zero. As $P$ is increased to approach a certain value $P_{tr}$, deviations from $O(R) = 0$ become visible and then become more and more pronounced as $P$ continues to increase. A well defined structure in $O(R)$ is clearly evident and stable throughout the simulation with $P > P_{tr}$. We identify the onset of this transition by the value of averaged $O(R)$, which displays a step-like increase at $P = P_{tr}$, indicating a phase transition that is rounded by the finite size and fluctuation effects.
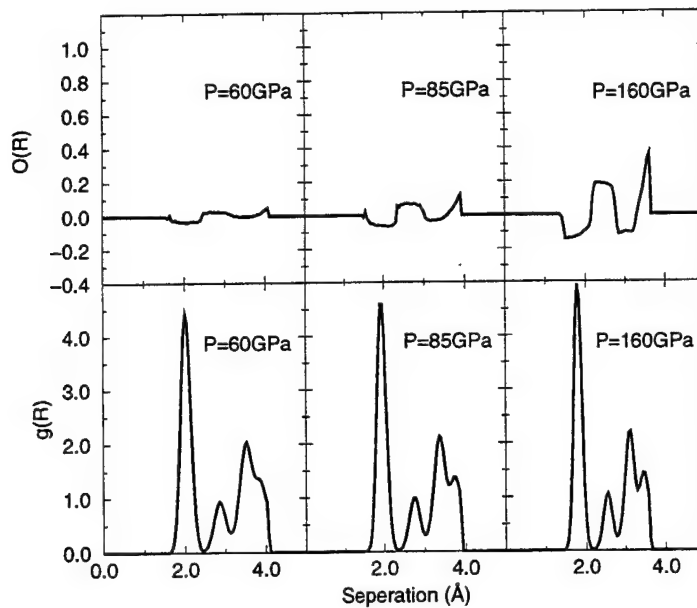
Figure 1: Orientational ordering phase transition in $D_2$ solid (HCP) at the temperature $T = 100$ K. The upper panel shows the orientational correlation function $O(R)$, defined in Eq. (7), at pressures $P = 60$, 85, and 160 GPa. The lower panel shows the structural correlation function $g(R)$ at the same pressures. These are calculated with $M = 8$ in PIMC.

Fig. 2 shows our resultant phase diagram in the $T - P$ plane for $D_2$. We have tested the effect of variable number of particles $N$ ($N = 32, 48, 64, 96$), as well as different choices of the cell geometry, in both HCP and FCC phases. Although a lattice structural phase transition is allowed in our $NPT$ ensemble, no sign of this is observed. That is, the lattice stays in the start-up structure (either HCP or FCC) throughout a simulation run, even when passing through the orientational order-disorder phase transition. The positions of such transitions do, however, shift noticeably with different choices of the lattice, as is evident in Fig. 2.

Two sets of experiments have found three distinct phases for $D_2$ at pressures below 200 GPa, also shown in Fig. 2. [4, 5] The phases are alternatively referred to as phases I, II, and III, [4] or (orientationally disordered) HCP, broken-symmetry phase (BSP), and A phase, [5] respectively. A triple point is identified at $P_t \sim 150 - 165$ GPa and $T_t \sim 125$ K. For $T < T_t$, solid $D_2$ is observed to go through two phase transitions (I to II and II to III) as pressure is increased, while only one transition (I to III) occurs for $T > T_t$. The positive identification of these phases is still primitive. Single-crystal x-ray diffraction data has shown that the phase I, which extends to the more familiar low temperature and pressure region, has an HCP lattice structure. [4] The molecular orientations are disordered here, as for the solid under ambient pressures. [3] On the other hand, both phases II and III are believed to possess certain orientational orders, although the exact nature of these phases is still unknown. [4, 5]

In contrast to the experiments, only one phase transition, a pure orientational ordering, is observed here. Our results for the orientational disorder-order phase transition with an HCP lattice in the relatively low pressure region, $P < 130$ GPa, show excellent agreement with the experimental I–II phase boundary. At higher pressures, our data show an upward turn in the $T - P$ plane that is reminiscent of the I–III phase boundary in experiments. However, since we only observe one transition below the experimental triple point temperature, we
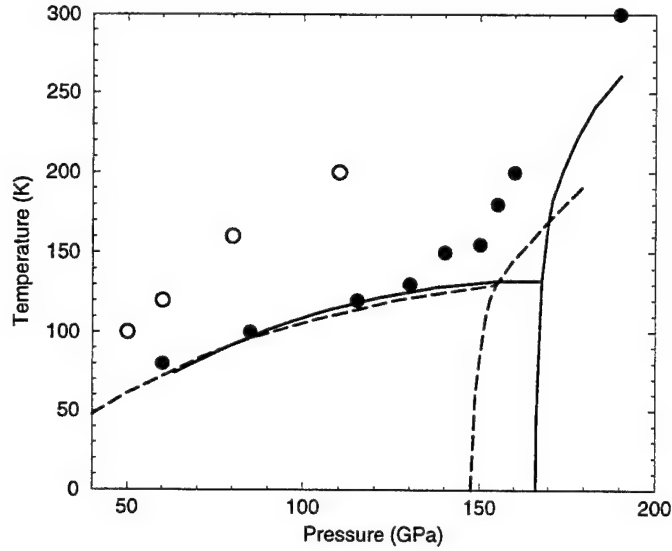
161

Figure 2: The phase diagram of $D_2$ solid. The solid and dashed curves are the experimental boundaries between three phases I, II, and III, from Refs. [4] and [5], respectively. The solid circles are our data for orientational order-disorder phase transition in HCP phase, while open circles are in FCC.

see no distinction between the regions of experimental phases II and III. The orientational correlation function, $O(R)$, is found to be rather similar for both FCC and HCP lattices in our ordered phases and resembles that for the Pa3 phase based on FCC. This is not too surprising since these lattices are similar in the first and second nearest neighbor separations, differing only substantially for longer range separations. With the energetics of the dense solids dominated by the short-range repulsions, the small difference in their energies from distances beyond second nearest-neighbor separations is unresolvable within the accuracy of our simulation.

In contrast with $D_2$, the phase diagram for solid $H_2$ has not yet been investigated experimentally in the same detail. Indeed it is still unclear whether an analogous phase diagram exists for $H_2$, in particular whether there exists a triple point, or alternatively a critical point that terminates the II-III phase boundary. [4, 5] Fig. 3 depicts the experimental II-III phase boundary and the expected I-II boundary from Ref. [5], together with our PIMC results. It is evident that our data based on the HCP phase with the scaled anisotropic interaction agrees with the expected I-II boundary rather well, consistent with the quality of our results for $D_2$. This consistency in achieving agreements with experimental data in EOS and the orientational phase diagram for *both* $H_2$ and $D_2$ is a remarkable validation of the potential used in these calculations. We expect this hybrid potential to be an excellent candidate in further theoretical investigations of the dense phases of hydrogen isotopes.

## 4    Discussion

In this extended abstract, we report results in applying the PIMC technique to study the phase diagrams of $D_2$ and $H_2$ up to pressures of megabars, in a constant-pressure ensemble.
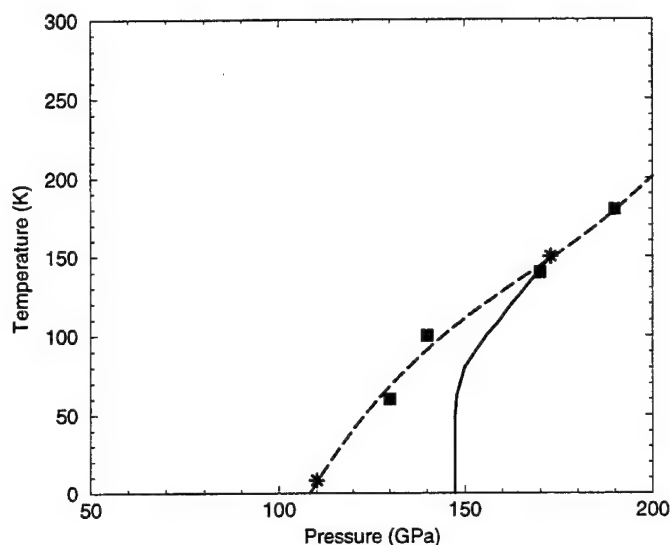
Figure 3: The phase diagram of $H_2$ solid. The solid curve is the experimental phase boundary between phases II and III. The dashed curve is the expected boundary between phases I and II, from the two measured data marked by stars. [5] The solid squares are our data in HCP phase for orientational order-disorder phase transition.

With a hybrid inter-molecular interaction potential determined to agree with the experimental equation of state over a large range of pressures, a rotational order-disorder phase transition is observed, in agreement with the I/II part of the phase diagram for both $D_2$ and $H_2$.

While such success should be noted, there remains the unsettling issue of why only one orientational order-disorder transition and no structural transitions are observed in our model. Possible explanations range from restrictions due to the small sample size, lack of stretching of the intramolecular bond, to consideration of the relevance of electronic rearrangments in phase III. These and other related issues will be extensively discussed elsewhere. [6]

## 5 Acknowledgements

# References

[1] E. Wigner and H. B. Huntington, J. Chem. Phys. **3**, 764 (1935).

[2] S. T. Weir, A. C. Mitchell, and W. J. Nellis, Phys. Rev. Lett. **76**, 1860 (1996).

[3] For reviews, see: I. Silvera, Rev. Mod. Phys. **52**, 393 (1980); J. van Kranendonk, *Solid Hydrogen*, Plenum Press, New York, 1983; H. Mao and R. J. Hemley, Rev. Mod. Phys. **66**, 671 (1994).

[4] R. J. Hemley, H. K. Mao, L. W. Finger, A. P. Jephcoat, R. M. Hazen, and C. S. Zha, Phys. Rev. B42, 6458 (1990); T. S. Duffy, W. L. Vos, C. S. Zha, R. J. Hemley, H. K. Mao, Science 263, 1590 (1994); A. F. Goncharov, I. I. Mazin, J. H. Eggert, R. J. Hemley, and H. K. Mao, Phys. Rev. Lett. 75, 2514 (1995); R. J. Hemley, H. K. Mao, A. F. Goncharov, M. Hanfland, and V. Struzhkin, Phys. Rev. Lett. 76, 1667 (1996).

[5] N. H. Chen, E. Sterer, and I. F. Silvera, Phys. Rev. Lett. 76, 1663 (1996); L. Cui, N. H. Chen, and I. F. Silvera, Phys. Rev. Lett. 74, 4011 (1995); Phys. Rev. B51, 14987 (1995).

[6] T. Cui, E. Cheng, A. J. Alder, and K. B. Whaley, to be published.

[7] J. Schaefer and W. Meyer, J. Chem. Phys. 70, 344 (1979); L. Monchick and J. Schaefer, *ibid.* 73, 6153 (1980); J. Schaefer and W. E. Köhler, Z. Phys. D13, 217 (1989).

[8] K. J. Runge, M. P. Surh, C. Mailhiot, and E. L. Pollock, Phys. Rev. Lett. 69, 3527 (1992).

[9] D. M. Ceperley, Rev. Mod. Phys. 67, 279 (1995).

[10] I. R. McDonald, Mol. Phys. 23, 41 (1972); R. Eppenga and D. Frenkel, Mol. Phys. 52, 1303 (1984).

[11] M. L. Klein, D. Levesque, and J.-J. Weis, Can. J. Phys. 59, 530 (1981); S. Nosé and M. L. Klein, Phys. Rev. Lett. 50, 1207 (1983).

# Monte Carlo Simulations of the Structures and Optical Absorption Spectra of Na/Ar Clusters and Solids: An Application of Spectral Theory of Chemical Binding

Jerry A. Boatz, Mario Fajardo, and Jeffrey A. Sheehy
Phillips Laboratory
Propulsion Sciences Division
OLAC PL/RKS
Edwards AFB, CA 93524-7680

and

Peter W. Langhoff[†]
Department of Chemistry
Indiana University
Bloomington, IN 47405-4001

## ABSTRACT

Classical Monte Carlo simulation techniques have been used in conjunction with a recently developed spectral theory of chemical binding to predict the structures and optical absorption spectra of Na/Ar clusters and solids. The new spectral theory, which is a broad generalization of the Balling and Wright model (B&W) for predicting the $^2P$ excited state potential energy surfaces of alkali atoms in the presence of an arbitrary number and arrangement of rare gas perturbers, is based on the use of a direct product of complete sets of atomic eigenstates and an optical - potential analysis in finite subspaces of this representation. This technique extends the approximation of simple pairwise additivity to include interactions between multiple diatomic potential energy curves. An important consequence of the interactions between multiple surfaces is a more sensitive dependence of the predicted transition energies on the angular arrangement of rare gas perturbers in comparison to the first-order degenerate perturbation theory-based B&W theory. Specifically, an angular dependence of the shift of the centroid of the absorption band is obtained which is absent in the B&W treatment. Internally contracted multi-reference configuration interaction calculations from a state-averaged complete active space reference wavefunction, using augmented (18s13p6d5f2g1h)/[8s7p6d5f2g1h] atomic natural orbital basis sets for both Na and Ar, were used to compute potential energy curves for the $X\,^2\Sigma^+$, $A\,^2\Pi$, $B\,^2\Sigma^+$, $C\,^2\Sigma^+$, $D\,^2\Delta$, $E\,^2\Pi$, and $F\,^2\Sigma^+$ states of Na-Ar, plus the corresponding dipole moments and transition moments. The calculated potential energy curves and moment data are used in conjunction with the transformation properties of atomic angular momentum eigenstates under rotations in the computational implementation of this theory.

# I. Introduction

As an extension of our work presented at the 1995 HEDM Contractors conference[1] and elsewhere,[2] we present here the latest results of our ongoing simulations of the structures and absorption spectra of argon atoms doped with a single sodium atom, within the framework of Langhoff's spectral theory of chemical binding.[3] The present work utilizes the recently computed internally contracted multireference CI Na-Ar potential energy curves ($X\ ^2\Sigma^+$, $A\ ^2\Pi$, $B\ ^2\Sigma^+$, $C\ ^2\Sigma^+$, $D\ ^2\Delta$, $E\ ^2\Pi$, and $F\ ^2\Sigma^+$), dipole moments ($\mu_X$, $\mu_A$, $\mu_B$, $\mu_C$) and transition moments ($\mu_{X-A}$, $\mu_{X-B}$, $\mu_{B-C}$, $\mu_{A-C}$) of Sheehy.[4] One of the central issues examined in the current study is the question of how many atomic product states must be included in the spectral theory equations to achieve "convergence" of the $NaAr_n$ structures and absorption spectra.

# II. Theoretical Methods

Our method for the simulation of the structures and absorption spectra of sodium-doped argon clusters uses a combination of the classical Metropolis Monte Carlo algorithm[5] in conjunction with the recently developed spectral theory of chemical binding.[3] The latter theory, of which the B&W first-order degenerate perturbation theory model,[6] diatomics-in-molecules (DIM) methods,[7] and pairwise additivity approximations are special cases, provides a systematic method for obtaining an increasingly accurate manifold of eigenstates via incorporation of non-additive contributions to the total energy. The foundation of the spectral theory is pairwise summation of projections of the fully antisymmetrized electronic wavefunctions of the diatomic components into a partially antisymmetrized atomic-product basis (via the so-called "U matrix" transformation[1,3]). By expanding the number of diatomic and atomic-product states included in the spectral theory formalism, in principle one systematically increases the accuracy of the computed potential energy surfaces.

The following is a brief outline of the spectral theory (for more details, see ref. [3]) The diatomic Na-Ar wavefunctions are written as a superposition of atomic product states constructed from the direct product of Na and Ar atomic states: Na $\{3S,3P,4S,3D,....\} \otimes$ Ar $\{^1S_0,....\}$. Since the excited states of Ar are much higher in energy than those of Na, it is assumed that the most important non-additive contributions will be described by atomic products containing Na atom excited states and the Ar atom ground state. In matrix/vector notation,

$$(1) \qquad \Psi = \Phi U^t$$

where $\Psi$ denotes the row vector of diatomic states (e.g., $X\ ^2\Sigma^+$, $A\ ^2\Pi$, $B\ ^2\Sigma^+$,....), $\Phi$ denotes the row vector of atomic product states (e.g., $|3S> \cdot |^1S_0>$, $|3P_0> \cdot |^1S_0>$, $|4S> \cdot |^1S_0>$,....), and U is the unitary transformation connecting the diatomic and atomic-product representations. An important point to be noted is that the atomic-product basis is not used for computations. Rather, all computations are performed in the (fully antisymmetrized) diatomic basis, followed by projection onto the atomic-product basis via the unitary U matrix transformation defined in Eq. (1) (see ref. [3] for more details.)

166

The explicit form of Eq. (1) for the case in which the ten atomic-product states Na {3S,3P,4S,3D} ⊗ Ar {$^1S_0$} are used is given by the following expressions:

(2) $\quad |X> = <3S|X>|3S> + <3P_0|X>|3P_0> + <4S|X>|4S> +$

$\qquad <3D_0|X>|3D_0>$

(3) $\quad |B> = <3S|B>|3S> + <3P_0|B>|3P_0> + <4S|B>|4S> +$

$\qquad <3D_0|B>|3D_0>$

(4) $\quad |C> = <3S|C>|3S> + <3P_0|C>|3P_0> + <4S|C>|4S> +$

$\qquad <3D_0|C>|3D_0>$

(5) $\quad |F> = <3S|F>|3S> + <3P_0|F>|3P_0> + <4S|F>|4S> +$

$\qquad <3D_0|F>|3D_0>$

(6) $\quad |A_+> = <3P_{+1}|A_+>|3P_{+1}> + <3D_{+1}|A_+>|3D_{+1}>$

(7) $\quad |E_+> = <3P_{+1}|E_+>|3P_{+1}> + <3D_{+1}|E_+>|3D_{+1}>$

where the individual elements of **U** are in bold and the Ar ground state $|^1S_0>$ term of each atomic product on the right hand side of Eqs. (2)-(7) has been omitted for brevity. Eqs. (2) - (5) express the 4 lowest Na-Ar $^2\Sigma^+$ states in terms of the appropriate atomic-product states and Eqs. (5) - (6) describe the two lowest $^2\Pi$ states. Numerical values of the **U** matrix elements are derived from first-order perturbation approximations based on calculated dipole moment and transition moment functions (see Appendix A in ref. [1].) Because of the approximations used in obtaining the **U** matrix elements, the present results should be regarded as suggestive rather than quantitative predictions of NaAr$_n$ cluster geometries and absorption spectra.

In the present study, the spectral theory method is used to calculate the many-body potential energy surfaces for the ground and first three excited states (i.e., the excited states which correspond to the excited $^2P$ states of atomic Na) "on the fly" at each of the cluster configurations generated by the Monte Carlo sampling. However, only the Na-Ar portion of the potential energies are determined within the spectral theory framework; the residual Ar-Ar interactions are assumed to be strictly pairwise additive and are obtained using the "HFD-B2" Ar-Ar potential of Aziz and Slaman.[8] At each configuration, the transition energies from the ground state to the first three excited states are binned, and the resulting histogram of energies over the sampled configurations is taken to be the predicted absorption spectrum.

The radial probability distribution functions (RPDFs) and absorption spectra of several NaAr$_n$ clusters (n=1,2,3,6,11,12,55,147) have been predicted as a function of the number of atomic-product states included within the spectral theory formalism. Specifically, starting with the single atomic product state consisting of ground state Na (3s) and Ar, the excited atomic product states corresponding to Na 3p, 4s, and 3d levels (and the corresponding diatomic states A $^2\Pi$, B $^2\Sigma^+$, C $^2\Sigma^+$, D $^2\Delta$, E $^2\Pi$, and F $^2\Sigma^+$ ) are successively included in the spectral theory formalism. Individual elements of the U matrix, which define the diatomic/atomic-product transformation and can be thought of as "configuration interaction (CI) coefficients" or as descriptions of Na atom orbital hybridizations, were obtained from Sheehy's[4] computed Na-Ar dipole moment ($\mu_X$, $\mu_A$, $\mu_B$, $\mu_C$) and transition moment ($\mu_{X-A}$, $\mu_{X-B}$, $\mu_{B-C}$, $\mu_{A-C}$) functions, using the same first-order perturbation theory approximations as outlined in Appendix A of ref. [1]. All simulations were performed using a classical temperature of 10 K and the structures and absorption spectra were obtained from averages over approximately 50,000 configurations.

## III. Results and Discussion

Although the structures and absorption spectra of several different clusters have been examined in this work, only the results for NaAr$_{11}$ are discussed in detail here. Shown in Figure 1 and summarized in Table I are the RPDFs of NaAr$_{11}$ as a function of the number of atomic-product and diatomic states included in the spectral theory calculation of the cluster ground state energy surface. Each of the three peaks in each curve in Figure 1 denotes a "shell" of argon atoms at the indicated distance from the sodium atom (which is located on the surface of the cluster) and the integrated area under each peak gives the number of argon atoms in the "shell" (5, 5, and 1 argon atoms, respectively, from left to right.)

RPDF (a) is obtained using simple pairwise additivity to compute the ground state energy of the cluster. RPDF (b) is obtained using the spectral theory formalism in which mixing of only the Na atom 3S and 3P atomic states is allowed. The Na 3S, 3P, and 4S states are included in the spectral theory to obtain (c), and finally the complete set of 10 states arising from the Na atom 3S, 3P, 4S, and 3D levels were used in generating RPDFs (d).

In curve (a), the maximum of the first nearest-neighbor peak is located at about 5.1 angstroms, with the second and third nearest-neighbor peaks located at 7.7 and 8.8 angstroms, respectively. Trace (b), which is obtained using the Na atom 3S and 3P atomic states in the spectral theory, shows a slight contraction of all 3 peaks in the RPDF relative to (a). In particular, the first nearest-neighbor peak maximum is centered at 5.0 angstroms, and the second and third nearest neighbor peaks are likewise shifted to smaller R by similar amounts. However, upon adding futher Na atomic states to the spectral theory, only rather small changes in the predicted RPDFs are observed; i.e., the peak maxima in traces (b) - (d) are all located at approximately 5.0, 7.6, and 8.7 angstroms. Since the RPDFs are functions of only the ground state potential energy surface, this suggests that the spectral theory is essentially "converged" at the 3S+3P level for the ground state in this region of the surface. In other words, nearly all of the non-additive contributions to the total ground state energy are accounted for by the 3S+3P interactions, as described by the U matrix in Eq. (1).

Although the ground-state surface of NaAr$_{11}$ is apparently converged at the 3S+3P spectral theory level, the same cannot be said for the first three excited states. Evidence for this is seen in the predicted absorption spectra as a function of spectral theory level, which are shown in Figure 2 and summarized in Table II. Spectra (a) - (d) in Figure 2 were generated in a manner entirely analogous to RPDFs (a) - (d) in Figure 1. Spectrum (a) is obtained using simple pairwise additivity to compute the ground state and the B&W model for the first three excited states; i.e. corresponding, in the spectral theory notation, to U in Eq. (1) being equal to the identity matrix. In obtaining spectrum (b), mixing of only the 3S and 3P states is allowed in the calculation of the ground and excited states. Further inclusion of the 4S state in the spectral theory yields curve (c), and the full set of 10 states corresponding to the Na atom 3S, 3P, 4S, and 3D levels were used in generating spectrum (d). (The remaining spectra (e) - (g) are discussed later on in this section.)

The general characteristics of each spectrum shown in Figure 2 include a fully resolved "doublet" feature centered at approximately 17,000 cm$^{-1}$ and a broad, blue-shifted "satellite" peak above 17,500 cm$^{-1}$. However, the location of the peaks vary as a function of spectral theory level (see Table II.) This is especially true for the satellite peak, which is centered at 17590 cm$^{-1}$ when the Balling and Wright model is used (spectrum (a) in Figure 2 and Table II), but is shifted an addtional 150 cm$^{-1}$ to the blue when using the 3S + 3P spectral theory level (trace (b).) Successive inclusion of the 4S and 3D atomic levels (spectra (c) and (d), respectively) result in continued (albeit reduced) variation in the location of this peak, which suggests that the excited states are not yet fully converged at the 3S + 3P + 4S + 3D spectral theory level.

However, the issue of convergence of the predicted spectra is complicated by two factors. First, unlike the RPDFs which depend solely on the ground state potential energy surface of the cluster, the spectra are functions of both the ground (initial) and excited (final) states. The second factor concerns the proper choice of sequence of spectral theory levels to use in examining convergence of the excited states. For the ground state, it is reasonable to examine convergence of the spectral theory by successively addition of Na atomic states in the order 3S (i.e., using pairwise additivity), 3S + 3P, 3S + 3P + 4S, and finally 3S + 3P + 4S + 3D. However, for the first three excited states of the cluster (which correlate with the Na atom 3P states), it is perhaps more reasonable to assess their convergence using the order 3P (i.e., the B&W model), 3P + 4S, 3P + 4S + 3D, and finally 3S + 3P + 4S + 3D. The addition of states in this order is based upon the energy spacings between the 3S, 3P, 4S, and 3D atomic energy levels of the Na atom, which are 0, 16968, 25740, and 29173 cm$^{-1}$, respectively (ignoring spin-orbit coupling.) That is, the atomic level closest in energy to the 3P is 4S, followed by 3D, and in turn followed by 3S.

In order to address these two factors, an additional series of simulations were performed in which a "hybrid" spectral theory approach was utilized. In these simulations, separate spectral theory levels were used in computing the ground state and the set of first three excited states. In particular, the complete set of 10 atomic Na states (3S, 3P, 4S, 3D) were used to compute the ground state surface, while the three excited state surfaces were computed separately, using the 3P, 3P + 4S, and 3P + 4S + 3D spectral theory levels (spectra (g), (f), and (e), respectively, in Figure 2 and Table II.) Since the ground state surface is apparently converged at the 3S + 3P + 4S + 3D level (see the discussion above concerning the RPDFs), this technique eliminates incomplete convergence of the ground state as a possible source of variation in the calculated

absorption spectra, as well as utilizing the (presumably) proper sequence of additional states in the spectral theory for convergence of the excited state potential energy surfaces.

Examination of the "hybrid" spectra (g), (f), and (e) in Figure 2 and Table II show less variation of the absorption peak positions as a function of excited-state spectral theory level than the sequence of spectra (a) - (d). For example, the location of the blue-shifted satellite peak varies by only 60 $cm^{-1}$ in spectra (g) - (e). Therefore, it appears that the first three excited state cluster energies are closer to convergence that initially indicated by the analysis of spectra (a) - (d). However, the effects of including additional atomic states (e.g., 4P and 5S) in the spectral theory formalism must be examined in order to conclusively determine the degree to which the set of first three excited states are converged.

## IV. Conclusions

The structures, radial probability distribution functions, and absorption spectra of several $NaAr_n$ (n=1,2,3,6,11,12,55,147) have been predicted using an approximate implementation of Langhoff's spectral theory of chemical binding in combination with the classical Metropolis Monte Carlo simulation technique. Analysis of the $NaAr_{11}$ RPDFs indicate that the ground state potential energy surface (at least in the vicinity of the global minimum) is apparently converged at the 3S + 3P spectral theory level. Examination of the $NaAr_{11}$ absorption spectra indicate that the set of first three excited states (i.e., those corresponding to the final states in the absorption process) may not yet be fully converged even at the 3S + 3P + 3D + 4S spectral theory level. Additional simulations using an expanded set of atomic states (e.g., including the 4P and/or 5S atomic-product states) will be required to resolve this issue.

## References

1. Boatz, J.A.; Fajardo, M.; Langhoff, P.W. "Proceedings of the High Energy Density Matter (HEDM) Contractors' Conference", Patrick G. Carrick and Simon Tam, eds., 1996.

2. a) Boatz, J.A.; Fajardo, M.E. *J. Chem. Phys.*, **1994**, 101, 3472-3487.
   b) Fajardo, M.E.; Boatz, J.A. *J. Comp. Chem.*, in press.

3. a) Langhoff, P.W. "Proceedings of the High Energy Density Matter (HEDM) Contractors' Conference", T.L. Thomson and S.L. Rodgers, eds., 1994.
   b) Langhoff, P.W. "Proceedings of the High Energy Density Matter (HEDM) Contractors' Conference", Patrick G. Carrick and Simon Tam, eds., 1996.
   c) Langhoff, P.W. *J. Phys. Chem.*, **1996**, 100, 2974-2984.
   d) Sheehy, J.A.; Boatz, J.A.; Fajardo, M.E.; Langhoff, P.W. "Spectral Theory of Physical and Chemical Binding in HEDM Systems", these proceedings.

4. Sheehy, J.A. "Calculation of van der Waals Molecules Relevant to HEDM Studies", these proceedings.

5. Metropolis, N.; Rosenbluth, A.W.; Rosenbluth, M.N.; Teller, A.H.; Teller, E. *J. Chem. Phys.* **1953**, 21, 1087-1092.

6. Balling, L.C.; Wright, J.J. *J. Chem. Phys.* **1983**, 79, 2941-2944.

7. Tully, J. "Modern Theoretical Chemistry", G.A. Segal, ed., Plenum, NY, 1977, Vol. 7, 173-200.

8. Aziz, R.A.; Slaman, M.J. *Mol. Phys.* **1986**, 58, 679-697.

## Figure Captions

1. Calculated radial probability distribution functions (RPDFs) of $NaAr_{11}$ at a classical simulation temperature of 10 K, using (a) pairwise additivity, (b) 3S + 3P, (c) 3S + 3P + 4S, and (d) 3S + 3P + 4S + 3D spectral theory levels.

2. Calculated absorption spectra of $NaAr_{11}$ at a classical simulation temperature of 10 K, using (a) pairwise additivity for the ground state and the Balling and Wright model for the first three excited states, (b) 3S + 3P, (c) 3S + 3P + 4S, and (d) 3S + 3P + 4S + 3D spectral theory levels for both the ground and first three excited states. Spectra (e) - (g) are obtained using the 3S + 3P + 4S + 3D spectral theory for the ground state and (g) Balling and Wright, (f) 3P + 4S, and (e) 3P + 4S + 3D spectral theory levels for the excited states.

**Table I.  Radial Probablity Distribution Function Peak Locations.**

| RPDF[a] | Peak Maxima Locations[b] | | |
|---|---|---|---|
| (d) | 4.98 | 7.60 | 8.75 |
| (c) | 4.98 | 7.60 | 8.66 |
| (b) | 4.96 | 7.57 | 8.68 |
| (a) | 5.14 | 7.70 | 8.84 |

[a] RPDF labels correspond to those in Figure 1.
[b] In angstroms.


**Table II.  Absorption Spectrum Peak Locations.**

| Spectrum[a] | Peak Maxima Locations[b] | | |
|---|---|---|---|
| (g) | 16940 | 17120 | 17660 |
| (f) | 16960 | 17120 | 17600 |
| (e) | 16940 | 17120 | 17600 |
| (d) | 16940 | 17120 | 17640 |
| (c) | 16920 | 17120 | 17660 |
| (b) | 16920 | 17100 | 17640 |
| (a) | 16910 | 17060 | 17590 |

[a] Spectrum labels correspond to those in Figure 2.
[b] In $cm^{-1}$.

# NaAr11
# RPDF



R (angs)

Fig. 1

$4\pi R^2 g(R) dR$

# NaAr11
## Absorption Spectra



(g)

(f)

(e)

(d)

(c)

(b)

(a)

Absorbance (arb)

16500    17000    17500    18000    18500

E (cm⁻¹)
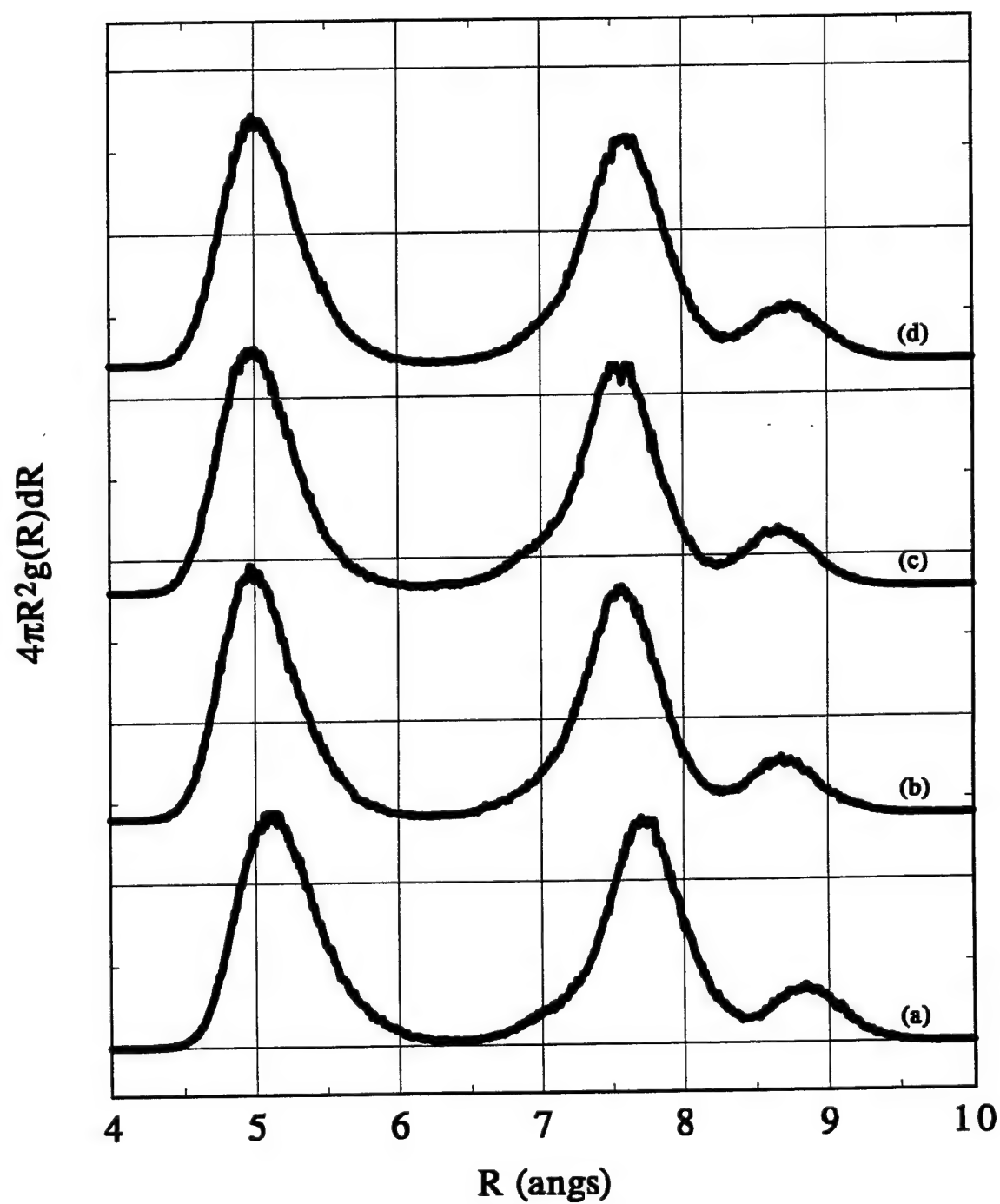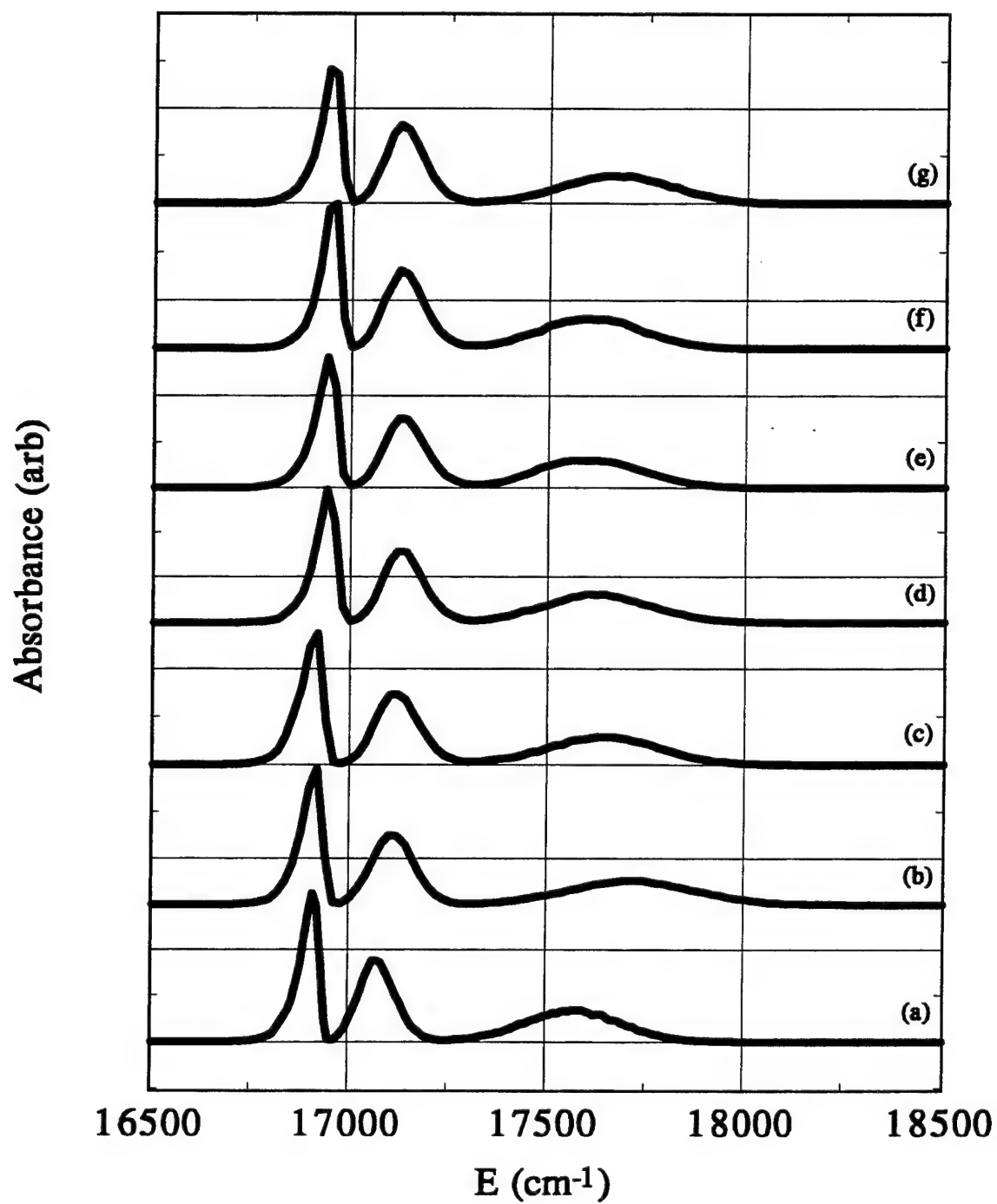
Fig. 2

174

# THEORETICAL STUDY OF THE STRUCTURE AND STABILITY OF M - H$_2$ VAN DER WAALS COMPLEXES (M=Li, Be, B, C, Na, Mg, Al, Si).

Galina Chaban and Mark S. Gordon
Department of Chemistry
Iowa State University
Ames, Iowa 50011

Ab initio calculations have been performed for a series of Van der Waals complexes M---H$_2$ (where M=Li, Be, B, C, Na, Mg, Al, and Si ), in order to estimate their thermodynamic and kinetic stabilities. The calculations were done using quadratic configuration interaction method QCISD(T)[1] with Dunning's correlation consistent valence-triple-zeta (cc-pVTZ) basis sets [2]. The Al-H$_2$ potential surface was also studied at the multi-reference CI level based on a full-valence active space MCSCF(5,6) wavefunction.

## *Complexes of s-elements.*

According to our calculations, s-elements in their ground states ($^2$S, Li, Na and $^1$S , Be, Mg) form very weak linear complexes with H$_2$ molecule. The dissociation energies are about 15 cm$^{-1}$ for Li and Na and 30 cm$^{-1}$ for Be and Mg. In their excited states ($^2$P Li,Na and $^3$P Be,Mg), these elements form very stable perpendicular complexes with C$_{2v}$ symmetry due to interactions of occupied p-orbitals with $\sigma^*$(H-H). For $^2$B$_2$ complexes of Li and Na the dissociation energies are 18 and 9 kcal/mol; for $^3$B$_2$ complexes of Be and Mg they are 20 and 6 kcal/mol, respectively. However, these complexes may be unstable kinetically due to crossings with ground state A$_1$ surfaces. These crossings suggest that sufficiently strong non-adiabatic coupling between the states could result in pre-dissociation of the excited state complexes.

## *Complexes of p-elements*

P-elements ( ground states) form much stronger complexes due to interaction of an occupied p-orbital with H$_2$ molecule (Table 1). P-elements form complexes with both linear and perpendicular geometries. The most stable of these correspond to a perpendicular orientation of the H$_2$ molecule, with the occupied p-orbital parallel to the H-H bond. Thermodynamic stability of perpendicular complexes increases from B, Al to C, Si. Kinetic stability is important to consider for C$_{2v}$ complexes, since stable MH$_2$ compounds with this symmetry exist for M=B, Al, C, Si. Complexes are stable only if barriers to insertion are high enough. Van der Waals complexes and MH$_2$ compounds have different electronic states, and the energy of their crossing is the upper limit for the barrier of the reaction, which can proceed via an avoided crossing.

No complex is found on the $^1A_1$ surface for either C-$H_2$ or Si-$H_2$: the insertion of singlet C and Si into $H_2$ proceeds with no barrier at all. Although Van der Waals complexes with $D_e$=324 cm$^{-1}$ and 720 cm$^{-1}$ are found for the $^3A_2$ potential surfaces of C ---$H_2$ and Si---$H_2$, they are probably unstable kinetically (see Figure 1 and 2). $^3B_1$ crosses $^3A_2$ only 1.5 kcal/mol above the C ($^3P$) + $H_2$ dissociation energy. In the case of Si, the $^3A_2$ - $^3B_1$ crossing is in the region of 20 kcal/mol above the Si-$H_2$ complex. However, the $^1A_1$ state crosses $^3A_2$ about 5 kcal above the complex, so the stability of the Si-$H_2$ complex depends on how strong is the interaction between triplet and singlet states near the crossing region.

Unlike C and Si, the complexes formed by B and Al are predicted to be kinetically stable (Figure 3 and 4). MRCI calculations of the B-$H_2$ potential surface performed by Alexander [3], and our study of the B-$H_2$ and Al-$H_2$ systems showed that the most stable Van der Waals complexes for these species correspond to a $^2B_2$ state and have dissociation energies of 121 and 204 cm$^{-1}$ respectively. Less stable complexes were found on the $^2B_1$ and $^2\Sigma$ potential energy surfaces of B-$H_2$ and Al-$H_2$.

*Al-$H_2$ potential energy surface*

Contour plots of the MCSCF(5,6) energy as a function of R (Al-$H_2$) and r (H-H) distances for pure $^2A_1$ and $^2B_2$ states are shown in Figure 5a. The thick solid line on these pictures corresponds to the crossing seam between the $^2A_1$ and $^2B_2$ states. The $^2A_1$ state is lower in energy for short R (Al-$H_2$) and long r (H-H) distances (upper left portion of the figures) and has an AlH$_2$ minimum (stable hydride) that is 17 kcal/mol lower than dissociation products Al + $H_2$. In addition to the AlH$_2$ minimum, the $^2A_1$ potential energy surface has a stationary point corresponding to a transition state, but this point is located on the higher part of the $^2A_1$ surface and is 76 kcal/mol above the Al + $H_2$ dissociation limit at the MRCI level of theory. In contrast, the $^2B_2$ state is lower for longer R (Al-$H_2$) and shorter r (H-H) distances (lower right portion of the figures). There is only a slight minimum on the $^2B_2$ surface corresponding to a weak Van der Waals complex.

The minimum energy crossing point for the $^2A_1$ and $^2B_2$ states is found to be 27 kcal/mol above the Al + $H_2$ dissociation limit at the MRCI level of theory. The geometry of the minimum energy crossing point corresponds to R (Al-H2) = 1.51 Å and r (H-H) = 1.68 Å. A MCSCF(5,6) steepest descent path was determined starting from the minimum energy crossing point in the direction of the negative of the gradient on both the $^2A_1$ (downhill in energy to the stable AlH$_2$ compound) and $^2B_2$ (downhill to Al + $H_2$ ) surfaces (see Figure 5a).

MRCI calculations based on the two-state-averaged MCSCF reference wavefunction were performed for several fragments of $C_s$ potential surfaces (Fig 5b). These calculations showed very little interaction between the two lowest $^2A'$ states resulting from the $^2B_2$ and $^2A_1$ states that cross at $C_{2v}$ symmetry. The distortion to $C_s$ symmetry by changing the angle between the Al - $H_2$ axis and H-H bond from 90 to 80 degrees resulted in only a few cm$^{-1}$ energy lowering of the lower $^2A'$ state at about 89.5 degrees, and then the energies of both states go up. This suggests that the energy of the crossing point can be considered as a good approximation to the height of the barrier for the Al + $H_2$ -> $AlH_2$ insertion reaction. Little interaction between the two lowest $^2A'$ states, as well as the high energy location of the crossing point (~ 27 kcal/mol ) suggest that the probability of the adiabatic reaction Al---$H_2$ -> $AlH_2$ through an avoided crossing is very low.

*Al-(H$_2$)n clusters*

The structures and stabilization energies for several Al-($H_2$)n complexes were calculated with n = 1-6 (Figure 6). The addition of $H_2$ molecules increases the stability of the complex almost additively.

Preliminary calculations at the MP2 level of theory showed that the approximate barrier to Al atom migration from one site to another in a face-centered cubic lattice of $H_2$ molecules is about 5 kcal/mol.

**References:**

1. Pople, J. A.; Head-Gordon, M.; Raghavachari, K. J. Phys. Chem. 1987, 87, 5968.
2. T.H. Dunning, Jr., J. Chem. Phys. 90, 1007 (1989); R.A. Kendall, T.H. Dunning, Jr., and R.J. Harrison, J. Chem. Phys. 96, 6796 (1992); D.E. Woon and T.H. Dunning, Jr., J. Chem. Phys. 98, 1358 (1993).
3. M. H. Alexander. J. Chem. Phys. 1993, 99, 6014.

**Table 1**. Characteristics of Van der Waals complexes of B, Al, C, and Si atoms with $H_2$ molecule.

| M | State | R (M-X[a]), Å | $D_e$, cm$^{-1}$ | M | State | R (M-X), Å | $D_e$, cm$^{-1}$ |
|---|---|---|---|---|---|---|---|
| B | $^2\Sigma$ | 3.87 | 93 | Al | $^2\Sigma$ | 4.62 | 89 |
|  | $^2B_2$ | 3.11 | 130 |  | $^2B_2$ | 3.25 | 204 |
|  | $^2B_1$ | 3.33 | 78 |  | $^2B_1$ | 3.60 | 103 |
| C | $^1\Sigma$ | 3.61 | 120 | Si | $^1\Sigma$ | 4.25 | 112 |
|  | $^3\Pi$ | 3.54 | 81 |  | $^3\Pi$ | 4.15 | 84 |
|  | $^3A_2$ | 2.21[b] | 324 |  | $^3A_2$ | 2.25[b] | 720 |

[a] X - midpoint of H-H bond. [b] Equilibrium distance r(H-H)=0.75 and 0.76Å for C-$H_2$ and Si-$H_2$ $^3A_2$ complexes, and 0.743 Å for other complexes.

Figure 2. QCISD(T)/aug-pvtz potential energy surfaces for Si - H$_2$ (C$_{2v}$ symmetry).



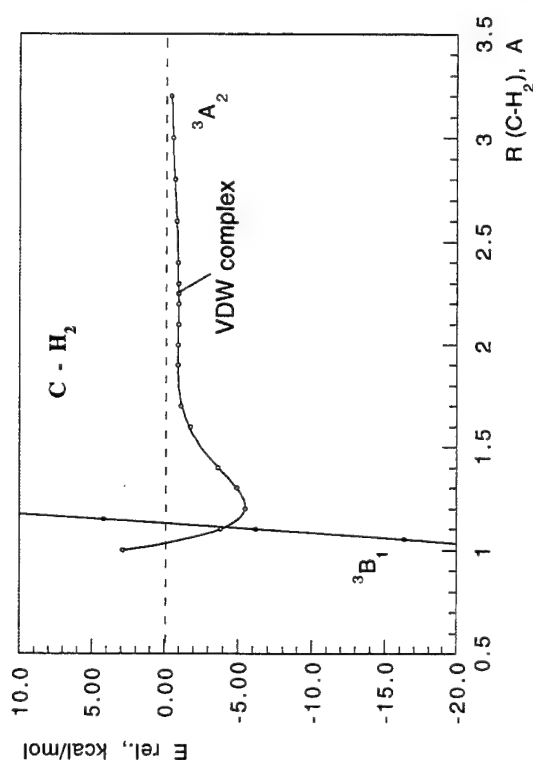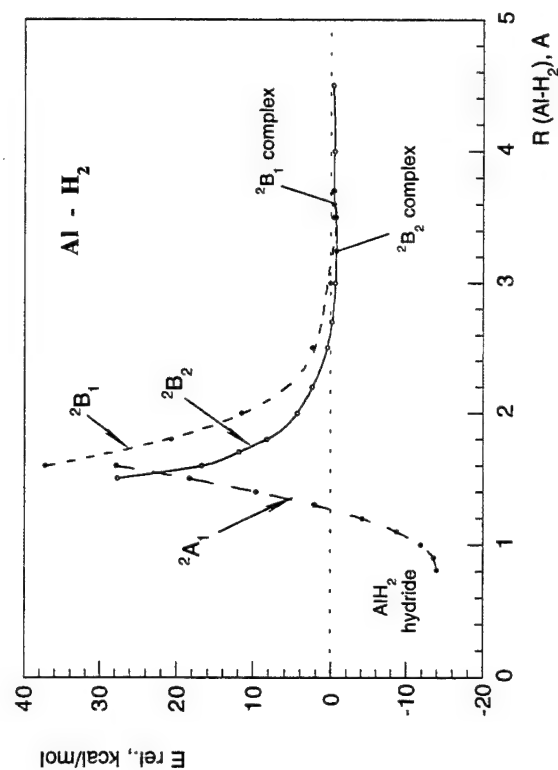Figure 4. QCISD(T)/aug-pvtz potential energy surfaces for Al-H$_2$ (C$_{2v}$ symmetry).



Figure 1. QCISD(T)/aug-pvtz potential energy surfaces for C-H$_2$ (C$_{2v}$ symmetry).



Figure 3. QCISD(T)/aug-pvtz potential energy surfaces for B-H$_2$ (C$_{2v}$ symmetry)

178

## (a) Single state MCSCF

2-A1 state



2-B2 state



## (b) State-averaged MCSCF

2-A' state (90 deg.)



2-A' state (85 deg.)
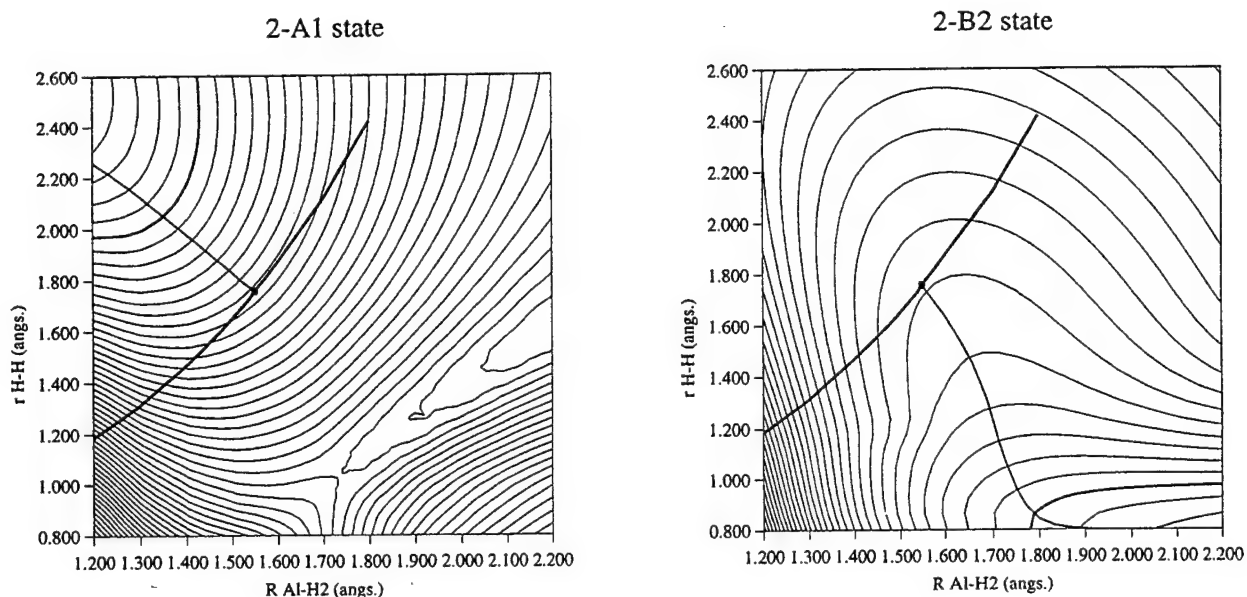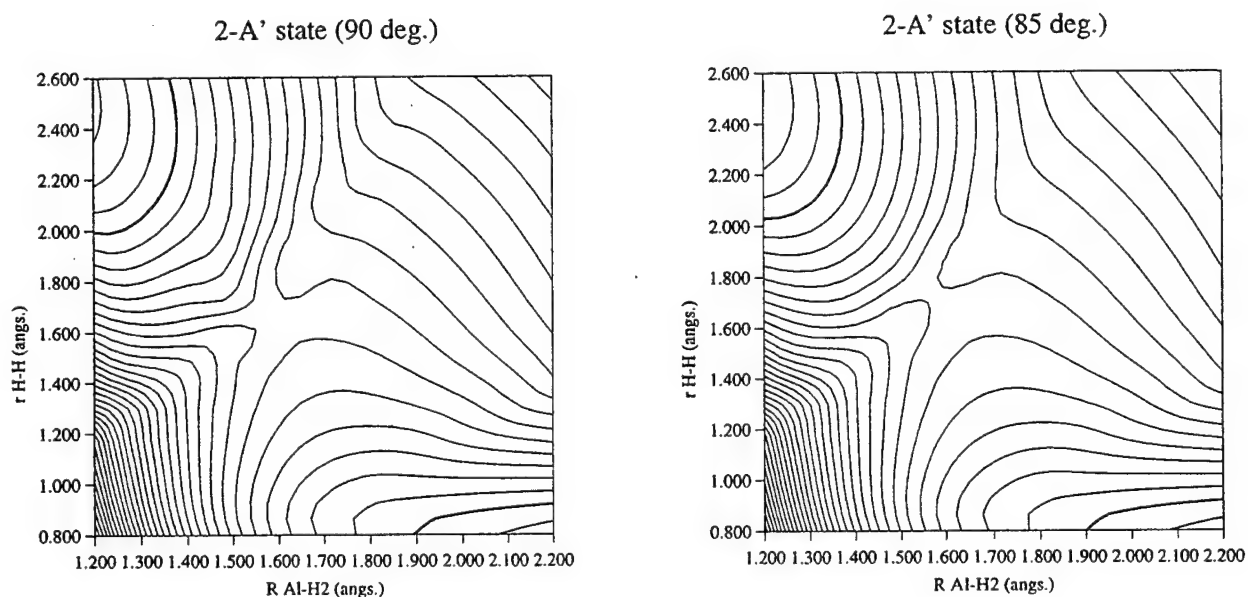


Figure 5. (a) MCSCF(5,6)/aug-cc-pvtz potential energy surfaces of Al-$H_2$ in $C_{2v}$ symmetry: $^2A_1$ and $^2B_2$ states; (b) SA-MCSCF(5,6)/aug-cc-pvtz potential energy surfaces of Al-$H_2$ in $C_S$ symmetry: angle Al XH = 90° and 85°, X = midpoint of H-H bond. Thick contour lines correspond to -243.030 a.u., energy increment is 0.005 a.u.

179
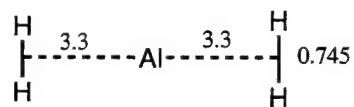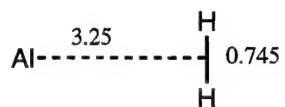
$D_e$, cm$^{-1}$  QCISD(T)  204  398

MP4SDQ  184  371
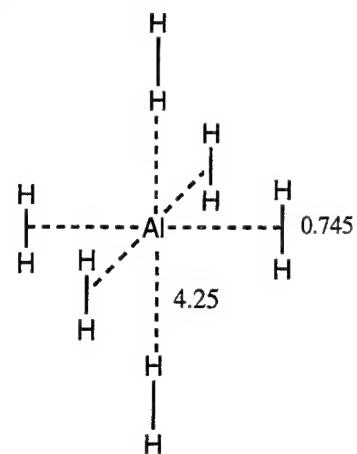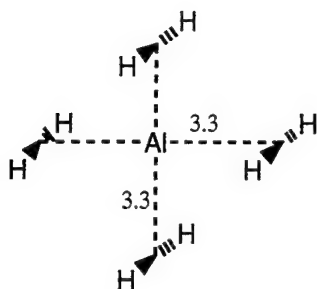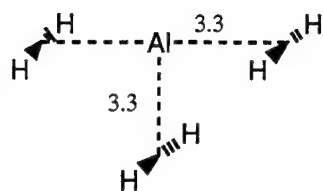
MP4SDQ  560  747  942

Figure 6. Van-der-Waals complexes of Al with $H_2$ molecules.

# Calculations of van der Waals Molecules Relevant to HEDM Studies

**Jeffrey A. Sheehy**

**Hughes STX Corporation**

**Propulsion Sciences Division**
**USAF Phillips Laboratory**
**Edwards AFB, CA   93524-7680**

## Introduction

Research aimed at enhancing the performance of rocket propulsion systems by employing atom- or molecule-seeded cryogenic fuels or oxidizers continues to be an important component of the high energy density matter (HEDM) program [1]. This concept is viewed as a novel yet potentially feasible means of achieving significant improvements in operating characteristics such as the specific impulse, which is the total impulse, or time-integrated thrust force, per unit weight of propellant.  Calculations suggest that the addition of even a few mole percent of selected atomic or molecular species to solid hydrogen may provide specific impulse increases of as much as 25% by comparison with current liquid-hydrogen/liquid-oxygen rocket engines [2]. Supporting this area of HEDM research is the development, implementation, and testing of a spectral theory of chemical binding, applicable to the construction of exact many-body potential-energy surfaces of HEDM-doped aggregates, with the goal of predicting structural and spectroscopic properties of such cryogenic solids [1,3-5]. Initial work along these lines has focused on alkali metals in rare-gas matrices [6-8], as these prototypical systems have been studied experimentally under the auspices of the HEDM program [9-10].

In the present study *ab initio* quantum-chemical calculations of the ground and several excited states of NaAr are reported. Potential-energy, dipole-moment, and transition-moment functions for the $X\,^2\Sigma^+$, $A\,^2\Pi$, $B\,^2\Sigma^+$, $C\,^2\Sigma^+$, $D\,^2\Delta$, $E\,^2\Pi$, and $F\,^2\Sigma^+$ states, based on internally contracted [11,12] multireference single- and double-excitation configuration-interaction (IC-MRCI) calculations from state-averaged complete-active-space self-consistent-field (SA-CASSCF) wave functions in extensive Gaussian basis sets, are compared with computed [13,14] and measured [15-18] values in the literature. The present calculations provide essential data for applications of the spectral theory to sodium-doped argon clusters and solids [3-5].

The ground-state bending potential of NaAr$_2$ is also calculated, employing the single- and double-excitation coupled-cluster approach including a perturbative correction for connected triple excitations [19], denoted CCSD(T). Analogous computations are performed for the ground states of Ar$_2$, NaAr, Na atom, and Ar atom, and because energies obtained in this manner are size extensive, scaling properly with the number of electrons, the non-pairwise-additive energy in the triatomic system may be extracted and compared with

predictions of the spectral theory. Further calculations on these and other systems, including examinations of basis-set-superposition and sodium core-valence electron correlation effects, are also indicated.

## Computations

The IC-MRCI potential-energy, dipole-moment, and transition-moment functions for NaAr are obtained by supplementing the $(17s\ 12p\ 5d\ 4f)/[7s\ 6p\ 4d\ 3f]$ atomic-natural-orbital basis sets of Widmark *et al.* [20] with a $(1s\ 1p\ 1d\ 1f\ 2g\ 1h)$ set of functions to yield $[8s\ 7p\ 6d\ 5f\ 2g\ 1h]$ contracted basis sets for both atoms. The supplemental (diffuse) $s$, $p$, $d$, and $f$ exponents are selected as even-tempered extensions of the original basis sets, employing a factor of 2.5 between successive exponents. The two $g$ exponents are 0.226 and 0.0904 for Na, and 0.835 and 0.334 for Ar, whereas the single $h$ exponent is 0.271 for Na and 1.002 for Ar, obtained by employing standard scaling relationships [21]. Only the pure spherical harmonic components of the higher angular momentum functions are retained. The calculations are performed in $C_{2v}$ symmetry, with CASSCF active spaces as large as $(7a_1\ 3b_1\ 3b_2\ 1a_2)$ depending on the number of states averaged, and the full configuration list so obtained forms the MRCI reference space.

The CCSD(T) calculations of the ground electronic states of Na atom, Ar atom, NaAr, $Ar_2$, and $NaAr_2$ utilize the aug-cc-pVQZ and aug-cc-pV5Z basis sets of Dunning and Woon [22,23]; the quadruple-zeta set is always used for Na, whereas both sets are variously employed for Ar. Sodium ($2s$ and $2p$) core correlation effects are examined in some cases, using appropriate extensions to the basis set, giving an aug-cc-pCVQZ basis set for Na [23]. Basis-set superposition error is estimated employing the full counterpoise procedure [24]. The non-pairwise-additive energy in $NaAr_2$, defined as that which remains after accounting for the energies of the three diatomic pairs comprising the molecule, is computed relative to separated-atom limits at appropriate geometries as

$$E_{NPA} = E(NaAr_2) - E(Ar_2) - 2E(NaAr). \tag{1}$$

All electronic structure calculations are performed using the program system MOLPRO [25] on IBM RS/6000 and Cray C90 computers. The PAM/6000 library of disk striping routines [26] has been utilized to circumvent file size limitations on the IBM work stations.

## Results

Potential-energy curves for the NaAr $X\ ^2\Sigma^+$, $A\ ^2\Pi$, $B\ ^2\Sigma^+$, $C\ ^2\Sigma^+$, $D\ ^2\Delta$, $E\ ^2\Pi$, and $F\ ^2\Sigma^+$ states are given in Fig. 1, as are the appropriate separated-atom limits. Figures 2-4 show more detail of the individual electronic states, comparing present results with other calculated potential curves [13,14] and available experimental values of $D_e$ and $r_e$ [15-18]. The present calculations are generally in excellent accord with experiment, representing significant improvements over the earlier theoretical results (Figs. 2-4). It should be noted that the study of Laskowski *et al.*, which employs effective-core potentials and relatively small basis sets, is primarily concerned with surveying the repulsive region for several electronic states of both NaAr and NaXe.

The ground state potential of Saxon *et al.* is too deeply bound by comparison with experiment and present results (Fig. 2), probably as a consequence of superposition error in the one-particle basis set. Preliminary (CASSCF) calculations of the higher $G\,^2\Pi$, $H\,^2\Sigma^+$, and $I\,^2\Sigma^+$ states, dissociating to Na $4p$ and $5s$ excited atoms, are shown in Fig. 5 along with the states dissociating to the Na $3d$ limit. (Argon is in its $^1S$ ground state in all cases.) The most noteworthy feature of Fig. 5 is the avoided crossing of the $F\,^2\Sigma^+$ and $H\,^2\Sigma^+$ states at about 4 Å.

In addition to accurate potential-energy curves, an important outcome of the present study is the calculation of a consistent set of dipole- and transition-moment functions. Figures 6 and 7 depict these data, which are in some cases significantly more accurate than that which was previously available [13,14], while otherwise they represent the first such results to be reported. As the signs of the transition moments are arbitrary, they are depicted in Fig. 7 as positive functions in order to show the greatest possible detail. Clearly, the avoided crossing of the $F\,^2\Sigma^+$ and $H\,^2\Sigma^+$ states substantially perturbs the moment functions involving the former (Figs. 6 and 7), which undergo large amplitude changes between about 3.5 and 4.5 Å, commensurate with a dramatic change in the character of the wave function.

The ground state $Ar_2$ potential, calculated in both the aug-cc-pVQZ and the aug-cc-pV5Z basis sets, is shown in Fig. 8. The result obtained in the larger basis is in excellent agreement with the widely used potential for this system in the literature [27], but the smaller-basis calculation is also quite adequate for most purposes. Consequently, the smaller argon basis set is used in the $NaAr_2$ calculations in order to make them tractable. The triatomic system is calculated for various Ar–Na–Ar angles at a fixed Na–Ar separation of 4.0 Å. The non-pairwise-additive potential energy in $NaAr_2$, evaluated by Eq. (1) employing superposition-error-corrected energy values, is compared with predictions based on various levels of the spectral theory [3-5] in Fig. 9. At present, quantitative agreement between the spectral theory and the directly calculated result is lacking, perhaps indicating that more diatomic states need to be included in the spectral theory treatment of this system, and also possibly signifying that the *ab initio* calculation, which in this case does not include sodium core-valence correlation, needs further refinement. Nevertheless, the results are of the same general magnitude, and in all cases the non-additive energy is negative at small angles and positive at large angles. Note that a directly calculated *ab initio* value cannot be reliably computed for Ar–Na–Ar angles smaller than 30°, as for such geometries the short Ar–Ar internuclear distance introduces various computational difficulties, such as linear dependence of the basis set. Notwithstanding the lack of quantitative accord in these preliminary results, this sort of comparison should provide an important benchmark for the spectral theory as its development continues.

## Summary

High-level *ab initio* calculations of NaAr ground and excited states are in good accord with available experimental data and show significant deviations from computations in the literature. The calculated potential-energy, dipole-moment, and transition-moment

functions form an accurate set of data that is used in computational implementations of the spectral theory of chemical binding. Direct calculations of the non-pairwise-additive energy in NaAr$_2$ are suggestive if not yet definitive; more exacting studies, along with calculations of the triatomic in excited states and at other Na–Ar separations, are in progress. Additionally, the present diatomic calculations are being extended to even higher excited states, in order to assist in examining the convergence properties of the spectral theory. Calculations of this type will be extended to other atom-seeded rare gas systems, and to HEDM-doped H$_2$ and He, concomitant with continued development of the spectral theory and experimental progress in the HEDM program.

## Acknowledgments

## References

[1] See, for example, *Proceedings of the High Energy Density Matter (HEDM) Contractors Conference*, ed. by P. G. Carrick and S. Tam (Phillips Laboratory, Edwards AFB, CA, 1995), Report PL-TR-95-3039.

[2] P. G. Carrick, *Theoretical Performance of High Energy Density Cryogenic Solid Rocket Propellants*, 31st Joint Propulsion Conference, July 1995, San Diego, CA, AIAA 95-2893.

[3] P. W. Langhoff, *J. Phys. Chem.* 100 (1996) 2974.

[4] J. A. Boatz, M. E. Fajardo, J. A. Sheehy, and P. W. Langhoff, *Monte Carlo Simulations of the Structures and Optical Absorption Spectra of Na/Ar Clusters and Solids: An Application of Spectral Theory of Chemical Binding*, these proceedings.

[5] J. A. Sheehy, J. A. Boatz, M. E. Fajardo, and P. W. Langhoff, *Spectral Theory of Weakly Bonded Atomic Aggregates*, these proceedings.

[6] J. A. Boatz and M. E. Fajardo, *J. Chem. Phys.* 101 (1994) 3472.

[7] J. A. Boatz and M. E. Fajardo, *Monte Carlo Simulations of the Structures and Optical Absorption Spectra of Na Atoms in Ar Clusters, Surfaces, and Solids: A Detailed Presentation of the Theoretical Methods Used* (Phillips Laboratory, Edwards AFB, CA, 1994), Report PL-TR-94-3024.

[8] M. E. Fajardo and J. A. Boatz, *J. Comput. Chem.*, in press.

[9] M. E. Fajardo, P. G. Carrick, and J. W. Kenney III, *J. Chem. Phys.* 94 (1991) 5812.

[10] S. Tam and M. E. Fajardo, *J. Chem. Phys.* 99 (1993) 854.

[11] H.-J. Werner and P. J. Knowles, *J. Chem. Phys.* 89 (1988) 5803.

[12] P. J. Knowles and H.-J. Werner, *Chem. Phys. Lett.* 145 (1988) 514.

[13] R. P. Saxon, R. E. Olson, and B. Liu, *J. Chem. Phys.* 67 (1977) 2692.

[14] B. C. Laskowski, S. R. Langhoff, and J. R. Stallcop, *J. Chem. Phys.* 75 (1981) 815.

[15] R. E. Smalley, D. J. Auerbach, P. S. H. Fitch, D. H. Levy, and L. Wharton, *J. Chem. Phys.* 66 (1977) 3778.

[16] J. Tellinghuisen, A. Ragone, M. S. Kim, D. J. Auerbach, R. E. Smalley, L. Wharton, and D. H. Levy, *J. Chem. Phys.* 71 (1979) 1283.

[17] G. Aepfelbach, A. Nennemann, and D. Zimmerman, *Chem. Phys. Lett.* 96 (1983) 311.

[18] F. van den Berg, R. Morgenstern, and C. Th. J. Alkemade, *Chem. Phys.* 93 (1985) 171.

[19] J. D. Watts, J. Gauss, and R. J. Bartlett, *J. Chem. Phys.* 98 (1993) 8718.

[20] P.-O. Widmark, B. J. Persson, and B. O. Roos, *Theoret. Chim. Acta* 79 (1991) 419.

[21] T. Helgaker and P. R. Taylor, in *Modern Electronic Structure Theory*, ed. by D. R. Yarkony (World Scientific, London, 1995), pp. 725-856.

[22] D. E. Woon and T. H. Dunning, Jr., *J. Chem. Phys.* 98 (1993) 1358.

[23] D. E. Woon, private communication.

[24] A concise summary of issues related to basis-set superposition error and various approaches to its estimation is contained in Ref. 21.

[25] MOLPRO is a package of *ab initio* programs written by H.-J. Werner and P. J. Knowles, with contributions from J. Almlöf, R. D. Amos, M. J. O. Deegan, S. T. Elbert, C. Hampel, W. Meyer, K. Peterson, R. Pitzer, A. J. Stone, P. R. Taylor, R. Lindh, M. E. Mura, and T. Thorsteinsson.

[26] PAM/6000 is a licensed program of asynchrous I/O routines developed by IBM (London).

[27] R. A. Aziz and M. J. Slaman, *Mol. Phys.* 58 (1986) 679.

**Figure 1.  NaAr Potential-Energy Curves**

$E^2\Pi$

$F^2\Sigma^+$

$D^2\Delta$

Na $(3d)$ $^2D$ + Ar $^1S$

$C^2\Sigma^+$

Na $(4s)$ $^2S$ + Ar $^1S$

$B^2\Sigma^+$

$A^2\Pi$

Na $(3p)$ $^2P$ + Ar $^1S$

$X^2\Sigma^+$

Na $(3s)$ $^2S$ + Ar $^1S$

Potential Energy (cm$^{-1}$)

Internuclear Distance (Angstroms)
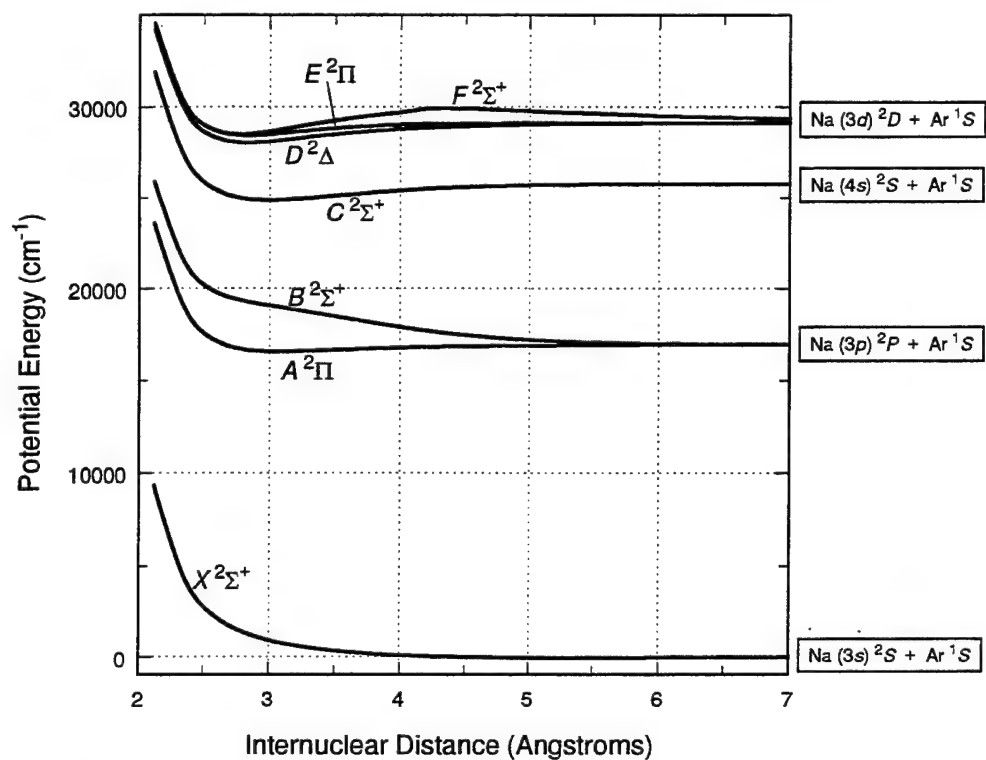


**Figure 2.  NaAr Ground-State Potential-Energy Curve**

Present results
Saxon *et al.*
Laskowski *et al.*
Expt. $r_e$, $D_e$

$X^2\Sigma^+$

Na $(3s)$ $^2S$ + Ar $^1S$

Potential Energy (cm$^{-1}$)

Internuclear Distance (Angstroms)
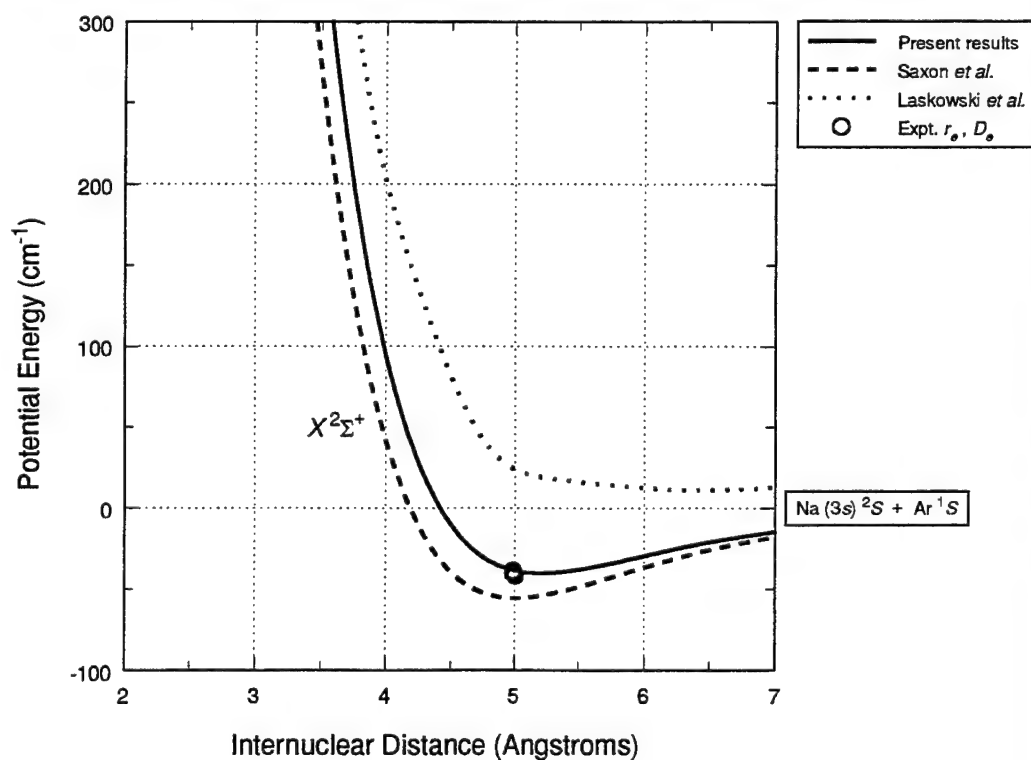
Figure 3. NaAr Excited-State Potential-Energy Curves
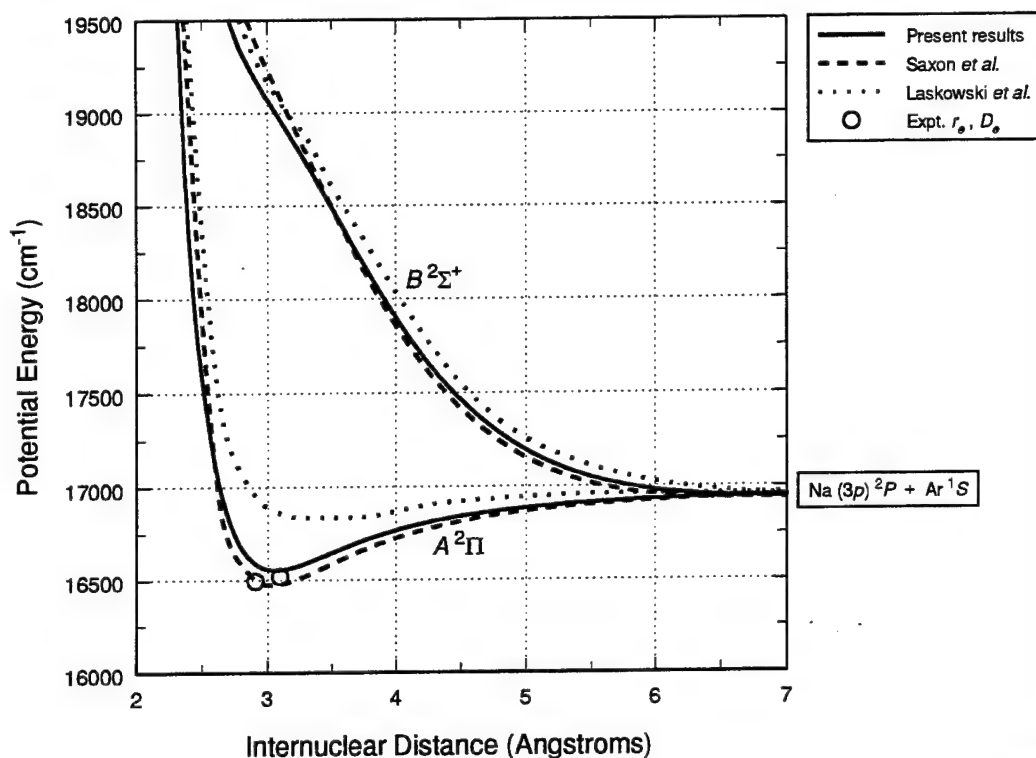


Figure 4. NaAr Excited-State Potential-Energy Curves
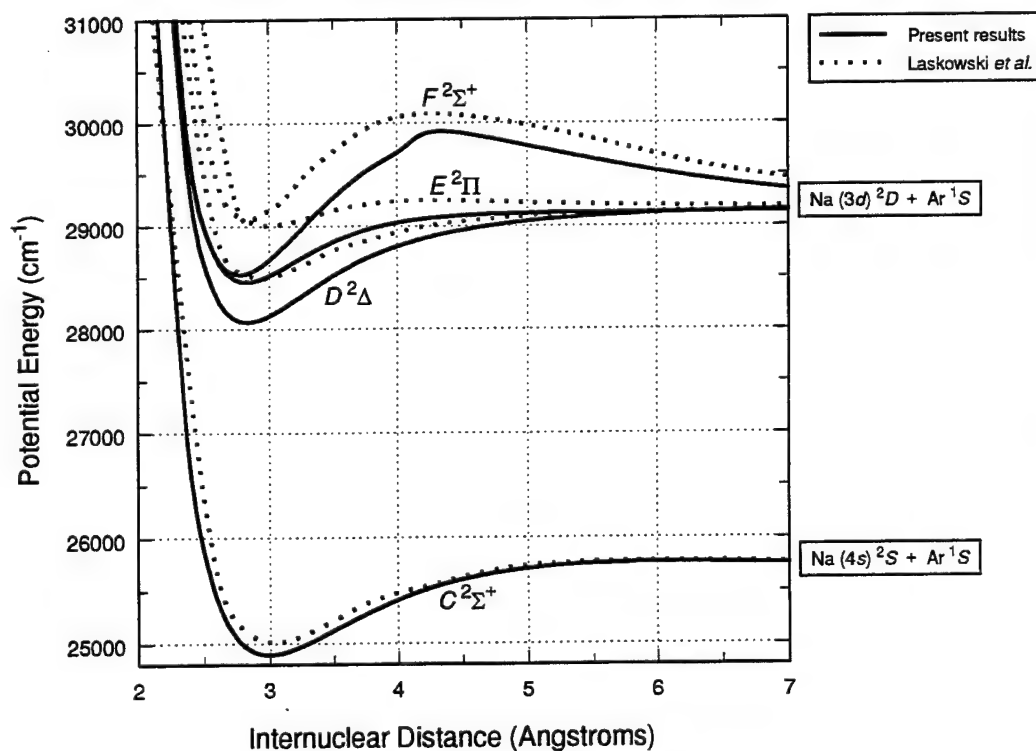
Figure 5. NaAr Potential-Energy Curves
Preliminary (CASSCF) results for higher excited states
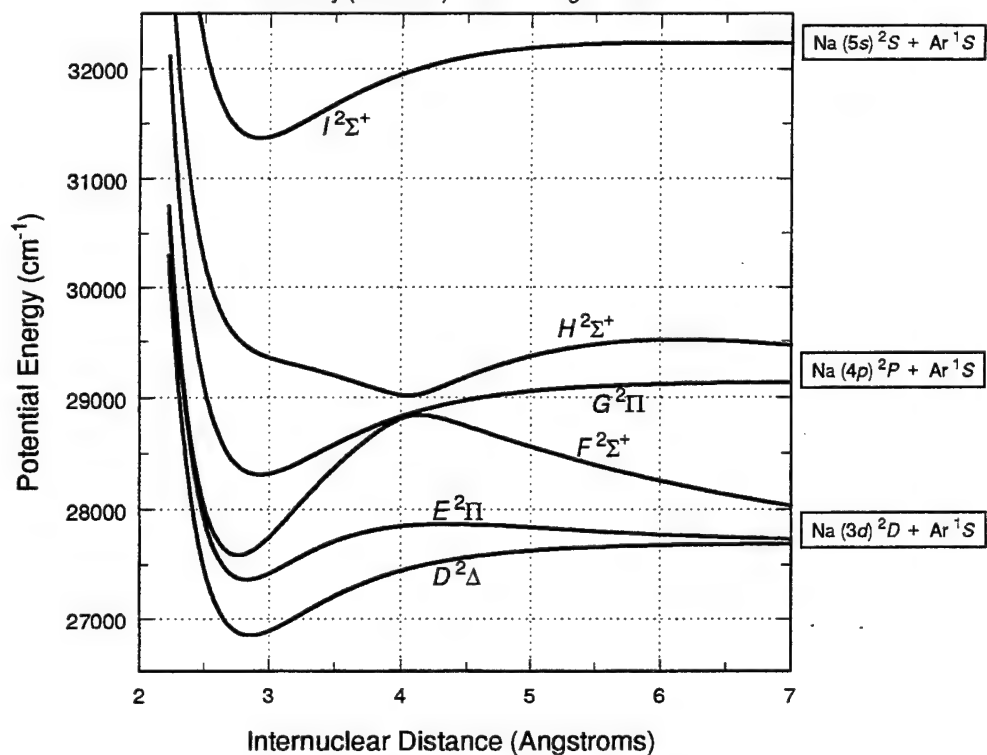


Figure 6. NaAr Dipole-Moment Functions

188
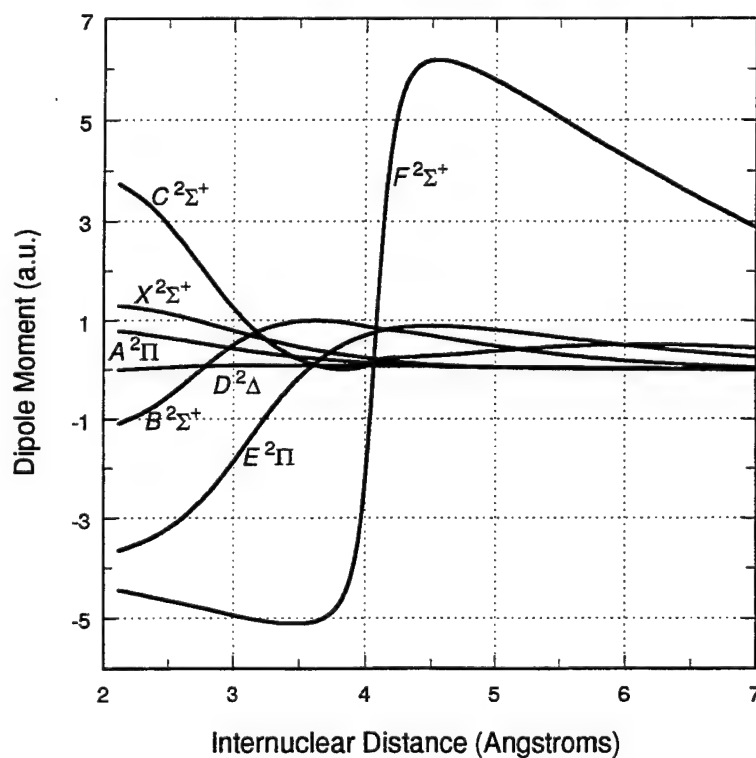
**Figure 7. NaAr Transition-Moment Functions**

Transition Moment (a.u.) vs. Internuclear Distance (Angstroms)

Curves labeled: B - E, A - D, F - B, X - A, E - A, B - X, C - A, C - B, E - D, F - C, F - E, F - A, B - A, C - E, C - X, F - X, X - E
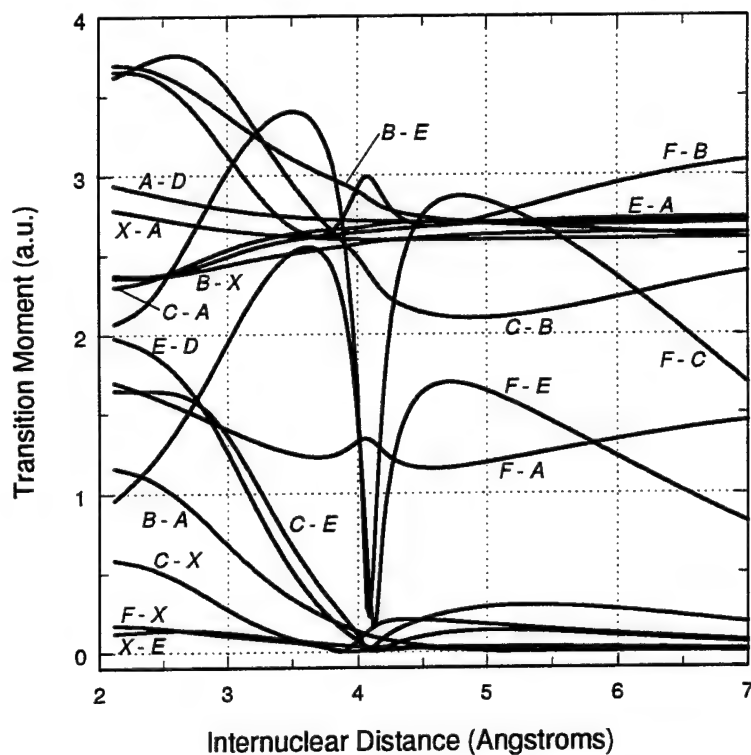


**Figure 8. Ar₂ Ground State Potential-Energy Curve**

Comparison of CCSD results in different basis sets

Potential Energy (cm⁻¹) vs. Internuclear Distance (Angstroms)

$X^1\Sigma_g^+$

$Ar\,^1S + Ar\,^1S$

Legend: aug-cc-pV5Z (solid line), aug-cc-pVQZ (dashed line)
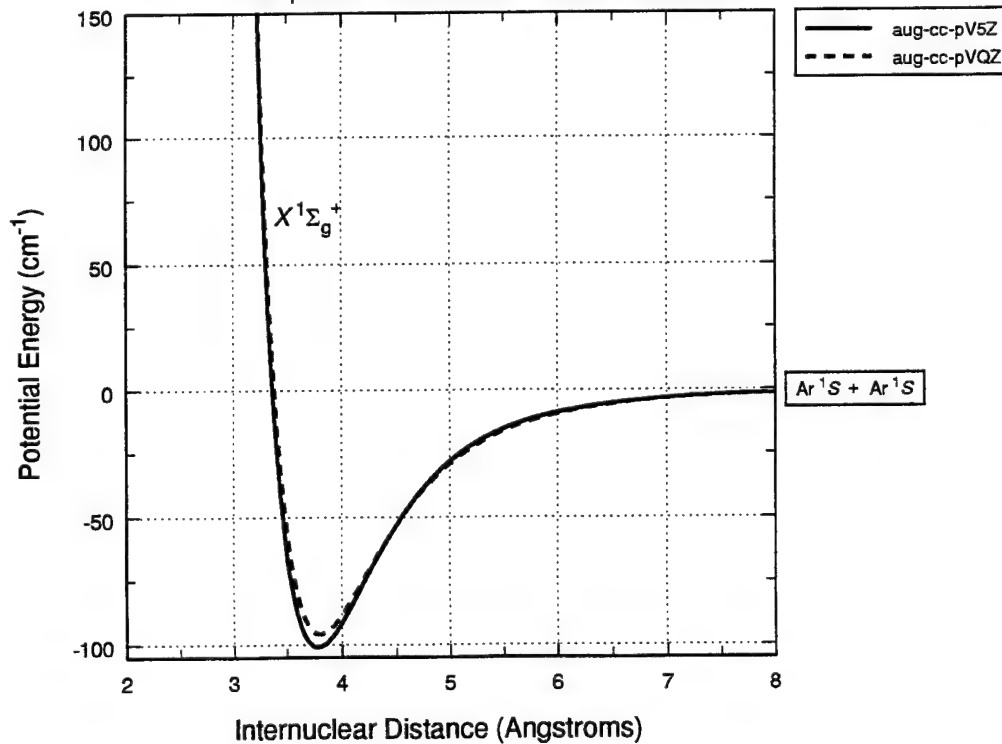
**Figure 9. NaAr$_2$ Ground State Non-Additive Potential Energy**

Na-Ar internuclear distance fixed at 4.0 Angstroms

Legend:
- Theory 3s, 3p
- Theory 3s, 3p, 4s
- Theory 3s, 3p, 4s, 3d
- Calc. w/ BSSE corr.

Y-axis: Non-additive Potential Energy (cm$^{-1}$)

X-axis: Ar-Na-Ar Angle (degrees)
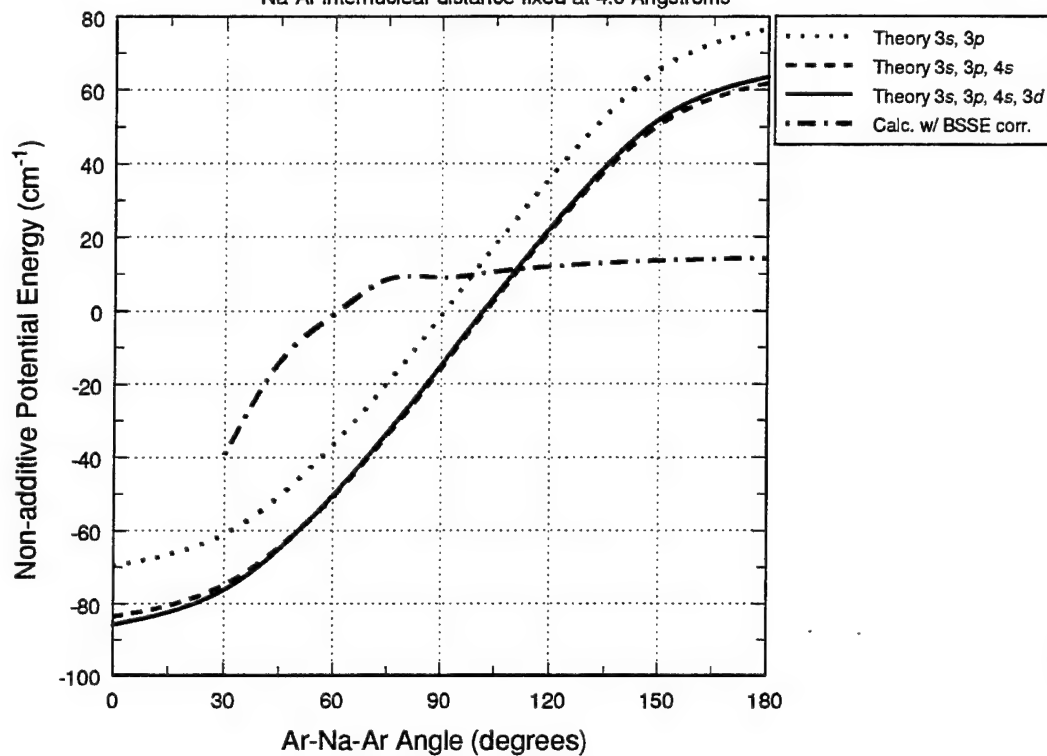
# Single Atom Doping of Clusters

Leslie S. Perkins[*]

Phillips Laboratory, OLAC PL/RKS, 10 East Saturn Blvd, Edwards Air Force Base, CA 93524-7680

## Abstract

The doping of cryogenic solids with single atoms has been of particular interest in recent years.[1] This is due to the thermochemical estimates of Carrick[2] of light metal atoms trapped in cryogenic solid hydrogen. Unfortunately, recent experimental studies of the doping of rare gas matrices with alkali metal atoms[3,4] suggest that codeposition of the dopant atoms with rare gas atoms to form the atom-doped matrix gives concentrations on the order of 1%. The calculations of Carrick are based upon a 5% atom doping. An proposed method of accomplishing a higher percentage of atom doping of a solid is to first dope the clusters in the gas phase with the required atom and then deposit these clusters on an appropriate cryogenic substrate. This in theory should give less diffusion of these single atoms in the solid and therefore allow less recombination.

In this paper, I will cover recent results of molecular dynamics simulations of doping $Ar_{55}$ with Ar and Na. The capture of the doping atoms by the cluster will be examined as a function of the temperature of the cluster, the initial kinetic energy of the doping atom, and the impact parameter of the doping atom.

### Computational Method

Molecular dynamics calculations of the single atom doping of $Ar_{55}$ clusters were performed using the molecular dynamics program constructed during my tenure at Phillips Laboratory The velocities of the cluster atoms were chosen from a Boltzmann distribution of the required temperature, specifically 30K, 40K, and 50K. The initial kinetic energies of the doping gas atom were set to be 0.05 eV, 0.10 eV, and 0.20 eV. The gas atom was started at 15 Angstroms above the top of the cluster and aimed at the cluster using the impact parameter. The impact parameter, b, is defined in this study as:

$$b = \sqrt{(x^2 + y^2)} \tag{1}$$

Figure 1 shows a schematic of the impact parameter for an atom colliding with an $Ar_{55}$ cluster. For a given

---

[*]National Research Council Postdoctoral Research Associate

1 Angstrom range of impact parameter, 250 trajectories were run, with each trajectory spanning 6 ps. This time scale allows for the short time scatter of the gas atom if it will occur. This is also the estimated time for the cluster to be doped and then deposited in experiment.[5].

The interactions of the cluster atoms with other cluster atoms and the doping atoms were modelled using pairwise-additivity of *ground* state potentials. The Ar HFD-B2 potential of Aziz and Slaman[6] was used for the Ar-Ar interactions. The Na-Ar ground state interactions were modelled using a pair potential constructed from MRCI calculations of J. Sheehy[7]. Table 1 lists the equililbrium diatomic interaction energies of Ar with Ar, Na, and B.

The analysis for these clusters consisted of determining whether or not a gas atom was captured by the cluster. Encapsulation of the dopant atom was not considered in this study. An atom is labelled "trapped" or "captured" when it meets two criteria. (1) The doping atom is a distance less than or equal to 1.10 the equilibrium binding distance of the two atom moieties at the end of the simulation time. (2)The doping atom has spent at least 3 ps bound (by the above criteria) to the cluster.

## Results and Discussion

Figure 2 shows the fraction of Ar atoms captured by a 30K $Ar_{55}$ cluster. This is plotted as a function of the impact parameter of the incoming gas molecule for the three incident kinetic energies. The solid line in the graph indicates the average cluster radius during the simulation.

It is immediately apparent that an atom can be captured by the edge of the cluster and beyond by approximately a nearest-neighbor distance from the edge. The fraction of atoms captured within this range decreases for increasing kinetic energy of the doping atom. The capture efficiency at the edges of the cluster is significantly smaller than at smaller impact parameters. The smaller impact parameter indicates that the doping atom is directly hitting an atom of the cluster or it is impinging on a face of a cluster. This merely suggests that capture by the edges and near the edges is more difficult than for a face of the cluster. The fraction of "edge captures" is largest for the trajectories with 0.05 eV dopant atoms, while the smallest fraction is shown for the 0.20 eV dopant atoms.

Examining the small impact parameter trajectories, it is surprising to see that capture seems slightly more efficient for higher kinetic energy dopant atoms than for lower kinetic energy dopant atoms. It might be expected that the higher kinetic energy atoms would be more likely to scatter off of the cluster. However, it is possible that the transfer of kinetic energy to the vibrational modes of the cluster is more efficient with higher kinetic energy and therefore leads to a greater possibility of capture.

The set of histograms for a 40K $Ar_{55}$ cluster, shown in figure 3 reveal the same qualitative trends for the kinetic energies as shown in figure 2. One small point to note is that the maximum capture impact

parameter has increased from 11 Angstroms for a 30K cluster to 12 Angstroms for a 40K cluster. This is due to the increased area occupied by the cluster due to larger vibrations from the thermal energy of the cluster.

The 50K trajectories, presented in figure 4, again show the same qualitative trends of the 30K and 40K trajectories. There is not as significant an enhancement of capture with higher kinetic energies of the dopant atoms as in the two other studies, but it is present for the range of 0-1 Angstrom impact parameter. We also see an increase in the maximum impact parameter to 13 Angstroms for a 50K cluster.

Figure 5 shows the capture of a Na atom by a 30K $Ar_{55}$ cluster for the 3 kinetic energies. Please note that for this graph, the range of the ordinate has been decreased from 1.0 to 0.30. The capture fractions for Na are smaller than for Ar, which is consistent with the smaller $D_e$ for Na-Ar interaction relative to Ar-Ar (Table 1).

It is apparent from figure 5 is that there is no capture of Na dopant atoms beyond the edge of the cluster for energies larger than 0.05 eV. It is also shown that there is a significant decrease in capture of the Na atom with increasing kinetic energy. The most striking difference in the capture profile relative to Ar-$Ar_{55}$ occurs at small impact parameters. In Ar-$Ar_{55}$, the smallest impact parameters had the largest capture fractions. For a Na atom, the peak in fraction captured is between 2 and 3 Angstroms for kinetic energies of 0.05 and 0.20 eV and between 4 and 5 Angstroms for kinetic energies of 0.10 eV.

The capture of Na by a 40K $Ar_{55}$ cluster (figure 6) shows the largest capture fractions for the smallest impact parameters, which is in line with the Ar-$Ar_{55}$ studies. As in the 30K graph in figure 4, we find that there is little capture for atoms with energies larger than 0.05 eV at the edge of the cluster and beyond. Figure 7 exhibits the same qualitiative trends for the Na atom being captured by a 50K cluster of $Ar_{55}$.

The total capture efficiency was calculated for each pair of kinetic energy and cluster temperature. These efficiencies were calculated as

$$efficiency = \frac{\sum captured\ trajectories}{\sum total\ trajectories} \quad . \tag{2}$$

The results were tabulated for impact parameters up to 13 Angstroms and can be found in Table 2.

The efficiency of capture of an Ar atom by a $Ar_{55}$ cluster decreases with increasing cluster temperature for a given kinetic energy. The oppositetrend is seen for Na atoms captured by $Ar_{55}$. For both systems, the efficiency decreases with increasing gas atom kinetic energy for a given cluster temperature.

# References

1.    *Proceedings of the High Energy Density Matter(HEDM) Conference, June 1995*, edited by S. Tam (USAF Phillips Laboratory, Edwards Air Force Base, CA 1995) .

2.    P.G. Carrick, *Specific Impulse Calculations of High Energy Density Solid Cryogenic Rocket Propellants. I. Atoms in solid $H_2$* (USAF Phillips Laboratory, Edwards Air Force Base, CA 1993).

3.    S. Tam and M.E. Fajardo, J. Chem Phys. **99**, 854 (1993).

4.    M.E. Fajardo, P.G. Carrick, and J.W. Kenney III, J. Chem. Phys **94**, 5812 (1991).

5.    M. Macler, private communication.

6.    R.A. Aziz and M.J. Slaman, J. Chem. Phys. **92**, 1030 (1990).

7.    J.A. Sheehy (to be published)

Table 1: Interaction energies (De, in cm$^{-1}$) for the listed atoms with Ar

|     | $D_e$ |
| --- | --- |
| Ar  | 99.0 |
| Na  | 40.0 |
| B   | 94.5 |

Table 2: Total capture efficiencies for Ar and Na atom capture by Ar$_{55}$ clusters.

|     |          | 30K   | 40K  | 50K  |
| --- | -------- | ----- | ---- | ---- |
| Ar  | 0.05 eV  | 0.59  | 0.54 | 0.52 |
|     | 0.10 eV  | 0.43  | 0.42 | 0.44 |
|     | 0.20 eV  | 0.40· | 0.39 | 0.38 |
| Na  | 0.05 eV  | 0.10  | 0.12 | 0.14 |
|     | 0.10 eV  | 0.02  | 0.05 | 0.07 |
|     | 0.20 eV  | 0.00  | 0.01 | 0.01 |



**Figure 1**

Figure 2

Ar-Ar$_{55}$
T$_{clus}$=30K



Figure 3

Ar-Ar$_{55}$
T$_{clus}$=40K



196

Figure 4



Ar-Ar$_{55}$
T$_{clus}$=50K

- 0.05 eV incident kinetic energy
- 0.10 eV incident kinetic energy
- 0.20 eV incident kinetic energy

fraction trapped

impact parameter (Angstroms)

Figure 5



Na-Ar$_{55}$
T$_{clus}$=30K

- 0.05 eV incident kinetic energy
- 0.10 eV incident kinetic energy
- 0.20 eV incident kinetic energy

fraction trapped

impact parameter (Angstroms)

Figure 6



Na-Ar$_{55}$
T$_{clus}$=40K



Figure 7

Na-Ar$_{55}$
T$_{clus}$=50K
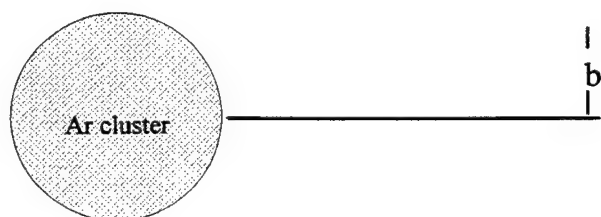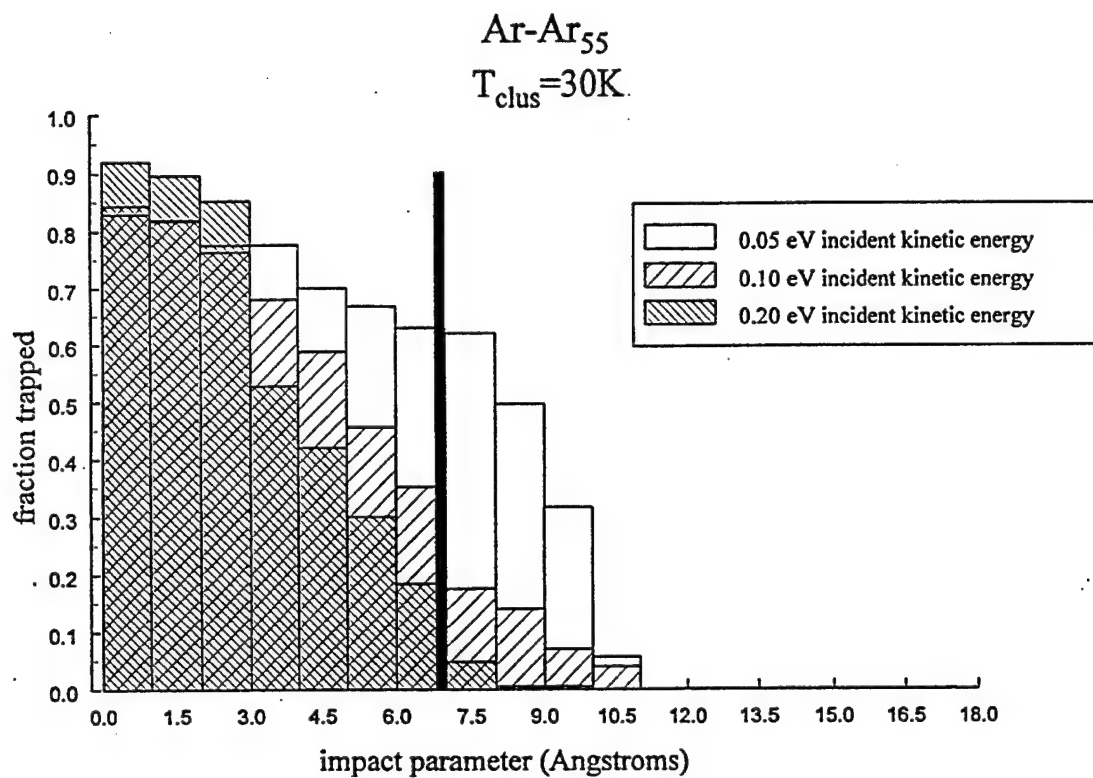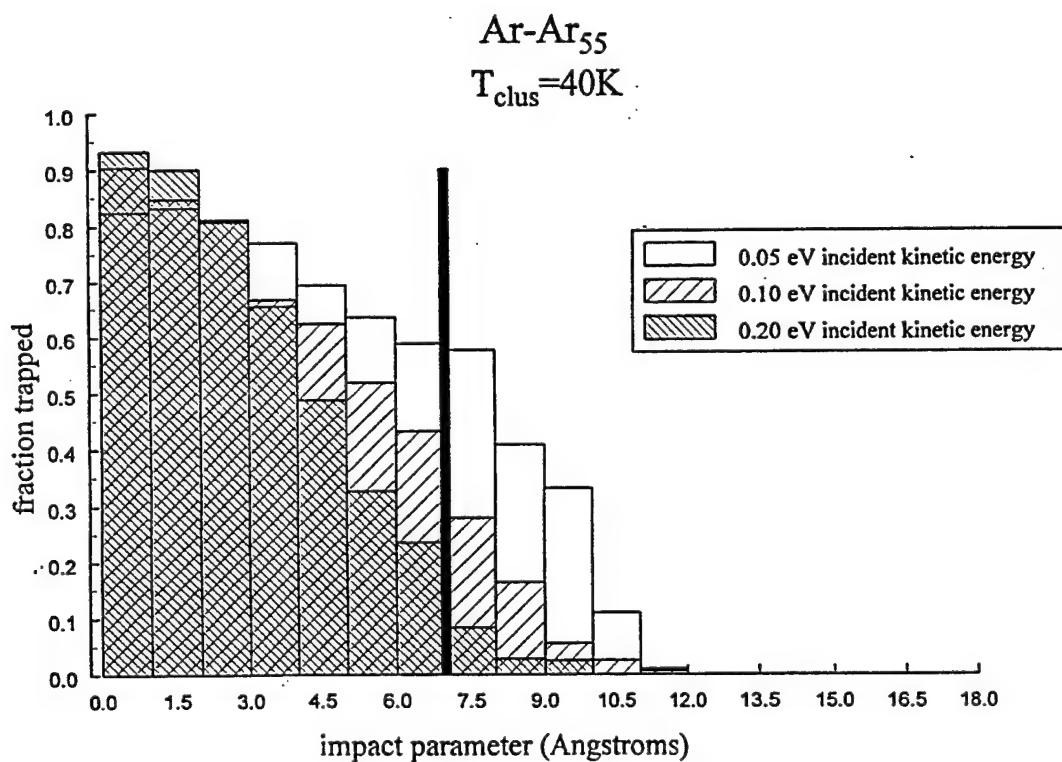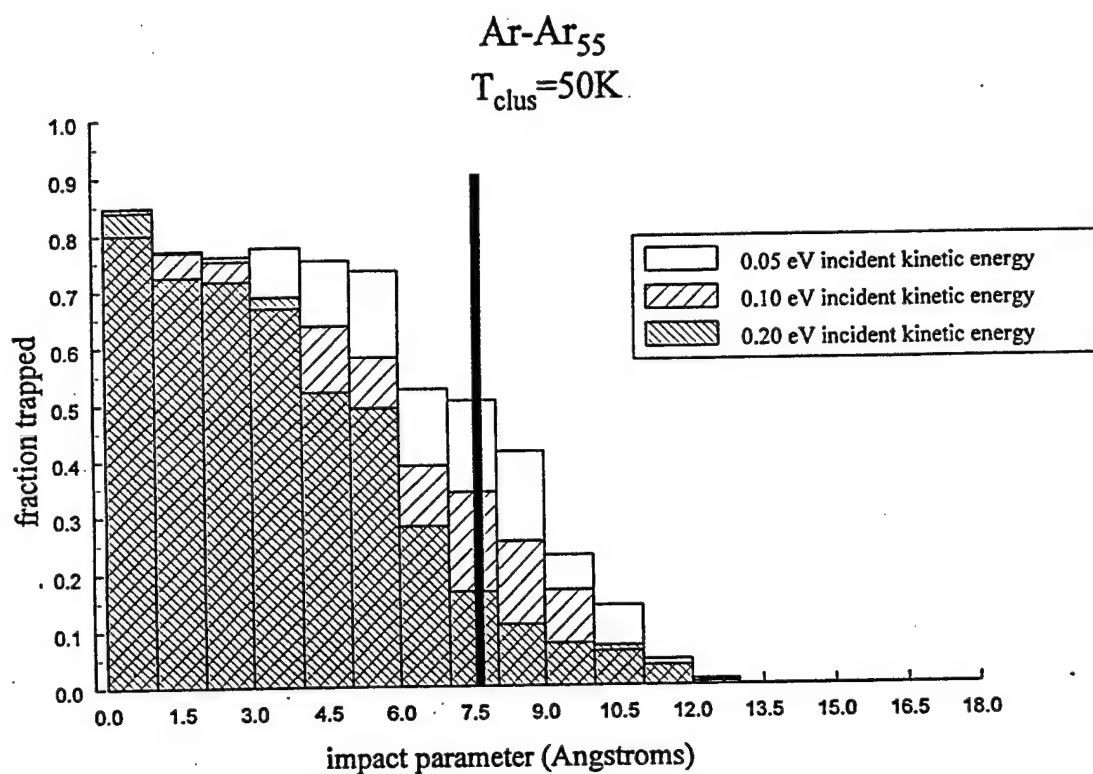
# Theoretical Studies of Some HEDM Species; Cyclic O4, Cyclic O3, and Cubane.

Stephen P. Walch
Thermosciences Institute
MS 230-3
NASA Ames Research Center
Moffett Field, CA 94035-1000

## Extended Abstract

Calculations have been carried out for a number of HEDM species using CASSCF/derivative and CASSCF/ICCI methods. Systems which have been studied to date include: cyclic $O_4$, cyclic $O_3$, tetrahedral $N_4$, and the singlet potential energy surface of cubane.

Cyclic $O_4$ is of interest both as a potential HEDM species and because of its possible role in the ozone deficit problem in atmospheric chemistry. We have studied the pathway for decomposition from the $D_{2d}$ minimum through a saddle point of $C_2$ symmetry (See Fig. 1. ). This result is in agreement with the work of Seidl and Schaefer[1]. The approximate location of the singlet triplet crossing was obtained by computing the triplet energies at the geometries along the pathway for the singlet state. The barrier to decomposition is found to be about 9 kcal/mol from ICCI calculations with the cc-pVDZ basis set. Calculations with larger basis sets (see Table I) have been carried out using the ACPF method. These calculat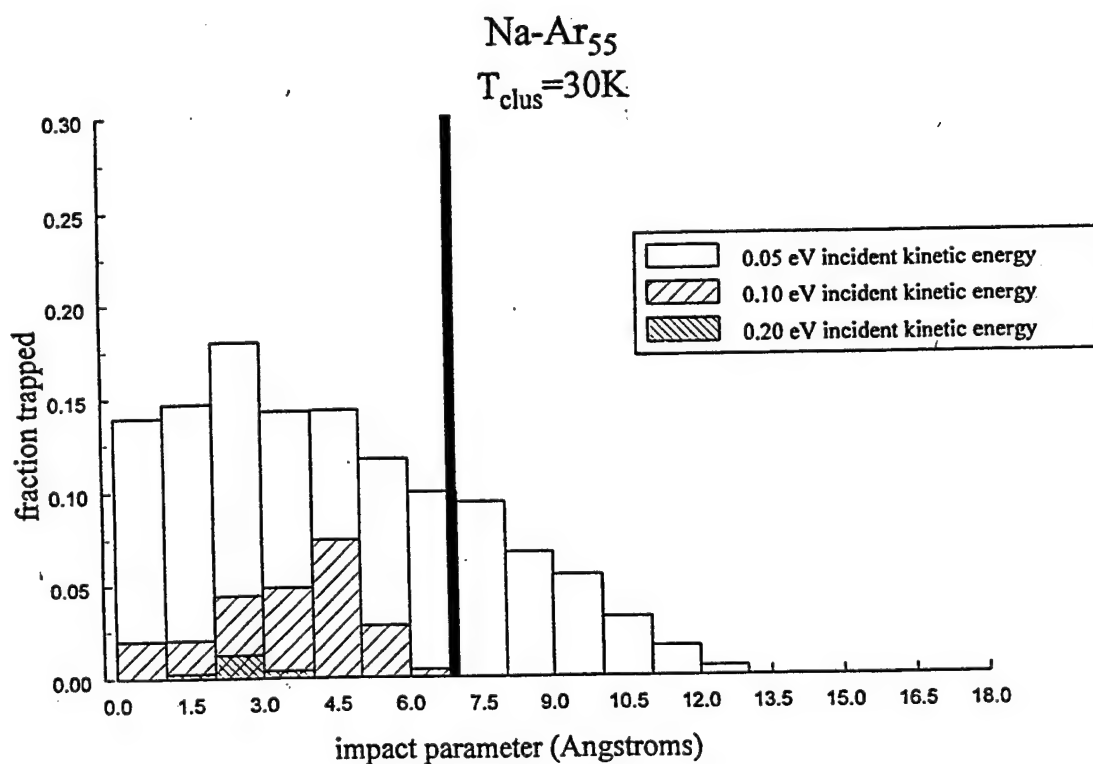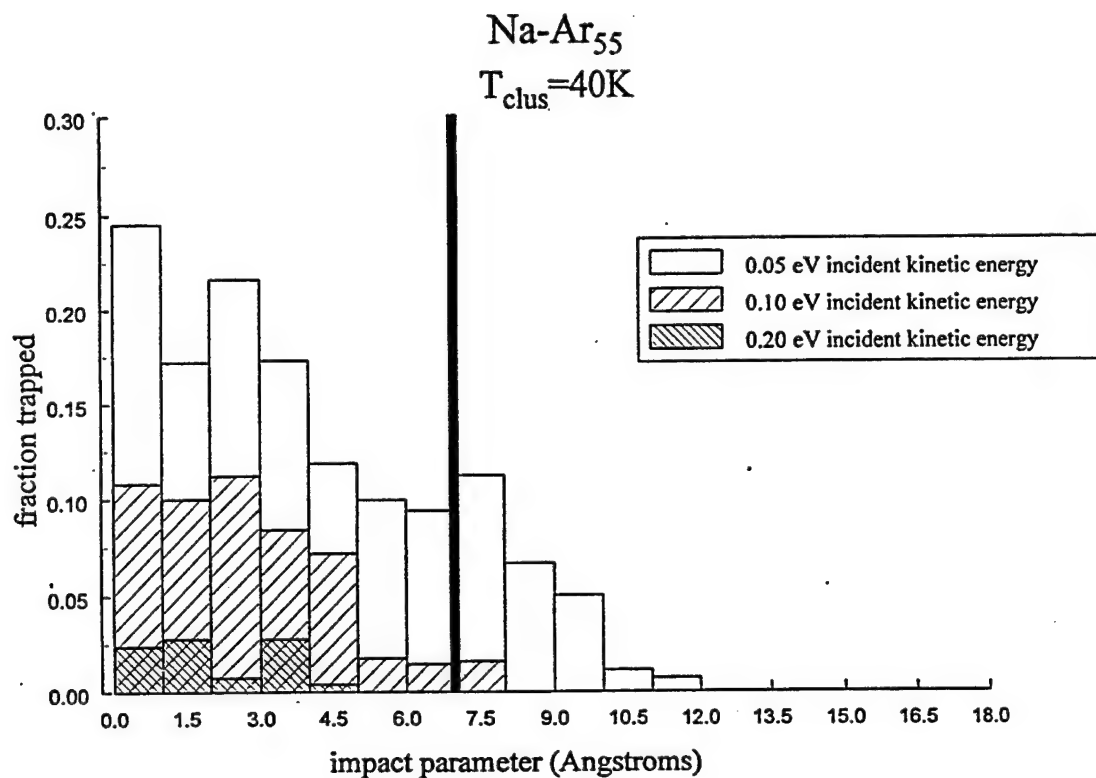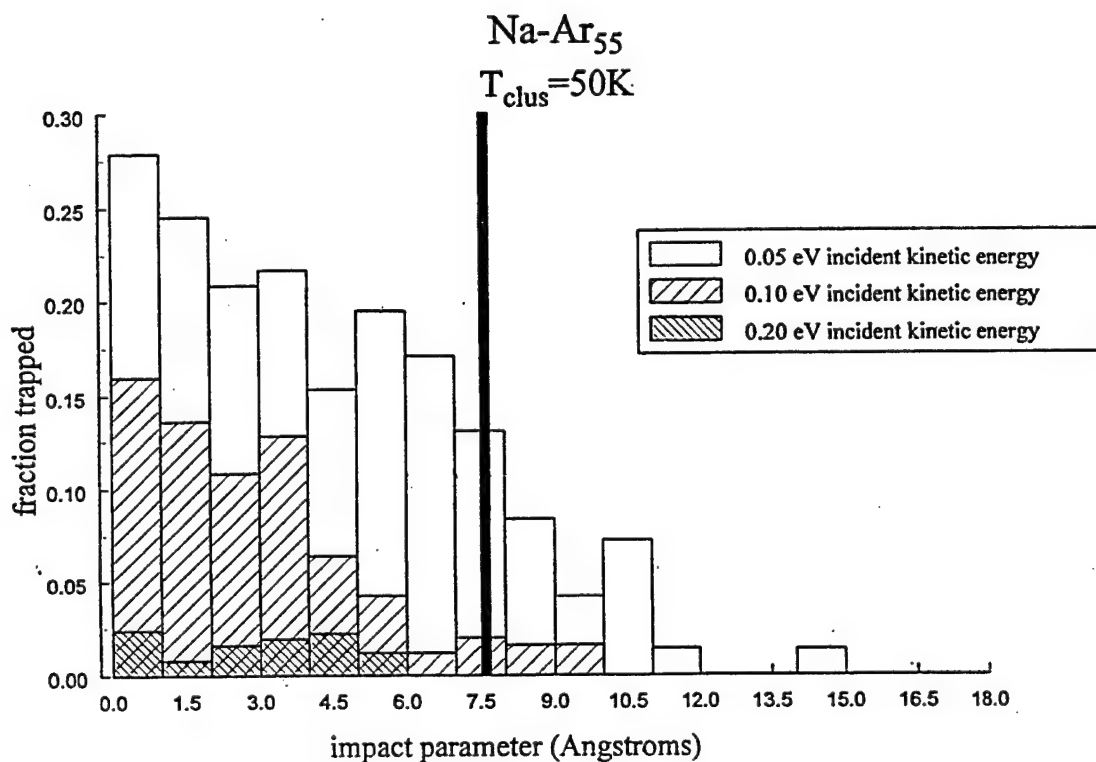ions show an increase in the barrier height of 5.7 kcal/mol for the cc-pVTZ basis set as compared to the cc-pVDZ basis set. Also correlating the $O2s$ like orbitals, which were frozen in the ICCI calculations, lowers the barrier height by 0.6 kcal/mol for the cc-pVTZ basis set. Combining these effects leads to a best estimate for the barrier height of 14 kcal/mol. From Fig. 1 it is seen that the singlet triplet crossing occurs near the saddle point for dissociation on the singlet surface. It is expected that larger basis sets would lower the singlet surface with respect to the triplet surface and shift the crossing to be outside the barrier.

For cyclic $O_3$ we have focused on the crossings between the lowest five surfaces ( $X^1A_1$, $2^1A_1$, $^1A_2$, $^1B_1$, and $^1B_2$) to provide some insight into ways to form cyclic $O_3$ photochemically. These are state averaged CASSCF/ICCI calculations with the cc-pVTZ basis set, for $C_{2v}$ constrained geometries, over a grid in the OO distance and OOO angle, which spans the region between the ring and open forms

of ozone. ( See Fig. 2.) The crossing region between the $X^1A_1$ and $2^1A_1$ surfaces is in agreement with the work of Xantheas et al [2]. The calculations show a crossing between the $^1A_2$ state and the $^1A_1$ manifold near the crossing region of the $X^1A_1$ and $2^1A_1$ surfaces. Excitation to appropriate rovibrational levels of the $^1A_2$ state may constitute a photochemical route to the ring form of ozone. This is a point that merits further study. Excitation to the $2^1A_1$ or $^1B_2$ states is not likely to lead to ring ozone, since these states are known to photodissociate.

We have studied the decomposition pathways for cubane to benzene plus acetylene and to cyclooctatetraene on the singlet surface (See Fig. 3). This process has been studied previously[3] at a lower level of theory. We have also studied the ground and excited states for the photochemical ring closure step. (See Fig. 4 and Table II.) Fig. 4 shows the $1^1A_1$ and $2^1A_1$ states of cubane along the pathway for ring opening on the $1^1A_1$ surface. Table II shows the vertical excitation energies and oscillator strengths at the equilibrium geometry of the intermediate which undergoes photocyclization. The $2^1A_1$ state, which closes to cubane, can be described as a double triplet $\pi$ to $\pi^*$ excitation with respect to the ground state. Thus, this state has only a small oscillator strength with respect to the ground state. However, there is a singlet $\pi$ to $\pi^*$ state ($^1B_2$) at nearly the same energy and excitation to this state followed by intersystem crossing could lead to the triplet $\pi$ to $\pi^*$ state. It has been stated in the literature that the photocyclization step does not occur for cubane itsself but does for substituted cubanes. These calculations suggest that if appropriate levels of the $^1B_2$ state were excited that ring closure could occur. It is possible that the experimental attempts to bring about the ring closure have not involved the correct ( i.e. high enough in energy) excitation to bring about the closure step. It would be useful for experimental studies of this process to be carried out using the computed results as a guide. Another possibility is to generate the $2^1A_1$ state in solution using triplet energy transfer. This would have the advantage of rapid vibrational relaxation of the initially formed cubane molecule.

References.
1. E.T. Seidl and H.F. Schaefer, III., J. Chem. Phys., **96**, 1176(1992).
2. S.S. Xantheas, G.J. Atchity, S.T. Elbert, and K. Ruedenberg, J. Chem. Phys., **94**, 8054(1991).

3. G.W. Griffin and A.P. Marchand, Chem. Rev., **89**, 997(1989).

Table I. Computed Barrier Height for Dissociation of Cyclic O4 ( ACPF calculations with (4/4) CASSCF reference).

|  | pVDZ (O2s frozen) | pVTZ (O2s frozen) | pVTZ (O2s correlated) |
|---|---|---|---|
| sp2 | -299.50956 | -299.68493 | -300.06190 |
| min1 | -299.52077 | -299.70520 | -300.08120 |
| $\Delta E$[a] | 7.0 | 12.7 | 12.1 |

[a] Barrier height in kcal/mol.

Table II. Vertical Excitation Energies for Cubane at the Equilibrium Geometry of the Photocyclization Intermediate.

| State | ICCI[a] | $\Delta E$[b] | T.M.[c] |
|---|---|---|---|
| $2\,^1A_1$ | -307.09335(-.09339) | 188.6 | -0.009 |
| $^1A_2$ | -307.09991(-.10432) | 181.8 | 0.0 |
| $^1B_2$ | -307.10921(-.11246) | 176.6 | 0.611 |
| $^3A_2$ | -307.24433(-.24442) | 93.8 | |
| $^3B_2$ | -307.24495(-.24504) | 93.4 | |
| $X\,^1A_1$ | -307.39381(-.39396) | 0.0 | |

[a] ICCI(ICCI +Q + 307.) where +Q denotes the multireference Davidson's correction.
[b] Energy difference in kcal/mol.
[c] Transition moment integral in atomic units.
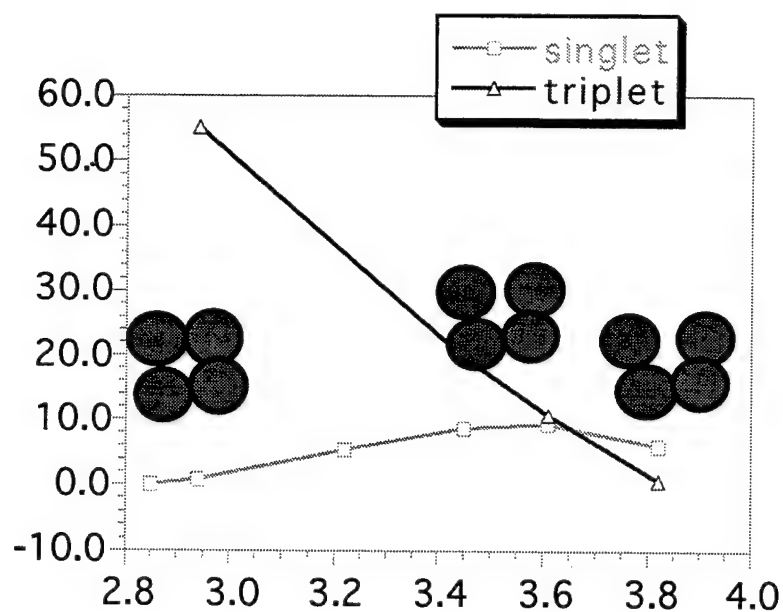
*Fig. 1 Pathway for dissociation of cyclic O4.  From ICCI calculations with the cc-pVDZ basis set and an (8/8) CASSCF active space. (Energies in kcal/mol.)*
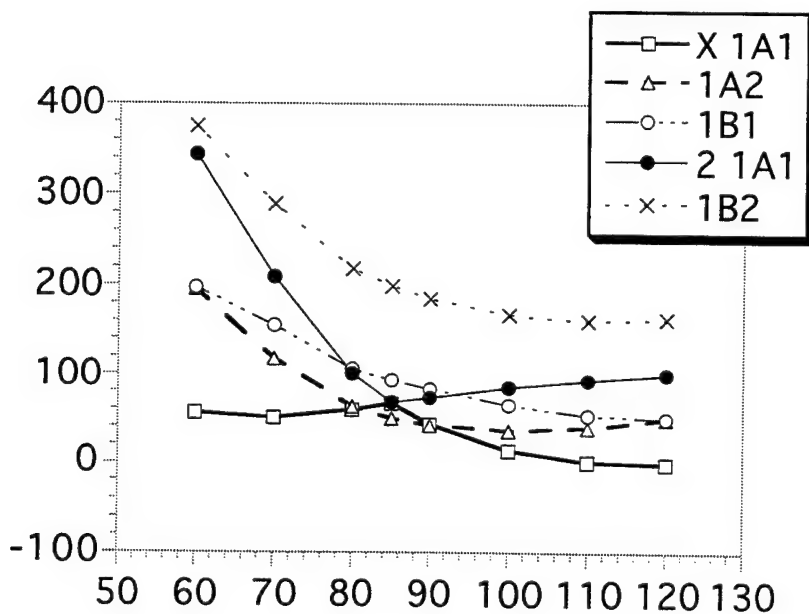


*Fig. 2. Cuts through the lowest five potential energy surfaces for ozone. The absissa is the OOO angle in degrees. The OO distance is fixed at the equilibrium value for the open form of ozone. (Energies in kcal/mol.)*
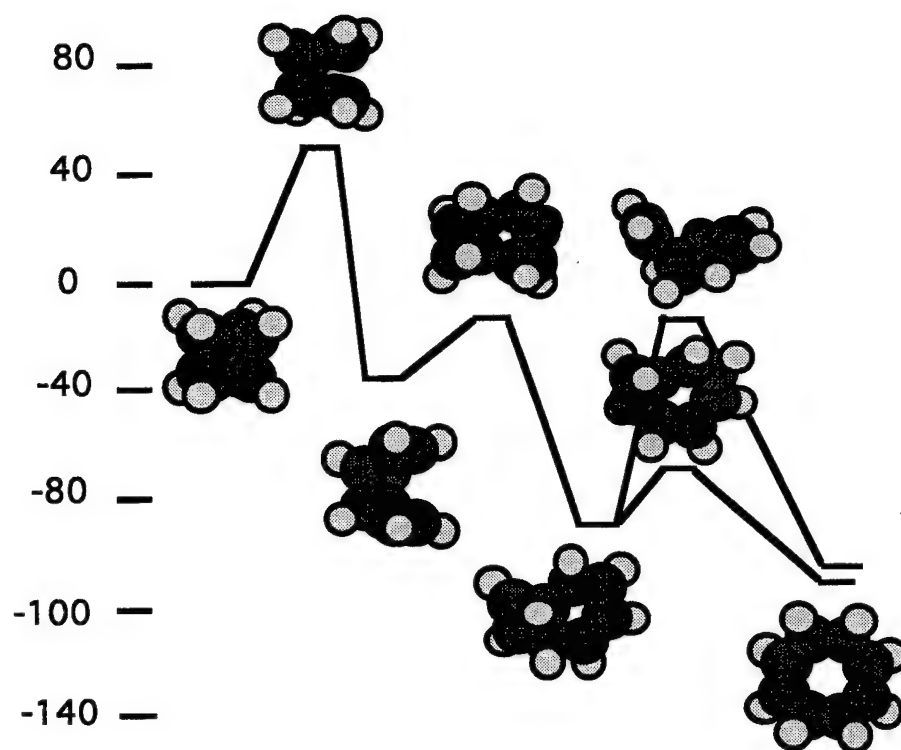
Fig. 3. Decomposition pathways for cubane. (Energies in kcal/mol.)
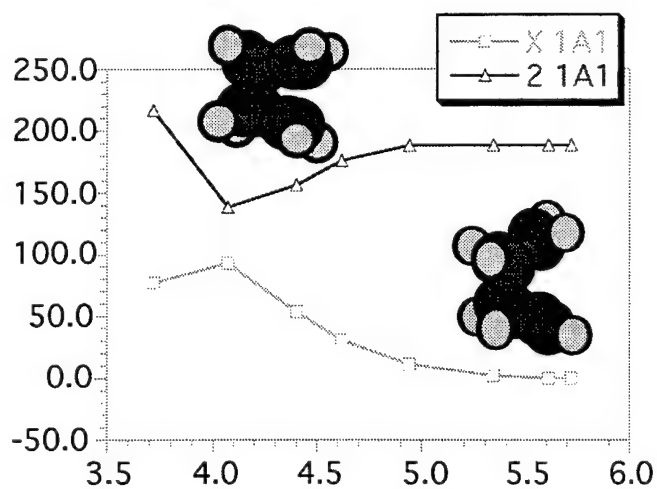


Fig. 4. The crossing region of the $1^1A_1$ and $2^1A_1$ states of cubane. (Energies in kcal/mol.)

# Theoretical *Ab Initio* Study of $CN_2O_2$ Structures: Prediction of Nitryl Cyanide as a High-Energy Molecule.

Anatoli A. Korkin,[i] Jerzy Leszczynski,[ii] and Rodney J. Bartlett[i]

[i]*The Quantum Theory Project, University of Florida, Gainesville, Fl, 32611-8435,*
[ii]*Department of Chemistry, Jackson State University, Jackson, MS 39217*

In our previous work[1] we have considered a number of potentially metastable and energetic molecules, such as $N_3H_3$,[1a] $N_4$, $N_8$,[1b,c] $HN_5$, $N_{10}$[1d] and others. Other classes of energetic species built upon $C-NO_2$ and $N-NO_2$ linkages, strained ring systems and allenic type bonds are under consideration. The question arises whether simple systems involving C ,N, O and other light atoms offer uninvestigated molecules, potentially interesting in the search for new types of rocket propellants and explosives.

Extending our theoretical search and investigation of high-energy molecules, we have accomplished a correlated *ab initio* study of $CN_2O_2$ structures, energies, interconversion and decomposition barriers, as well as their precursors and decomposition products for a series of possible reactions (see Fig. 1 and 2.).[2] Dissociation and transformation barriers and dissociation energies were computed at an uniform highly correlated level to estimate the potential stability and chemical reactivity of different isomeric forms. Geometrical parameters of stationary structures, minima and transition states (TS), for the $CN_2O_2$ potential energy surface (PES) and related molecules and radicals were optimized at the MBPT(2)/6-31G* level and then characterized by calculations of analytical harmonic vibrational frequencies. More

rigorous couple cluster methods[3] including single, double and triple excitations (CCSD(T)) combined with larger TZ2P basis sets have been employed for computations of single-point energies. All calculations were done with the ACES II program system.[4] Energy comparisons are discussed at the CCSD(T)/ZT2P//MBPT(2)/6-31G* level.

The most energetically favorable $CN_2O_2$ form, *trans*-nitrozoisocyanate (**1**) is 113 kcal/mol higher in energy than the most stable dissociation products, $N_2$ and $CO_2$, but its 18 kcal/mol dissociation barrier is rather small for any but low temperature gas phase or matrix observation. As a collision complex in combustion of nitrogen-containing compounds,[5] **1** is responsible for a non-Arrhenius behavior of the rate constant in the gas phase reaction between NCO and NO radicals. Formation of **1** from NCO and NO is exothermic by 33 kcal/mol.



**1**, $C_s$ (0)

**2**, $C_{2v}$

**3**, $C_s$

**4**, $C_{2v}$
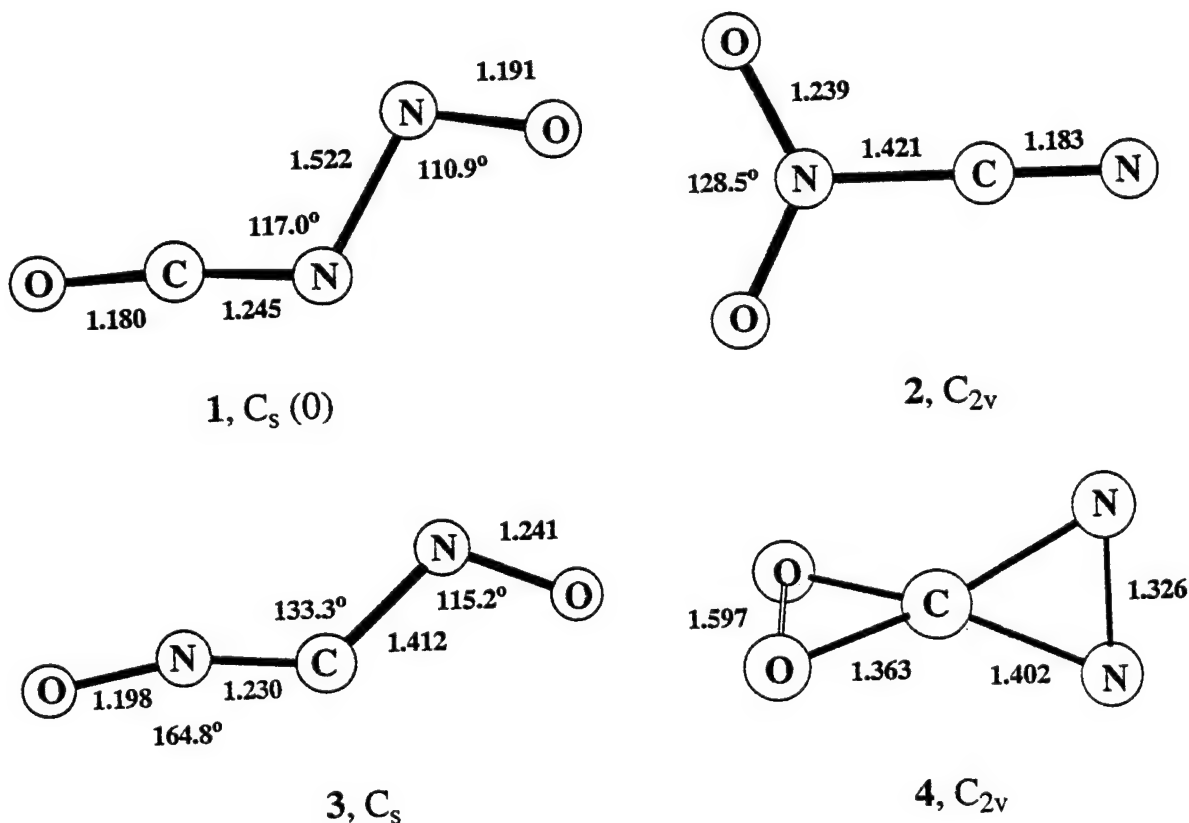
We believe that three higher energy isomers nitryl cyanide (**2**), nitrozofulminate (**3**) bicyclic form (**4**) are potentially interesting species for experimental verification. Relative energies of **2**, **3** and **4** are higher by 38, 69 and by 77 kcal/mol than **1**, respectively. Thus their energy releases are also higher by these values than the heat of dissociation of **1** into $N_2$ and $CO_2$.

The reasonably large values of the C-N bond dissociation energy (59 kcal/mol), and of the barrier to decomposition into $N_2$ and $CO_2$ (54 kcal/mol), make nitryl cyanide potentially interesting as a rocket propellant or an explosive. Our estimate of the heat of formation of **2** and its exothermicity in decomposition into $N_2$ and $CO_2$ are 60 kcal/mol and 150-155 kcal/mol, respectively. The rough estimation of the specific impulse ($I_{sp} =$ 380 sec) for **2** shows its propulsion capacity to be comparable to the hydrazine-oxygen mixture: $N_2H_4$ (g) + $O_2$ (g) $\rightarrow$ $N_2$ (g) + $H_2O$ (g) (390 sec). Furthermore, dimers and trimers of nitryl cyanide can readily be envisioned which have similar energy/mass ratio but might offer higher stability and alternative synthetic routs. One of $O_2NCN$ self-agregates, aromatic 2,4,6-trinitro-1,3,5-triazine (**5**) is under our current consideration (see Fig. 3).[6] Although **5** is somewhat less energetic than **2**, it is expected to be more stable and have a higher density. Our estimated heat of formation of **5** (110 kcal/mol) suggests its higher propulsion and explosive capacity than RDX.

Nitrozofulminate (**3**) is potentially more energetic than nitryl cyanide, but it is also less stable, as its 32 kcal/mol C-N bond dissociation energy is only about half of the nitromethane value. Two equivalent topomeric forms of **3** have 12 kcal/mol interconversion barriers, which can be possibly verified by a low temperature dynamic NMR study.

The bicyclic form, $C_{2v}$ **4** (suggested in ref. 7) is the most energetic, but it can also be least stable due to its ring strain, and relatively low barrier to decomposition (29 kcal/mol) and high energy release in decomposition to $N_2$ and $CO_2$ (190 kcal/mol).

Selected triplet $CN_2O_2$ structures, considered in this study, have considerably higher energies than the corresponding singlets, and apparantly do not offer alternative (lower energy) decomposition paths.

(1) (a) Magers, D.H.; Salter, E.A.; Bartlett, R.J.; Salter, C.; Hess, B.A., Jr.; Schaad, L.J. *J. Am. Chem. Soc.* **1988**, *110*, 3435. (b) Lauderdale, W.J.; Myers, W.J.; Bernholdt, D.E.; Stanton, J.F.; Bartlett, R.J. *Proceedings of the High Energy Density Materials Contractors Conference, 25-28 February, Long Beach, CA, 1990*, p. 121. (c) Lauderdale, W.J.; Stanton, J.F.; Bartlett, R.J. *J. Phys. Chem.* **1992**, *96*, 1174. (d) Ferris, K.F.; Bartlett, R.J. *J. Am. Chem. Soc.* **1992**, *114*, 8302. (e) Stanton, J.F.; Gauss, J.; Bartlett, R.J.; Helgaker, T.; Jorgensen, P.; Jensen, H.J.; Taylor, P.R. *J. Chem. Phys.* **1992**, *97*, 1211. (f) Cernusak, I.; Beck, S.; Bartlett, R.J. *J. Phys. Chem.* **1992**, *96*, 10284. (g) Cernusak, I.; Urban, M.; Ertl, P.; Bartlett, R.J. *J. Am. Chem. Soc.* **1992**, *114*, 10955. (h) Korkin, A.A.; Balkova, A.; Bartlett, R.J.; Boyd, R.J.; Schleyer, P.v.R. *J. Phys. Chem.* **1996**, *100*, 5702.

(2) Korkin, A.A.; Leszczynski, J.; Bartlett, R.J. *J. Phys. Chem.* (in press).

(3) Bartlett, R.J.; Stanton, J.F. In *Reviews in Computational Chemistry* ; Lipkowitz, K.B.; Boyd, D. B., Eds. VCH Publishers: New York, 1994, Vol. 5, Chap. 2.

(4) Stanton, J.F.; Gauss, J.; Watts, J.D.; Lauderdale, W.J.; Bartlett, R.J.; with contributions from Nooijen, M.; Oliphant, N.; Perera, S.A.; Gwaltney, S.R. ACES II; Quantum Theory Project: University of Florida.

(5) Lin, M.C.; He, Y.; Melius, C.F. J. Phys. Chem. 1993, 97, 9124.

(6) Korkin, A.A.; Bartlett, R.J. To be published.

(7) Averyanov, A.S.; Khait, Yu.G.; Puzanov, Yu.V. *J. Mol. Struct. Theochem.* (in press).

# Decomposition pathways of ON-NCO (1)
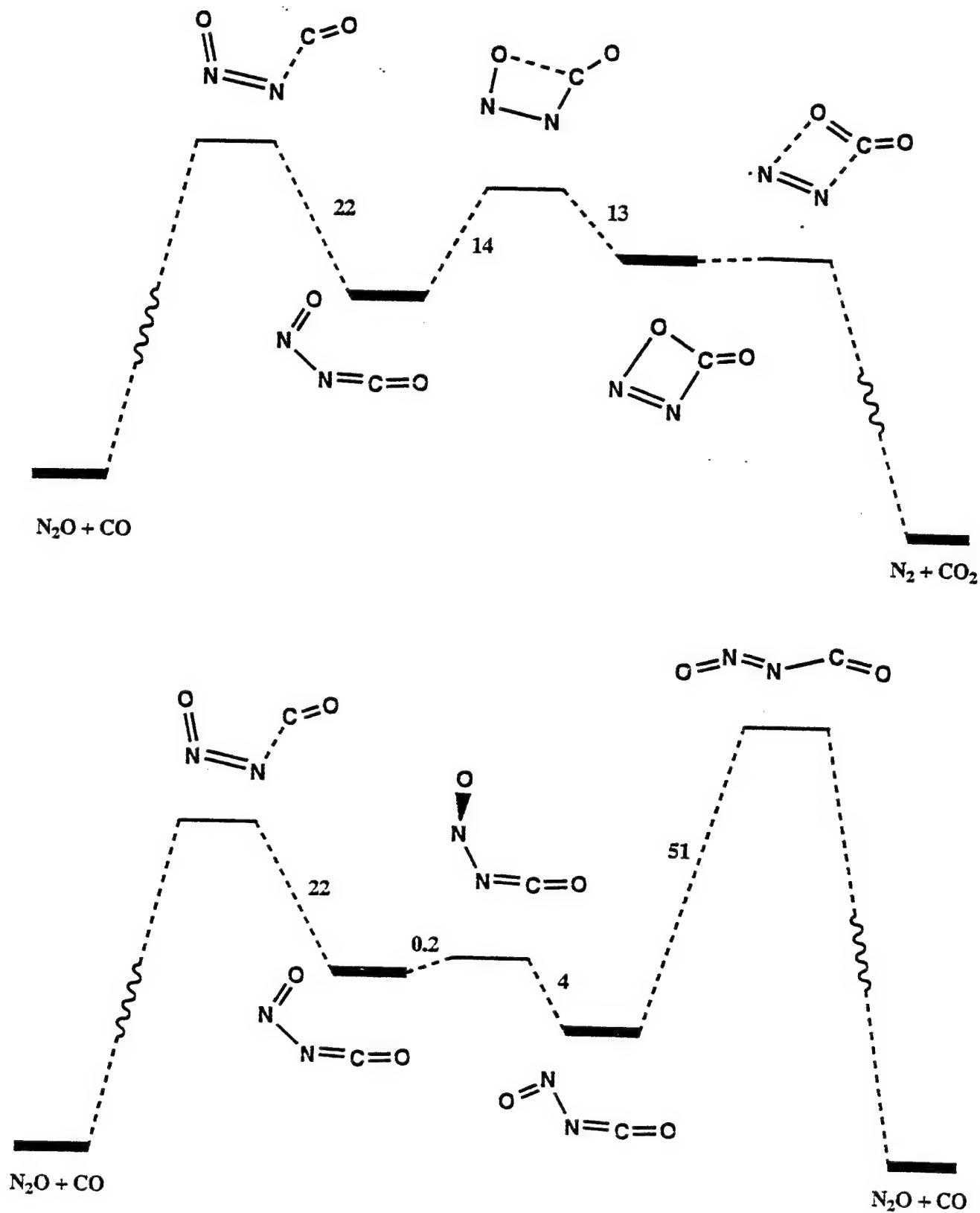


Fig.1
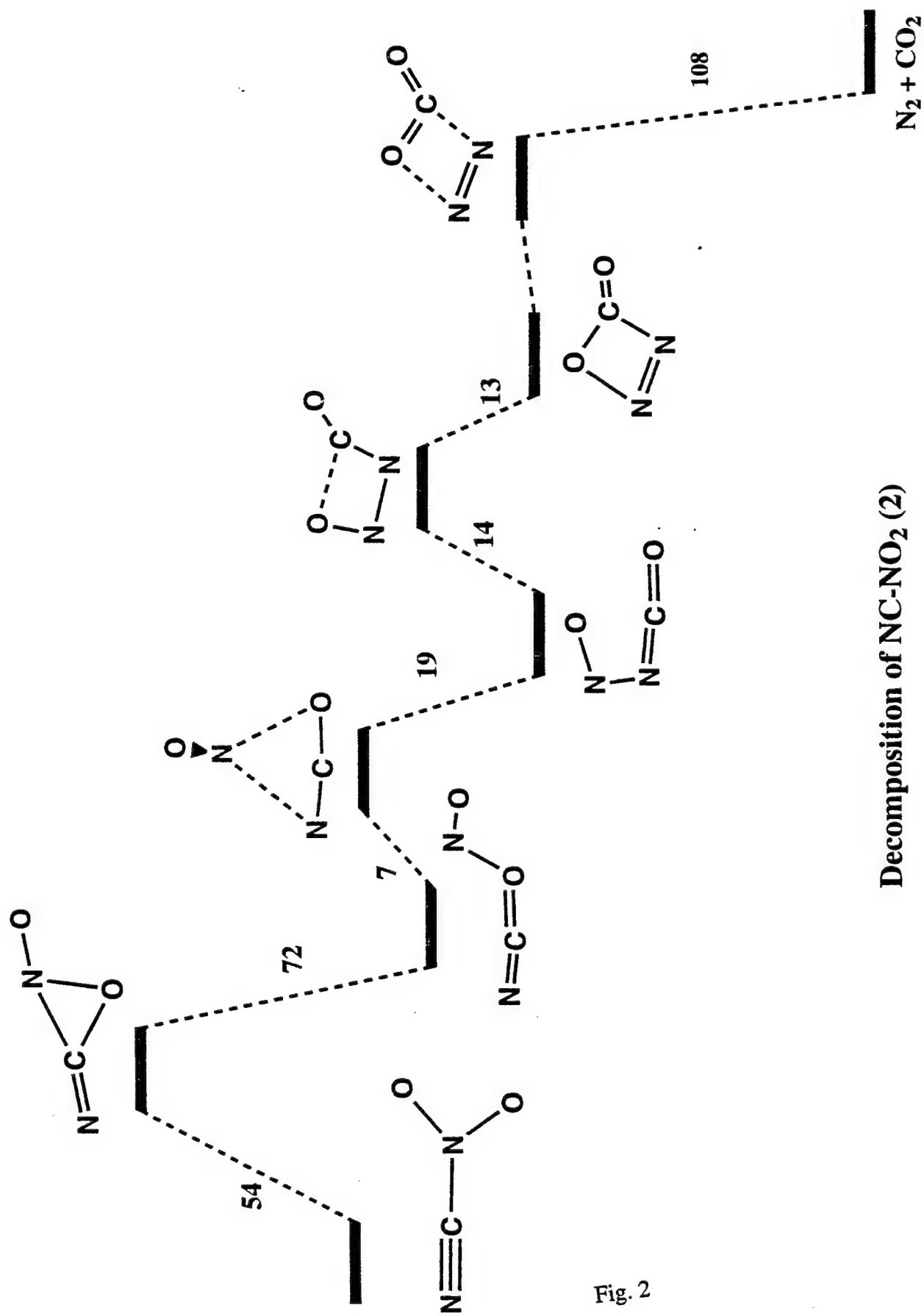
Decomposition of NC-NO$_2$ (2)

Fig. 2

209

# 2,4,6-TRINITRO-1,3,5-TRIAZINE (5)

$$3 \quad N \equiv C - N \overset{O}{\underset{O}{\lessgtr}} \quad \xrightarrow{\quad \Delta E = -70 \text{ kcal/mol} \quad}$$





Planar



Perpendicular
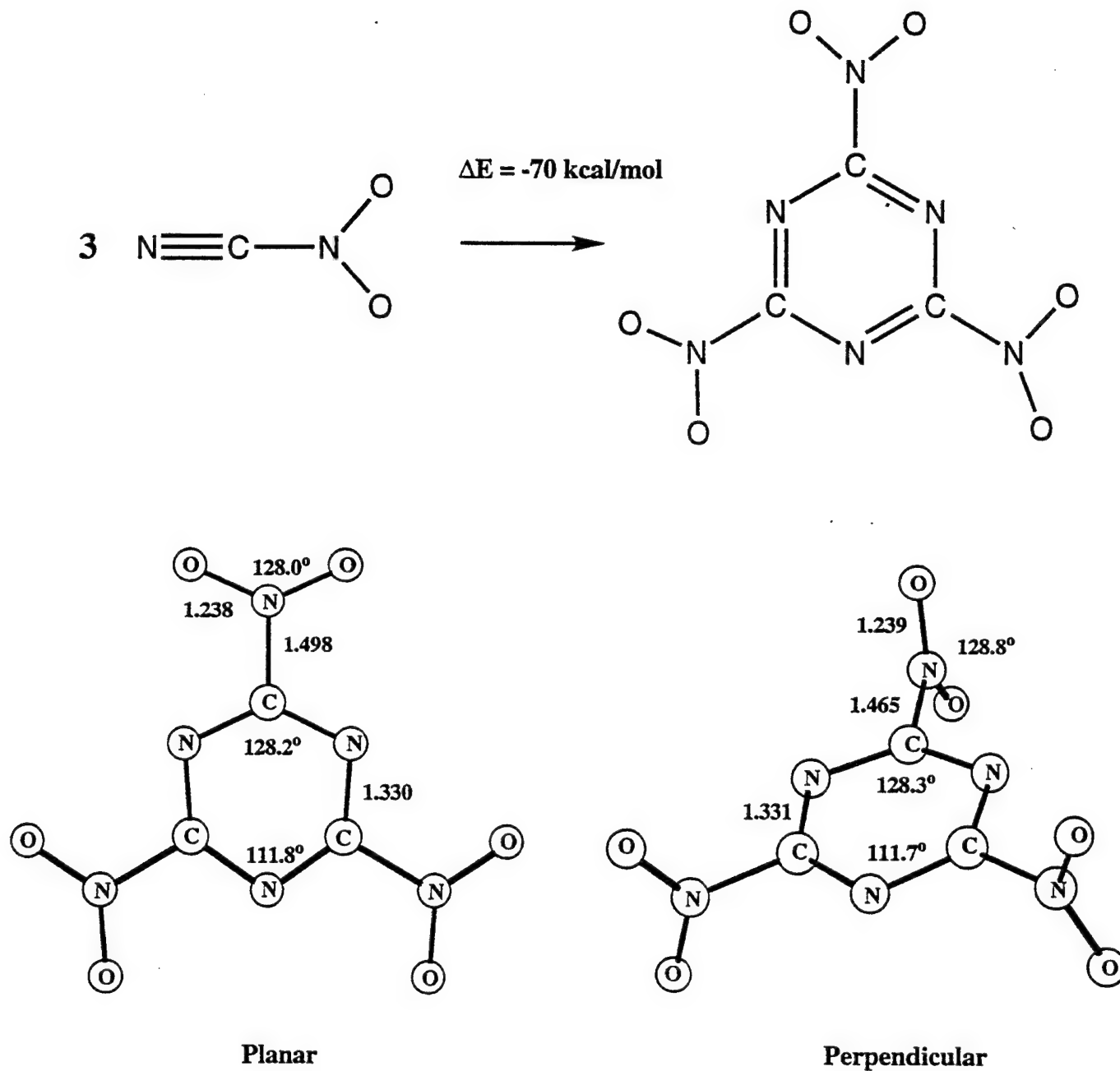
**Selected Data:** $\Delta H^{o}_{f} = 110$ kcal/mol; $\Delta H^{o}_{explos.} = 1.77$ kcal/g; $I_{sp} = 353$ sec

Fig. 3

## Theoretical Studies of 1,3,3-trinitroazididine (TNAZ) and 1,3-dinitro-1,3-diazacyclobutane

H. H. Michels
United Technologies Research Center
East Hartford, CT 06108

### ABSTRACT

We have carried out an extensive set of calculations on 1,3,3-trinitroazididine (TNAZ). Eight possible conformations of TNAZ were examined at the HF/3-21G and HF/6-31G* levels of theory. The ground state conformation has the nitro groups at ring positions **1** and **3** in a perpendicular trans-arrangement, relative to the azididine ring. A second very low-lying conformation (+0.3 kcal) has the nitro groups at ring positions **1** and **3** in a perpendicular cis-arrangement to the azididine ring. There appears to be nearly free rotation of the nitro-groups at ring position **3**. We calculate a transition state energy of +2.0 kcal when both nitro groups at position **3** are perpendicular to the azididine ring. Calculations at the MP2/6-31G* level of theory are in progress on TNAZ. If similar energetics are found at this correlated level of theory, there may be more than one polymorph of this compound.

Based on a fully optimized $C_S$ structure (25 geometric parameters), we have calculated the heat of formation of this molecule using the method outlined by Ibrahim and Schleyer [M. R. Ibrahim and P. v R. Schleyer, Journal of Computational Chemistry, 6, 157 (1985). We obtain a value, $\Delta H_f^0$ (25°C) of + 35.0 kcal/mol, for the gas phase heat of formation. Estimated corrections for the sublimation energy indicate that TNAZ is more energetic than 3-nitro-1,2,4-triazol-5-one [NTO] but less energetic than the recently synthesized [SRI, private communication] 1-amino-3-nitro-1,2,4 triazole compound. Our calculated density [H. H. Cady, Report LA-77LO-MS, Los Alamos Scientific Laboratory, 1979] for TNAZ is 1.78 g/cc, slightly greater than that for NTO (1.75 g/cc).

In addition to our studies of TNAZ, we have undertaken an evaluation of cyclodimethylenedinitramine (1,3-dinitro-1,3-diazacyclobutane). This compound is the smallest ring member in the RDX, HMX nitramine series. We find a stable $C_{2v}$ structure with $^1A_1$ symmetry. Our estimated heat of formation of this new compound is +54 kcal/mol, indicating that this is a much more energetic structure than either RDX or HMX. Our calculated solid density is 1.76 g/cc (Cady's method), a value somewhat smaller than that for RDX (1.80 g/cc).

Correlated calculations were also undertaken for this smallest ring member in the RDX, HMX nitramine series. A stable $C_{2v}$ structure with $^1A_1$ symmetry is found at the MP2/6-31G* level of theory. The lowest frequency mode [$a_1 = 64$ cm$^{-1}$] is a symmetric axial stretch of the C-N-C-N ring indicating that this compound may have lower ring strain energy than expected, offering some chance for ring closure in synthesis attempts.

## Discussion

Cyclic nitramines that also contain geminal dinitroalkyl groups have recently been synthesized.[1-4] These compounds may exhibit an increase in oxygen balance over the corresponding compounds with mononitroalkyl groups. A compound of primary interest in this group is 1,3,3-trinitroazididine [TNAZ], a four-membered ring in the RDX, HMX series which exhibits a single dinitroalkyl group. Other compounds in this series include 1,3,5,5-tetranitrohexahydropyrimidine [DNNC] and 1,3,3,5,7,7-hexanitro-1,5-diazacyclooctane [HNDC], which are analogues of RDX and HMX, respectively.

We have carried out an extensive set of *ab initio* calculations on 1,3,3-trinitroazididine (TNAZ). Eight possible conformations of TNAZ were examined at the HF/3-21G and HF/6-31G* levels of theory. We find two low-lying conformations for TNAZ as illustrated in Figures 1 and 2. The ground state conformation, shown in Figure 1, has the nitro groups at ring positions **1** and **3** in a perpendicular trans-arrangement, relative to the azididine ring. A second very low-lying conformation (+0.3 kcal), shown in Figure 2, has the nitro groups at ring positions **1** and **3** in a perpendicular cis-arrangement to the azididine ring. There appears to be nearly free rotation of the nitro-groups at ring position **3**. We calculate a transition state energy of +2.0 kcal when both nitro groups at position **3** are perpendicular to the azididine ring. Figure 3 illustrates the geometry of this transition state. If similar results are found at a correlated level of theory, there may be more than one polymorph of this compound.

Correlated calculations of the ground state of 1,3,3-trinitroazididine (TNAZ) were next attempted. This system, however, proved to be too extensive for our current computer capabilities. Based on a fully optimized $C_s$ structure (25 geometric parameters), we have calculated the heat of formation of this molecule using the method outlined by Ibrahim and Schleyer.[5] We obtain a value, $\Delta H_f^o$ (25°C) of + 35.0 kcal/mol, for the gas phase heat of formation. Estimated corrections for the sublimation energy indicate that TNAZ is more energetic than 3-nitro-1,2,4-triazol-5-one [NTO] but less energetic than the recently synthesized 1-amino-3-nitro-1,2,4 triazole compound.[6] Our calculated density for TNAZ is 1.78 g/cc (Cady's method), slightly greater than that for NTO (1.75 g/cc).

In addition to our studies of TNAZ, we undertook an evaluation of cyclodimethylenedinitramine (1,3-dinitro-1,3-diazacyclobutane). This compound is the smallest ring member in the RDX, HMX nitramine series. We find a stable $C_{2v}$ structure with $^1A_1$ symmetry as illustrated in Figure 4. Our estimated heat of formation of this new compound is +54 kcal/mol, indicating that, on a mass basis, this is a much more energetic structure than either RDX or HMX. Our calculated solid density is 1.76 g/cc (Cady's method), a value somewhat smaller than that for RDX (1.80 g/cc).

Correlated calculations of cyclodimethylenedinitramine (1,3-dinitro-1,3-diazacyclobutane) were undertaken for this smallest ring member in the RDX, HMX nitramine series. A stable $C_{2v}$ structure with $^1A_1$ symmetry is found at the MP2/6-31G* level of theory. The lowest frequency mode [$a_1 = 64$ cm$^{-1}$] is a symmetric axial stretch of the C-N-C-N ring indicating that this compound may have lower ring strain energy than expected, offering some chance for ring closure in synthesis attempts. We suggest HEDMX as an identifier for this new cyclic nitramine.

## References

1. Cichra, D. A. and H. G. Adolf: Journal of Orgamic Chemistry, 47, p. 2474, 1982.

2. Cichra, D. A. and H. G. Adolf: Synthesis, p. 830, 1983.

3. Levins, D. A., C. D. Bedford and S. Staats: J. Explos. Prop. Pyrtech., 8, p. 74, 1983.

4. Archibald, T. G. and K. Baum: ONR-2-6 (Interim Report), Office of Naval Research, Washington, D. C., 1984.

5. Ibrahim, M. R. and P. vR. Schleyer: Journal of Computational Chemistry, 6, p. 157, 1985.

6. Schmitt, R.: private communication, SRI International, 1995.

**(nitro groups at ring positions 1 and 3 are trans to ring)**



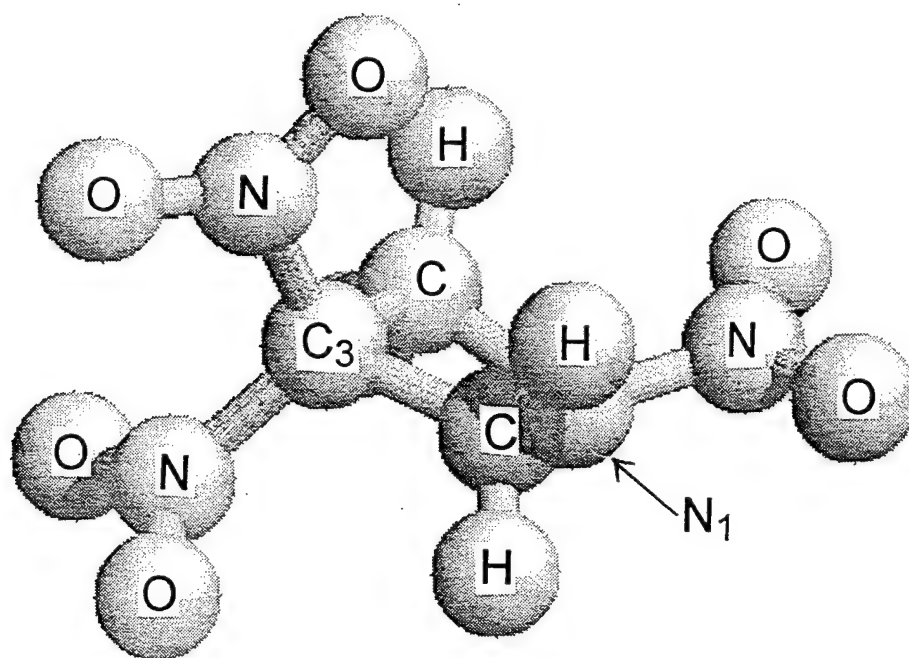Figure 1. 1,3,3-trinitroazididine (trans) in $C_s$ Symmetry - [$^1A'$]

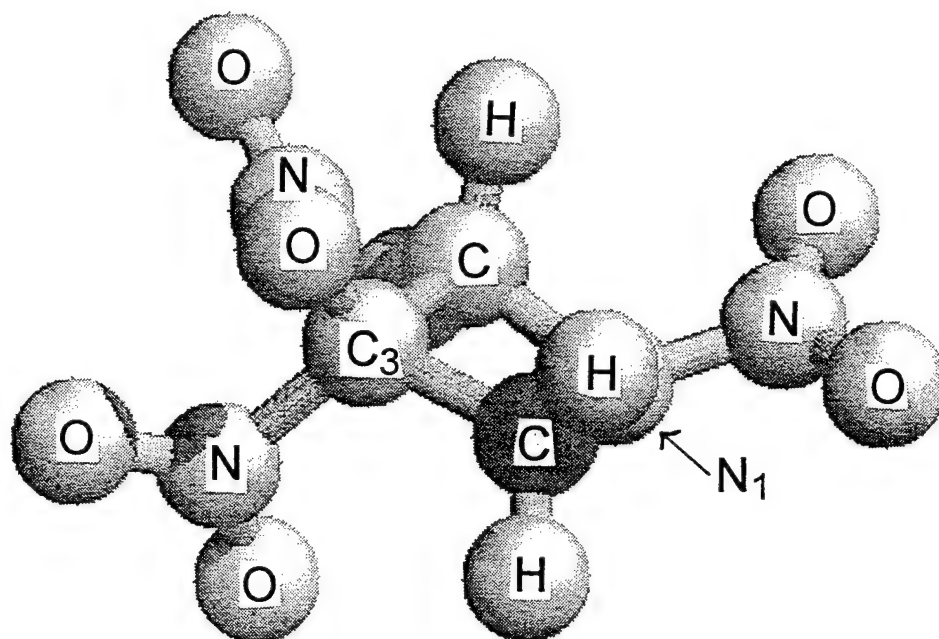**(nitro groups at ring positions 1,3 are cis to ring)**



Figure 2.  1,3,3-trinitroazididine (cis) in $C_s$ Symmetry  -  $[^1A']$
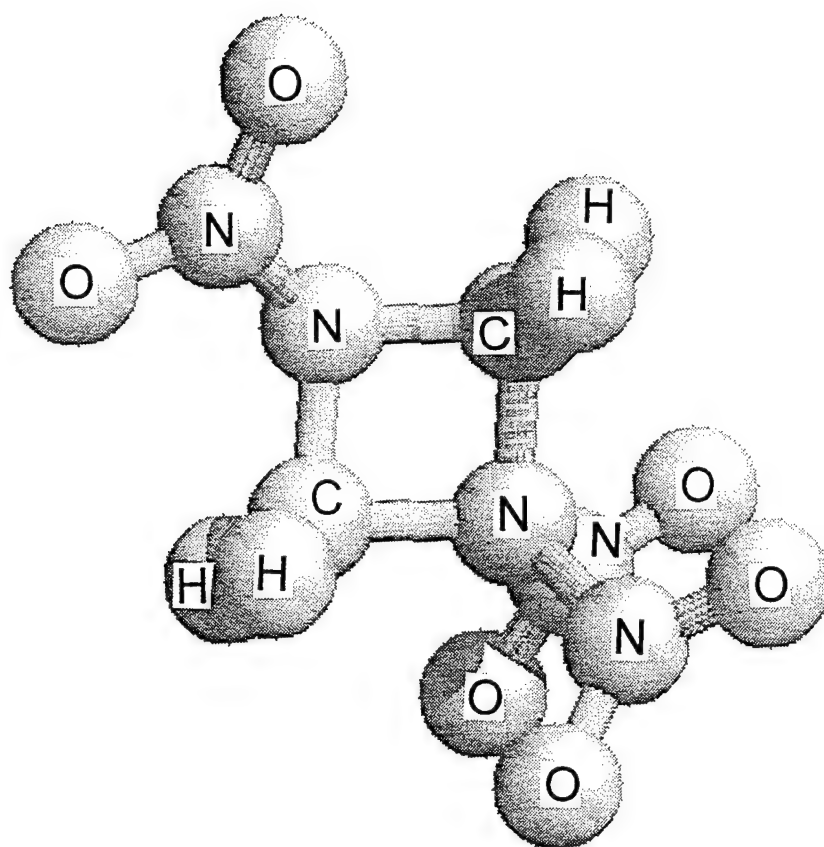
Figure 3. 1,3,3-trinitroazididine Transition State in $C_s$ Symmetry - [$^1A'$]

**(smallest member of RDX, HMX nitramine series)**
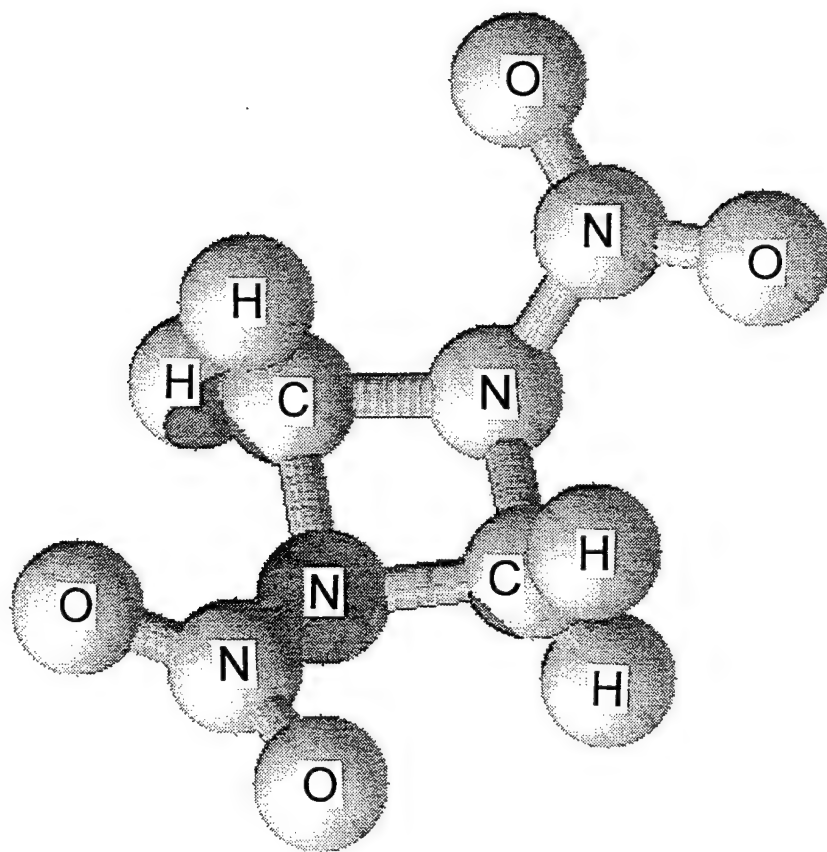


Figure 4.  1,3-dinitro-1,3-diazacyclobutane in $C_{2v}$ Symmetry  -  $[^1A_1]$

# NTO — Tautomerism, Ionization, and Bond Dissociations.

Nathan J. Harris and Koop Lammertsma

Department of Chemistry, University of Alabama at Birmingham, Birmingham, Alabama 35294-1240.

5-Nitro-2,4-dihydro-3H-1,2,4-triazolone (NTO) is a high energy explosive that is less sensitive than the commonly used nitramine explosives RDX and HMX. Considerable experimental effort has been spent to understand the mechanism for thermal decomposition of NTO.[1] This ab initio molecular orbital study aims contribute to these efforts. Our approach is related to our previous ab initio studies on nitroaromatic explosives.[2] The work extends a previous ab initio study of NTO tautomerism by Ritchie.[3]

Calculations were carried out using the Gaussian 94 suite of programs. The optimized geometries and harmonic vibrational frequencies for neutral tautomers, anions, and radicals (a total of 31 structures) were computed at the (U)HF/6-31+G* theoretical level. A subset of the most important structures (see Figure 1) was selected for higher level calculations at the B3LYP/6-311+G**//B3LYP/6-31+G* and MP2/6-311+G**//MP2/6-31+G* theoretical levels.

Calculations were also done on tautomerization, ionization, and bond dissociations for nitromethane, as a small test molecule. Again, energies were computed at the SCF, MP2, and B3LYP theoretical levels. These were compared with more accurate energies computed using G1 and G2 theories.[4]

NMR properties for the NTO tautomers and anions were computed using the continuous set of guage transformations (CSGT) method, which is standard in Gaussian 94, at the B3LYP/6-311+G** theoretical level. These calculations included proton NMR chemical shifts (referenced to tetramethylsilane), and magnetic susceptibility anisotropies.

The computed energies for ionization, tautomerization, and bond dissociation energies of nitromethane (a small test molecule) are listed in Table 1. The MP2 and B3LYP energies are quite similar, and are better than the Hartree-Fock energies. Both the

MP2 and B3LYP methods underestimate the C-N bond dissociation energy by 7-8 kcal/mol. Otherwise, these two methods give satisfactory energies in comparison with more accurate energies computed with G1 and G2 theories.

X-ray crystal structures were reported for the 1,3-diaminoguanidinium and ethylenediammonium salts of NTO.[5] In both salts NTO is deprotonated at N4, corresponding to structure **9** in Fig. 1. Table 2 presents a comparison of the theoretical geometry for **9** with the experimental geometry for the diaminoguanidinium salt. The MP2 and B3LYP geometries are generally in good agreement with the experimental geometry. The largest differences between theory and experiment are in the N2-C3 bond length and in the angles around the carbonyl group (Table 2). Crystal packing effects might explain these differences.

Anion **9**, deprotonated at N4 (see Fig. 1), is more stable than anion **8**, deprotonated at N2, but the energy difference is small (Table 3). Anion **9** is delocalized over two nitrogens (N1 and N4), while **8** is delocalized over N2 and C5. The electronegativity difference between carbon and nitrogen explains the greater stability of **9**. The difference in stabilities would be larger without the presence of the electron withdrawing $NO_2$ substituent at C5. The computed gas phase proton affinity for the NTO anion is a low 321 kcal/mol, indicating a high acidity for NTO. This high acidity is expected from the delocalized aromatic character of the NTO anions.

The hydroxy tautomers **2** and **4** (Fig. 1) are only 4-5 kcal/mol less stable than NTO at the MP2/6-311+G** level (Table 4). This small energy difference indicates these hydroxy tautomers are quite stable, which we attribute to the aromatic character of the 1-H-1,2,4-triazole skeleton.

Magnetic properties such as the magnetic susceptibility anisotropy and magnetic shielding (i.e. proton chemical shifts) are well established criteria for aromaticity. Aromatic molecules show a characteristic low frequency shift for the resonance of a hydrogen nucleus bonded to the ring, and exalted magnetic susceptibility anisotropies. We have computed the $^1H$ NMR chemical shifts ($\delta$) and magnetic susceptibility anisotropies ($\chi_{anis}$) for the NTO tautomers and anions. These are given in Figure 1. From the computed magnetic properties, the aromaticity of the NTO tautomers is in the order **4 > 2 > 3 > 1**.

Comparison of the $\chi_{anis}$ values suggests anions **8** and **9** are more aromatic than NTO (**1**).

Homolytic bond cleavages and hydrogen atom transfers are known to play a role in initiating the decomposition of other nitroaromatic explosives, so we have computed several bond dissociation energies for NTO and its tautomers (Table 5). As expected, the bond dissociation energies computed with UHF theory are very much underestimated.

The C-NO2 bond strength in NTO is 61.1 kcal/mol at the B3LYP/6-311+G** level. We note that the C-$NO_2$ bond strength in nitromethane is underestimated by 9 kcal/mol at this level of theory, so our best estimate for the true bond strength in NTO is 70 kcal/mol. This value is quite reasonable compared with the observed C-$NO_2$ bond strength of 71.4±2.0 kcal/mol in nitrobenzene. We conclude that C-$NO_2$ bond homolysis can play an important role in the NTO decomposition at high temperatures or under conditions of shock or impact. The importance of C-$NO_2$ bond cleavage under such conditions is well understood for other nitroaromatic explosives.

The B3LYP/6-311+G** bond strengths for the N2-H and N4-H bonds of NTO are respectively 97.7 and 93.4 kcal/mol. These are not unusually weak N-H bonds, but that does not rule out the possibility that hydrogen atom transfers play a role in the decomposition of NTO. Indeed, the observed[6] primary deuterium kinetic isotope effect for decomposition of NTO in the condensed phase suggests that the N-H bond is important in the decomposition mechanism.

The B3LYP/6-311+G** bond strength for the N-OH bond in aci-nitro tautomer **5** is a low 38 kcal/mol. This suggests that the N-OH bond could break to release a reactive hydroxy radical in the initial stages of the NTO decomposition. The importance of N-OH bond cleavage is recognized for other nitroaromatic explosives, such as 2,4,6-trinitrotoluene, picramid, and picric acid. In these compounds the aci-nitro tautomers can be formed by a concerted intramolecular hydrogen atom rearrangement. In NTO this concerted route for formation of the aci-nitro tautomer is not possible, but the aci tautomer might be formed by a base-catalyzed pathway in the condensed phase.

REFERENCES:

[1]     (a) Oxley, J.C.; Smith, J.L.; Zhou, Z.L. J. Phys. Chem. 1995, 99, 10383. (b)
        Prabhakaran, K.V.; Naidu, S.R.; Kurian, E.M. Thermochim. Acta 1994, 241, 199. (c)
        Williams, G.K.; Palopoli, S.F.; Brill, T.B. Comb. Flame 1994, 98, 197. (d) Ostmark,
        H.; Bergman, G. Thermochim. Acta 1993, 213, 165. (e) Botcher, T.R.; Beardall,
        D.J.; Wight, C.A. J. Phys. Chem. 1996, 100, 8802. (f) Rothgery, E.M.; Audette, D.E.;
        Wedlich, R.C.; Csejka, D.A. Thermochim. Acta 1991, 185, 235.

[2]     K. Lammertsma, On the viability of nitronic acids in the decomposition of
        nitroaromatics: a theoretical study of nitronic acids, Wright Laboratory / Armament
        Directorate (Eglin AFB), WL-TR-93-7062, 1993.

[3]     Ritchie, J.P. J. Org. Chem. 1989, 54, 3553.

[4]     Curtiss, L.A.; Carpenter, J.E.; Raghavachari, K.; Pople, J.A. J. Chem. Phys. 1992,
        96, 9030.

[5]     Cromer, D.T.; Hall, J.H.; Lee, K.Y.; Ryan, R.R. Acta Cryst. 1988, C44, 1144 and
        2206.

[6]     Menapace, J.A.; Marlin, J.E.; Bruss, D.R.; Dascher, R.V. J. Phys. Chem. 1991, 95,
        5509.

Figure 1. NTO tautomers, anions, and radicals. ^{1}H NMR chemical shifts for NH protons are in small italic type. Magnetic susceptibility anisotropies are in parentheses. (Magnetic properties were computed at the B3LYP/6-311+G** level.)
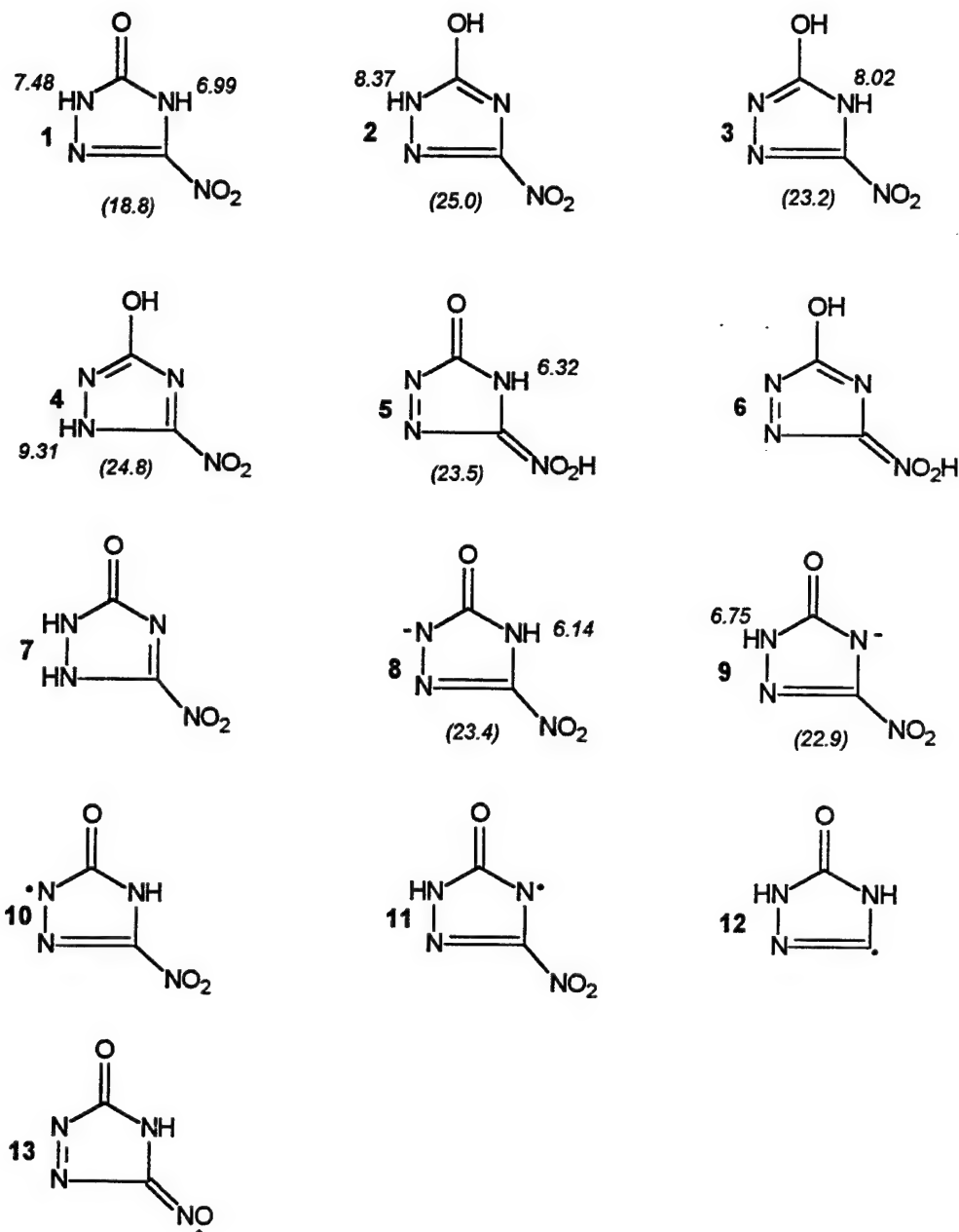
Table 1. Energies in kcal/mol for Nitromethane Tautomerism, Ionization, and Bond Dissociations, computed with 6-311+G** basis.

|  | (U)HF | B3LYP | MP2 | G2 |
|---|---|---|---|---|
| $CH_3NO_2/CH_2NO_2H$ | 16.2 | 18.2 | 13.7 | 14.1 |
| $CH_3NO_2/CH_2NO_2^- + H^+$ | 360.7 | 359.3 | 352.1 | 355.2 |
| $CH_3NO_2/CH_3 + NO_2$ | 36.1 | 52.4 | 52.6 | 61.0 |
| $CH_3NO_2/CH_2NO_2 + H$ | 75.7 | 98.6 | 95.1 | 101.3 |
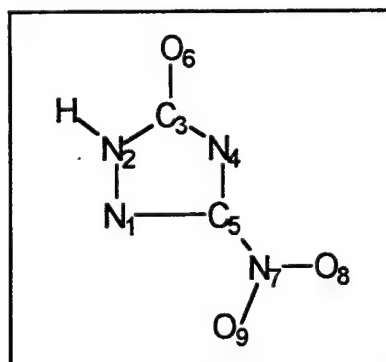


Table 2. Experimental and B3LYP/6-31+G* Geometries for NTO Anion 9.

| Bond Lengths (angstroms) | | | Bond angles (degrees) | | |
|---|---|---|---|---|---|
| Bond | B3LYP | Expt. | Angle | B3LYP | Expt. |
| 1-2 | 1.359 | 1.363 | 1-2-3 | 113.0 | 111.2 |
| 2-3 | 1.416 | 1.367 | 2-3-4 | 105.0 | 107.7 |
| 3-4 | 1.373 | 1.353 | 3-4-5 | 103.5 | 102.2 |
| 4-5 | 1.328 | 1.309 | 4-5-1 | 118.9 | 118.6 |
| 5-1 | 1.344 | 1.334 | 5-1-2 | 99.6 | 100.3 |
| 3-6 | 1.243 | 1.267 | 2-3-6 | 123.6 | 125.3 |
| 5-7 | 1.453 | 1.449 | 1-5-7 | 118.6 | 120.4 |
| 7-8 | 1.241 | 1.222 | 5-7-8 | 118.6 | 118.7 |
| 7-9 | 1.236 | 1.224 | 8-7-9 | 123.6 | 124.0 |

Table 3.  NTO Deprotonation Energies in kcal/mol, computed with 6-311+G** Basis.

| Anion | RHF | MP2 | B3LYP |
|-------|-----|-----|-------|
| 8 | 333.4 | 324.8 | 321.3 |
| 9 | 326.3 | 319.7 | 320.6 |

Table 4.  Relative Energies of NTO Tautomers in kcal/mol, computed with 6-311+G** Basis.

| Tautomer | RHF | MP2 | B3LYP |
|----------|-----|-----|-------|
| 1 | 0.0 | 0.0 | 0.0 |
| 2 | 5.4 | 4.4 | 8.8 |
| 3 | 12.6 | 11.6 | 14.4 |
| 4 | 9.6 | 4.7 | 9.7 |
| 5 | 29.6 | 31.9 | 26.2 |
| 6 | 37.4 | 28.0 | 29.7 |
| 7 | 16.5 | 17.7 | 18.3 |

Table 5.  Bond Dissociation Energies in kcal/mol, Computed with 6-311+G** Basis.

|  | UHF | B3LYP |
|--|-----|-------|
| NTO/10 + H | 72.6 | 97.7 |
| NTO/11 + H | 69.4 | 93.4 |
| NTO/12 + NO2 | 42.4 | 61.1 |
| 5/13 + OH | -14.4 | 38.3 |

# Towards the Synthesis and Identification of Tetrahedral $N_4$.

### Christopher E. Dateo
Thermosciences Institute, MS 230-3
NASA Ames Research Center, Moffett Field, CA 94035-1000

### Timothy J. Lee
Mail Stop 230-3, NASA Ames Research Center, Moffett Field, CA 94035-1000

**ABSTRACT**: Tetrahedral $(T_d)$–$N_4$ has attracted attention as a high energy density material candidate. Although computational studies have shown $T_d$ $N_4$ to be a stable structure on the ground-state potential energy surface, it has yet to be experimentally observed. This study investigates possible synthetic pathways via excited state surfaces. Preliminary results include a comparison of vertical excitation energies from $T_d$ $N_4$ using CIS, CIS(D), LRCCSD, and CASSCF *ab initio* methods. Previous studies have predicted weak IR vibrational intensities. Therefore, alternative detection schemes of $T_d$ $N_4$ will also be investigated, such as UV and vibrational Raman spectroscopy.

## Introduction

Tedrahedral $N_4$ has attracted considerable interest as a possible high energy density material. [1-4] The energy difference between $T_d$ $N_4$ and two ground state $N_2$ molecules has been determind to be 186 kcal/mol, while the barrier separating these species was found to be about 61 kcal/mol.[1] This large barrier is due to the electronic configurations of $T_d$ $N_4$ and two ground state $N_2$ molecules differing by a double excitation. The barrier (transition state) is the result of an avoided crossing between the two electronic states dominated by these configurations.

The existence of a singlet–triplet crossing with the $^3A''$ surface was found to lower the barrier to approximately 28 kcal/mol (about half the spin-allowed decay channel).[2] This intersystem crossing must be considered when determining the $T_d$ $N_4$ lifetime.

**Goals of this study**

- $T_d N_4$ has yet to be experimentally observed. This study investigates possible synthetic pathways via excited electronic states. If an excited electronic state of $N_4$ with near–tedrahedral geometry exists, it may be possible to approach the ground state $T_d N_4$ by forming the excited electronic state and then decaying to the ground state.

- The preliminary studies here are to investigate excited state methods appropriate for the $N_4$ system. The methods presented here include CASSCF, CIS, CIS(D), and LRCCSD. In addition, CASPT2 and MRCI methods will be investigated.

- Preliminary construction of a symmetry and orbital correlation between electronic states of $N_4$ and $N_2$ diatom fragments.

**Excited State Methods**

1) **CASSCF** — complete active space self-consistent field. This method includes mainly non-dynamical electron correlation and can therefore exhibit large errors when dynamical correlation is important. The size of active space is also rather limiting --- in the present case only the $2p$ orbitals and electrons could be included in the active space (12 electrons in 12 orbitals).

2) **CIS** — configuration interaction singles, or diagonalization of the CI singles matrix. Takes advantage of the fact that the ground (reference) state has a zero matrix element with singly excited states due to Brillouin's theorem. The excited state energies effectively contain no electron correlation contribution (neither dynamical nor non-dynamical) and therefore CIS can often produce large errors.

3) **CIS(D)** — second-order perturbation correction to CIS. This is essentially the excited state equivalent of MP2 for ground electronic state calculations. Benchmark studies indicate that for valence excited states CIS(D) is usually pretty good, within about 0.2--0.5 eV for vertical excitation energies of much more sophisticated calculations. Rydberg states are not as well described.

4) **LRCCSD** — linear response singles and doubles coupled-cluster theory. This method gives identical excitation energies to the Equations of Motion method (EOM-CCSD). Benchmark studies, comparing to very accurate experiments or multireference CI calculations, indicate that LRCCSD vertical excitation energies are usually accurate to about ±0.1 eV provided that the excited state is primarily a single excitation away from the ground (reference) state (i.e., a singles weight of 0.7 or greater).

## Basis Sets

<u>One-particle basis sets:</u>

1) DZP — the standard Huzinaga-Dunning $[4s2p]$ double zeta basis augmented with a single set of $d$ polarization functions ($\alpha_d = 0.80$).

2) TZ2P — the standard Huzinaga-Dunning $[5s3p]$ triple zeta basis augmented with two sets of $d$ polarization functions ($\alpha_d = 1.654$ and $0.469$; these are from Dunning's correlation consistent basis sets).

3) ANO — Atomic natural orbital basis sets. A $4s3p2d1f$ ANO basis set is denoted [4321], for example.

## Results

**Table 1.** $T_d N_4$ Vertical excitation energies (eV).[a]

| State | main excitation | CASSCF | | SA–CASSCF[b] | |
|-------|-----------------|--------|--------|--------|--------|
|       |                 | DZP | TZ2P | DZP | TZ2P |
| $^1A_1$[c] |           | 0.857 865 63 | 0.882 995 75 | 0.838 841 11 | 0.866 248 35 |
| $^1T_1$ | $(e{\rightarrow}t_1)$ | 11.06 | 11.18 | 10.00 | 9.96 |
| $^1T_2$ | $(e{\rightarrow}t_1)$ | 12.56 | 12.68 | 11.13 | 11.14 |
| $^1A_2$ | $(t_2{\rightarrow}t_1)$ | 13.86 | 14.01 | 11.49 | 11.61 |
| $^1E$ | $(t_2{\rightarrow}t_1)$ | 14.25 | 14.40 | 11.87 | 12.00 |
| $^1T_1$ | $(t_2{\rightarrow}t_1)$ | 14.29 | 14.42 | 12.02 | |
| $^1T_2$ | $(e{\rightarrow}t_2)$ | 14.68 | 14.80 | 13.31 | |

[a] Using CCSD(T)/ANO[432] ground state geometry of Lee and Rice.[1]

[b] Using [12+12] CAS which includes all N(2p) orbitals. CASSCF results use ground state orbitals, SA-CASSCF use state averaged orbitals — all sixteen states for DZP basis set and lowest ten states for TZ2P basis set results.

[c] Ground state energies are given as $-(217 + \text{value})\ E_H$.

**Table 2.** $T_d N_4$ Vertical excitation energies (eV)[a]

| State | main excitation | CIS | CIS(D) | LRCCSD | |
| --- | --- | --- | --- | --- | --- |
| | | | | Energy | wgt.[b] |
| $^1T_1$ | $(e \rightarrow t_1)$ | 9.06 | 9.67 | 9.36 | 0.833 |
| $^1T_2$ | $(e \rightarrow t_1)$ | 10.61 | 9.96 | 10.03 | 0.790 |
| $^1A_2$ | $(t_2 \rightarrow t_1)$ | 11.23 | 9.88 | 10.05 | 0.767 |
| $^1E$ | $(t_2 \rightarrow t_1)$ | 10.54 | 10.21 | 10.09 | 0.813 |
| $^1T_1$ | $(t_2 \rightarrow t_1)$[c] | 10.25 | 10.39 | 10.26 | 0.825 |
| $^1T_2$ | $(e \rightarrow t_2)$ | 11.49 | 10.74 | 10.66 | 0.812 |

[a]  Using CCSD(T)/ANO[432] ground state geometry of Lee and Rice.[1]   All methods used TZ2P basis set

[b]  Norm of singles amplitudes.

[c]  Main excitation for CIS state is $(e \rightarrow t_2)$ though there is a considerable contribution from $(t_2 \rightarrow t_1)$

## Conclusions

- CASSCF results are not adequate. They give qualitatively accurate descriptions, but the energetics are inaccurate. CASPT2 and MRCI methods will add dynamical correlation, but become costly (and difficult).

- It appears that CIS(D) gives reasonably accurate agreement with LRCCSD and may be the method to use to search further details of excited states surfaces.

- Considering energetics alone, it does not appear too likely that excited singlet states will give an experimental synthetic route, though further studies are necessary.

- We will also be investigating pathways via states of $N_3$ + N, triplet states, and excited states of cation $N_4{}^+$.

- In addition, previous studies have predicted fairly weak IR vibrational intensities.[1]  Future work will investigate alternative detection schemes of $T_d N_4$, such as UV and vibrational Raman spectroscopy.

## References

1)     T. J. Lee and J. E. Rice, J. Chem. Phys. **94** 1215 (1991).

2)     D. R. Yarkony, J. Am. Chem. Soc. **114**, 5406 (1992).

3)     W. J. Lauderdale, J. F. Stanton, and R. J. Bartlett, J. Phys. Chem. **96**, 1173 (1992).

4)     K. M. Dunn and K. Morokuma, J. Chem. Phys. **102**, 4904 (1995).

# CRYOGENIC MONOPROPELLANT FOR ADVANCED ROCKET PROPULSION
by
Dr. Thomas M. Flynn

CRYOCO Inc.
511 North Adams Ave.
Louisville CO 80027
tel (303) 665-8302
fax (303) 665-0222
email: Tflynn3113@AOL.COM

This program demonstrated the feasibility of a new cryogenic rocket propellant, made by mixing liquid Methane and liquid Oxygen (MOX). Liquid oxygen and liquid methane are completely miscible in all proportions, and therefore MOX is completely homogeneous under all conditions of use. Impact tests (147 in all) proved that MOX has a very narrow range if impact sensitivity. MOX is safe to make, transport and handle. MOX is unique in the field of advanced rocket propulsion, MOX combines the best features of solid and liquid rocket propulsion: the simplicity of solid rockets with the controllability of liquid rockets. MOX provides an unprecedented means for less expensive access to space through a revolution in rocket design. Work is in progress on a Phase II SBIR to demonstrate save production and handling techniques, prove a detonation arrestor, and examine the impact of MOX on future rocket designs.

# PRODUCTION OF DOPED SOLID HYDROGEN FILMS FOR OPTICAL AND THERMAL MEASUREMENTS

K.S. Ketola, W. Homsi, H.J. Maris, G.M. Seidel

Department of Physics, Brown University, Providence, Rhode Island 02912

## I. Introduction

We have constructed an apparatus to study the optical and thermal properties of doped solid hydrogen films at temperatures down to 0.4 K, and are currently in the process of testing the cryostat. The films will be produced by depositing hydrogen from the vapor phase onto a substrate held at T≤2 K, while the impurity atoms are co-deposited by laser ablation of a rotating target. In this paper, we will focus on several unique features of the design which will allow for control of most of the parameters effecting the structure of the deposited film.

## II. Overview of the Experimental Cells

The deposition will take place within a vacuum chamber (see Figure 1), referred to as the main cell, which is mounted within the common-vacuum region of the dewar. The main cell has been constructed from a 11.43 cm diameter thin wall (0.64 mm) stainless steel tube which is 12.7 cm long. There are eight optical access ports which have been welded to the 11.43 cm diameter tube, 45 degrees apart around the circumference and halfway along the length of the cell. Hydrogen will enter the main cell through a feedthrough in a 9.5 mm thick copper plate which is sealed to the top of the cell with an indium o-ring. During the deposition process, hydrogen will flow into the main cell and impurity atoms will be ablated from a rotating target and a film will be deposited onto a 1 mm thick quartz substrate which is part of a smaller cell (deposition cell) mounted at the bottom of the main cell and held at a temperature less than 2 K. The deposition cell is mounted into a hole in the center of a 9.5 mm thick copper plate mounted to the bottom of the main cell. The deposition cell consists of a copper tube with flanges at both ends for quartz windows, which is soldered to a stainless steel support structure which can be bolted into the hole in the bottom copper plate of the main cell. The $^4$He and $^3$He pots are located below the main cell and they serve to cool the bottom copper plate and the deposition cell, respectively.

## III. Design Features

One of the most important features that we wanted to incorporate into the design was the ability to use a helium buffer gas to reduce the kinetic energy of the ablated atoms before they reached the deposition substrate. If the impurity atoms reach the substrate with a high energy, the resulting local heating of the film may result in appreciable restructuring of the film including recombination of the impurities. The idea is to thermalize the impurity atoms by having them undergo several collisions with helium atoms on the way to the deposition substrate. The helium gas density will be approximately $10^{15}$ cm$^{-3}$ and will be adjusted so

that an impurity atom will undergo several collisions with helium atoms before reaching the substrate, but also so that there will be a low probability of two impurity atoms colliding. To make *in situ* measurements of the helium gas pressure in the main cell, we built a Pirani type of pressure gauge (see Figure 2). This gauge makes use of the dependence of the thermal conductivity of the gas on the pressure. An 0.8 mm diameter 1.5 cm long copper cylinder is wrapped with approximately 200 turns of 0.05 mm diameter CrNi heater wire and is held in place inside of a copper tube (4.5cm long, 0.74 cm diameter) which is in good thermal contact with the top plate of the main cell. Current in the heater wire will raise the temperature of the 0.8 mm diameter copper cylinder relative to the temperature of the copper tube which surrounds it and this temperature gradient will increase with decreasing helium gas pressure. A thermocouple made of AuFe wire (.07% Fe) and CrNi wire (80% Cr, 20% Ni) is used to measure this temperature gradient. The dimensions of the wires and the copper tube were choosen to optimize the sensitivity in the pressure range of interest, namely $10^{-3}$-$10^{-5}$ Torr.

Since we wanted to have hydrogen flowing into the main cell as vapor and then be deposited as a solid, the cell had to be able to support a temperature gradient between 10 K at the top plate of the main cell and 2 K at the bottom. To sufficiently reduce the heat flow from the top to the bottom of the cell, we used 0.64 mm thick stainless steel for the walls. The deposition substrate had to be transparent so that we could study the transmission of light through the doped hydrogen film and yet we also wanted to have superfluid on the back side of the substrate during the deposition process in order to more efficiently remove heat from the film as it is deposited. So, a separate deposition cell was designed which was simply a copper tube with windows at either end and a fill line which allowed helium to be added to the region between the two windows. This deposition cell had to be in good thermal contact with the $^3$He pot so that the film could be cooled to 0.4 K, but at the same time, the $^4$He pot had to be cooling the part of the cell that supported the deposition cell so as to limit the heat load on the $^3$He pot. The solution was to have both pots below the bottom of the cell, with the $^4$He pot linked to a copper ring mounted to the bottom of the main cell, and then have the deposition cell mounted into the hole in the copper ring. The copper body of the deposition cell had to be weakly linked to this copper ring so as to reduce the amount of heat flowing into the deposition cell and so a stainless steel support structure was soldered to the copper deposition cell. This support structure incorporates a thin-wall (0.25 mm) stainless steel tube attached to a stainless steel flange which is then bolted to the hole in the copper ring at the bottom of the main cell.

So, during deposition, the temperature of the hydrogen vapor at the inlet to the main cell and the temperature of the deposition substrate will be able to be independently regulated. The hydrogen deposition rate will also be able to be controlled. A schematic for the hydrogen flow system is shown in Figure 2. The hydrogen flows from a high pressure tank through a liquid nitrogen cooled trap, a needle valve, and through a capillary which leads into the dewar and connects to a copper can filled with a catalyst to promote ortho-para conversion. This copper can is mounted to a copper platform which is weakly linked to the 4 K stage of the refrigerator. The temperature of this platform will be able to be regulated at a temperature above the triple point of hydrogen, say at 14 K. Para-hydrogen flows out of the bottom of the converter through a capillary which forms the high impedance section of the hydrogen flow system. Most of the capillary is wrapped around a copper post mounted to another separate copper platform. This other platform also has a weak thermal link to the 4 K stage

and can be regulated separately from the ortho-para converter. By controlling the pressure of the liquid hydrogen in the ortho-para converter, we should be able to control the flow of hydrogen through the impedance into the main cell. In order to quickly stop the flow of hydrogen through the impedance, the regulating heat applied to the impedance platform will be turned off and solid should rapidly form inside the impedance.

There were several requirements which needed to be fulfilled for the design of the target holder. First, the target had to be rotated so that each pulse from the excimer laser would be incident on an unablated region of the target. If each pulse was incident on the same spot, then the plume of ablated atoms would change from pulse to pulse as a pit developed in the target. We also wanted the target to be at a 45 degree angle relative to the deposition substrate. The design that we settled upon was to use a motor driven shaft which extends from outside of the cryostat into the main cell. The shaft turns a gear which is coupled to another gear which has the desired orientation relative to the deposition substrate. This second gear has a target holder mounted to it which can accept target disks 2 cm in diameter and up to several mm thick.

## IV. Summary

During the deposition process, we will have control over many of the parameters which can effect the structure of the doped hydrogen film. These parameters include:

- temperature and flow rate of the hydrogen vapor at the inlet to the main cell

- temperature of the deposition substrate

- pressure of the helium buffer gas in the cell

- energy per pulse and repetition rate of the excimer laser

Our optical and thermal measurements will provide information about the structure of the doped film and so we will be able to investigate how changes in the above parameters effect the structure of the film.
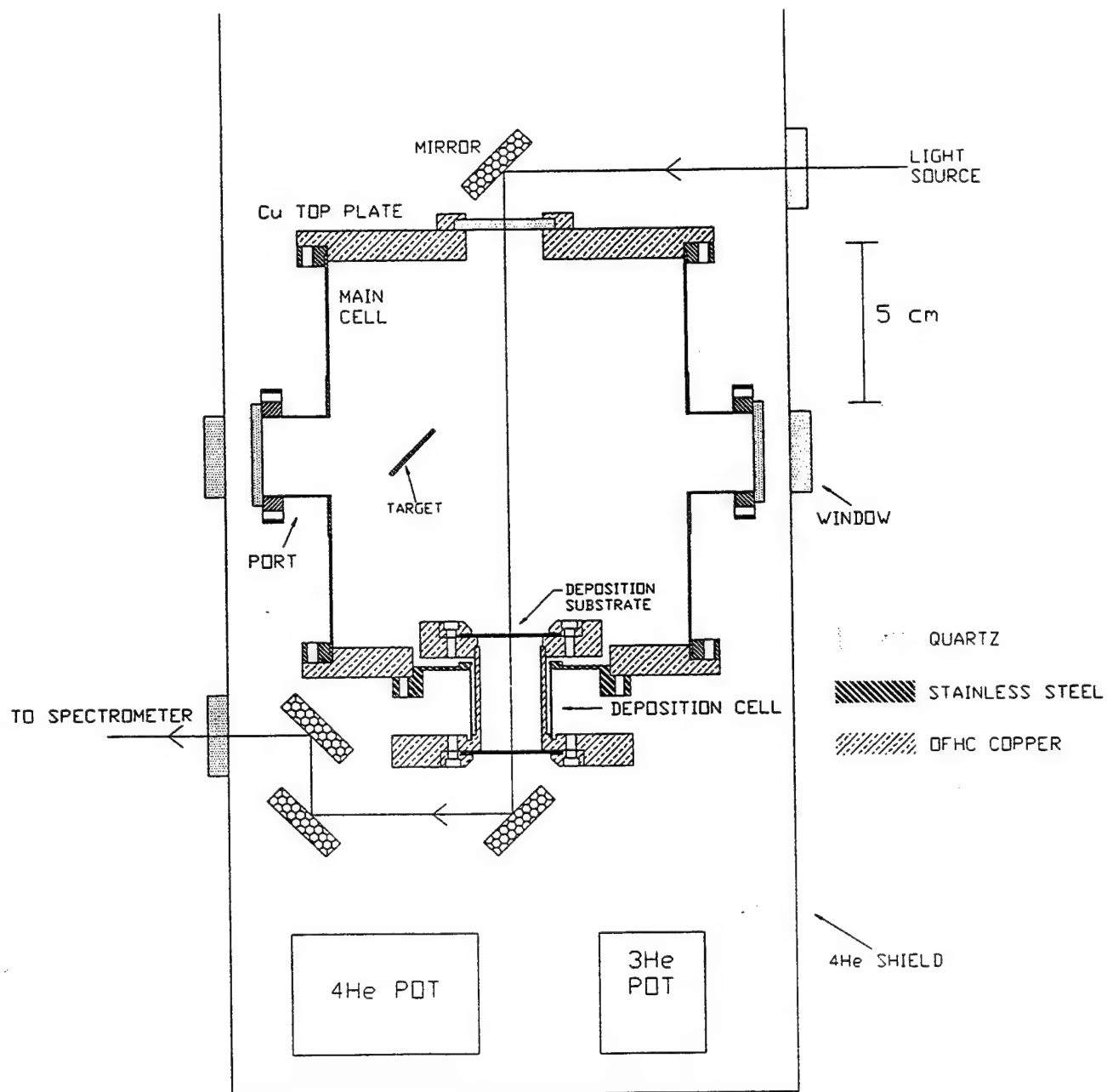
Figure 1: Cross-sectional view of the experimental cells. Certain features have been omitted for clarity, such as the hydrogen inlet, target support mechanism, and Pirani gauge.
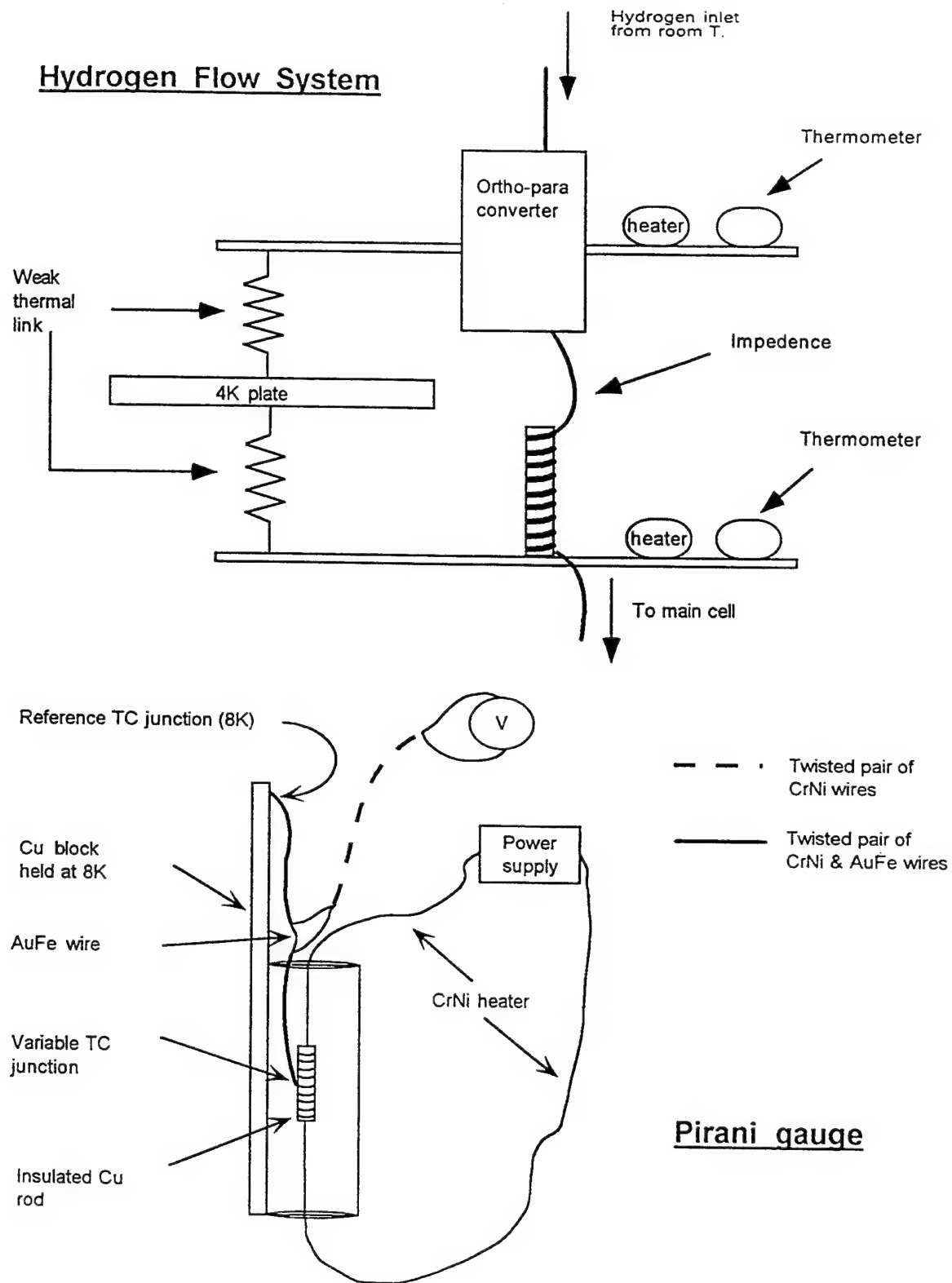
Figure 2: Schematic diagrams for the Pirani gauge and the hydrogen flow system.

234

# FTIR spectroscopy of the $\nu_2(a_1)$ vibration of $BC_2$ in solid Ar

J. D. Presilla-Márquez, C. W. Larson, P. G. Carrick, and C. M. L. Rittby
Phillips Laboratory
Edwards AFB, CA

## ABSTRACT

The products of vaporization of boron/carbon mixtures around 3000 K were trapped in argon matrices at 10 K and their Fourier transform infrared spectra were measured. Analysis of the spectra combined with the predictions of density functional theory (DFT) calculations have resulted in the assignment of a previously observed vibration at 1194.4 $cm^{-1}$ to the $\nu_2(a_1)$ symmetric "breathing" vibrational fundamental of cyclic symmetric $BC_2$. The assignment is supported by $^{10}B$, $^{11}B$ and $^{13}C$ isotopic data and is in good agreement with the theoretical predictions.

# NEW DEVELOPMENTS IN THE MCD SPECTROSCOPY OF HEDM-DOPED CRYOGENIC SOLIDS

Extended Abstract
1996 HEDM Meeting
Boulder, Colorado

*John W. Kenney, III*
*Heidi A. Terrill-Stolper*
*Chemical Physics Laboratory*
*Eastern New Mexico University*
*Portales, NM USA 88130*

## *Theory--Introduction:*

The theory of Monte-Carlo-Magnetic Circular Dichroism (MC-MCD) simulations of the MCD spectra of cryogenic alkali metal (M)/rare gas (Rg) matrices has been presented by Kenney[1] and demonstrated by Terrill-Stolper and Kenney.[2] The MC-MCD theory is a straightforward extension of the development of Boatz and Fajardo[3] for treating the $^2S \rightarrow {}^2P$ electronic absorption spectra of M/Rg systems and that of Lawrence and Apkarian[4] for treating the electronic spectra of $^2P$ halogen atoms isolated in Rg matrices.

## *Setting up MC-MCD Simulations:*

The MC-MCD simulations here displayed for the $^2S \rightarrow {}^2P$ MCD spectra of Na/Ar are based upon the same sodium/argon potentials employed by Boatz and Fajardo.[3] The M/Rg lattice vibronic behavior is determined from the lattice "simulation temperature" of 10 K. Boltzmann population ratios of the Zeeman-split $^2S$ ground manifold of Na/Ar are determined by a variable, user selected "magnetic temperature". The $^2P$ spin-orbit splitting is assumed to be the atomic splitting for sodium (17 cm$^{-1}$), and the magnetic field in the simulation is taken to be 1.0 T, a typical value for actual MCD experiments. In some simulations the spin-orbit splitting is changed in magnitude and/or in sign from the free atomic Na value.

## *Variations Induced by Changes in Assumed Magnitude and Sign of $^2P$ Spin-Orbit Splitting:*

MC-MCD simulations reported in the 1995 HEDM Conference showed an MCD sign change in the Na/Ar violet triplet as the Na $^2P$ spin-orbit splitting was reduced from large positive values ~170 cm$^{-1}$ to small positive values $\leq$ 17 cm$^{-1}$ for simulation and magnetic temperatures of 10 K with a 1.0 T magnetic field.[2] The extant experimental M/Rg MCD

[1] Kenney, J. W., III *Theory of Monte-Carlo Simulations of the Magnetic Circular Dichroism (MCD) Spectra of Alkali Metal/Rare Gas Matrices*, Final Report, RDL-SFRP AFOSR, **1995**.

[2] Kenney, J. W., III; Terrill-Stolper, H. A. "Monte-Carlo Simulations of the Magnetic Circular Dichroism Spectra of the Matrix-Isolated $^2S \rightarrow {}^2P$ 'Violet Triplet'", In *Proceedings of the High Energy Density Matter (HEDM) Conference*, June **1995**, Woods Hole, MA, *PL-TR 95-3039*, pp. 237-240.

[3] Boatz, J.; Fajardo, M. E. *J. Chem. Phys.* **1994**, *101*, 3472-3487.

[4] Lawrence, W. G.; Apkarian, V. A. *J. Chem. Phys.* **1994**, *101*, 1820-1831.

spectra in the literature are characterized by two down peaks at lower energy and one up peak at higher energy ($\downarrow\downarrow\uparrow$ $h\nu$ $\rightarrow$).[5] The $^2P$ spin-orbit splittings extracted from these $^2S \rightarrow {}^2P$ MCD spectra by moment analysis methods are large and negative. It is significant to note that MC-MCD simulations in which a large negative spin-orbit splitting is assumed (e.g., -170 cm$^{-1}$) give similar band profiles to those MC-MCD simulations in which a small positive spin-orbit splitting is assumed (e.g., 17 cm$^{-1}$). In other words, caution is in order in extracting parameters from experimental MCD spectra.

*Magnetic Temperature Variations in Simulated MC-MCD Spectra:*

Since most experiments with alkali metals isolated in cryogenic rare gas matrices are performed in the 2-15 K range, it was desirable to explore this same temperature range in the MC-MCD simulations. It was found that the MC-MCD spectra for a Na/Ar single substitutional site with spin-orbit splittings ranging from a few wavenumbers to a few tens of wavenumbers changed as magnetic temperature was lowered over the range 10 K to 6 K from a ($\downarrow\downarrow\uparrow$ $h\nu$ $\rightarrow$) high temperature pattern to an inverted ($\uparrow\downarrow\downarrow$ $h\nu$ $\rightarrow$) low temperature pattern (See Figure 1). For a 3-Ar atom vacancy substitutional site, the MC-MCD spectra of Na/Ar changed from a ($\downarrow\uparrow\uparrow$ $h\nu$ $\rightarrow$) pattern at 10 K to an almost perfect mirror image ($\uparrow\downarrow\downarrow$ $h\nu$ $\rightarrow$) low temperature pattern at 6 K (See Figure 1). The sign change/inversion does not occur at a single temperature but over a range of temperatures in the 10 - 6 K region. No temperature-dependent MC-MCD sign changes/inversions were found for the cases of large assumed positive $^2P$ spin-orbit coupling, nor was a sign change/inversion found for small assumed $^2P$ spin-orbit splittings less than 1 cm$^{-1}$.

*Effects of Other Perturbations on the MC-MCD Simulations:*

The MC-MCD sign change/inversion temperature was explored for the specific case of a 17 cm$^{-1}$ spin-orbit splitting for Na and a 1.0 T magnetic field under a variety of different situations. For the most part, there was no change in the magnetic temperature of the MC-MCD sign change/inversion with regard to changes in the lattice simulation temperatures and number of Ar atom vacancies in the Na trapping sites. The MC-MCD sign change/inversion for all trapping sites studied--one-, two-, three-, four-, five-, six-, and thirteen-Ar atom vacancy trapping sites for the Na--occurred around an 8.3 K magnetic temperature. However, the MC-MCD spectra for the symmetric and asymmetric trapping sites are strikingly different (See Figure 1). For, example in an asymmetric 3-Ar atom vacancy trapping site, the MC-MCD spectra consist of a pair of closely spaced lower energy bands and another band of low intensity that appears at much higher energy. This same asymmetric splitting of the triplet

[5] (a) Lund, P. A.; Smith, D.; Jacobs, S. M.; Schatz, P. N. *J. Chem. Phys.* **1984**, *88*, 31-42. (b) Rose, J.;

absorption profile is found in simulated MC-absorption spectra of the asymmetric 3-Ar atom vacancy trapping site.[3] The most striking difference resulting from site symmetry considerations has to do with temperature-dependent changes in the MC-MCD band profile. In all of the symmetric trapping sites, the center band of each simulated MC-MCD spectrum remained negative ($\downarrow$) at all magnetic temperatures investigated. In the case of the asymmetric two-, three-, and five-Ar atom vacancies sites, all bands in each MC-MCD spectrum changed sign as the magnetic temperature was ramped through the sign change temperature regime.

As yet, there are no temperature-dependent experimental Na/Ar MCD data to test the predictions of these MC-MCD simulations.[6] Since no sign change was observed in the simulated MC-MCD spectra when the assumed $^2P$ spin-orbit splitting is negative or very small, not observing the sign change/inversion in temperature-dependent experimental MCD spectra could be taken to indicate either (a) the spin-orbit splitting of Ar-matrix isolated $^2P$ Na atoms is negative or (b) the dynamic Jahn-Teller effect operating in the $^2P$ manifold of Na/Ar has effectively quenched the $^2P$ spin-orbit coupling to a very small value.

For the range of $^2P$ Na spin-orbit splittings examined, the simulated MC-MCD spectra at lower temperatures resemble those MC-MCD spectra obtained in simulations postulating a large positive $^2P$ spin-orbit splitting, while the simulated MC-MCD spectra at higher temperatures resemble those MC-MCD spectra for which large negative spin-orbit splittings are assumed.

### *The Problem of Choosing Appropriate Lattice Simulation Temperatures:*

The commonly chosen lattice simulation temperature value of 10 K tends to underestimate the zero-point vibrational motion of the Na/Ar lattice. This can be compensated for by increasing the simulation temperature above the actual experimental temperature being simulated while keeping the magnetic temperature governing the Boltzmann populations of the Zeeman terms in the $^2S$ ground manifold at this desired experimental temperature. Estimates of lattice simulation temperatures required to mimic a given experimental temperature can be obtained by evaluating the average positions of the first- and second-nearest neighbor Ar atoms in simulated solid Ar matrices for which experimental temperature vs. nearest neighbor distance data are well known.[7] (See Figure 2). The primary effect of increasing the lattice simulation temperature is to broaden the MC-absorption and MC-MCD spectra about the barycenter of the triplet (See Figure 3). The key point is that no MC-MCD sign changes/inversions are generated by increasing the lattice simulation temperature.

---

Smith, D.; Williamson, B. E.; Schatz, P. N.; O'Brien, M. C. M. *J. Chem. Phys.* **1986**, *90*, 2608-2615.
[6] Experimental Na/Kr MCD spectra were acquired recently by Kenney *et. al.* The MCD pattern for Na/Kr prepared by laser ablation of the Na is similar to that observed in Na/Xe and Li/Xe (see Ref. 5).
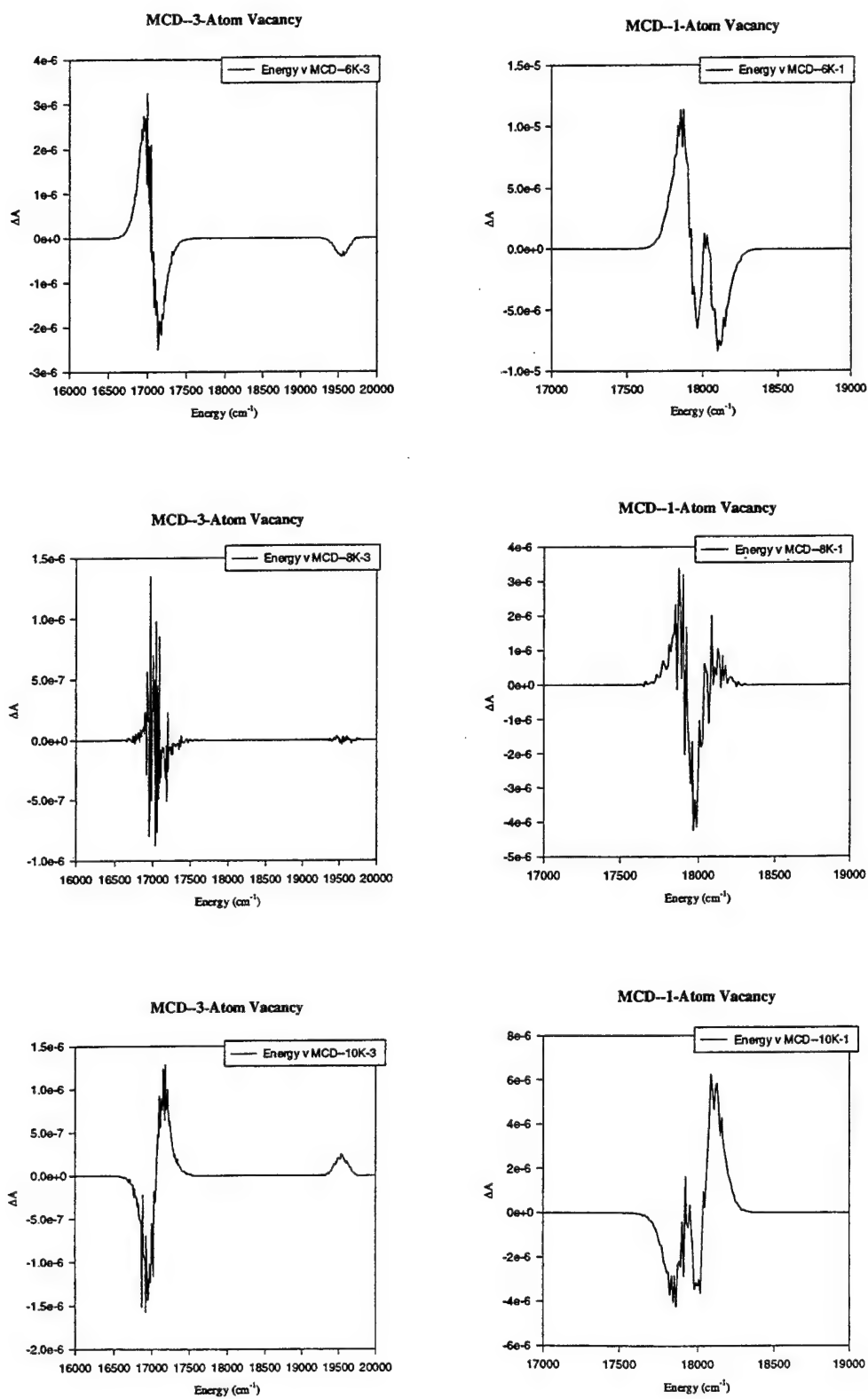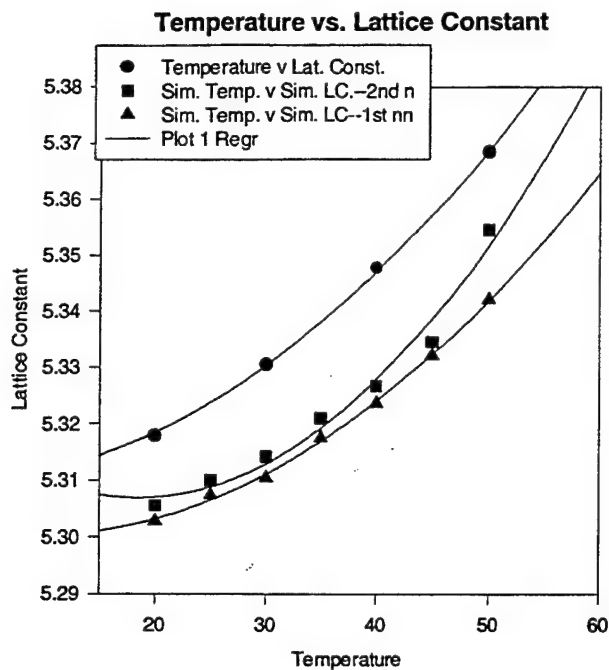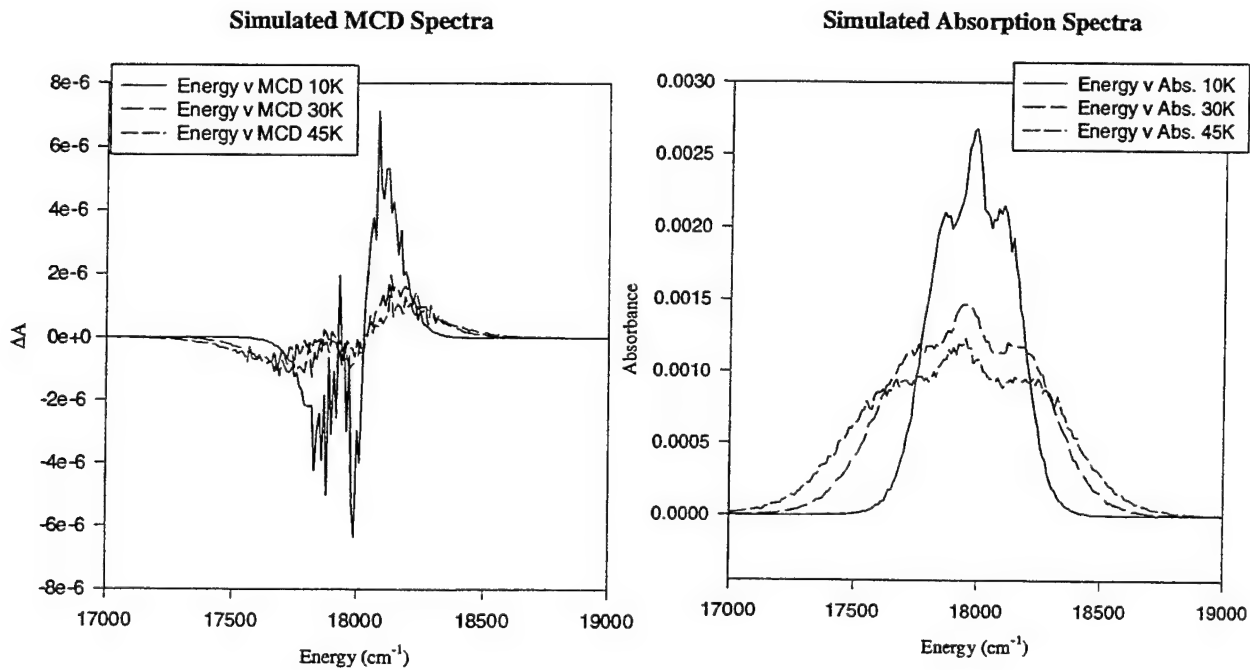[7] Klein, M. L.; Venables, J. A. *Rare Gas Solids, Vol 1.* Academic: New York, **1976**.

**Figure 1.** MC-MCD Simulated $^2S \rightarrow {}^2P$ Spectra for Na/Ar

**Figure 2.** Temperature (K) vs. Lattice Constant (Angstroms) for Simulated Ar Matrices



**Figure 3.** MC-Absorption and MC-MCD Spectra for Na/Ar at Various Simulation Temperatures

# A New Application of Absorbing Boundary Conditions for Computing Collinear Quantum Reactive Scattering Matrix Elements

R. S. Calfas and D. E. Weeks
Air Force Institute of Technology

The search for High Energy Density Matter ( HEDM ) continues to be a priority for basic Air Force research towards higher $I_{sp}$ rocket fuels[1]. An important aspect of this research is the development of reliable theoretical and computational methods to support experimental efforts. Theoretical approaches focused on chemically based spacelift strategies can be divided roughly into two categories. The first is concerned primarily with the structures and electronic energies of potential HEDM candidates. These efforts typically employ the Born - Oppenheimer approximation to determine electronic energy levels for fixed nuclear positions. A potential energy surface ( PES ) is constructed from the lowest electronic energy level as a function of nuclear position, and the ground state equilibrium structures are then determined by minima of the PES. A second category of theoretical and computational research is concerned with the dynamics of chemical reactions. These efforts typically begin with a PES and use either Hamilton's equations of motion to perform a semi - classical analysis, or Schrödingers equation to perform a quantum analysis of the molecular dynamics of a HEDM candidate.

Strategies for determining quantum dynamical information about chemical reactions focus on computing scattering matrix ( S - matrix ) elements[2]. Elements of the S - matrix in the momentum representation yield the probability, as a function of relative kinetic energy, that reactants in some internal reactant eigenstate will form products in some internal product eigenstate. In an effort to develop a more efficient time dependent approach for calculating scattering matrix (S-matrix) elements, we have combined absorbing boundary conditions (ABC)[3] together with the channel packet method (CPM)[4]. The CPM is based on the Møller operator formulation of scattering theory and divides the computational effort into two parts[5]. The first is the application of Møller operators to initial reactant and product wave packets producing two Møller states. The second is the computation of the time dependent correlation function between the two Møller states. The time dependent correlation function is efficiently computed by individually propagating the Møller states using ABC as they exit the interaction region of the potential. The utility of this approach derives from the fact that the Møller states are initially fairly well localized in the interaction region of the potential. As a Møller state evolves in time, it will be attenuated by the ABC without reflecting off the edge of the grid thereby permitting the use of a much smaller grid. The Fourier

transform of the correlation function is then used to compute S-matrix elements. The use of ABC together with the CPM results in an order of magnitude improvement in the time required to calculate the correlation function[4] on the LSTH H + $H_2$ potential energy surface[6]. The corresponding S-matrix elements compare favorably with previous calculations and serve to validate the computational procedure. Larger computational savings are realized when computing S-Matrix elements for reactions on a potential energy surface with a well that can trap long lived quasi-bound states.

The CPM begins with the definition of two initial wave packets $\Psi^{1,v}_{in}$ ( X, Y ), and $\Psi^{2,v'}_{out}$ ( X, Y ) at t = 0 where X and Y are bond coordinates describing the separation between three collinear atoms A, B, and C. The first wave packet $\Psi^{1,v}_{in}$ ( X , Y ) is used to describe the incoming reactants A + BC( v ) in arrangement channel 1 where the diatom is prepared in a single vibrational eigenstate labeled v. The second wave packet $\Psi^{2,v'}_{out}$ ( X , Y ) is used to represent outgoing products AB( v' ) + C in arrangement channel 2 where the diatom is in a single vibrational eigenstate v'. The next step is to compute a pair of intermediate states obtained from the initial states by propagating $\Psi^{1,v}_{in}$ ( X, Y ) backwards to time t = -∞ using the asymptotic channel Hamiltonian $H^1_0$, and propagating $\Psi^{2,v'}_{out}$ ( X, Y ) forwards to time t = +∞ using the asymptotic channel Hamiltonian $H^2_0$. The intermediate states are then propagated back towards the interaction region of the potential using the full Hamiltonian. Since each wave packet is localized in a single arrangement channel, the propagation can be done efficiently using a long narrow grid. Using bra - ket notation, the resulting states are given by,

$$
\left| \Psi^\gamma_\pm \right\rangle = \Omega^\gamma_\pm \left| \Psi^\gamma_{in \atop out} \right\rangle = \lim_{t \to \mp\infty} \left[ \exp\{ i H t \} \exp\{ -i H^\gamma_0 t \} \right] \left| \Psi^\gamma_{in \atop out} \right\rangle ,
$$

where $\Omega^\gamma_\pm$ are the Møller operators, γ labels the arrangement channel and internal quantum states of the reactants or products, and the $| \Psi^\gamma_\pm \rangle$ are called Møller states. Møller states for the H + $H_2$ reaction are shown in figure 1.

The correlation function,

$$
C_{\gamma\gamma}( t ) = \left\langle \Psi^\gamma_- \right| \exp\left\{ \frac{-i H t}{\hbar} \right\} \left| \Psi^\gamma_+ \right\rangle ,
$$

between the Møller states $\Psi^{1,v}_+$ ( X , Y ) and $\Psi^{2,v'}_-$ ( X , Y ) is then computed and used to calculate S – matrix elements,

$$
S^{\gamma\gamma}_{\pm k'_\gamma \pm k_\gamma} = \frac{\hbar \left\{ | k'_\gamma | | k_\gamma | \right\}^{1/2}}{2 \pi \mu \, \eta^*_-( \pm k'_\gamma) \eta_+( \pm k_\gamma)} \int_{-\infty}^{+\infty} dt \exp\left\{ \frac{i E t}{\hbar} \right\} C_{\gamma\gamma}( t ) ,
$$

where E is the total energy, $k_\gamma$ is the relative momentum between reactants, and $k'_\gamma$ is the relative momentum between products. The $\eta_\pm( \pm k_\gamma )$ are expansion coefficients used to construct the initial

channel packets $\Psi^{1,v}_{in}$ ( X, Y ), and $\Psi^{2,v'}_{out}$ ( X, Y ) as a linear combination of plane waves.

Absorbing boundary conditions are used to efficiently compute the correlation function, and are imposed by employing an imaginary potential of the form,

$$V = V_I \pm i\, V_a \ ,$$

where $V_I$ describes the interaction between the reactants and products, $V_a$ is given by,

$$V_a ( X, Y ) = A\, (\, exp\left\{ \frac{(X - X_o)^2}{B} \right\} + exp\left\{ \frac{(Y - Y_o)^2}{B} \right\}\, ) \ ,$$

and the constants A and B are chosen to minimize reflection caused by $V_a$. The location of ABC relative to the reactant and product Møller states is shown in figure 1 for the H + $H_2$ reaction. The correlation function, $C_{\gamma'\gamma}( t ) = \langle\, \Psi^{2,0}_- \,|\, \Psi^{1,0}_+ \,( t )\, \rangle$ is computed as the reactant Møller state evolves in time and bifurcates into the reactant and product channels. The evolving Møller state will eventually reach the ABC and exponentially attenuate as illustrated in figure 2. However, since since the attenuation occurs where the product Møller state is zero, the ABC do not influence the value of the correlation function. The corresponding S - matrix elements for the H + $H_2$ reaction is shown in figure 3.

# References

1) USAF Scientific Advisory Board, New World Vistas: Air and Space Power for the 21st Century, Space Technology Volume ( USAF Scientific Advisory Board, 1995 ) p. 21.

2) R.D.Levine, Quantum Mechanics of Molecular Rate Processes, (Oxford University Press, New York, NY, 1969).

3) D.Neuhauser, M.Baer, R.S.Judson, and D.J.Kouri, Computer Phys. Comm. 63, 460 (1991).

4) R.S.Calfas and D.E.Weeks , Chem. Phys. Letts. ( submitted for publication ).

5) D.J.Tannor and D.E.Weeks, J. Chem. Phys. 98, 3884 (1993); D.E.Weeks and D.J.Tannor, Chem. Phys. Letts. 207, 301 (1993); D.E.Weeks and D.J.Tannor, Chem. Phys. Letts. 224, 451, 1994.

6) P.Siegbahn and B.Liu, J. Chem. Phys. **68** (1978) 2457; D.G.Truhlar and C.J.Horowitz, J. Chem. Phys. **68** (1978) 2466.
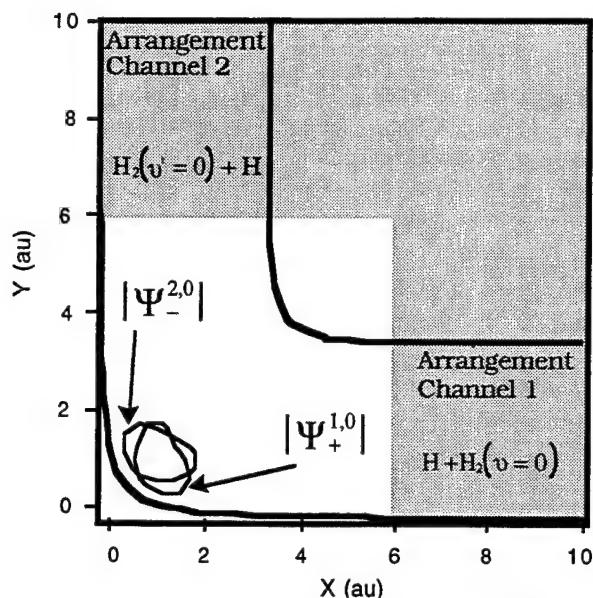
**Figure 1** The 0.1 au contours of the reactant Møller states, $\left|\Psi_+^{1,0}(X,Y)\right|$ and $\left|\Psi_-^{2,0}(X,Y)\right|$ respectively, at time $t = 0$ au. The thick lines are the 0.08 au contours of the LSTH potential energy surface and the shading illustrates where the absorbing boundary conditions are non-zero.
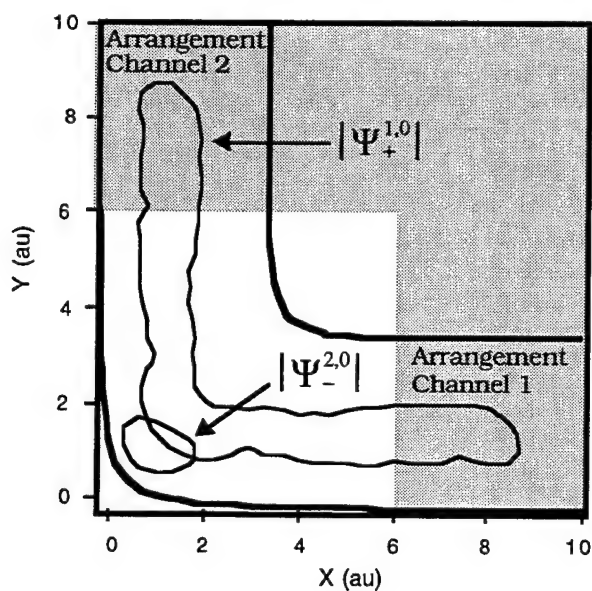


**Figure 2** The 0.05 au contour of the reactant Møller state, $\left|\Psi_+^{1,0}(X,Y)\right|$, at time $t = 3500$ au, and the 0.1 au contour of the product Møller state, $\left|\Psi_-^{2,0}(X,Y)\right|$, at time $t = 0$ au used to compute the correlation function, $C_{\gamma'\gamma}(t) = \left\langle \Psi_-^{2,0} \mid \Psi_+^{1,0} \right\rangle$. This figure illustrates how the absorbing boundary conditions attenuate the evolving Møller state and prevent reflection from the edge of the grid. Note that since the attenuation occurs where the product Møller state is zero, the absorbing boundary conditions do not influence the value of the correlation function. The thick lines are the 0.08 au contours of the LSTH potential energy surface and the shading illustrates where the absorbing boundary conditions are non-zero.
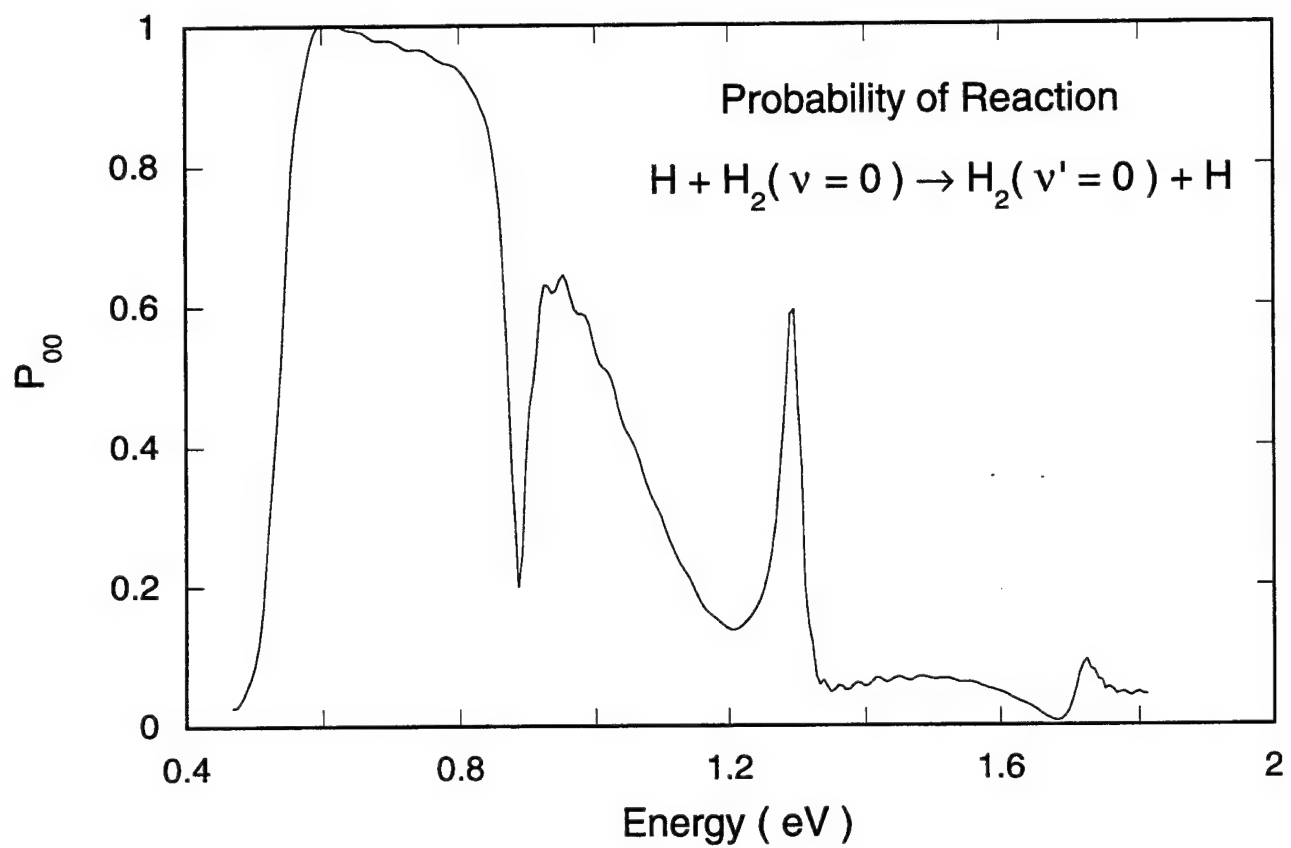
244

Figure 3 The probability, $P_{v'v}$ for the reaction $H + H_2(\, v = 0 \,) \rightarrow H_2(\, v' = 0 \,) + H$.

# DETERMINATION OF MEAN CLUSTER SIZES BY WATER CAPTURE

Michel Macler and Young K. Bae
Hughes STX/USAF Phillips Laboratory
OLAC PL/RKS, 10 East Saturn Blvd.
Edwards AFB, CA 93524-7680, USA

## ABSTRACT

Ar clusters produced in a supersonic expansion were doped with water using the pick-up method and subsequently electron impact ionized. Charged fragments were detected by a triple quadrupole mass spectrometer. The intensities of the water containing fragment peaks versus water pressure followed Poisson distributions, from which capture cross-sections were derived. These cross-sections corresponded to cluster sizes in agreement with published results for our range of stagnation conditions.

## EXPERIMENTAL

Clusters were produced by expanding Ar at pressures larger than 1 atm. into a $10^{-2}$-$10^{-1}$ Torr vacuum through a 0.17 mm diameter sonic nozzle. The resulting beam was skimmed and differentially pumped twice. The ultimate chamber pressure was $10^{-7}$ Torr. In order to produce different mean cluster sizes, the stagnation pressure was varied in the 1.15-3.4 atm. range, while the stagnation temperature spanned the 100-300 K range.

Water doping occurred in the third pumping stage using the pick-up method [1], with a doping path of about 1 meter. The water pressure was increased progressively from 0 to $10^{-4}$ Torr, resulting in an increasing level of Ar cluster doping, up to the formation of pure water clusters. Clusters were ionized by 100 eV electrons. The ionized fragments were detected by a triple quadrupole mass spectrometer. Phase sensitive detection was used. Scanning of the mass spectrometer, and data acquisition were controlled by a personal computer.

## RESULTS AND DISCUSSION

The intensities of the water containing fragment mass peaks versus pick-up cell pressure followed Poisson distributions [2], i.e. the pick-up of water molecules by Ar cluster was a random event. For one water molecule picked-up, we have:

$$I = K \times (\alpha L) \times \exp(-\alpha L) \qquad (1)$$

where I is the peak intensity, K is a constant, and L the length of the pick-up region. The parameter $\alpha$ is given by:

$$\alpha = n\sigma_{capture}F_{a_0}(\infty, x) \qquad (2)$$

where $\sigma$ is the capture cross-section, n is the number density of water, and $F_{a_0}(\infty, x)$ is a velocity averaging correction factor for

an assumed velocity independent hard-sphere potential. Tabulated
values are available [2].

$$x = c/\upsilon, \upsilon = \sqrt{2kT/m_S} \qquad (3)$$

where c is the cluster beam velocity. Equations (1), (2), and (3)
were used to derive cross-sections. A sample of data and its fit
is showed in Figure 1.

Results such as those of Figure 1 were averaged for several
masses corresponding to fragments containing 4 to 7 Ar atoms. In
this mass region, the cross-section reaches its asymptotic value.
Cross-sections derived for these fragments showed little
dispersion.

Assuming the sticking coefficient of water on Ar to be unity,
and the clusters to be spherical, cross-sections were converted
into mean cluster sizes using equations (4) and (5).

$$R_c = \sqrt{\frac{\sigma}{\pi}} \qquad (4)$$

where $R_c$ is the cluster radius, and $\sigma$ the cluster cross-section.
Assuming the Ar van der Waals radius $R_w$ to be $3.6 \times 10^{-8}$ cm, the
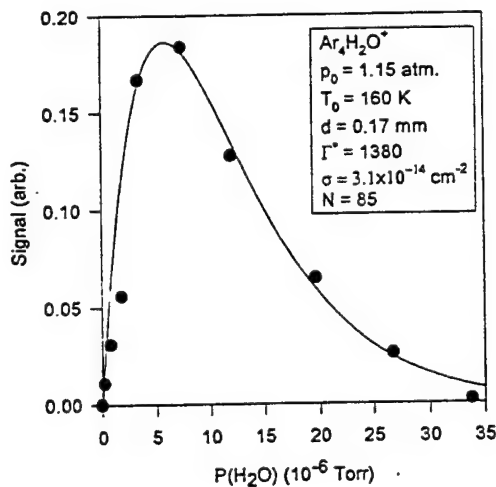cluster size N is defined as:



Figure 1 shows the variation of the peak intensity at mass
178, corresponding to a fragment containing 4 Ar and 1 water, with
water pressure in the pick-up cell. The line represent the
Poisson fit to the data. The quality of the fit is representative
of most recorded data. The stagnation conditions are given in the
text box. The derived cluster size is N = 85. The parameter $\Gamma^*$ is
the Hagena condensation parameter (see below).

$$N = \frac{4}{3}\pi\left(\frac{R_c}{R_{rw}}\right)^3 = 9 \times 10^{-2} R_c^3 \tag{5}$$

with $R_c$ expressed in Angstroms.

Scaling laws for both pressure and temperature variations were derived (see Figures 2 and 3). They were in agreement with published results [3]. We also compared our mean cluster sizes with those previously published, using the condensation parameter $\Gamma^*$ as a scaling factor [4,5]. This parameter accounts for both bimolecular and unimolecular reactions governing cluster growth and decay. It is dimensionless, defined as the ratio of a flow characteristic parameter to a species specific parameter:

$$\Gamma^* = \frac{\Gamma}{\Gamma_{ch}} \tag{6}$$

The parameter $\Gamma$ correlates flow properties with clustering in the following manner:

$$\Gamma = n_0 d^q T_0^{0.25q-1.5} (0.5 < q \leq 1) \tag{7}$$

where n is the number density, d the nozzle diameter, and T the temperature. The subscript 0 refers to stagnation conditions at the nozzle. The exponent q is 0.85 for Ar. $\Gamma_{ch}$ is defined by:

$$\Gamma_{ch} = r_{ch}^{q-3} T_{ch}^{0.25q-1.5} \tag{8}$$

where $r_{ch}$ is a characteristic length based on the species solid properties, and $T_{ch}$ is derived from the species sublimation enthalpy. $\Gamma_{ch}$ can be calculated for various species, therefore allowing to compare the condensation properties of metals and rare gases by the use of $\Gamma^*$ [4].

In Figure 4 we used $\Gamma^*$ as a scaling parameter, even though we only plotted Ar data, because it is a universal parameter. Our results match well those derived from corrected time of flight spectroscopy [6], Rayleigh scattering [7], and electron diffraction [8]. However, the results of Farges et al. [9] show consistently higher cluster sizes than all other measurements. The "slow down" measurements of Cuvellier et al. [10] are in agreement with those of Farges et al. for small clusters, but converge with those of others for larger clusters. In Figure 4 we fitted all data, but that of reference 9. Our results fall well within the confidence range of this fit. The results of Farges et al. have been considered by many to be the most accurate and have been used by some for calibration. This would imply that, especially for smaller clusters, most other measurements are substantially underestimating actual cluster sizes. Our numbers rely on three assumptions:

-1. The water on Ar sticking coefficient is unity.

-2.     Clusters are spherical.
-3.     The average water containing fragment ion originated
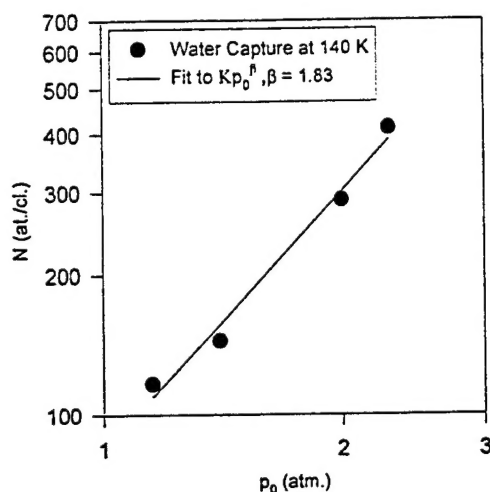        from an average size cluster.



Figure 2 shows the variation in cluster size at 140 K, with a nozzle diameter of 0.17 nm for a range of stagnation pressures. The pressure exponent of 1.83 is within the range of previously published data [3].
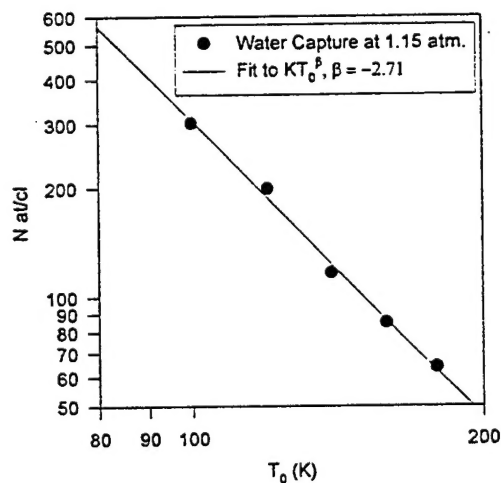


Figure 3 shows the variation in cluster size at 1.15 atm., with a nozzle diameter of 0.17 mm for a range of stagnation temperatures. The temperature exponent of -2.71 is within the range of previously published data [3].

249

The first two assumptions will not be correct for really small clusters. Assumption -1. gives a lower limit, since the sticking coefficient can be less that one. Assumption -2. gives an upper limit, since an icosahedral cluster can have a larger cross-section than a spherical cluster with the same number of atoms. These errors may or may not balance out the result, depending on the actual clusters. Based on water electrostatic properties, assumption -3. appears reasonable, since we expect water to "stick" to the ionized, detected moiety.

Our first two assumptions are much better suited for larger clusters. However, one needs to consider a potential pitfall: for large Ar clusters the mean number of dopant can be larger than one. In that case, the statistics of the doped cluster fragmentation becomes crucial, i.e. one needs to know whether or not the average doped cluster fragments will retain the original number of dopant. If so, cross-sections derived from fragments containing this number of water molecules would reflect the actual mean cluster size. When considering the water dimer bonding energy and electrostatic properties, it seems plausible that the water molecules would remain on the ionic fragment detected by the mass spectrometer. Therefore, one would need to investigate fragments containing the appropriate number of water molecules and use the proper Poisson expressions to extract the actual cross-sections and cluster sizes.



$$N = 3.3 \times 10^{-5} \times \Gamma^{*2}$$
$$\Gamma^{*} = 1275 \times (p_0/\text{atm.}) \times (d/\text{mm})^{0.85} \times (T_0/300 \text{ K})^{-2.29}$$

Legend:
- ● This work
- □ Karnbach et al.
- △ Hagena 1987
- ▽ Farges et al. 1986
- ◇ Cuvellier et al.
- ⬡ Bell et al.
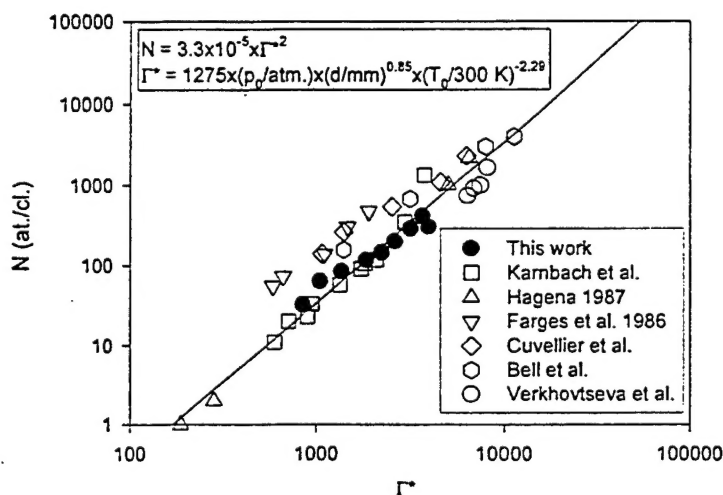- ○ Verkhovtseva et al.

Figure 4 shows a comparison between the cluster sizes obtained from this work and some of those previously published. The line is a fit of all data but that of Farges et al., since it is consistently offset from all other measurements.

## CONCLUSION

Water capture appears to be a simple, reliable, and inexpensive way of measuring Van der Waals cluster mean sizes. It does not require expensive scientific apparatus, such as that needed for electron diffraction measurements or Rayleigh scattering. The data analysis is simple, unlike that needed for corrected cluster sizes derived from time of flight mass spectrometry.

## REFERENCES

[1]   Gough T, Mengel M, Rowntree P, and Scoles G. Infrared spectroscopy at the surface of clusters: $SF_6$ on Ar. *J Chem Phys*, 1985, 83: 4958-4961

[2]   Lewerenz M, Schilling B, and Toennies JP. Successive capture and coagulation of atoms and molecules to small clusters in large liquid helium clusters. *J Chem Phys*, 1995, 102: 8191-8207

[3]   Hagena OF and Obert W. Cluster formation in expanding supersonic jets: effect of pressure, temperature, nozzle size and test gas. *J Chem Phys*, 1972, 56: 1793-1802

[4]   Hagena OF. Condensation in free jets: comparison of rare gases and metals. *Z Phys D: Atoms, Molecules, and Clusters*, 1987, 4: 292-299

[5]   Hagena OF. Cluster ion sources. *Rev Sci Instrum*, 1992, 63: 2374-2379

[6]   Karnbach R, Joppien M, Stapelfeldt J, Woermer J, and Moeller T. CLULU: an experimental setup for luminescence measurements on van der Waals clusters with synchroton radiation. *Rev Sci Instrum*, 1993, 64: 2838-2849

[7]   Bell AJ, Mestdagh J-M, Berlande J, Biquard X, Cuvellier J, Lallement A, Meynadier P, Sublemontier O and Visticot J-P. Mean cluster size by Rayleigh scattering. *J Phys D: Appl Phys*, 1993, 26: 994-996

[8]   Verkhovtseva ET, Bondarenko EA, and Doronin YuS. Cluster size effects in vuv radiation spectra of argon and krypton supersonic jets. *Chem Phys Lett*, 1987, 140: 181-188

[9]   Farges J, de Feraudy MF, Raoult B, and Torchet G. Noncrystalline structure of argon clusters. II. Multilayer icosahedral structure of $Ar_N$ clusters 50<N<750. *J Chem Phys*, 1986, 84: 3491-3501

[10]  Cuvellier J, Meynadier P, de Pujo P, Sublemontier O, Visticot J-P, Berlande J, Lallement A, and Mestdagh J-M. A simple method to determine the mean cluster size in a molecular beam. *Z Phys D: Atoms, Molecules, and Clusters*, 1991, 21: 265-269